STRESS ANALYSIS OF

OVERLAPPED CRANKSHAFTS

by

Anthony P. Sime, B.Eng

Thesis submitted to the University of Nottingham

for the degree of Doctor of Philosophy

October 1998

TABLE OF CONTENTS

CHAPTER 5 GEOMETRIC INVESTIGATIONS

ABSTRACT

The crankshaft is a complex component, and as such, the influence of its geometric parameters on stresses seen under service loads is not well understood. The objectives of this work are to investigate the effects of a wide range of geometric parameters on stresses in overlapped crankshafts, to find correlation between results and to formulate simple methods of predicting peak stress levels. It is intended to achieve this by use of the Finite Element (FE) and Boundary Element (BE) methods.

Individual crankthrows are loaded under the important loadcases of bending and torsion. Stress concentration factors are determined by normalising peak stresses with respect to the nominal stress occurring in the most appropriate section in the neck between the fillets. Analyses are carried out in 2D and 3D, making use of symmetry as far as possible.

Many of the governing dimensions of the crankthrow are included in the analyses; crankpin and journal diameters, crankpin and journal overlap, and web thickness. Variations in SCF are plotted over a wide range for each of these parameters. Additionally, features such as fillet size and shape, bore-holes, dimples, cut-back webs and oil holes are investigated. It is found that the effects on stress of individual parameter changes can be superimposed to accurately predict the effect of combining various parameter changes in one model.

The crankpin and journal fillet radii and the length of the minimum section between the fillets are shown to be the critical parameters in determining the peak stress levels in the crankshaft. SCFs obtained from the range of analyses performed show good agreement with the classical theory of SCFs in notched bars.

Bore-holes and dimples are found to offer significant benefits in terms of peak stress reduction, in addition to their common usage of reducing the out of balance crankpin mass.

The FE and BE methods give accurate results for stress analysis of crankshafts and offer several advantages over traditional experimental techniques; they are ideally suited to parametric analyses, can be carried out relatively quickly, results are repeatable because boundary conditions can be exactly defined, and the cost of analysis is significantly reduced.

ACKNOWLEDGEMENTS

I would like to express my gratitude to the many people who have assisted me during the course of this research. Special thanks must go to my supervisors Professor Tom Hyde and Dr Nick Warrior for their continued support, guidance and friendship. Thanks are also due to Professor Henry Fessler for his constant inspiration and enthusiasm for the subject which has provided the foundations of several ideas presented in this thesis.

Thanks must also go to the industrial sponsors, Mirrlees Blackstone, in particular Dr Ian Bickley and Vincent D'Olier, who have both greatly assisted in my understanding of the subject. Funding for the research was provided by Mirrlees Blackstone (Alstom Engines) and the EPSRC under the CASE agreement and this is gratefully acknowledged.

Finally, thanks to Helen for her constant companionship and invaluable support over the past three years.

NOMENCLATURE

α	angular position in fillets - Figure 5.1
β	angular position in fillet measured about a notional centre - Figure 5.3
Δ	recess of fillet - Figure 2.2
ϕ	angle of dimension H to vertical - Appendix 1
ν	Poisson's ratio
θ	angular position around crankpin/journal - Appendix 1
σ	direct stress
τ	shear stress
Ω	fixed dimension in compound fillet - Figure 5.1
A	cross-sectional area of nominal stress bar - Appendices 4 and 5
B	web width - Appendix 1
C	maximum width of crankpin and journal overlap - Appendix 1
D_j	diameter of journal - Appendix 1
D_p	diameter of crankpin - Appendix 1
E	eccentricity (throw) - Appendix 1
E	Young's modulus
F_{rp}	radial force exerted on crankpin - Appendix 1
H	minimum distance between crankpin and journal fillets - Appendix 1
I	stress index
J	radial distance from crankpin centreline - Appendix 1
K	stress concentration factor

L	distance from journal centre to web centre - Appendix 1
L_t	crankthrow span - Appendix 1
L_x	axial distance between F_{rp} and Q_{rj} - Appendix 8
M_{rj}	radial couple exerted on journals (pure bending) - Appendix 1
N	normal force on minimum section
P	change in web thickness - Appendix 8
Q_{rj}	reaction load at journal - Figure 2.3
R_{pn}	crankpin fillet radius n - Figure 5.1
S	overlap of crankpin and journal - Appendix 1
T	web thickness - Appendix 1
T_j	torque exerted on journals - Appendix 1
U	resultant displacement of inner web face
V	axial distance between end-points of section H - Appendix 1
W	moment of resistance
X	axial undercut of fillet - Figure 5.1
Y	radial extent of fillet - Figure 5.1

Non-dimensional notation

b	B/D_p
c	C/D_p
δ	Δ/D_p
d	D/D_p
e	E/D_p
h	H/D_p

r	R/D_p
s	S/D_p
t	T/D_p
x	X/D_p
y	Y/D_p

Suffices

'	maximum stress
add	addition due to engine misalignment and bedplate deformation
b	bending
B	bore hole
c	compressive
+c	including compression
centre	at crankpin centre
f	final
F	due to radial force on pin
i	initial
j	at journal
p	at crankpin
pin	based on crankpin section
new	after variation in web thickness
nom	nominal
q	shearing
r	in radial direction

s	spiral
t	due to torsion
v	equivalent
w	at web centre
x	in x direction - Appendix 1
y	in y direction - Appendix 1
θ	in tangential direction

Abbreviations

SS	Standard crankpin / standard journal
SR	Standard crankpin / reduced journal
RS	Reduced crankpin / standard journal
RR	Reduced crankpin / reduced journal
ERS (SG)	Electrical resistance strain gauges
OCF	Optimised crankpin fillet
CD	Crankpin dimple
JD	Journal dimple
RO	Reduced overlap
Pin	Crankpin
Jnl	Journal

CHAPTER 1

INTRODUCTION

1.1 Overview

The crankshaft is an integral part of the internal combustion engine, yet there is still much debate regarding the distribution of stresses within it. In particular, the influence of geometric parameters on the stresses within these complex components is not well understood. The investigation reported in this thesis deals with overlapped crankshafts of large, medium speed Diesel engines, commonly used in ships, railways and electrical power generation. Such engines are built to fulfil four fundamental requirements; reliability, durability, ease of maintainance and economy of operation.

In the process of converting the linear reciprocating motion of the pistons into a rotational output, the crankshaft undergoes both bending and torsion. As these forces are transmitted through the crankshaft, it becomes highly stressed, particularly so at the crankpin/web and the journal/web intersections of the cranked shaft. As a consequence, fillet radii are used in these areas to reduce the stresses, but if the shaft is not carefully designed, these stresses can still reach unacceptably high levels with regard to material strength and fatigue life. Classification societies (discussed further in Chapter 2) exist to ensure that crankshafts are designed to exceed minimum standards.

1.2 Design of overlapped crankshafts

Every marine Diesel engine manufacturer must adhere to the strict rules laid down in the CIMAC Unified Requirement M53 rules [1], regarding the design of crankshafts. Many in the industry maintain that these rules contain hidden factors of safety, allowing the stated safety factor to take the relatively small value of 1.15. It is claimed that these hidden safety factors result in oversized crankshafts, which makes it difficult for the designer to produce a crankshaft that is acceptable in terms of the required engine specification and yet conforms to the M53 rules. It is anticipated that the work presented in this thesis will help to determine if the M53 rules do result in oversized crankshafts.

In addition to the M53 rules, there are several other constraints placed upon the design of crankshafts. Overall dimensions are a prime consideration for engines used in rail and marine propulsion applications where space is limited. Such crankshafts are designed with a large overlap of crankpins and journals, in order to permit narrow crank webs. The cylinder centre distance on the engine (and thus the total engine length) is therefore controlled by only the cylinder bore dimensions. The crankpins and journals are designed with large diameters, in order to have sufficient bearing areas to sustain the high firing pressures. The bore and stroke of the engine, and thus the engine capacity and power output are therefore directly related to crankshaft design. The designer must balance all of these parameters to produce an engine that fulfils the many criteria placed upon it.

1.3 Objectives of the thesis

Although many authors have analysed different aspects of the crankshaft geometry, this author has found no one work that details a thorough analysis of every major geometric parameter on the crankshaft. It is intended that this thesis will go some way to correcting this, providing a full documentation of the effects on stresses of every parameter on a typical overlapped crankshaft. It is anticipated that this will prove a useful addition to the knowledge of the crankshaft designer.

The basic crankshaft, upon which the analyses are based is designed by Alstom Engines, Mirrlees Blackstone Ltd [2]. It is used in a twelve cylinder vee-engine, designated 12MB430, which is a medium speed, four stroke, direct injection, tubocharged and intercooled engine. The 12MB430 produces 11750bhp at 600rpm and 21bar bmep. This engine has dimensions 8465 × 4990 × 4780mm and weighs approximately 100,000kg.

The methods of analysis are the numerically based Finite Element (FE) and Boundary Element (BE) methods. These have several advantages over more traditional experimental methods, not least of which speed of analysis, repeatability and the potential for significantly reduced cost of analyses. Both methods have only fairly recently been developed to a stage where it is reasonable to accurately analyse the stress distributions in such a geometrically complex component as the crankshaft. This is fundamentally due to an improvement in pre and post-processing interfaces and the rapidly increasing processor power available. The results from these two numerical

methods are validated against each other and against previously obtained experimental data.

A convenient method of analysing the stresses in the crankshaft is to consider the forces acting on a single crankthrow, of which the journals are supported in the centre of the adjacent bearings. This is the same statically determinate system as the CIMAC M53 rules consider. Although this will result in an approximation of the loads that would act in a continuous beam crankthrow, it tends to err on the safe side since it ignores the clamping effect of adjacent journals. However, this is of little consequence since this thesis is only concerned with the effects of changes to the crankshaft geometry on the stress distributions. It is not intended to determine operating stress levels.

Geometric analyses of the following crankshaft parameters and features are presented in this thesis; fillet size and shape, crankpin and journal diameter, crankpin and journal overlap, crank web thickness, bores and dimples, cut-back webs and oil holes.

The important loadcases of radial bending, pure bending and pure torsion are analysed. Respectively, these represent bending at top dead centre (T.D.C) as the load is transmitted from a firing piston, bending loads transmitted by cranks adjacent to the crankthrow considered, and torques transmitted from adjacent cranks. The loadcase of tangential bending, where the crankthrow is at some angle around it's cycle, is not considered. To analyse the whole crank cycle under such a loading is beyond the

scope of this thesis, and it is felt that there would be little real value in obtaining the stress distributions at, say, just one angle in the cycle.

The presentation of a successful application of the FE and BE methods to the analysis of crankshaft stresses, could be put forward as a case to CIMAC to allow the use of such numerical methods as a means of determining crankshaft safety. Alternatively, a new set of rules, based on results obtained by the FE and BE methods could be formulated and adopted as standard.

CHAPTER 2

LITERATURE REVIEW

2.1 Introduction

There is a great deal of literature available on the subject of crankshaft stress analysis. However, very little of this presents a full investigation into the effects (on crankshaft operating stresses) of every parameter defining the crankshaft geometry. Additionally, a lack of common standards makes it difficult to compare and combine results presented by different authors.

Historically, the classification societies (eg. Lloyds Register of Shipping, Bureau Veritas), in an effort to reduce the risk of crankshaft failures, carried out basic research into marine Diesel crankshafts and formulated rules which governed the design of such components. Marine engine manufacturers required approval for their crankshafts from all the major classification societies, even though the rules of individual societies differed considerably.

2.2 Design rules

During 1972-1979, a working group of the Counseil International Des Machines A Combustion (CIMAC) proposed a new set of rules with the aim of standardising the many different rules issued by the major classification societies. This unified set of rules [1], which is still in use today, is based on the bending and torsion investigations over a large geometric range, carried out by the German Internal Combustion Engine Research Association (ForschungsVereinigung Verbrennungskraftmaschinen, or FVV).

The CIMAC proposal assumes that the highest stresses occur in the fillet transitions between the journal/web (Figures 2.1 & 2.2a) and the crankpin/web (Figures 2.1 & 2.2b). In order to determine if the crankshaft is adequately dimensioned, the nominal alternating bending and nominal alternating torsional stresses are multiplied by the appropriate stress concentration factors (Equations 2.1 - 2.14). This results in an equivalent stress which is then compared with the fatigue strength of the selected crankshaft material. The fatigue strength can vary depending on the method of crankshaft manufacture (eg. continuous grain flow forging, steel castings, semi-built shrink fits [3]). FVV concluded that when calculating the equivalent stress under bending, an additional shear contribution should be also be added to the journal fillet only (Equation 2.2).

The calculation of nominal stresses is based upon a statically determinate system, where one single crankthrow is considered (Figure 2.1 and Appendix 1). The single crankthrow consists of one crankpin, surrounded by two webs and two half journals. The throw is simply supported at the journal bearing centres and is subject to gas and inertia forces, causing bending and torsion. Crankthrows with one connecting rod (in-line engine) and two connecting rods (vee-engine) acting on the crankpin are considered by the rules. Bending moments at the centre of the web, $Q \times L$, are calculated accordingly, based on a triangular bending moment distribution due to the radial component of the connecting rod force (Figure 2.3).

The nominal bending stress is defined as the ratio of the bending moment in the web centre to the "resistance moment" of the web cross-section (see Equation 2.3). The

nominal torsional stress is defined as the ratio of the nominal torque to the polar second moment of area of the respective crankpin or journal. The stress concentration factors, by which the nominal stresses are multiplied, are calculated from formulae derived by FVV relating to several geometric parameters of the throw.

The equivalent (or maximum) bending stresses are calculated as follows;

$$\sigma_{bp} = K_{bp} . \sigma_{bnom}$$ Maximum bending stress in crankpin fillet (2.1)

$$\sigma_{bj} = K_{bj} . \sigma_{bnom} + K_{q} . \sigma_{qnom}$$ Maximum bending stress in journal fillet (2.2)

where K_{bp} = Bending stress concentration factor in crankpin fillet

K_{bj} = Bending stress concentration factor in journal fillet

K_{q} = Shear stress concentration factor

σ_{bnom} = Nominal bending stress

σ_{qnom} = Nominal shearing stress

The nominal stresses are calculated as follows;

$$\sigma_{bnom} = \frac{M_{bnom}}{W}$$ Nominal bending stress (2.3a)

where $M_{bnom} = QL$ Nominal bending moment (2.3b)

and $W = \frac{BT^2}{6}$ Web cross-section "moment of resistance" (2.3c)

$$\sigma_{qnom} = \frac{Q}{A}$$ Nominal shear stress (2.4a)

where $Q = \frac{F_{rp}}{2}$ Shear force (2.4b)

and $A = BT$ Area of web cross section (2.4c)

The bending stress concentration factors are calculated as follows;

$$K_{bp} = 2.6914.f_p(s,t).f_p(t).f_p(b).f_p(r).f_p(d_{jb}).f_p(d_{pB}).f_p(\delta) \qquad (2.5)$$

where $f_p(s,t) = -4.1883 + 29.2004t - 77.5925t^2 + 91.9454t^3 - 40.0416t^4$

$$+(1-s)(9.5440 - 58.3480t + 159.3415t^2 - 192.5846t^3$$

$$+85.2916t^4) + (1-s)^2(-3.8399 + 25.0444t - 70.5571t^2$$

$$+87.0328t^3 - 39.1832t^4)$$

$$f_p(t) = 2.1790w^{0.7171}$$

$$f_p(b) = 0.6840 - 0.0077b + 0.1473b^2$$

$$f_p(r) = 0.2081r^{(-0.5231)}$$

$$f_p(d_{jB}) = 0.9993 + 0.27d_{jB} - 1.0211d_{jB}^2 + 0.5306d_{jB}^3$$

$$f_p(d_{pB}) = 0.9978 + 0.3145d_{pB} - 1.5241d_{pB}^2 + 2.4147d_{pB}^3$$

$$f_p(\delta) = 1 + (\delta_p + \delta_j)(1.8 + 3.2s)$$

$$K_{bj} = 2.7146.f_j(s,t).f_j(t).f_j(b).f_j(r).f_j(d_{jB}).f_j(d_{pB}).f_j(\delta) \qquad (2.6)$$

where $f_j(s,t) = -1.7625 + 2.981t - 1.5276t^2 + (1-s)(5.1169 - 5.8089t$

$$+3.1391t^2) + (1-s)^2(-2.1567 + 2.3297t - 1.2952t^2)$$

$$f_j(t) = 2.2422t^{0.7548}$$

$$f_j(b) = 0.5616 + 0.1197b + 0.1176b^2$$

$$f_j(r) = 0.1908r^{(-0.5558)}$$

$$f_j(d_{jB}) = 1.0012 - 0.6441d_{jB} + 1.2265d_{jB}^2$$

$$f_j(d_{pB}) = 1.0022 - 0.1903d_{pB} + 0.0073d_{pB}^2$$

$$f_j(\delta) = 1 + (\delta_p + \delta_j)(1.8 + 3.2s)$$

$$K_q = 3.0128.f_q(s).f_q(t).f_q(b).f_q(r).f_q(d_{pB}).f_q(\delta) \qquad (2.7)$$

where $f_q(s) = 0.4368 + 2.1630(1-s) - 1.5212(1-s)^2$

$$f_q(t) = \frac{t}{0.0637 + 0.9369t}$$

$$f_q(b) = -0.5 + b$$

$$f_q(r) = 0.5331r^{(-0.2038)}$$

$$f_q(d_{pB}) = 0.9937 - 1.1949d_{pB} + 1.7373d_{pB}^{\ 2}$$

$$f_q(\delta) = 1 + (\delta_p + \delta_j)(1.8 + 3.2s)$$

The equivalent torsional stresses are calculated as follows;

$\tau_p = K_{tp}.\tau_{nom}$ Maximum torsional stress in crankpin fillet (2.8)

$\tau_j = K_{tj}.\tau_{nom}$ Maximum torsional stress in journal fillet (2.9)

where K_{tp} = Torsional stress concentration factor in crankpin fillet

K_{tj} = Torsional stress concentration factor in journal fillet

τ_{nom} = Nominal torsional stress

The nominal torsional stress is calculated as follows;

$$\tau_{nom} = \frac{M_t}{W_p} \qquad \text{Nominal torsional stress} \qquad (2.10a)$$

where $M_t = T_j$ Applied torque (2.10b)

and $$W_p = \frac{\pi}{16}\left(\frac{D_p^4 - D_{pB}^4}{D_p}\right)$$ Polar "moment of resistance" of pin (2.10c)

or $$W_p = \frac{\pi}{16}\left(\frac{D_j^4 - D_{jB}^4}{D_j}\right)$$ Polar "moment of resistance" of journal (2.10d)

The torsional stress concentration factors are calculated as follows;

$$K_{tp} = 0.8.g(r,s).g(b).g(t) \quad (2.11)$$

$$K_{tj} = 0.8.g(r,s).g(b).g(t) \quad (2.12)$$

where $g(r,s) = r^{[-0.322+.1015(1-s)]}$

$$g(b) = 7.8955 - 10.654b + 5.3482b^2 - 0.857b^3$$

$$g(t) = t^{(-.145)}$$

Once the equivalent bending and torsional stresses have been calculated, they are combined at each fillet with the following equations;

$$\sigma_{vp} = \sqrt{(\sigma_{bp} + \sigma_{add})^2 + 3\tau_p^2}$$ Crankpin fillet equivalent stress (2.13)

$$\sigma_{vj} = \sqrt{(\sigma_{bj} + \sigma_{add})^2 + 3\tau_j^2}$$ Journal fillet equivalent stress (2.14)

where σ_{add} is an additional bending stress due to misalignment and bedplate deformation of the engine, the value of which varies depending on the type of engine.

2.3 Stress analysis methods

There are many different techniques available for analysing stress distributions in components. Some experimental methods have been established for many years and form the basis of much of the work carried out in the field of crankshaft stress analysis. These methods include brittle lacquers, extensometers, frozen stress photoelasticity and electronic resistance strain gauges (ERS). Table 2.1 shows which methods are popular in the literature.

Table 2.1 Experimental methods commonly used to analyse crankshaft stresses

References	Brittle Lacquer	Extensometers	Photoelasticity	ERS
Stahl [4]		✓		
Hoshino & Arai [5]				✓
Leikin [6]	✓			✓
Pfender et al. [7]		✓	✓	
Fessler & Sood [8]			✓	✓
Lowell [9]				✓
Arai [10]				✓

The brittle lacquer technique is a relatively simple and cheap method, and is primarily used to determine the positions and directions of principal strains. It's accuracy is typically ±20%, and it is therefore often used as a preliminary stage in an analysis with ERS gauges, to simply determine the critical positions and orientations of gauges. Leikin used this technique in reference [6]. A reflective undercoat is first sprayed onto the cleaned specimen surface. A lacquer is then selected, based on the temperature and humidity ranges of the test. This is applied to the specimen in a uniform coating by either spraying or brushing, and is then left to cure. When the specimen is loaded (incrementally), the lacquer cracks and gives a visual indication of the strain field.

Stahl [4] and Pfender, Amedick and Sonntag [7] made use of extensometers to determine stresses in crankshafts. Here, transducers are temporarily attached to the specimen surface. Under loading, the change in length between two points on the surface is measured and this is then converted to a stress. Extensometers tend to be bulky and are not ideally suited to measuring stresses in small fillets.

Frozen stress photoelasticity requires that a three-dimensional epoxy model, with the desired physical and optical properties for photoelastic analysis, be made of the crankthrow. The model is then loaded and subjected to a stress-freezing process, after which slices through various planes of interest are removed. Slices are examined in a transmission polariscope and the complete stress distribution in the plane of the slice can be obtained. The results from a carefully executed test can be considered to be the most precise and informative of the four experimental methods because a continuous stress distribution is obtained. However, photoelasticity requires that the model is sliced up after loading, thereby necessitating a new model for each test. Frozen stress photoelasticity is therefore not an ideal technique for investigating a wide range of model parameters.

ERS gauges are insulated conductors which are attached to the surface of a component, and measure direct strain at a point as a change in resistance. Careful preparation is essential and surfaces should be smooth and cleaned, but not polished. As will be seen from Table 2.1, most authors chose to use ERS gauges as the primary method for obtaining information about stress states in crankthrows. ERS gauges have the advantage of being particularly suited to measuring stresses in small fillets.

With the appropriate choice of gauge, principal stress directions and magnitudes can be determined. However, gauges are placed at discrete points on the model, and gauge lengths are typically in the order of 1mm, so stresses are effectively averaged over this length. Both of these factors mean that it is not guaranteed that the true peak stress will be obtained.

More recently, advances in technology have produced computers that are capable of quickly and efficiently running simulated analyses of geometrically complex components. The Finite Element (FE) Method has been established for many years as a means of analytically determining stresses, but its usage has been somewhat limited by the processing power available. Detailed FE stress analysis in fillets of crankshafts has only recently become commercially viable. In his reply to reference [11], G.C.Volcy [12] talks of Bureau Veritas' contribution (1979-1985) to the argument put to IACS (International Association of Classification Societies) for the adoption of the rules proposed by CIMAC. Bureau Veritas (BV) carried out FE analyses of a crankthrow and concluded that the FE calculations were laborious, expensive and the results were disappointing.

BV made use of the symmetry of crankthrows to reduce the size of the problem. Volcy concluded that although the stiffness and deformation of the crankshaft could be well represented, the exact supporting conditions were not easy to evaluate. The mesh produced by BV can be seen in Figure 2.4. There are no blend fillets modelled here, and the mesh would really only be useful for stiffness calculations. Volcy reported that, due to computer limitations, the required mesh refinement could not be achieved.

In 1993, Guagliano, Terranova and Vergani [13] showed that it was possible to accurately analyse crankthrows with the FE method, and to obtain excellent agreement with strain gauge tests. Their investigations were carried out with 2D and 3D meshes. The 2D mesh was constructed with 4 noded plane stress elements, with a total of 989 nodes, whilst the 3D model of a quarter crankthrow (Figure 2.5), used 8 noded elements with a total of 1945 nodes. The constraints imposed were the symmetrical ones and the loading was applied axially to the journal. The 2D results were found to be between 7 and 9% higher than the equivalent 3D results. 2D FE analyses can be run much more quickly than 3D analyses, requiring less processing time. In addition, large time savings can be achieved during pre-processing, especially when modelling such a complex geometry as the crankshaft. Guagliano et al. concluded that 2D models can be reliably used to predict stress concentration factors in 3D models, without any large errors, and with a considerable saving of calculation and test time. No indication is given in their paper of the number of models or the range of geometries used to arrive at this conclusion. It is felt that further investigation is necessary, making use of a wide range of geometries, to determine more precisely to what extent 2D results can be used to approximate 3D stress concentrations. It is also clear that 2D models are only useful for in plane bending loadcases, so for the analysis of the important torsional loadcase, 3D modelling is the only available option.

In their 1991 paper, McNamara and Trevelyan [14] used the crankshaft to highlight the advantages of combining the traditional Finite Element method with the relatively new and little used Boundary Element method. They observed that the method by which the geometric model is constructed is an important factor in the overall analysis time.

The Boundary Element (BE) method requires that only the surface of the component be modelled. This eliminates the difficulties of modelling the internals, which is necessary in the FE method, and substantially reduces the pre-processing period. McNamara and Trevelyan found that this reduction in model preparation time outweighed the increased BE analysis time. At most they ran a 70% BE, 30% FE model which took three times as long to run as the 100% FE model. They suggested that in the future, with developments in BE codes, it would be likely that complete crankshaft BE models would be practical.

In the BE approach the governing differential equations are transformed into integral identities. These are applicable over the surface (or boundary) and are numerically integrated over the boundary which is divided into small elements. Provided the boundary conditions are satisfied, a system of linear equations emerges for which a unique solution can be obtained (Becker [15]). The BE method emerged in the late 1960's with the development of high speed digital computers capable of solving problems with numerical methods. Although much work had already been published on integral equations, Rizzo [16] was the first to use displacements and stresses (or tractions) in an integral equation applicable over the boundary. BE formulations result in fully populated solution matrices which are unsymmetric with non-zero coefficients. This lengthens the processing time compared to FE (where the matrices are generally sparsely populated) and is one of the few disadvantages of the BE method. Other disadvantages, which are less applicable to crankshaft analysis, are that results are poor for thin shell analysis and interior modelling is necessary for non-linear problems. The main advantages of the BE method over the FE method are that less pre-processing

time is required as a result of the surface-only modelling, and for the same level of accuracy the BE method uses a lesser number of nodes and elements. Less unwanted information is obtained because generally stress concentrations and fracture occur at the surface. Unlike FE, the BE method can be easily applied to incompressible materials such as rubber, where Poisson's ratio is 0.5.

Numerical methods such as FE and BE methods have many notable advantages over the traditional experimental methods; analyses are relatively quick, constraints and loading conditions are exactly defined and are repeatable, and there is potential for significantly reduced cost of analyses. Another advantage, which is perhaps the most important for crankshaft analysis, is that geometries can be easily modified, making these methods (especially BE) ideal tools for performing parametric studies to determine stress levels in the crankshaft.

2.4 Effects of crankshaft geometry and shape

Stahl [4] published the first authoritative work on geometric parameters of crankshafts in 1958. He established the standard dimensionless parameters used commonly in the literature; R/D, B/D, T/D, and S/D. Stahl based his conclusions on results obtained from automobile crankshafts loaded under pure bending (uniform bending moment). As modern Diesel engines became more powerful, and cylinder firing pressures increased, it was necessary for the designer to increase the bearing areas for lubrication purposes. This was achieved by lengthening the crankpin and journal, and increasing their diameters. In order that the length of the engine and the stroke of the piston was not significantly altered, the resulting cranks were relatively thin webbed, with a large

overlap of crankpin and journal. Hoshino and Arai [5] noted that, despite such a tendency in the design of crankshafts, few reports were published concerning the effects of the dimensional proportions of these new crankshafts. They performed a series of strain gauge experiments to analyse these new crank shapes and derived formulae from fitted curves to calculate bending and torsion stress concentration factors, i.e.

$$K_b = 4.84 f_1\left(\frac{R}{D}\right).f_2\left(\frac{R}{D}.\frac{\Delta}{R}.\frac{S}{D}\right).f_3\left(\frac{B}{D}\right).f_4\left(\frac{T}{D}\right).f_5\left(\frac{T}{D}.\frac{S}{D}\right) \qquad (2.15)$$

$$K_t = 1.75 g_1\left(\frac{R}{D}\right).g_2\left(\frac{S}{D}\right).g_3\left(\frac{B}{D}\right) \qquad (2.16)$$

where for bending

$$f_1\left(\frac{R}{D}\right) = 0.420 + 0.160\sqrt{D/R - 6.864}$$

$$f_2\left(\frac{R}{D}.\frac{\Delta}{R}.\frac{S}{D}\right) = 1 + 81\left(0.769 - \left(0.407 - S/D\right)^2\right) \times \Delta/R\left(R/D\right)^2$$

$$f_3\left(\frac{B}{D}\right) = 0.285\left(2.2 - B/D\right)^2 + 0.785$$

$$f_4\left(\frac{T}{D}\right) = 0.444\left(D/T\right)^{1.4}$$

$$f_5\left(\frac{T}{D}.\frac{S}{D}\right) = 1 - \frac{\left(S/D + 0.1\right)^2}{\left(4T/D - 0.7\right)}$$

$$8 \le \frac{D}{R} \le 27, \quad 0 \le \frac{\Delta}{R} \le 1, \quad -0.3 \le \frac{S}{D} \le 0.3, \quad 1.2 \le \frac{B}{D} \le 2.1, \quad 0.36 \le \frac{T}{D} \le 0.56$$

and for torsion

$$g_1(\frac{R}{D}) = 31.6(0.152 - R/D)^2 + 0.67$$

$$g_2(\frac{S}{D}) = 1.04 + 0.317S/D$$

$$g_3(\frac{B}{D}) = 1.31 - 0.233B/D$$

$$7 \le \frac{D}{R} \le 45, \quad -0.286 \le \frac{S}{D} \le 0.222, \quad 1.14 \le \frac{B}{D} \le 2.00, \quad 0.30 \le \frac{T}{D} \le 0.558$$

Tests were conducted under radial bending (three point bending), pure bending and torsion. Fairly good agreement was obtained between the radial and pure bending stress concentration factors, which are therefore predicted by one formula for bending. The stress concentration factors in Equations 2.15 & 2.16 are based on a nominal stress calculated as the ratio of the bending moment at the web centre to the "resistance moment" of the crankpin cross section. These equations however are only applicable within the prescribed limits and when the crankpin diameter is equal to the journal diameter.

2.4.1 Crankpin and journal fillets

To allow further increases of crankpin and journal surface area, the crankpin and journal fillets are sometimes undercut into the web (see Figure 2.2b). Ideally, the fillets will have a large radius [5],[6], yet not occupy too great an axial distance. Compound fillets can be used to achieve the desired effect. Over the highly stressed region of the

fillet, the radius is large (the major radius), and elsewhere in the fillet, smaller (minor) radii can be used to tighten the fillet over lower stressed areas. It is therefore critical to have a clear understanding of where, in the fillet, the peak stresses will occur when the crank is subjected to the important loading modes of bending and torsion. Very little work has been published on stress distributions in compound crankshaft fillets, although some authors have investigated undercut (or recessed) fillets [5],[7],[8].

Hoshino and Arai [5] found that the stress concentration factor increased linearly with the depth of recessing at the fillets, but the rate of increase differed depending on the extent of overlap of the crankpin and journal. They also noted that the peak stress moved further around the fillet as the recess increased ($\alpha \approx 40°$ for flush fillets, $\alpha \approx 55°$ for recessed fillets where $\Delta/R = 1$, see Figure 2.2 for notation). Pfender, Amedick and Sonntag [7] (in which the FVV data was published) also observed an increase in peak stress when using recessed fillets.

Fessler and Sood [8] used the frozen stress photoelastic technique and strain gauges to investigate stress distributions in recessed fillets. They concluded that for their crankshaft geometry, the peak stresses occurred between 10° and 40° in the crankpin fillet, and between 25° and 60° in the journal fillet. They observed that a movement of 10° from the peak in the α direction led to significant reductions of the stress, and warned that great care should be taken when measuring fillet stresses with strain gauges.

It is generally acknowledged that the fillet stresses occuring under crankshaft bending are greater than those which occur under torsion (eg, [6],[11]). Donath and Seidemann [11] present data in their Table II (p9) relating to measurements of testbed stresses in a crankshaft of a four-stroke engine. In these tests, the peak bending stresses measured were between 3.5 and 4 times higher than the peak torsional stresses.

2.4.2 Overlap

The main consequences of modern crankshaft requirements have already been mentioned; increased overlap of crankpin and journal and reduced web thickness. Leikin [6] investigated the effects of overlap between the range of $-0.1 \leq S/D \leq 0.3$. He applied a pure bending moment to the crankthrow, and based the nominal bending stress on the web section $T \times B$. The stress concentration factors fell slowly as overlap was increased from -0.1 to 0.1, but fell more sharply between 0.1 and 0.3 (Figure 2.6). His graphs indicate that the maximum stress concentration factor occurs when $S/D \approx -0.1$ (no overlap of crankpin and journal). Hoshino and Arai [5], basing their nominal stress on the crankpin section, investigated the effects of overlap between the slightly larger range of $-0.3 \leq S/D \leq 0.3$. They too found that the stress concentration factor reached a maximum at an overlap of $S/D = -0.1$ (Figure 2.7). However, more recent crankshaft designs (particularly those dealt with in this thesis) have incorporated an even greater degree of overlap, where S/D is typically 0.45. Relatively few authors have investigated such extreme overlaps. The paper by Pfender et al. [7] is one such

publication where an overlap of $-0.5 \leq S/D \leq 0.5$ was studied, but these extremes require further investigation.

It is noted that, although the increased overlap has arisen partially because of increases in crankpin and journal diameters, little work has been published on the effects of such changes. Authors have instead concentrated on changing the throw (eccentricity) of the crankthrow whilst keeping diameters constant. However, it is not unusual for crankshafts to have different crankpin and journal diameters. This can be true not only at the design stage, but especially so in service when bearing failures necessitate regrinds of crankpin or journal. Regrinds are carried out as a means of refacing a damaged crankpin or journal bearing surface so that the crankshaft can continue in service. Typically 5% of the diameter is removed and fillets are machined radially inwards until they meet with the newly machined bearing surface (this incidentally also changes the fillet shape). The small-end/big-end bearing is then resized to the new crankpin/journal diameter.

The lack of research in this area suggests that the effects of changing diameters are currently not fully appreciated. Further research should be carried out so that the integrity of the crankshaft is not inadvertently compromised.

2.4.3 Web thickness

The dimensions of the web contribute significantly to the characteristics of the crankshaft, not only to it's length and stiffness, but also to it's ability to combat torsional vibration. Vibration of the crankshaft is caused mainly by out of balance masses, i.e. crankpins and webs. Counter-balance weights are secured to the crankshaft, in positions that will not impede it's rotation, to reduce the amplitude and change the natural frequency of vibration. In practice, the base of the web is the only area where such weights can be attached, and therefore the thickness of balance weight is determined by the thickness of the web. On a modern thin webbed Diesel engine crankshaft, the necessary balance weights are very large, thin, wedge shapes fanning out from the base of the web so as not to occupy too great a radial distance (see Figure 2.8). If the web thickness is reduced too far, the balance weight becomes impractically large, so a combination of geometric restrictions and acceptable stress levels must be taken into consideration when designing the crankshaft. Both Leiken [6] and Hoshino and Arai [5] studied web thickness and web width. They similarly concluded that at an overlap of S/D = -0.1 the SCFs increased as the web thickness was reduced (see Figures 2.6 & 2.7), and that web width generally had very little effect on fillet stress concentration factors. Leikin [6] did observe however, that for positive values of overlap, the SCFs decreased as the web thickness was reduced.

2.4.4 Bored crankpins and oil holes

The alternative to increasing the mass of the counter balance is to reduce the mass of the original out of balance components. One way this has been achieved is by boring a hole through the crankpin. Leikin [6], Pfender, et al. [7], Fessler and Sood [8], and Arai [10] have all investigated the effects of bore holes on stress concentration factors. Leikin [6] obtained, for a given R/T value, a basic stress concentration factor for a crankshaft without overlap or lightening holes. He then multiplied this basic factor by coefficients relating to crankpin bore, web width and overlap, the design curves for which are presented in [6]. Arai [10] briefly investigated the effects of crankpin bores. He concluded that the stress distribution in the journal fillet was changed by the presence of a crankpin bore, i.e. the peak stress moves from the $\theta_j = 0°$ plane, but it's value remains approximately the same as for a solid crankpin. Fessler and Sood [8] investigated the bore hole effect more rigorously, testing models with bored crankpins and bored/solid journals, under bending and torsion. They found, when applying a radial bending load to models with bored crankpins and journals, that the peak stress moved off the $\theta = 0°$ plane to a new position at $20° \leq \theta \leq 25°$ approximately. Stresses were symmetrical about the $\theta = 0°$ plane. Comparing the crankpin fillet stress distributions for models with bored and solid journals (Figure 2.9), the stress concentration factor in the bored model not only changed it's position in θ, but it's magnitude was significantly reduced (~27%). Under torsional loading, the algebraically greater stress concentration factors at positive and negative values of θ were plotted. The fillets close to solid sections showed a single peak around $\theta = 45°$, whilst the fillets close to bored sections showed significantly lower peaks at $\theta = 45°$ and $\theta = 0°$. Fessler and Sood [8] attributed the differences in distribution to the large

bores adjacent to the fillets, and the decrease in stress concentration factor to the greater flexibility of the hollow models. Pfender et al. [7] presented very similar findings to Fessler and Sood [8].

The stress redistribution that occurs when holes are present in the crankpin/journal should be considered when positioning the oil holes in the crankshaft. The oil holes transport oil to the bearings to provide lubrication between the small/big end bearings and the crankpin/journal. A typical oil hole configuration is shown in Figure 2.10. The main oil hole generally runs from the crankpin, through the web between the fillets, and into the journal. Smaller holes run from the main hole to the crankpin/journal surfaces. The effects of oil holes on stresses in the fillets are generally ignored in both the literature and stress calculations, even though the main oil hole is usually not close to the neutral axis of bending. Oil holes may have significant effects on the fillet stresses, and they warrant further investigation. Stresses at oil hole breakouts in both flat plates and at crankshaft bearing surfaces are generally more widely investigated, e.g. [17],[18],[19].

2.5 Definition of nominal stress

It is noticeable that of the many authors who have researched crankshaft stresses, few have based their calculated stress concentration values on the same nominal stress. Details of the components of the various nominal stresses are given in Table 2.2.

Table 2.2 The basis of the various nominal stresses used in the literature

	Bending			Torsion
Publications	Radial moment measured at	Pure bending only	Based on section through	Based on section through
Pfender, et al. [7]	FILLETS	-	PIN	-
Lowell [9]	FILLETS	-	PIN	-
Fessler, Sood [8]	PIN CENTRE	-	PIN	PIN
Hoshino, Arai [5]	WEB CENTRE	-	PIN	PIN
CIMAC [1]	WEB CENTRE	-	WEB	PIN/JNL
Stahl [4]	WEB CENTRE	-	WEB	-
Leikin [6]	-	✓	WEB	JNL
Guagliano, et al. [13]	-	✓	PIN	-

Because the stress concentration factors are generally based on slightly different nominal stresses, it becomes very difficult to make meaningful comparisons between them. In order to do so, it is necessary to multiply the SCF, K, by the nominal stress on which it is based, σ_{nomA}, and divide this by the new nominal stress, σ_{nomB}.

However, the data necessary to calculate the nominal stresses is often not readily available. This situation has arisen because there is no universal agreement as to which are the most realistic nominal stresses under the important loading modes. Lowell [20] observed this split in opinion, and wrote (in contrast to his earlier work in [9]),

"It is felt that consideration of a bending plane through the crankweb more clearly defines what is occurring than one through the crankpin section. Particularly in large power engines, standard practice inevitably dictates a web section modulus smaller than that of the crankpin, thus placing the bending plane developing the fillet stresses in the crankweb rather than in the crankpin."

Lowell's comments should be carefully considered. His suggestion that the stress region in the web (between the fillets) is the most appropriate, agrees with the classical theory of stress concentrations in notched bars [21], [22]. It is therefore suggested that further investigation is required in this fundamental area.

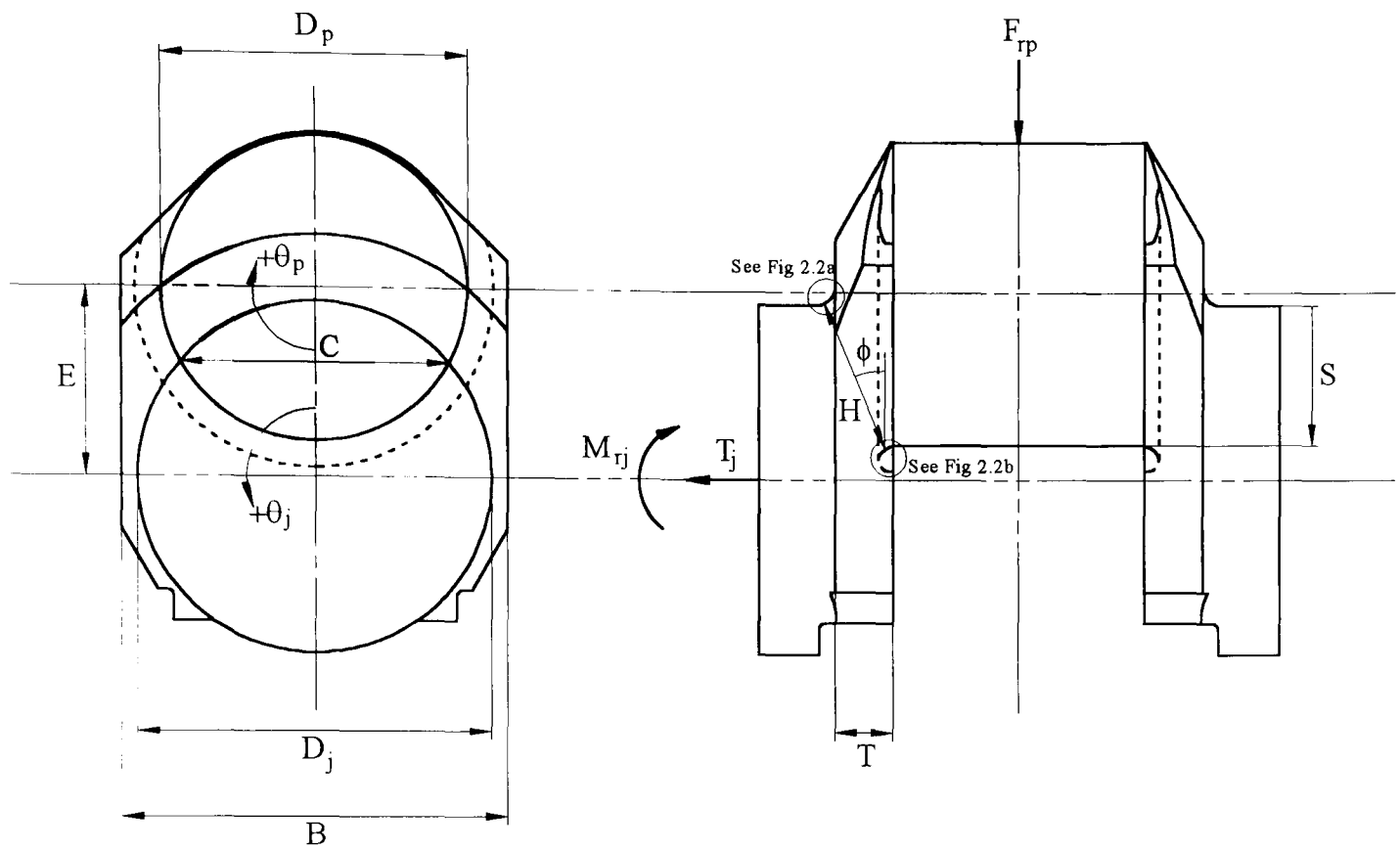

Figure 2.1. A single crankthrow

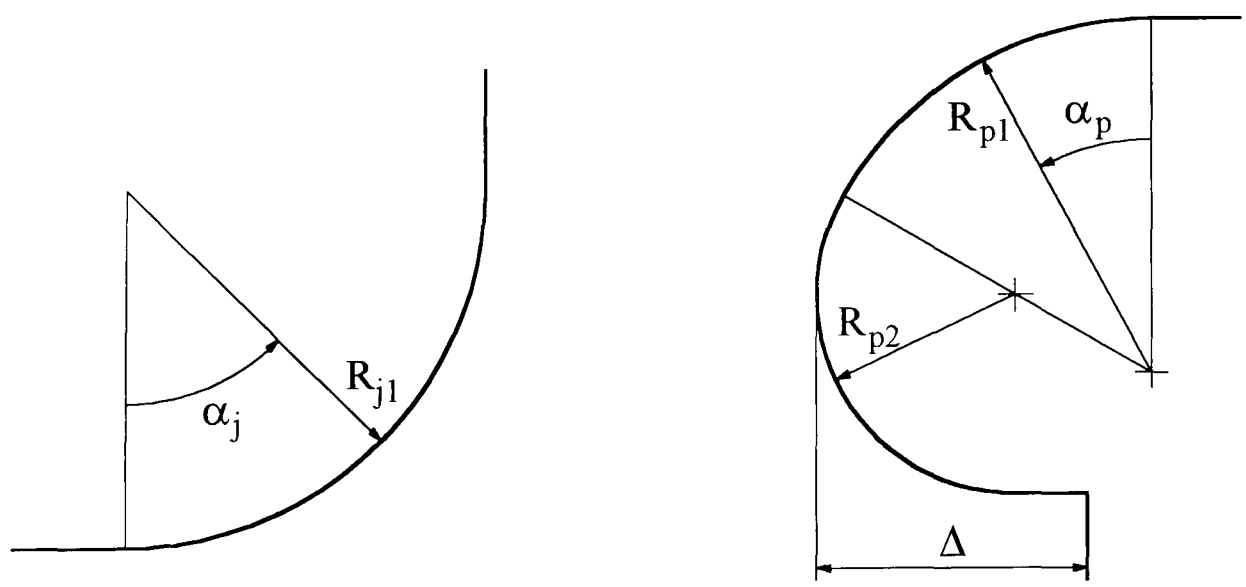

(a) Journal fillet (b) Crankpin fillet

Figure 2.2 Basic fillet geometries used in analyses

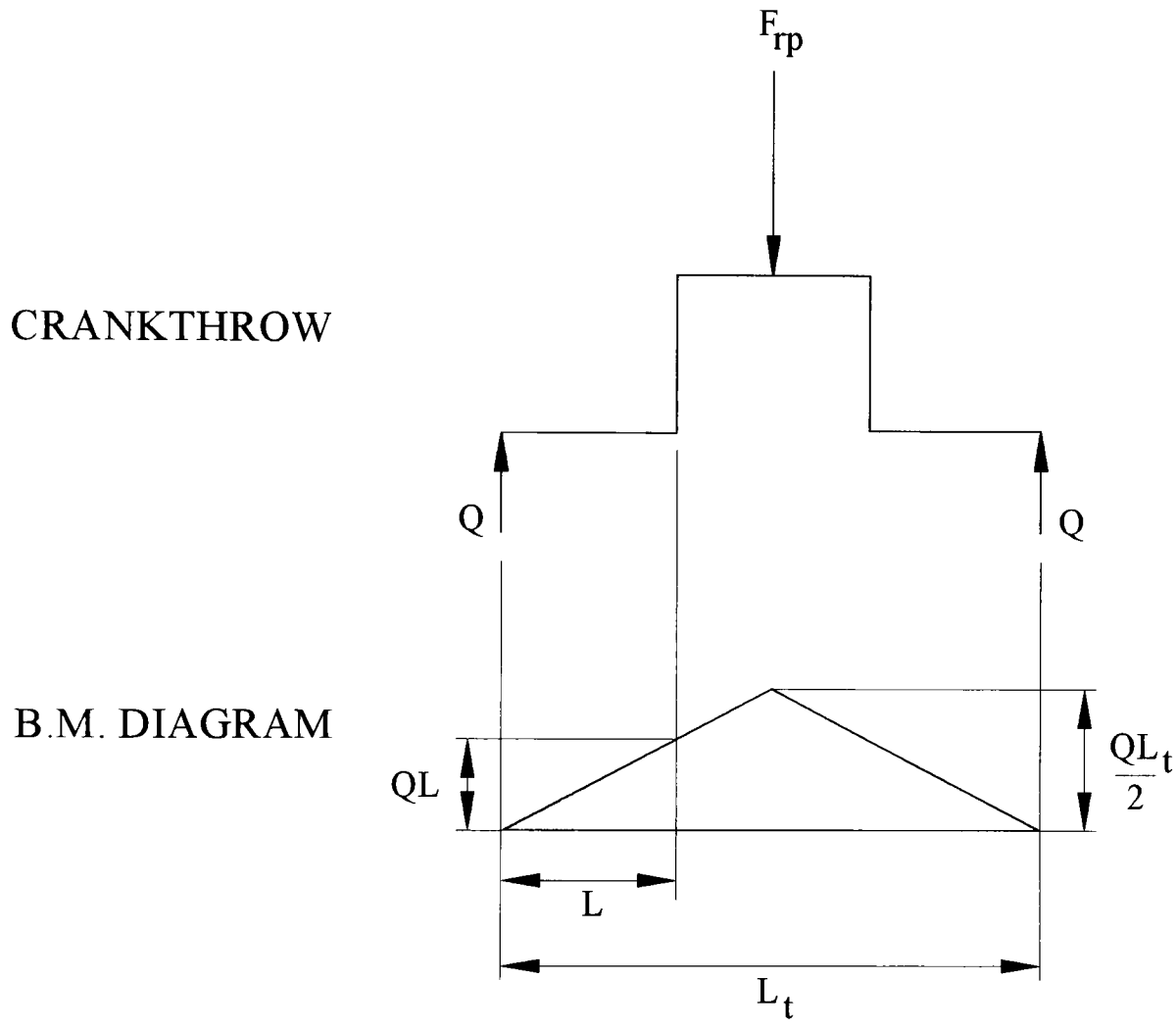

Figure 2.3. Bending moment diagram of the radial loads acting on a single crankthrow

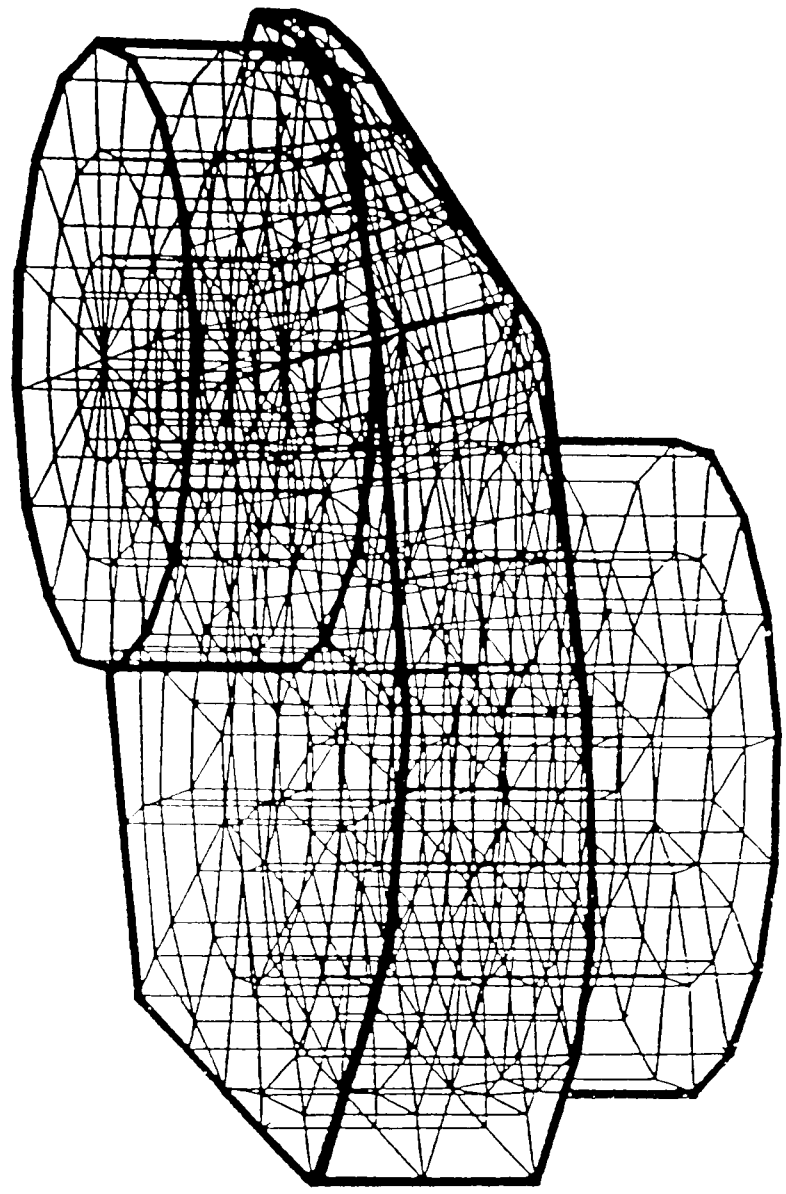

Figure 2.4. 3D FE model of a half crank
Donath & Seidemann (Discussion) [11]

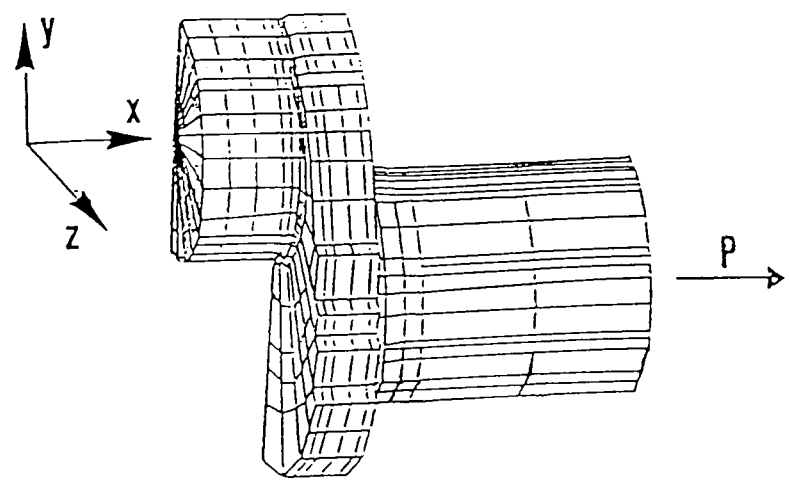

Figure 2.5. 3D FE model of a quarter crank
Guagliano, Terranova & Vergani [13]

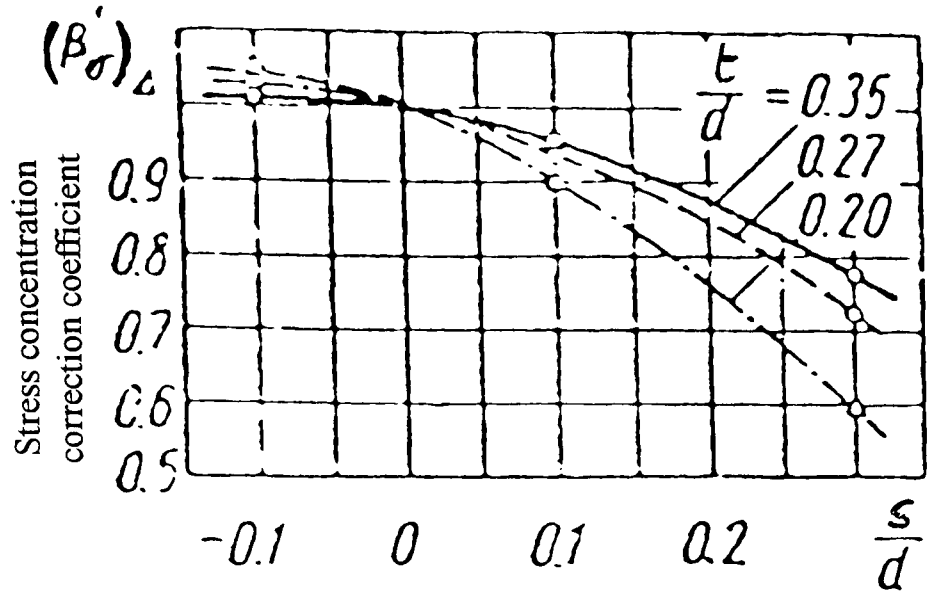

Figure 2.6. The effect of overlap and web thickness
Leikin [6]

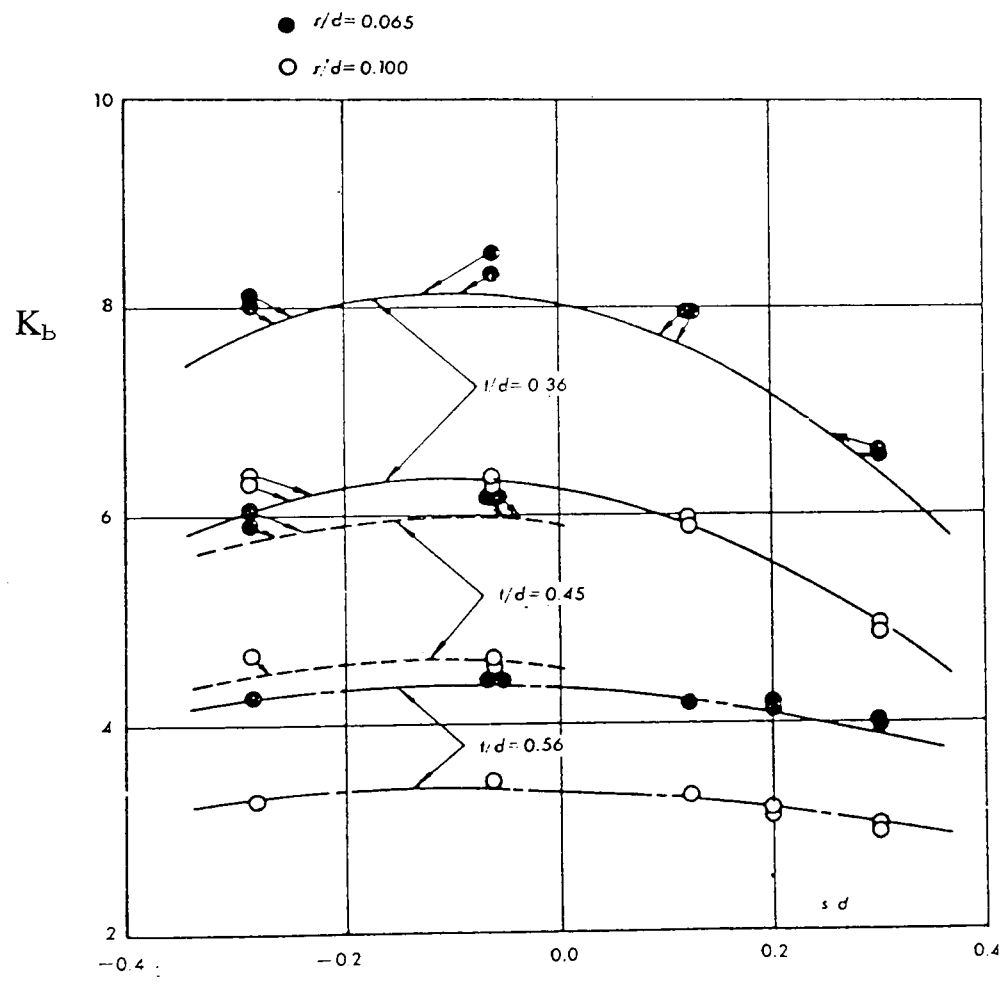

Figure 2.7. The effect of overlap and web thickness
Hoshino & Arai [5]

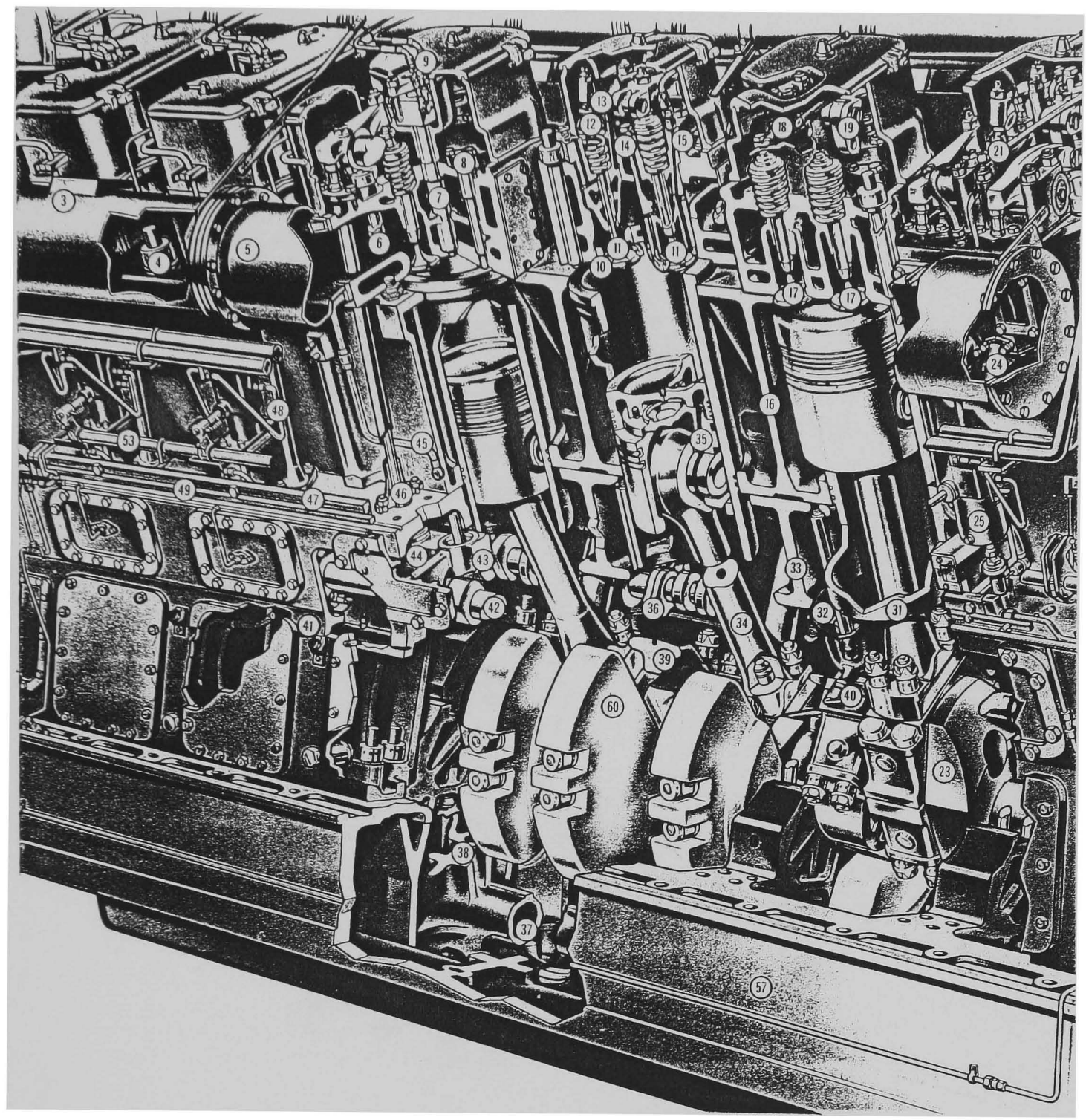

Figure 2.8. Figure showing balance weights (60) mounted on underside of crankwebs (23)
Alstom Engines, Mirrlees Blackstone [2]

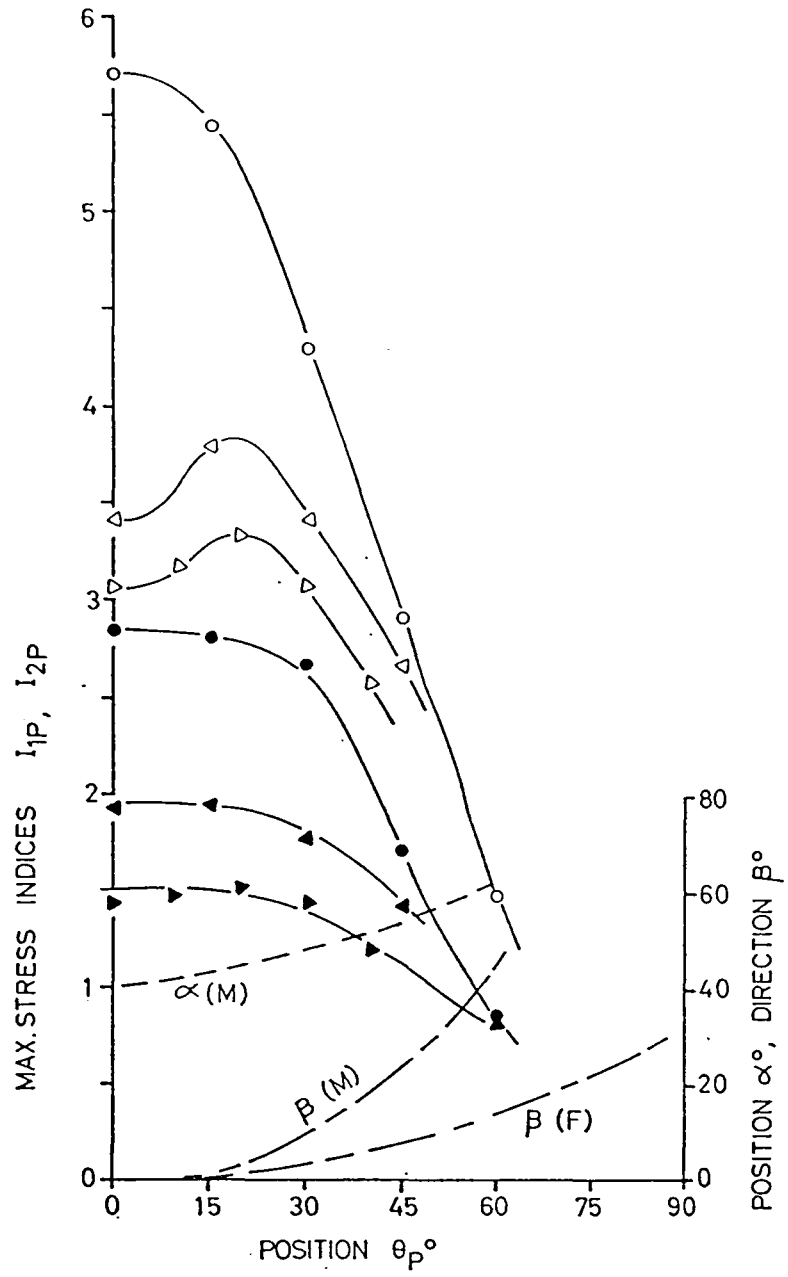

Loading mode:	Pure bending	Pure bending	3 point bending
Shape:	Solid journal	Bored journal	Bored journal
I_1	○	◁	▷
I_2	●	◀	▶

Figure 2.9. Principal stress indices due to bending plotted against θ_p
Fessler & Sood [8]

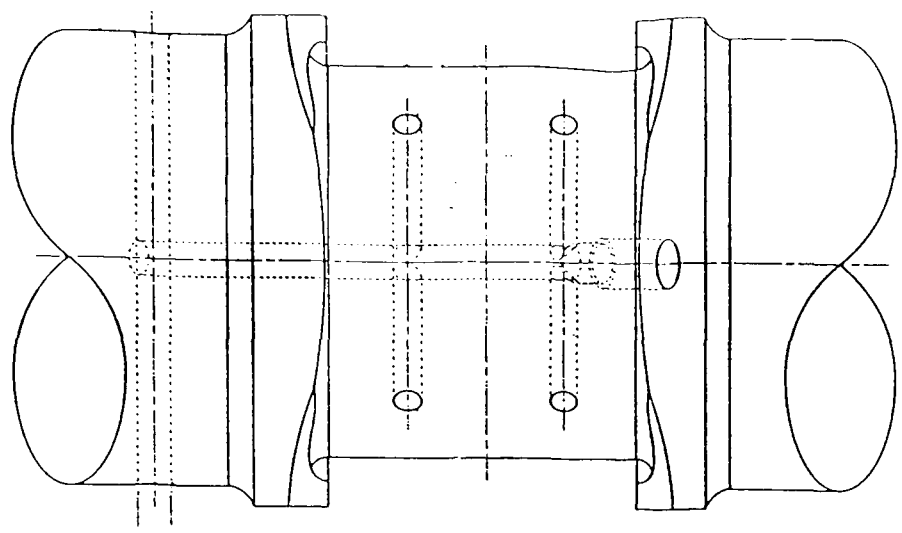

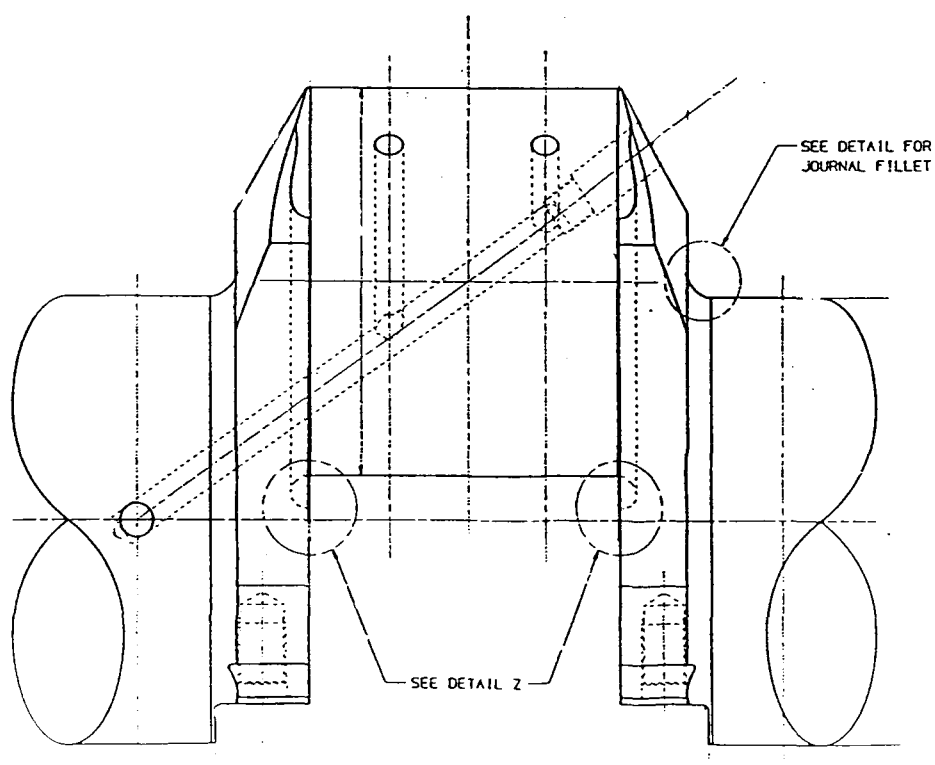

Figure 2.10. Typical oil hole locations
Alstom Engines, Mirrlees Blackstone [2]

CHAPTER 3

VALIDATION OF ANALYSIS METHODS

3.1 Introduction

In this investigation, two methods are used to determine stresses in overlapped crankshafts; the Finite Element (FE) Method [23],[24],[25], and the Boundary Element (BE) Method [26],[15]. The results from the two numerical methods (FE and BE) are validated by various techniques;

1. Comparison of numerical method results with experimental results (photoelastic and strain gauge).
2. Direct comparison of FE and BE results.

After the results have been validated, it is possible to use similar mesh densities and loading conditions to analyse slight variations of the crank geometry. This provides reliable information on how the stress levels are affected by changing geometric parameters of the crankshaft.

3.2 Validation of the FE method

The crankshaft initially modelled with the FE method was chosen because of the availability of photoelastic and strain gauge data for the same basic geometry. The geometry of this crankshaft was that of a design by Alstom Engines, Mirrlees Blackstone for use in a V12 engine. The fillet shapes used in the photoelastic and strain gauge work differed slightly, so the appropriate fillet geometries are modelled when comparisons are made between the FE and two sets of experimental results.

The loadcases chosen for investigation were radial bending, pure bending and pure torsion. Principal stress indices, at various positions around the crankpin and journal fillets were determined, normalised with respect to nominal stresses related to the crankpin dimensions.

3.2.1 2D radial bending

In order to reduce computer processing time, initial investigations were carried out with two-dimensional (2D) models. The geometries of these 2D models were created in FEMGEN [23], and were used to investigate the effects of mesh density, loading conditions, Poisson's ratio and plane strain/stress conditions on the stress distributions. The conclusions drawn from the 2D work could then be used when modelling in 3D to reduce the number of nodes in the models, which in turn determines the array size that is solved by the computer, and therefore the overall analysis time.

A 2D mesh of a crankthrow was created and refined to a point where the elemental stresses around the fillets were almost continuous and so that the predicted components of stress normal to the surfaces of the fillets were negligibly small around both the crankpin and the journal fillets. The elements used in the meshes were 6 and 8 noded quadratic, under plane strain conditions and were assigned a thickness of unity.

The models were loaded under radial bending only, with a point load applied at one quarter of the distance along the top surface of the crankpin (the quarter point). The crankshaft is designed for a vee-engine, and as such, each crankpin is subjected to loads from two connecting rods. Here, the only load considered to act on a single

throw at any one time is that closest to the fillets of interest, which will produce the higher stresses. The magnitude and position of the load chosen for the analyses was the same as that applied during the photoelastic work. The FE models were constrained such that;

1. The node at the bottom centre of the right-hand journal was constrained in the x and y directions*.
2. The node at the bottom centre of the left-hand journal was constrained in the y direction*.

* See Appendix 1 for the definition of the coordinate system.

The Young's Modulus, E, and Poisson's ratio, ν, appropriate to the stress frozen photoelastic analyses are 11.5 MPa and 0.5 respectively. A Poisson's ratio of 0.5 can cause problems in FE analyses because the term $1/(1-2\nu)$ appears in some formulations, hence a value of 0.49 was used in some analyses. However, in most of the 2D analyses, a Poisson's ratio of 0.3 was used because this is similar to the Poisson's ratio of a steel crankshaft. The results were normalised with the maximum bending stress occurring in the crankpin. All analyses were carried using ABAQUS [24], running on a DEC Vax-Alpha workstation.

3.2.1.1 Mesh refinement

Table 3.1 gives details of the Poisson's ratio, symmetry conditions, loading and element type used in each of the 2D mesh refinement analyses under radial bending. Each model is of one full crankthrow; one crankpin, two webs and two half journals.

Table 3.1 2D FE mesh refinement analyses

Model	Fig	ν	Journal length	Symmetry conditions	Loading	Standard/ Hybrid els	P.Stress/ P.Strain
V122Dq	3.1a	0.3	½ jnl	Full throw	Point-¼pt	Standard	P.Strain
V122Dh	3.1b	0.3	½ jnl	Full throw	Point-¼pt	Standard	P.Strain
N122Dd	3.1c	0.3	½ jnl	Full throw	Point-¼pt	Standard	P.Strain

The crankpin and journal fillet meshes for each model are shown in Figure 3.1. The number of elements around the two fillets is increased through the range of models, and the resulting principal stress indices are plotted in Figure 3.2.

As the mesh is refined, two effects are observed at both fillets;

1. The minimum principal stress index tends to zero, as would be expected. This indicates that the accuracy of the results is improving.
2. There is no further change in the maximum principal stress index when the greatest number of elements are used (compare results for V122Dh and N122Dd), i.e. convergence of results has been achieved.

It is therefore desirable, in the interest of reducing analysis time, to use the mesh discretisation that produces accurate results, but with fewer elements (V122Dh). This mesh was constructed from 3421 nodes and 1072 elements.

3.2.1.2 The effect of Poisson's ratio

Table 3.2 describes the models used to assess the effects of the value of Poisson's ratio used.

Table 3.2 2D FE Poisson's ratio analyses

Model	ν	Journal length	Symmetry conditions	Loading	Standard/ Hybrid els	P.Stress/ P.Strain
V122Dh	0.30	½ jnl	Full throw	Point-¼pt	Standard	P.Strain
V122Dj	0.35	½ jnl	Full throw	Point-¼pt	Standard	P.Strain
V122Dk	0.40	½ jnl	Full throw	Point-¼pt	Standard	P.Strain
V122Dg	0.45	½ jnl	Full throw	Point-¼pt	Standard	P.Strain
V122Dm	0.49	½ jnl	Full throw	Point-¼pt	Standard	P.Strain
H122Dh	0.30	½ jnl	Full throw	Point-¼pt	Hybrid	P.Strain
V122Do	0.49	½ jnl	Full throw	Point-¼pt	Hybrid	P.Strain
V122Dp	~0.5	½ jnl	Full throw	Point-¼pt	Hybrid	P.Strain

The results for the models with standard elements are presented in Figure 3.3. As the value of Poisson's ratio is increased, the maximum principal stress index curve becomes more unstable. There is a marked change in stress distribution at higher values of Poisson's ratio (ν=0.45 to 0.49), but this is a limitation of the element formulation which uses $1/(1-2\nu)$. The last three models in Table 3.2 use hybrid elements (6 and 8 noded, quadratic plane strain), which are designed to cope with incompressible materials ($\nu \approx 0.5$). In these cases it is not possible to obtain the solution to a problem in terms of the displacement history only. This is because a very small change in displacement will produce an extremely large change in stress, so that a

purely displacement based solution is too sensitive to be numerically useful and round-off on the computer may cause the method to fail. Hybrid elements, are effectively mixed formulation elements using a mixture of displacement and stress variables. However, the increase in accuracy of results is at the expense of increased computer run times.

Figure 3.4 shows the stress distributions for the three hybrid element models, which have Poisson's ratios of 0.3, 0.49 and 0.4999 respectively. At the crankpin and journal fillets, the stress distributions remain completely unaltered as ν is increased from 0.3 to 0.4999.

3.2.1.3 Effect of plane strain / plane stress assumptions

Table 3.3 describes two models, one of which is constructed with plane strain elements, and the other with plane stress elements.

Table 3.3 2D FE plane strain / plane stress analyses

Model	ν	Journal length	Symmetry conditions	Loading	Standard/ Hybrid els	P.Stress/ P.Strain
V122Dh	0.3	½ jnl	Full throw	Point-¼pt	Standard	P.Strain
V122Dl	0.3	½ jnl	Full throw	Point-¼pt	Standard	P.Stress

Figure 3.5 shows that the plane strain / plane stress assumptions have no bearing on the maximum principal stress indices. In both cases, and at both fillets, the respective maximum stress distributions are almost exactly equal. The only difference that arises between the two sets of results, is between the middle principal stress indices. Under plane strain, these are equal to the Poisson's ratio value (0.3) multiplied by the

maximum principal stress indices. Under plane stress conditions, they are equal to zero.

3.2.1.4 Loading and boundary conditions

The loading and boundary conditions of the models must, as far as possible, accurately simulate those acting on the real crankshaft. The models analysed in the mesh refinement and Poisson's ratio studies were loaded with point loads. In real engines, and in the photoelastic models (which were loaded by a cradle representing a bearing), non-uniform distributed loading exists. In order to study the effects of different loading and boundary conditions, analyses were performed with the conditions described in Table 3.4. The results are presented in Figure 3.6.

Table 3.4 2D FE loading and boundary condition analyses

Model	ν	Journal length	Symmetry conditions	Loading	Standard/ Hybrid	P.Stress/ P.Strain
V122Dh	0.3	½ jnl	Full throw	Point-¼pt	Standard	P.Strain
N122Dh	0.3	1½ jnl	Full throw	Point-¼pt	Standard	P.Strain
N122Di	0.3	1½ jnl	Full throw	Dist pin ld	Standard	P.Strain
V122Dx	0.3	1½ jnl	½ throw	Point-¼pt	Standard	P.Strain
V122Dy	0.3	+web	½ throw	Point-¼pt	Standard	P.Strain
DIST2D	0.3	1½ jnl	½ throw	Dist pin/jnl	Standard	P.Strain

The boundary conditions of the models are vital to ensure that they deform in the correct manner. A deformed plot of model V122Dh is presented in Figure 3.7a. There are two factors that require attention;

1. The end faces of the half journals (i.e. the centreplane of a full journal) are not deforming in-plane, as might be expected in a full crankshaft.

2. There is large deformation in the areas where the point loads and constraints are applied.

The first point can be addressed by applying a constraint to the face, or more easily by adding further material to the journals in order to force a more regular deformation to occur. The extra material added at both ends of the crankthrow is of a length $0.4D_p$, which represents a half journal plus slightly less than one web thickness of an adjacent crankthrow.

The results for this model (N122Dh) are also plotted on Figure 3.6. At the crankpin fillet, there is a remarkable change in the stress distribution. The stress concentration factor is reduced by 13% and it's position moves from $\alpha_p = 65°$ to $\alpha_p = 15°$. At the journal fillet, a less pronounced change is observed. The SCF increases by 2% and it's position moves from $\alpha_j = 54°$ to $\alpha_j = 43°$. A deformed plot of this new mesh is presented in Figure 3.7b. The centres of the journals now deform in-plane and represent a much more realistic deformation.

In order to address the second point, a uniformly distributed load was applied to one half of the crankpin to simulate the distributed load arising from one connecting rod in a vee-engine. These stress distributions are almost identical to the point loaded results, with the SCFs being within 0.5% of each other at both fillets. A deformed plot of this mesh is shown in Figure 3.7c. The large deformation at the crankpin load application point has been removed, and is also reduced at the reaction points at the journal centres by the extra journal material. The deformations at the reaction points are

investigated further in model DIST2D, where pin and journal distributed loads are applied. However, the results do indicate that when a point load is used, it is far enough from the fillets to have no significant effect on the fillet stress distributions.

Because the crank modelled is from a vee-engine, and the force transmitted from a firing piston only acts along one half of the crankpin, care must be taken if geometrical symmetry is to be exploited. A symmetrical section of a model must be constrained in such a way as to represent the constraint that would have been imposed by the missing section of the model. In the 2D vee-engine case, it is not sufficient to simply take one half of a crankthrow, load it at the quarter point, provide a constraint at the journal centre and constrain the centre of the crankpin axially (Figure 3.8a). This incorrectly implies that there would be an equal crankpin loading on the missing adjacent half crankthrow.

It is suggested that, as an approximation, the nodes on the crankpin centre can be assumed to remain in-plane under deformation. If this is so, a half crankthrow can be encastré at the crankpin centre and suitable loads applied to the crankpin and journal (Appendix 2) to simulate the con-rod load and bearing reaction (Figure 3.8b). Such a model is investigated (V122Dx). This mesh was constructed from 1769 nodes and 548 elements. The results for the full crankthrow and half crankthrow are virtually identical at both fillets and are presented in Figure 3.6.

While testing the effects of symmetry, the opportunity was taken to further test the validity of the extended journal results. A half crankthrow was mirrored about the

journal centre to create the mesh shown in Figure 3.9. The results for this model (also shown in Figure 3.6) prove that the simple journal extension is sufficient to simulate the constraints imposed by the adjacent crankthrows.

The final 2D model used to investigate boundary conditions is a half crankthrow which is encastré at the crankpin centre plane (DIST2D). However, instead of point loads, it has uniformly distributed loads applied at both the crankpin and journal (Figure 3.10). This is a much more accurate simulation of the true loads that would act on a real crankshaft. As would be expected, the distributed load at the journal removes the large local deformations seen with a point load or point constraint. Yet, comparing these results with those for the point loaded model (V122Dx) in Figure 3.6, it is clear that the relatively remote point load approximation has very little effect on the stresses at the fillets.

3.2.2 3D radial bending

Having established a reliable 2D mesh, this was recreated on the longitudinal plane of symmetry of 3D models constructed from 15 and 20 noded quadratic elements. Most investigations made full use of symmetry (a quarter crankthrow) to reduce the size of the mesh and thus the analysis time. Symmetry tests were also carried out to verify that the approximate symmetry used in the 2D modelling was applicable to the 3D work. The quarter models were loaded at the quarter point of the crankpin, with a reaction supplied at the base of the journal centre. The results were normalised with the maximum bending stress occurring in the crankpin.

3.2.2.1 Mesh refinement

The models analysed during the 3D mesh refinement investigations are detailed in Table 3.5.

Table 3.5 3D FE mesh refinement analyses

Model	Fig	ν	Journal length	Symmetry conditions	Loading	Standard/ Hybrid
N123Dd	-	0.3	½ jnl	¼ throw	Point-¼pt	Standard
N123Dh	-	0.3	½ jnl	¼ throw	Point-¼pt	Standard
V123Dr	3.12	0.3	1½ jnl	¼ throw	Point-¼pt	Standard

The first two models analysed were constructed to compare the effects of reducing the mesh discretisation in areas away from the fillet surfaces The peak principal stresses occur in the fillets on the centre-plane of the throw (θ_p=0, θ_j=0). The results are presented in Figure 3.11, and indicate that there is no loss of accuracy at the fillet surfaces when the mesh refinement is reduced. Because elements are swept around the crankpin and journal, savings of hundreds of nodes and elements can be made by a relatively minor change in the discretisation on the centre-plane of the crankthrow (the original 2D mesh). Model N123Dd was constructed with 21746 nodes and 5064 elements, but the same results were achieved at the fillets with a model having 16198 nodes and 3649 elements (N123Dh).

It should be noted that these models are constructed with the original half journal, so that the results can be compared with results from an extended journal model. Such a model was constructed, having the same discretisation as N123Dh, but with the journal extended $0.4D_p$ past the journal centre-plane (Figure 3.12), as modelled in 2D. The

results are presented in Figure 3.11. As was observed in the 2D analyses, the introduction of the journal extension reduces the SCF in the crankpin fillet, and increases it in the journal fillet. The resulting maximum principal distributions at both fillets show good agreement with those predicted by the 2D analyses, but the magnitudes of the SCFs are slightly different. At the crankpin fillet, the 2D SCF is 12% lower than the 3D prediction, and at the journal fillet, the 2D SCF is some 2% higher. The angular positions of the peak stress in the 2D and 3D fillets also show good agreement.

3.2.2.2 The effect of Poisson's ratio

Investigations were carried out into the effect of changing the value of Poisson's ratio in the 3D models. Two quarter models were constructed with extended journals, both with hybrid elements (Section 3.2.1.2). The models were assigned Poisson's ratio values of 0.3 and 0.4999 respectively. Table 3.6 describes these models further.

Table 3.6 3D FE Poisson's ratio analyses

Model	ν	Jnl length	Symmetry conditions	Loading	Standard/ Hybrid
V123Df	0.3	1½ jnl	¼ throw	Point-¼pt	Hybrid
V123Du	0.5	1½ jnl	¼ throw	Point-¼pt	Hybrid

The 3D results are presented in Figure 3.13, and show that, unlike 2D, the value of Poisson's ratio can affect the distribution of stresses in the fillets. The positions of the peak stresses are not greatly affected, but as the value of Poisson's ratio is increased, the SCF at the crankpin fillet is slightly reduced, and at the journal fillet it is increased, by less than 2% in both fillets.

3.2.2.3 Loading and boundary conditions

The loading and boundary conditions of the 3D models were validated with the models described in Table 3.7.

Table 3.7 3D FE loading and boundary condition analyses

Model	ν	Jnl length	Symmetry conditions	Loading	Standard/ Hybrid
V123Dr	0.3	1½ jnl	¼ throw	Point-¼pt	Standard
V123Ds	0.3	+web	¼ throw	Point-¼pt	Standard
V123Dv	0.3	1½ jnl	¼ throw	Dist pin/jnl	Standard
C123Dh	0.3	1½ jnl	¼ throw	Point-Centre	Standard

A model was created to confirm that the simple extension to the journal was sufficient to constrain the model in the same way as an adjacent throw. This was achieved in the same way as in the 2D, by mirroring a quarter throw about the journal centre. The results presented in Figure 3.14 show that the simple journal extension is an adequate constraint since it produces the same results as the adjacent throw model.

The oil film loading on a real crankshaft is clearly not only distributed axially along the crankpin (as was the case in the 2D analsyes), but it is also applied radially around the bearing surfaces. A simple simulation of this complex oil film load is achieved with model V123Dv. Here, uniform patches of pressure are applied to the quarter crankthrow at the crankpin and journal surfaces, centred on the quarter point of the crankpin and the centre of the journal respectively. At the crankpin, the pressure is applied to the region $180° < \theta_p < 218°$, over half of the crankpin length ($0.37D_p$), and at the journal fillet, the load is applied to the region $180° < \theta_j < 208°$, over an axial distance of $0.33D_p$. The results from these analyses are presented in Figure 3.14.

There is excellent agreement between the point load and distributed load results at both fillets, indicating that the point load approximations are valid.

It was of interest to establish if the quarter point load results could be reproduced by applying a load at the crankpin centre normalised so as to produce the same bending moment between the two fillets at the centre of the web. This calculation is detailed in Appendix 3. A successful result could potentially make analyses easier from the point of view of applying symmetry and boundary conditions. The results however show that it is not possible to use this approximation. The crankpin fillet SCF is 4% greater than the quarter point load SCF (Figure 3.14a), and at the journal fillet (Figure 3.14b), the SCF occuring in the centrally loaded model is 5% lower than the point loaded equivalent. This suggests that the method is correct, but the fillet stresses are sensitive to the axial position of the applied load. As the load is moved further towards the crankpin centre, the crankpin fillet stress increase and the journal fillet stresses fall.

3.2.2.4 Symmetry conditions

The work carried out in 2D indicated that it was possible to obtain accurate results by making use of symmetry, even if it this entailed a slight approximation of boundary conditions. Tests were carried out to ensure that results obtained from symmetrical sections remained valid in 3D. The models analysed are detailed in Table 3.8.

Table 3.8 3D FE symmetry condition analyses

Model	Fig	ν	Jnl length	Symmetry conditions	Loading	Standard/ Hybrid
V123Dr	3.16b	0.3	1½ jnl	¼ throw	Point-¼pt	Standard
N123Dg	-	0.3	1½ jnl	½ throw	Point-¼pt	Standard
N123Dj	3.16a	0.3	1½ jnl	Full throw	Point-¼pt	Standard

Three models are analysed; a quarter crankthrow, a half crankthrow (symmetric about the longitudinal centre-plane, i.e. that passing through the both the crankpin and journal centrelines), and a full crankthrow. The quarter throw is constrained as described in Section 3.2.2, but the half and full throws are loaded in a similar manner to the full 2D models - point loaded at the quarter point and simply supported at the journal centres. The results obtained (Figure 3.15) are virtually identical in all three cases. It is particularly useful that a quarter throw can be used to represent a full throw (even under a vee-engine loading) because of the large reduction in model size. The full crankthrow model (Figure 3.16a) required 27951 nodes and 6334 elements, compared to the quarter model which required only 16895 nodes and 3818 elements. This quarter model does actually consist of more than half the nodes of the full crankthrow because of higher mesh refinement in areas other than the centre-plane fillets (Figure 3.16b). The results from the full crankthrow indicate that the quarter model could have been constructed from as little as 10982 nodes and 2384 elements with no loss of accuracy in the results.

3.2.2.5 Comparison of FE and photoelastic results

Photoelastic measurements of a crankthrow loaded under radial bending had previously been made by Fessler and Hyde [27]. The FE results are compared with

these measurements in Figure 3.17. At the crankpin fillet the SCFs are identical, although the angular positions at which they occur are very slightly different depending on which method is used (FE: $\alpha_p = 20°$, photoelastic: $\alpha_p=25°$). At the journal fillet, the distributions are very similar, but the photoelastic results predict an SCF some 20% lower than the FE.

3.2.2.6 Comparison of FE and strain gauge results

Strain gauge measurements of a crankthrow loaded under radial bending were made by Warrior and Hyde [28] (discussed further in Section 5.3). The models analysed with strain gauges consisted of the same basic form as those analysed in the photoelastic work, with the exception of slightly different compound fillets. The load was also applied at the centre of the crankpin, even though the crankthrow is for a vee-engine. These differences were reflected in the corresponding FE models, which were constructed with fundamentally the same mesh of a 3D quarter crankthrow as that resulting from the mesh refinement studies. The central load made it possible to use full symmetry by applying suitable constraints on the symmetry planes of the quarter model, and simply supporting the crankthrow at the journal centre.

The FE and strain gauge peak stress distributions at the crankpin fillet (shown in Figure 3.18a) agree well over most of the strain gauge measurement range. It would appear that the strain gauges, which are placed at discrete intervals around the fillet, do not detect the absolute peak stress. The strain gauges used in the crankpin fillets are in strips of five, and as such only take a strain reading at approximately every 14°, which

is arguably too wide a range to measure the rapid strain changes in the compound fillet.

At the journal fillet, the experimental results are again lower than the FE predictions, but in this case, only by 9% at the SCF (Figure 3.18b). The strain gauges report a similar trend in stress distribution to the FE over the range measured, with the exception of their failure to report a slight increase in stress at $\alpha_j = 65°$. In the journal fillet, the gauges used are in strips of four, and take a strain reading at approximately every 10°.

As well as the inability of the strain gauges to produce continuous strain readings, there are other reasons why peaks in the stress distributions might fail to be reported.

1. There may be small inaccuracies in the fillet shapes of the strain gauge model. On the full scale crankshaft, the fillets are partially comprised of minor radii of length 10mm. The strain gauge (and photoelastic) models were constructed as one third scale models. This means that the smallest radii (in which the highest stresses are likely to occur) are of length 3.33mm, which can be difficult to accurately manufacture.
2. The gauges may not be bonded closely to the fillet surface due to the thickness of the adhesive, which can result in lower measured strains since the gauges are extended less than the deformed crank demands.

3.2.3 3D pure bending

The loadcase of pure bending is studied in order to simulate the loading a crankthrow will experience as an adjacent throw is loaded by radial bending. The crankthrow studied will be subject to a uniform bending moment, and this can be reproduced in an FE model by applying a couple which is remote from the crankpin and journal fillets. The results were normalised with the maximum bending stress occurring in the crankpin.

3.2.3.1 Loading and boundary conditions

A quarter crankthrow is used to reduce the number of nodes, and is restrained on the planes of symmetry. The basic mesh is the same as that used for the FE-strain gauge comparison under radial bending. The loading is achieved by extending the journal by $1.86D_p$ past the journal midpoint and applying a couple at the free face of the journal, in the plane $z = 0$ (Figure 3.19).

3.2.3.2 Comparison of FE and strain gauge results

The results of the FE pure bending analyses are presented in Figure 3.20. The strain gauge data for this particular geometry and loadcase are also presented. The agreement between the results from the two analysis methods is excellent, in terms of both trends and magnitude. It is clear that the position of the gauge strip at the journal fillet is not adequate to record the peak stress in the fillet, which underlines the advantages of numerical methods.

3.2.4 3D pure torsion

The pure torsion loadcase is studied to simulate the loading a crankthrow will experience due to the inertia and gas forces which create torques in the crankshaft. A small amount of data from strain gauge analyses of a crankthow was avaliable, and this was compared with the FE results. The results were normalised with the maximum shear stress occurring at the surface of the crankpin, arising from the torque applied at the journal.

3.2.4.1 Loading and boundary conditions

The strain gauge models were loaded such that they were subject to free-torsion. In this arrangement, the centrelines of the crankpin and journal were allowed to move relative to each other. The alternative to this arrangement is the restrained torsion loadcase. This loadcase would see the centres of the crankpin and journal fixed in position. An FE model was created and subjected to free torsion to enable comparison of the numerical and experimental results.

To study this particular loadcase, half (one end of) a crankthrow was modelled. It was necessary to model one half instead of one quarter of a crankthrow because the pure torsion loadcase removed one of the planes of symmetry. The basic mesh was the same as those used in the radial and pure bending FE-strain gauge comparisons. As with the pure bending loadcase, the journal was extended $1.86D_p$ past the centre of the journal (Figure 3.21). This was done to ensure that the point loads which were applied, were far enough from the fillets to appear to be a pure torque, and so that the local high stresses at the loading points did not affect the fillet stresses. These point

loads were applied to the free face of the journal as two perpendicular couples, thus creating a torque about the centreline of the journal. The plane of symmetry at the crankpin centre was encastré to provide the only symmetry condition.

3.2.4.2 Comparison of FE and strain gauge results

The peak principal stress index distributions around the crankpin and journal fillets are presented in Figure 3.22. The small amount of strain gauge data obtained for this loadcase are also presented on these graphs. Under pure torsion, the peak stresses do not occur on the centre-plane of the crankthrow, and instead move to a position near to the region where the two fillets overlap ($\theta_p' = 54°$, $\theta_j' = 40°$). The strain gauge data show general agreement with the trends seen in the FE results, but are in some cases significantly different in magnitude. The peak stresses predicted by both methods are seen to be in the same θ positions, but it should be noted that there are only two strain gauge readings (taken from rosettes) in each fillet. The FE results indicate that the maximum and minimum principal stresses are the double mirror image of each other. It would be reasonable to assume that the strain gauge results should also exhibit similar trends at the rosette on the $\theta = 0°$ plane. However, at both fillets, the strain gauge maximum and minimum principal stress results on the $\theta = 0°$ plane are not equal and opposite, which indicates that there may be some degree of error in the strain gauge torsion results. This is probably due to poor experimental boundary conditions, where it is difficult to emulate free torsion.

3.3 Validation of the BE method

The Finite Element method has it's limitations regarding analysis of stresses in more complex crankshaft geometries such as those with bored holes through the crankpin or those with oil holes drilled through the crankpin, web and journal. It would take a significant amount of time and effort to create these very complex meshes with the FE method. The Boundary Element method by definition requires the modelling of only the boundaries or external surfaces of the geometry. The surface only modelling greatly simplifies the creation of models with bore and oil holes and means that changes can also be made easily to the geometry such as new fillets, new web thickness and mesh refinement etc. As a means of validation, BE results were compared with FE results to ensure that satisfactory mesh refinement and loading conditions were achieved.

The BE software, BEASY [26], was used to perform all of the BE analyses. BEASY performs calculations mainly by efficiently reading and writing data from and to a hard disk, and as such can be run on a relatively fast desktop PC with a large hard disk (around 2Gb) but only a small amount of RAM. The analysis time for BEASY is largely determined by the processor speed and disk access rate. The PC was able to run the necessary analysis size in around 3 days. However, using a DEC Alpha Unix server with four 300MHz Alpha EV5 64-bit processors and 1 Gb (1024 Mb) memory, the same analyses could be run in under 24 hours.

In order to save time learning the BEASY pre-processor, a conversion program, FGVtoBEA, was written in Visual Basic [29] to convert an archive file of a FEMGEN

mesh to a file in a format that could be read by BEASY. This permitted changes to the crankshaft geometry to be made with ease in a familiar pre-processor.

The FE results showed that it is possible to make use of geometrical symmetry, even under the non symmetrical vee-loading arrangement, by applying suitable loads to represent the oil film loads between the connecting rod big end bearing and crankpin, and between the main bearing and journal. All of the BE analyses performed use a 3D mesh of one half (end) of a crankthrow (Figure 3.23). This not only reduced the amount of elements and nodes necessary, but also allowed the loadcases of radial bending, pure bending and pure torsion to be analysed, and the results could be compared with the equivalent FE results. The loads were initially applied in the form of distributed loads because it was more convenient to do so in BEASY.

3.3.1 3D radial bending

The crankshaft geometry used in the FE - BE comparison was the same as that used in the FE - photoelastic comparison, with the exception of a slightly more detailed compound crankpin fillet. This fillet has an initial minor radius to allow run-out of the grinding tool, and is a more commonly used shape than that used in the photoelastic analyses.

3.3.1.1 Mesh refinement

The corners and mid-points of elements created in BEASY are defined not by nodes, but by mesh points. Mesh points define the geometry of the element, which is always quadratic, whereas nodes are placed slightly inside the boundaries of the elements and

these are the positions where the values of the problem variables are calculated. Each 3D three or four sided element has six or nine mesh points respectively, belonging exclusively to that element, even if these mesh points are coincident with others belonging to adjoining elements (i.e. they are not automatically shared). The user can choose to either leave the model in this state, or to merge mesh points within a specified tolerance (it generally requires more than one merge command to merge all mesh points). The analysis speed is increased with fewer mesh points, but it was found that merging the mesh points can have a significant effect on the stresses obtained in the fillets. The following analyses were performed to study the effects of merging mesh points and to test convergence of results.

Table 3.9 3D BE mesh refinement analyses

Model	**Mesh discretisation**		**Mesh points**	**Loading conditions**	**Merges performed**
	Crankpin fillet	Journal fillet			
TEST1	14 elements	1 element	2323	Dist pin/jnl	All mesh pts
TEST3	14 elements	1 element	2366	Dist pin/jnl	One merge
TEST2	14 elements	1 element	3986	Dist pin/jnl	No merges
TEST4	8 elements	1 element	3622	Dist pin/jnl	No merges
NPJ3	9 elements	3 elements	3978	Dist pin/jnl	No merges
NPJ4	9 elements	5 elements	4094	Dist pin/jnl	No merges

As will be seen from Table 3.9, the first four models all had a refined crankpin fillet only, in order to reduce the analysis time. The first three tests investigate the effects of merging the mesh points. Figure 3.24 shows that as more mesh points are merged, the peak crankpin fillet stresses are reduced. This must be purely an effect of the BE formulation, since the geometry of the crankthrow and the loads applied are unaltered. Because an unpredictable number of mesh points are combined with each merge, the

most reliable results would be obtained from analyses with no merges performed, even though this had the detrimental effect of increasing analysis time.

The number of mesh points and elements was significantly reduced in TEST4 by modelling only eight elements around the crankpin fillet. This had no effect on the SCF, but the the stress distribution around the fillet did not appear to be defined in sufficient detail at the peak stress region. For this reason, one more element was added at the start of the crankpin fillet in model NPJ3. This extra element produces a stress distribution which shows good agreement with that from the crankpin fillet with fourteen elements. In addition to the refined crankpin fillet, this model had a refined journal fillet with three elements around the 90° blend. A further model was created, having five elements around the journal fillet, and the resulting stress distributions are presented in Figure 3.24b. The two distributions agree well, indicating that the results have converged, but the latter model produces a more well defined stress distribution. This mesh discretisation, with nine and five elements around the crankpin and journal fillets respectively, was used as the basis for all further BE analyses. The mesh was constructed from 4094 mesh points and 623 elements.

3.3.1.2 Loading and boundary conditions

As mentioned in the introduction, half of one crankthrow was modelled and analysed. As with the FE work, the crankpin centre of the BE model was encastré, and loads were applied to the crankpin and journal. Models were created with distributed and point loads. Because of limitations in the modelling process, the point loads are applied as a pressure over a very small area, instead of at discrete points. The results

from the two different loading methods are presented in Figure 3.25. They appear to contradict the findings from the FE method (both 2D and 3D), where it was shown that distributed loads can be approximated as point loads. Here, the point load SCFs are 2.6% lower at the crankpin fillet and 1.3% lower at the journal fillet than the distributed loaded models. There is no simple explanation why these results should differ. Care was taken to ensure that equal loads were applied in the two methods, and that the loads were centred at the same position. As was shown in the FE validation, the loads are remote from the areas of interest and the method of application has no effect on fillet stresses. It is noted that when comparing the results from the BE and FE methods (Section 3.3.1.3) the best agreement is obtained when the point loaded BE results are used. This perhaps indicates that the distributed loads are not interpreted by the BE code in the anticipated manner.

3.3.1.3 Comparison of BE and FE results

The crankthrow geometry used in the BE validation was created and analysed with the FE method. A quarter crankthrow was used, with loading (point loads) and boundary conditions as described in Section 3.2.2. The results from the two numerical methods are presented in Figure 3.26. Agreement between the results from both methods is very good. At the crankpin fillet, the SCF calculated by the BE method is 1.5% higher than that calculated by the FE method, whereas at the journal fillet, the two SCFs agree exactly. The two methods calculate similarly shaped stress distributions around the fillets. The only differences arise near the beginning and the ends of the fillets.

3.3.2 3D pure bending

The loadcase of pure bending was analysed with the BE method. The basic half crankthrow from the radial bending analyses is used, with the journal extended and a couple applied to the free journal face. The mesh was constructed from 4234 mesh points and 654 elements and is presented in Figure 3.27.

3.3.2.1 Loading and boundary conditions

The half crankthrow was constructed with the journal extended $1.55D_p$ past the journal midpoint. A couple was applied at the free face of the journal in the plane $z = 0$, and the mid-plane of the crankpin was encastré.

3.3.2.3 Comparison of BE and FE results

An FE quarter crankthrow was created with the same basic form as the pure bending model analysed with the BE method. The results from the two methods are presented in Figure 3.28. Agreement between the FE and BE results at both fillets is excellent. Slight differences are apparent in some areas because the BE mesh points are more widely spaced than the FE nodes. As with the radial bending comparison, there are also some differences near the ends of the fillets, especially so in the journal fillet.

3.3.3 3D pure torsion

The BE method was also used to investigate the pure torsion loadcase. As with the pure bending analyses, a half crankthrow with an extended journal was used in the torsion analyses. This mesh was constructed from 3830 mesh points and 578 elements.

3.3.3.1 Mesh refinement

The pure torsion mesh was changed so that there were more, smaller elements around the journal fillet, to produce accurate stresses away from the centre-plane of the crankthrow. In order to avoid a significant increase in analysis time, it was necessary to reduce the mesh discretisation elsewhere on the crank. This resulted in a more refined mesh in the fillet region, with less mesh points and elements than the mesh used in the pure bending investigations.

3.3.3.2 Loading and boundary conditions

A half crankthrow was constructed, and the journal extended $0.81D_p$ past the journal midpoint. Two perpendicular couples were applied at the free face of the journal, to produce a torque about the centreline of the journal. For the BE case, the journal was not extended to $1.86D_p$ because the couples were applied in the form of distributed loads. These caused significantly lower local stresses at the free journal face than the point loads which were applied in the FE models. This meant that journal could be shortened without affecting fillet stresses, which resulted in a reduction in the number of mesh points. As with previous models, the mid-plane of the crankpin was encastré.

3.3.3.3 Comparison of BE and FE results

A half crankthrow was created using the FE method, with the same basic form as the pure torsion model analysed with the BE method, except with a journal extension of $1.86D_p$. The results from the two methods are presented in Figure 3.29. These figures show the maximum principal stress in each fillet at various θ positions. It should be noted that the angular position of the maximum stress in the fillet, α', does not remain

constant as θ changes. The agreement between the results from the two methods is good at both fillets. The shapes of the stress distributions agree very well for both numerical methods, but the BE results are always slightly higher than the FE results (generally by less than 5%). It is suggested that this is an acceptable range of stress prediction.

3.4 Conclusions

The FE and BE methods have been shown to produce accurate results for the analysis of stresses in overlapped crankshafts. The two numerical methods have been successfully validated against two experimental methods (frozen stress photoelasticity and ERS gauges) and also against each other. This has been carried out for the three important loadcases of radial bending, pure bending and pure torsion. Good agreement has been observed between the results from the different methods under all loadcases.

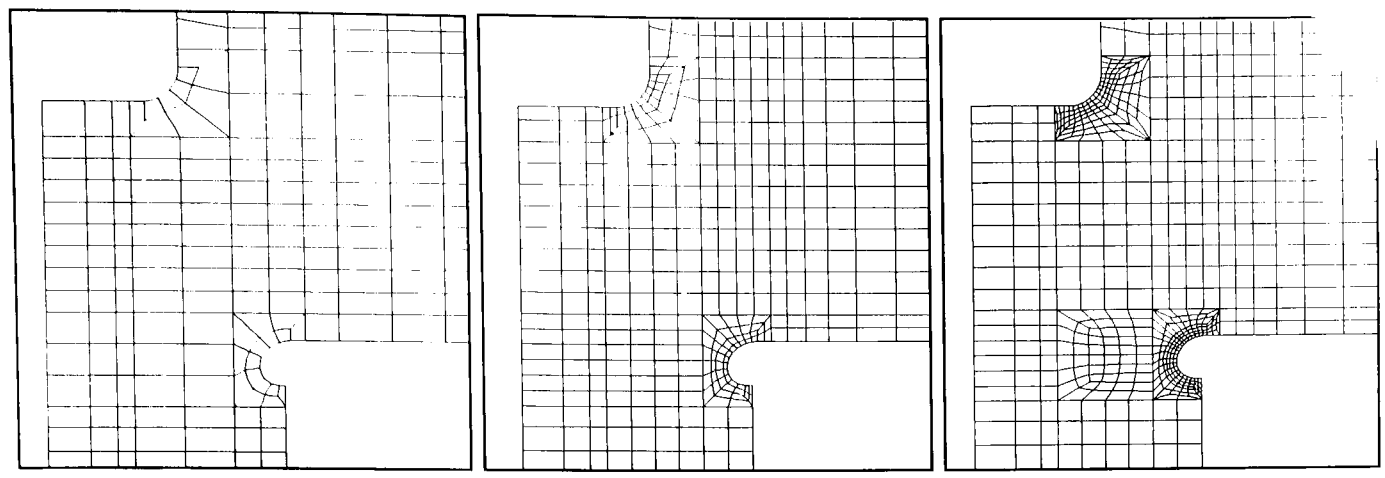

(a) V122Dq (b) V122Dh (c) N122Dd

Figure 3.1. Refinement of 2D FE crankpin and journal fillet mesh

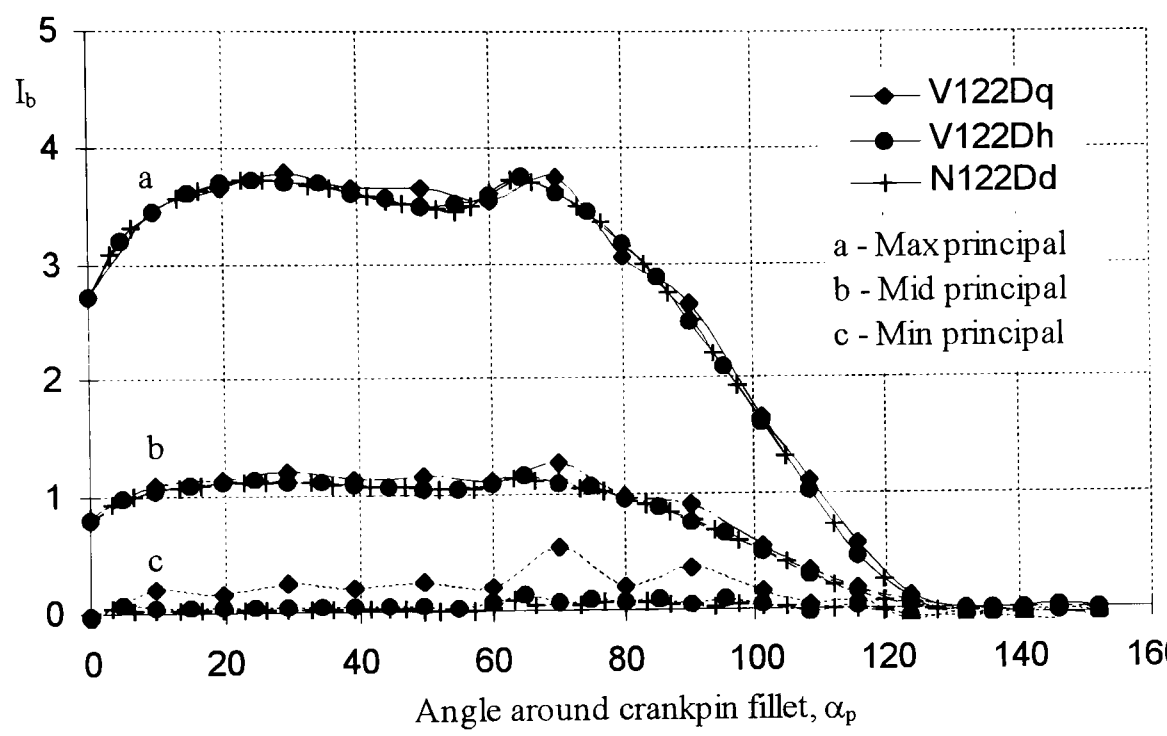

(a) Distribution around crankpin fillet (2D analyses)

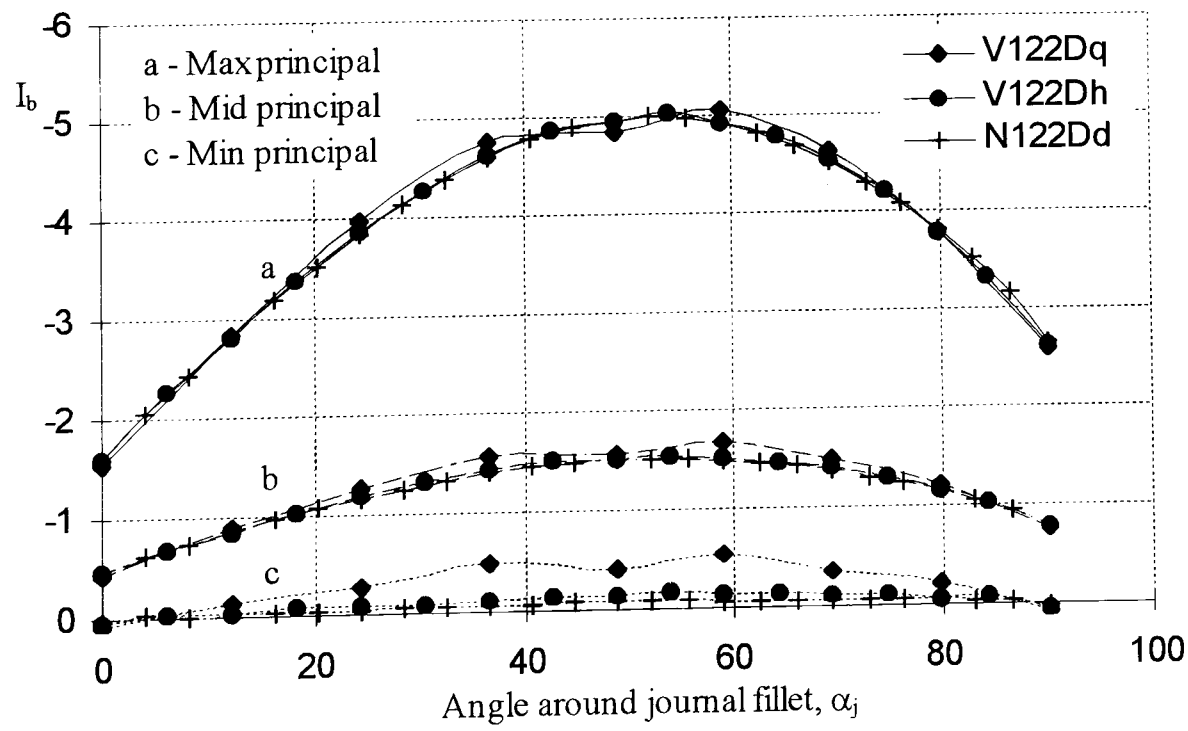

(b) Distribution around journal fillet (2D analyses)

Figure 3.2. Effects of fillet mesh refinement on radial bending principal stress distributions

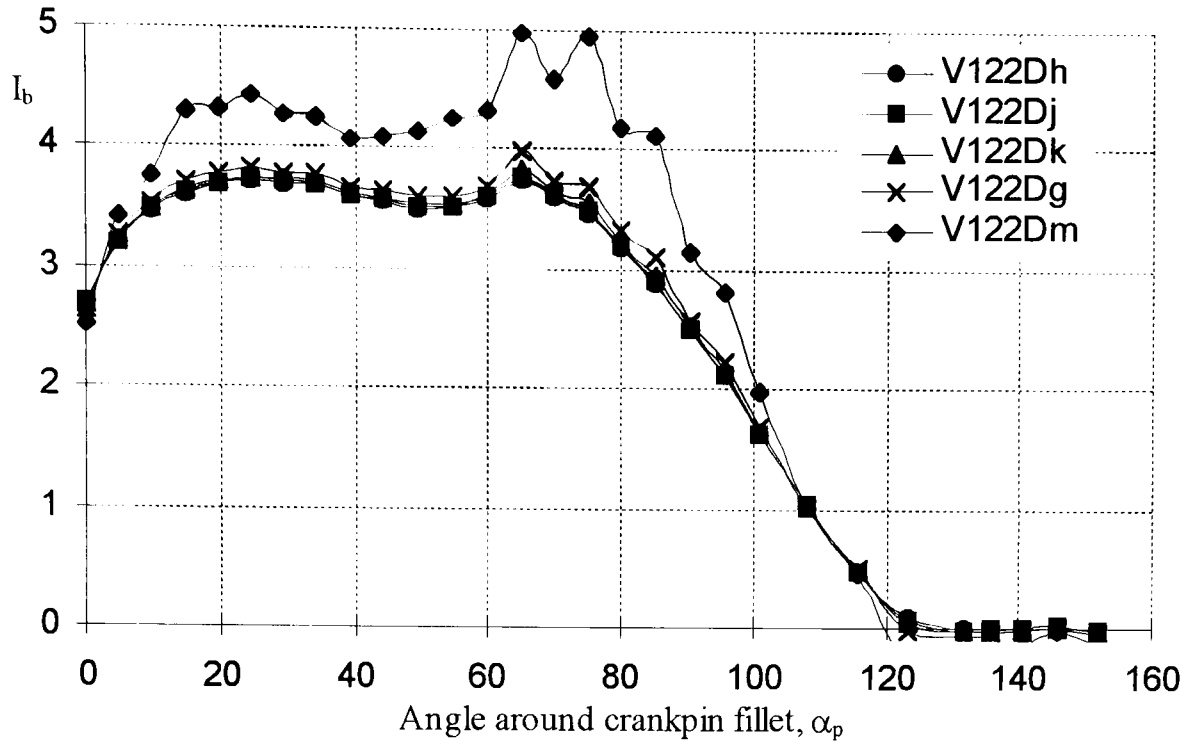

(a) Distribution around crankpin fillet (2D analyses)

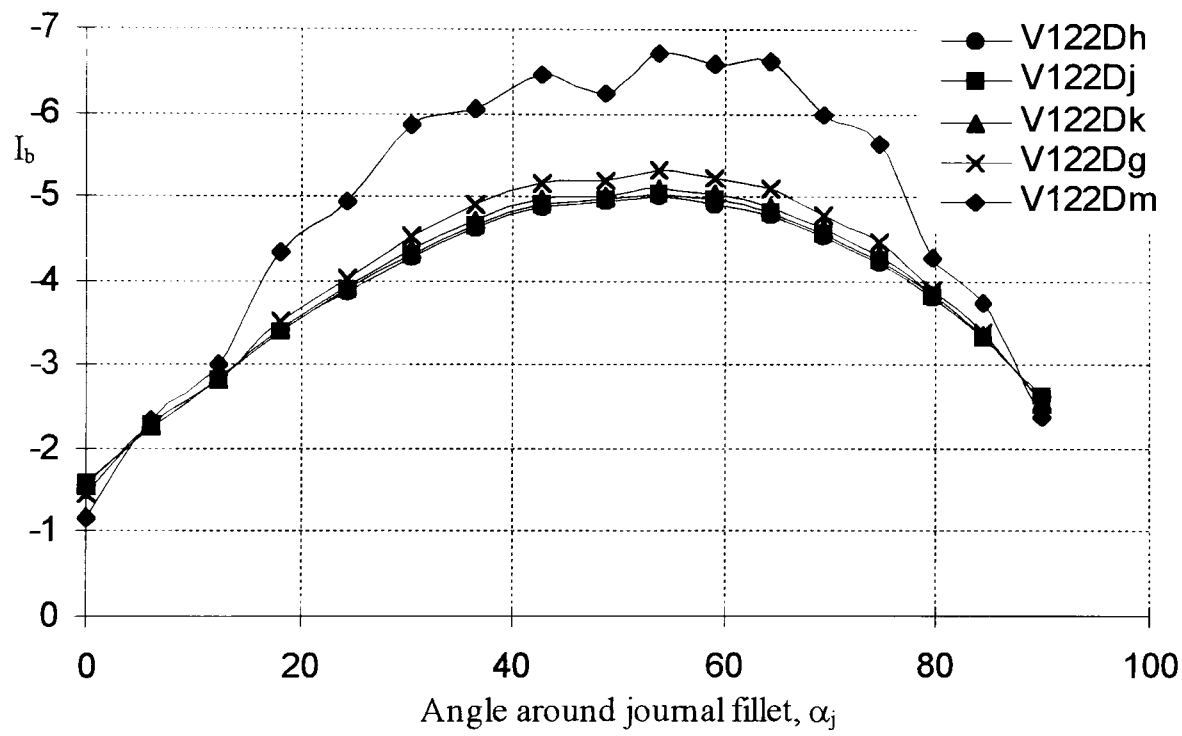

(b) Distribution around journal fillet (2D analyses)

Figure 3.3. Effect of Poisson's ratio on radial bending maximum principal stress distributions (standard elements used)

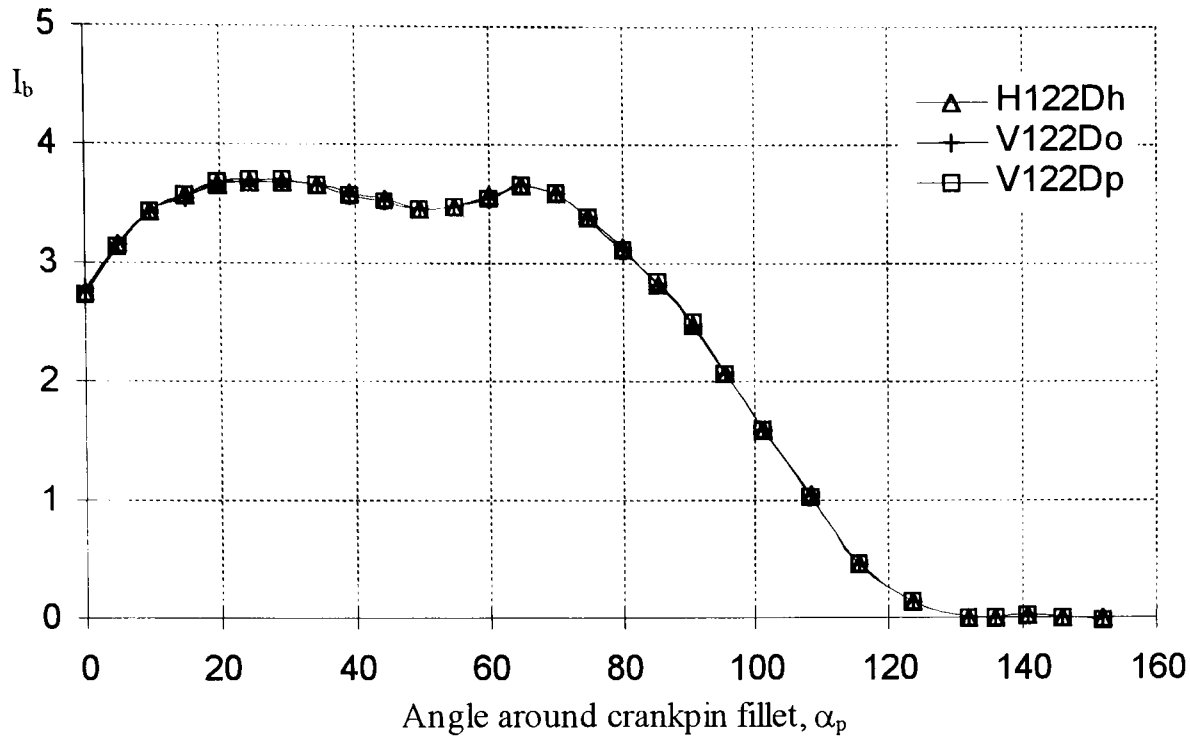

(a) Distribution around crankpin fillet (2D analyses)

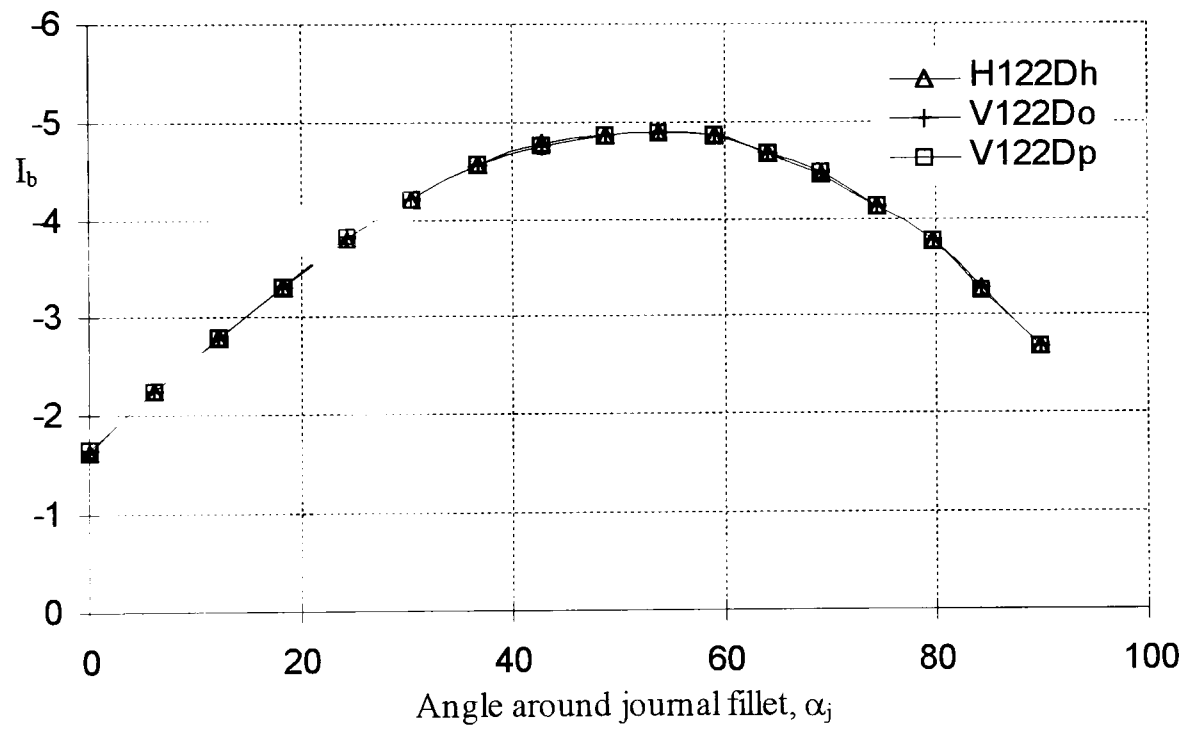

(b) Distribution around journal fillet (2D analyses)

Figure 3.4. Effect of Poisson's ratio on radial bending maximum principal stress distributions (hybrid elements used)

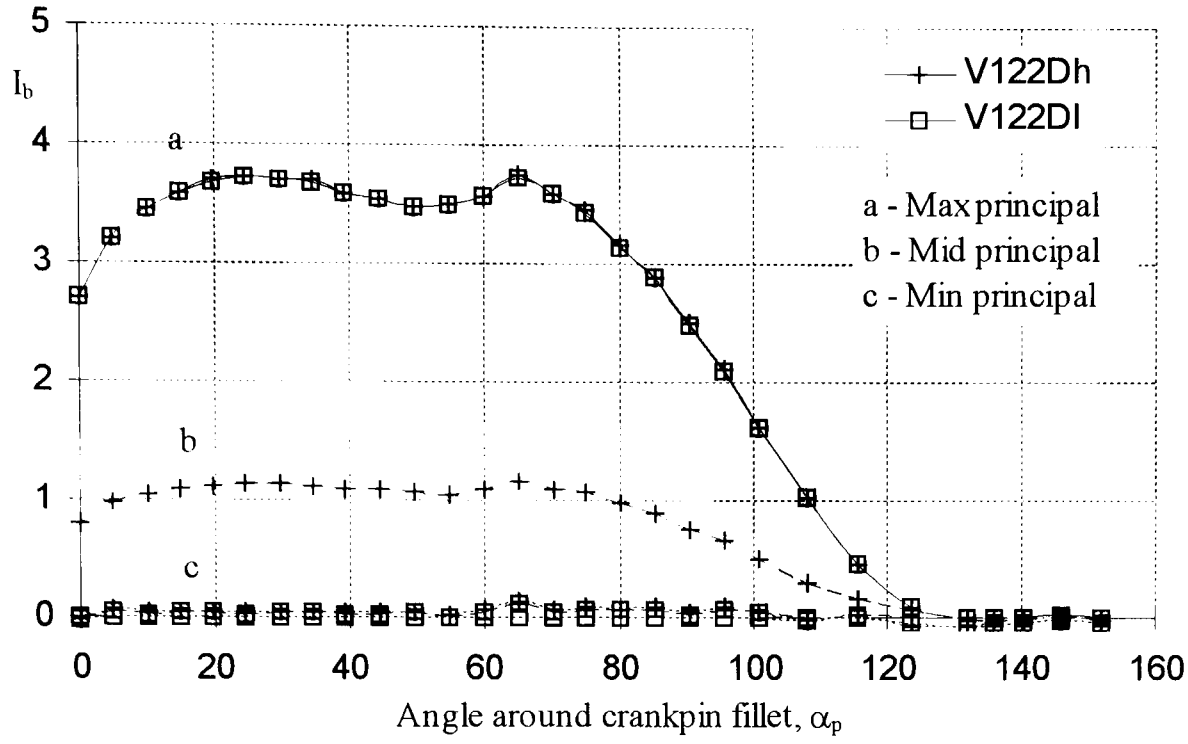

(a) Distribution around crankpin fillet (2D analyses)

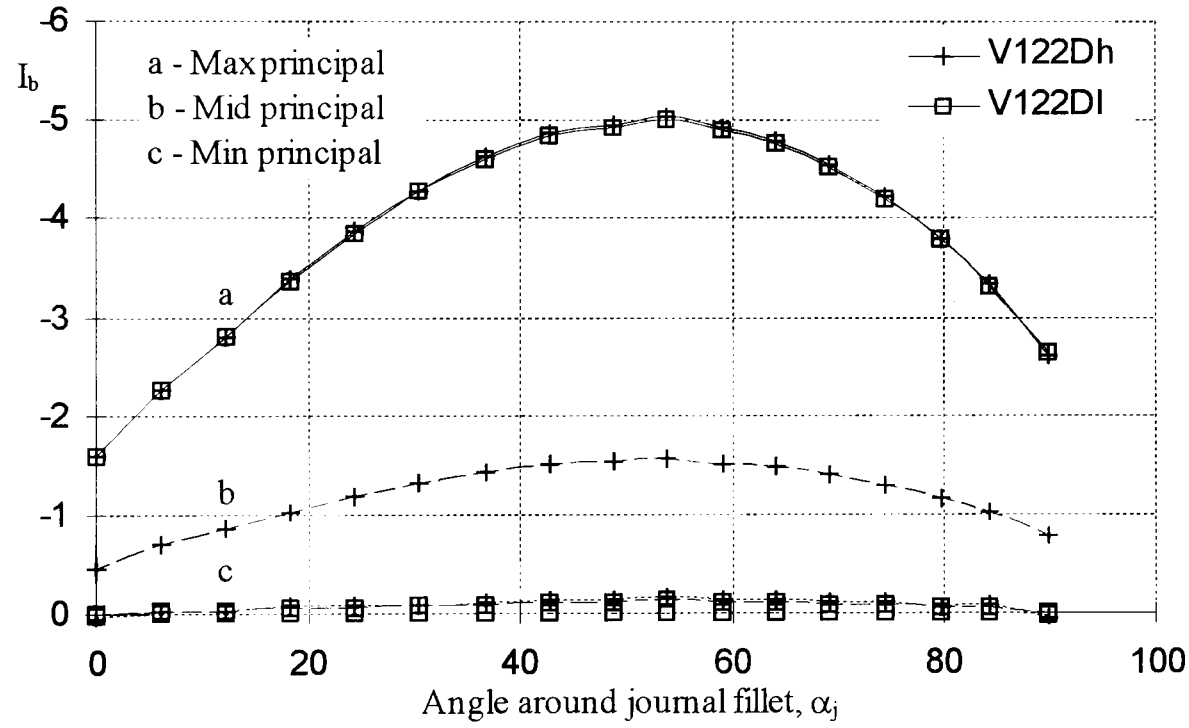

(b) Distribution around journal fillet (2D analyses)

Figure 3.5. Effect of plane strain / plane stress conditions on radial bending principal stress distributions

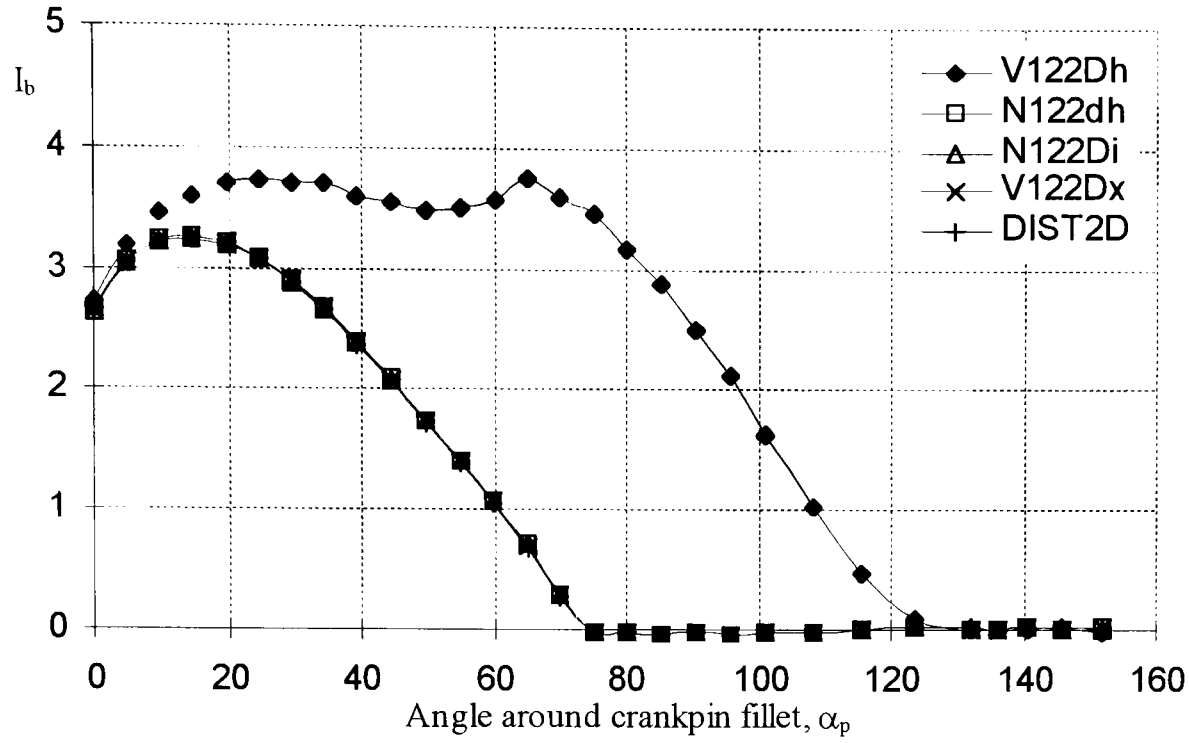

(a) Distribution around crankpin fillet (2D analyses)

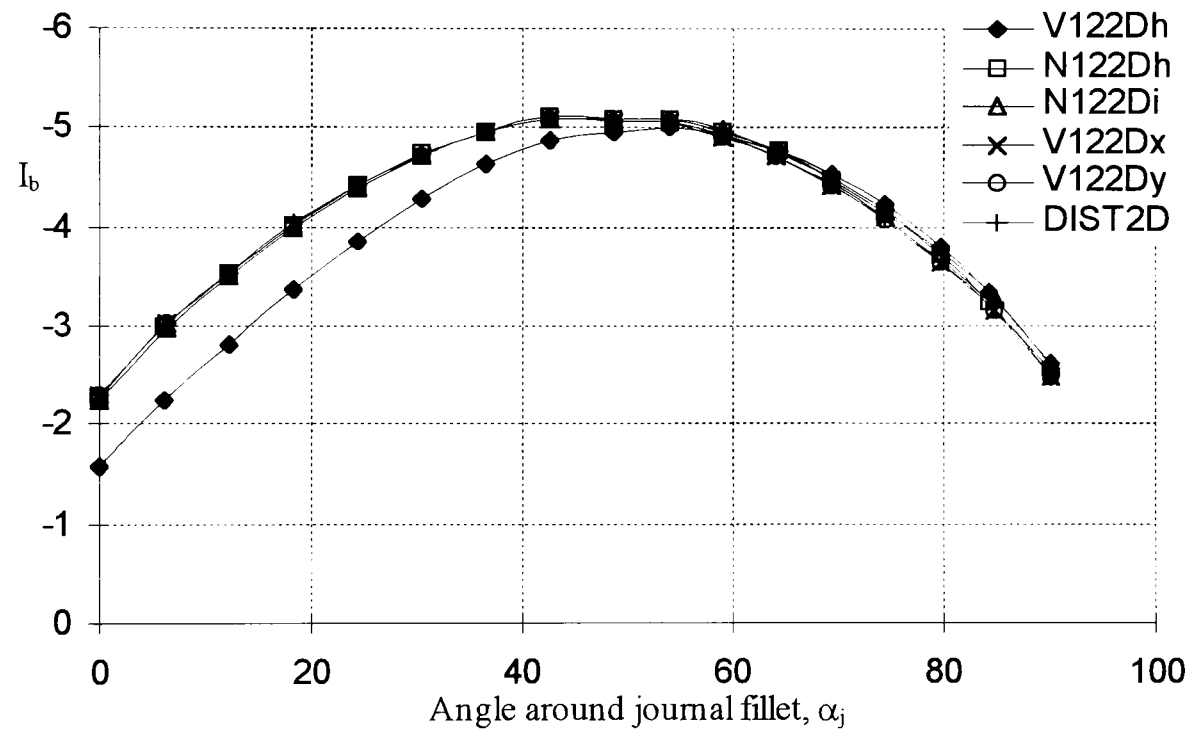

(b) Distribution around journal fillet (2D analyses)

Figure 3.6. Effect of loading and boundary conditions on radial bending principal stress distributions

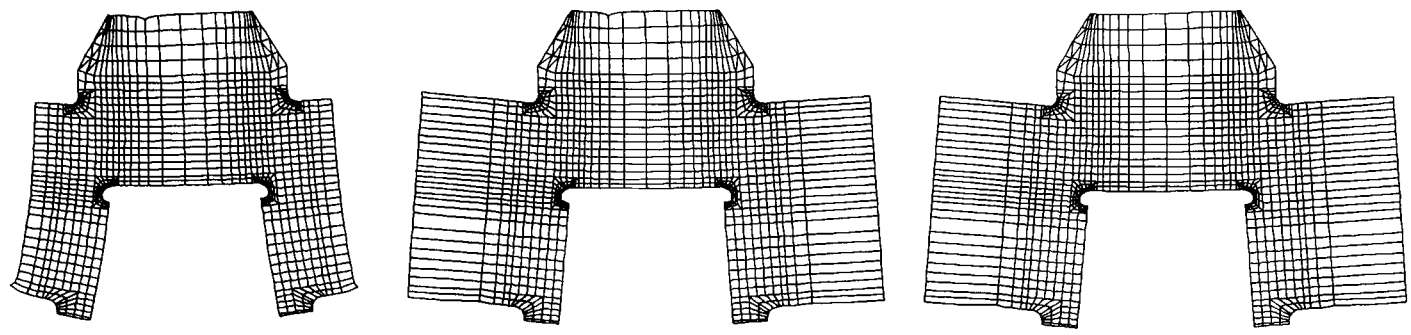

(a) V122Dh (b) N122Dh (c) N122Di

Figure 3.7. Crankthrow deformation under various loading and boundary conditions

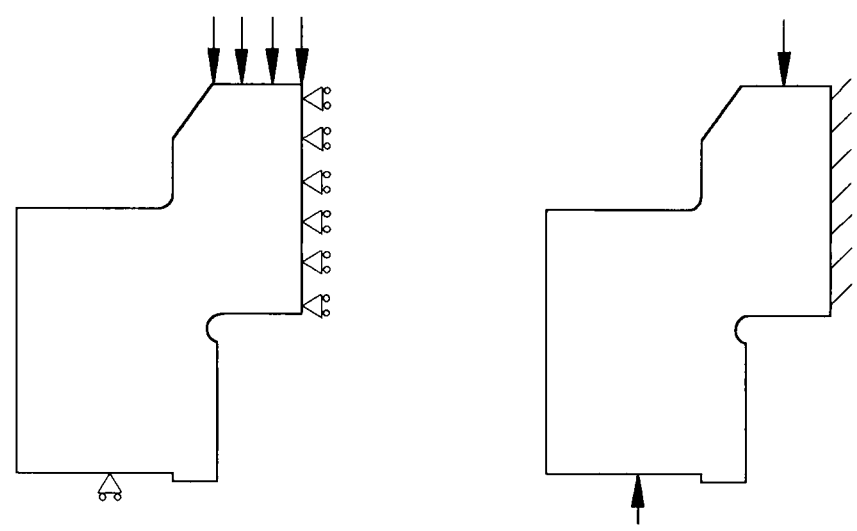

(a) (b)

Figure 3.8. Application of mesh symmetry with the non-symmetrical vee-engine loading

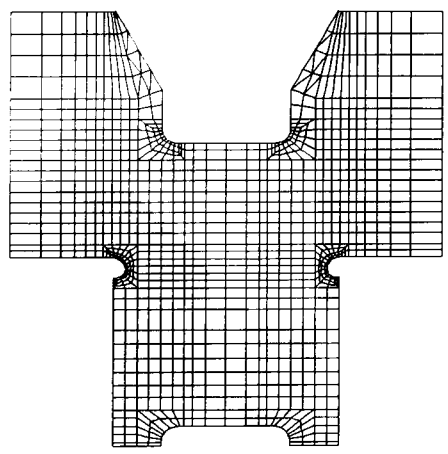

Figure 3.9. Modelling the adjacent crankthrow

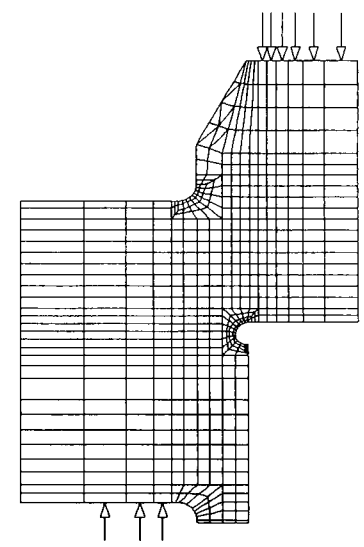

Figure 3.10. Modelling uniformly distributed loads

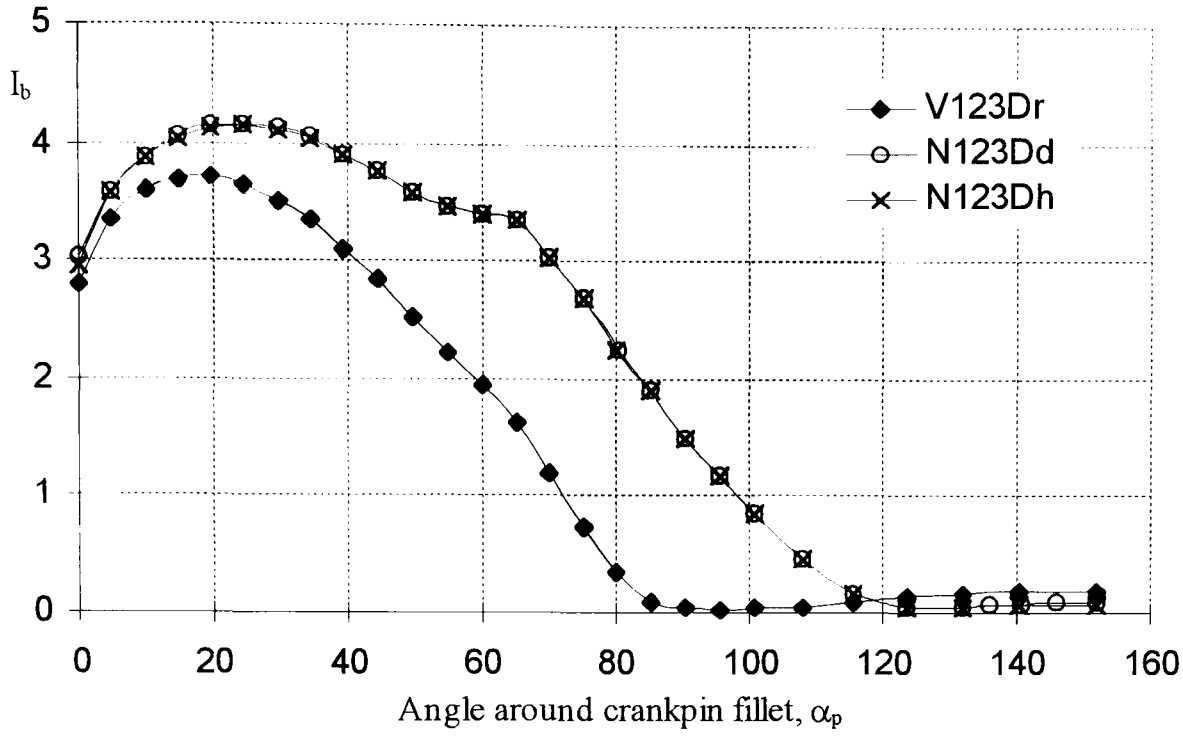

(a) Distribution around crankpin fillet (3D analyses)

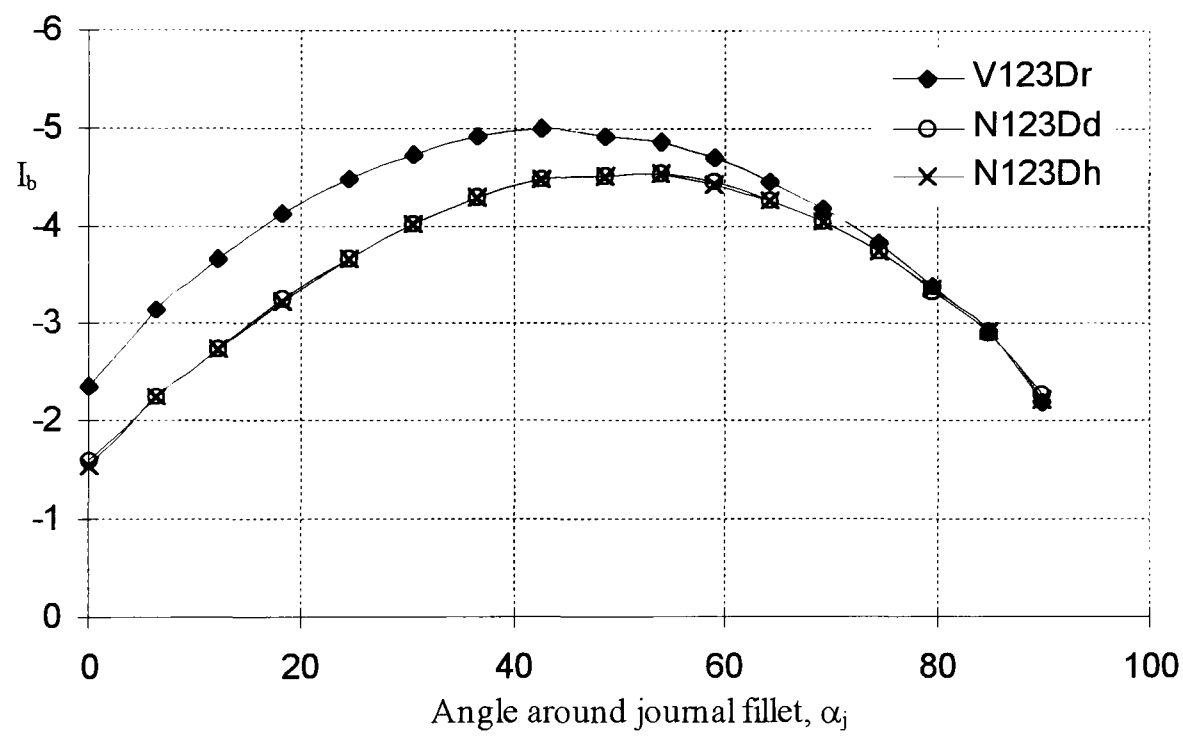

(b) Distribution around journal fillet (3D analyses)

Figure 3.11. Effects of mesh refinement on radial bending principal stress distributions

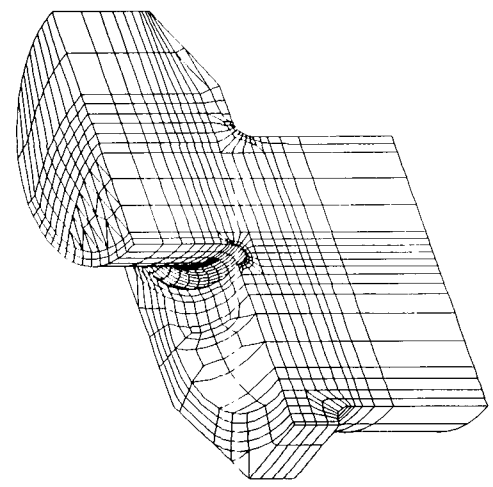

Figure 3.12. A typical FE quarter crankthrow with extended journal

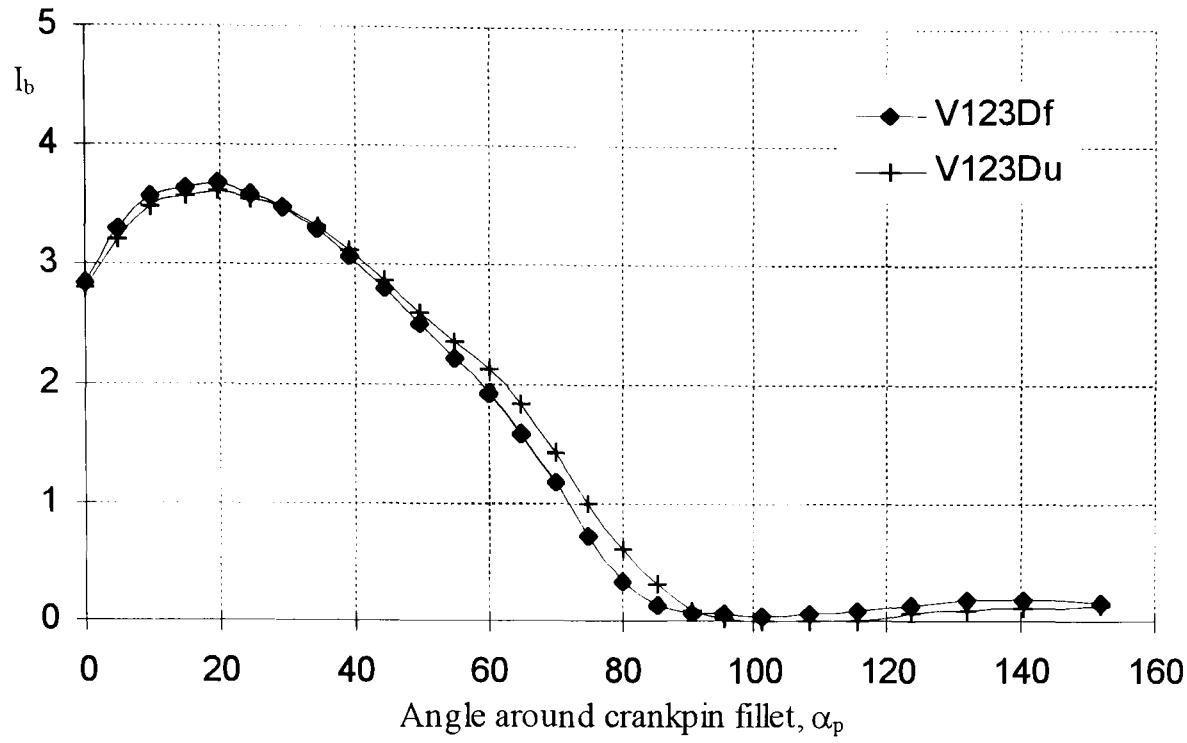

(a) Distribution around crankpin fillet (3D analyses)

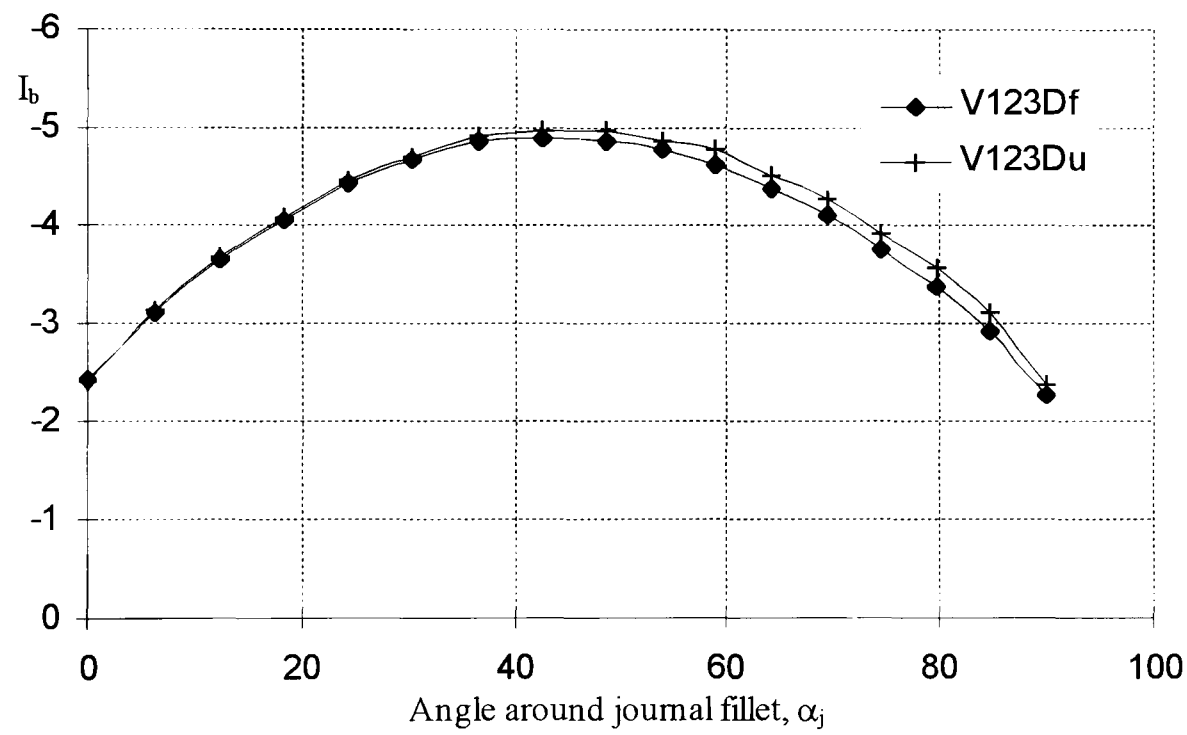

(b) Distribution around journal fillet (3D analyses)

Figure 3.13. Effect of Poisson's ratio on radial bending maximum principal stress distributions (hybrid elements used)

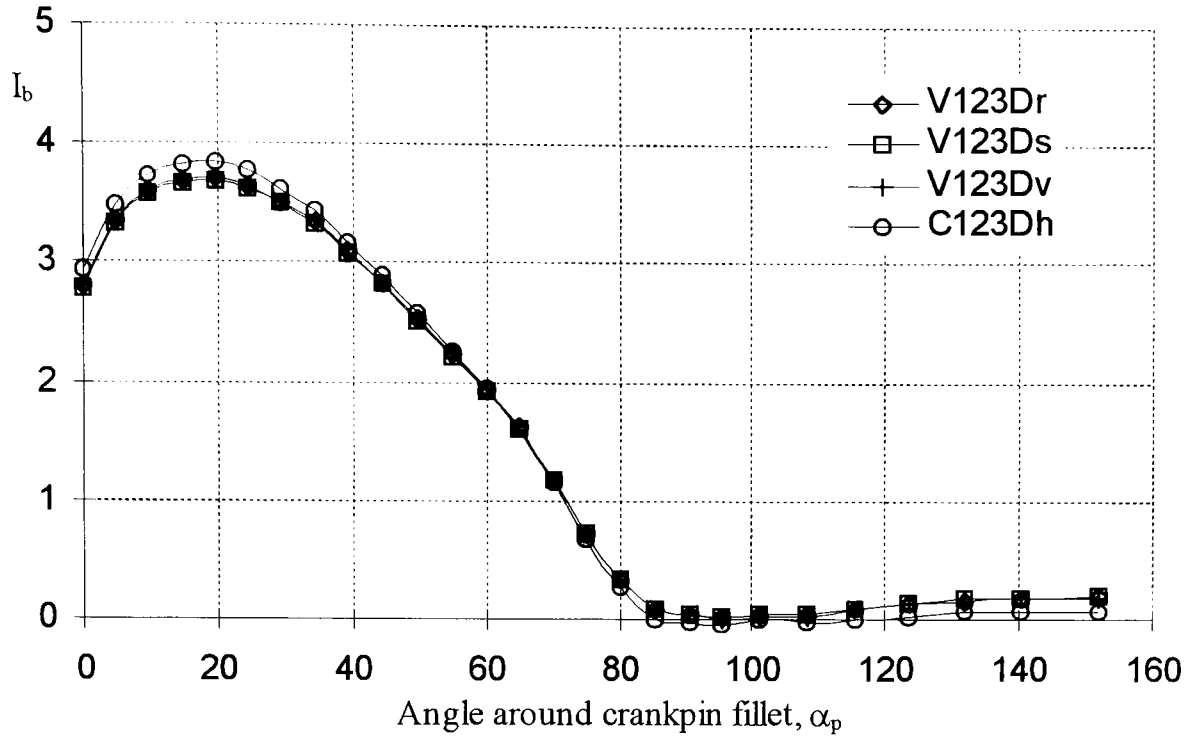

(a) Distribution around crankpin fillet (3D analyses)

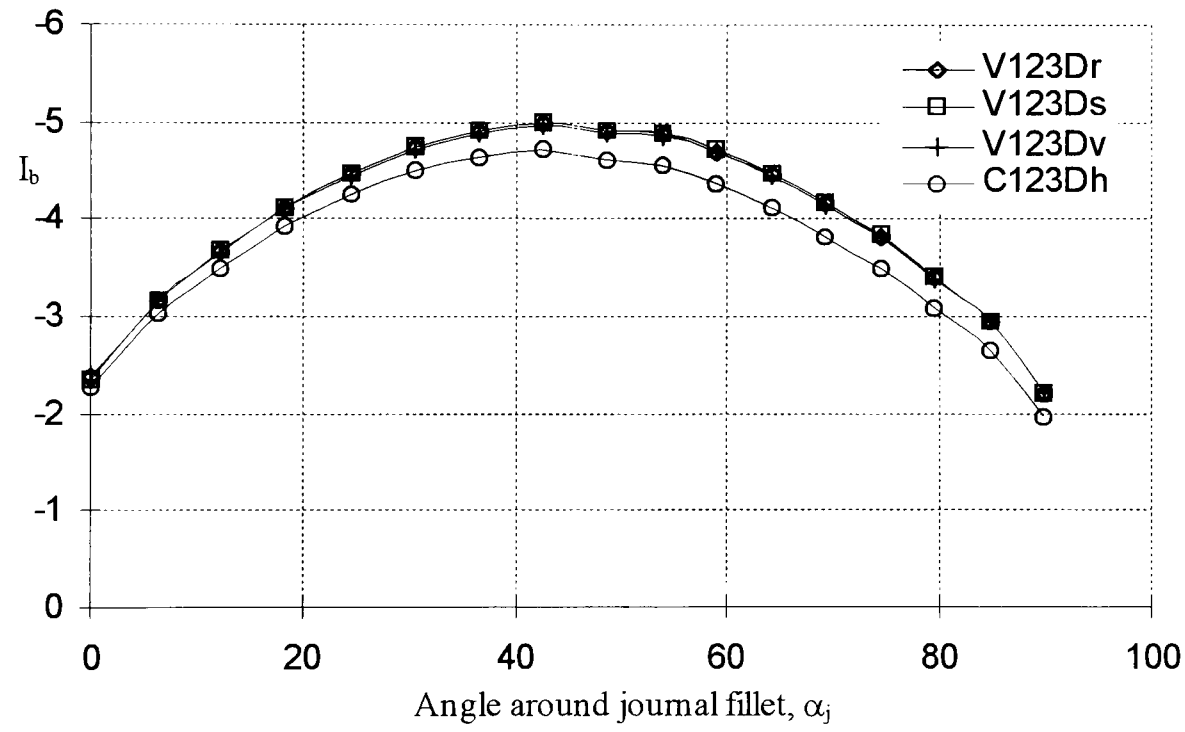

(b) Distribution around journal fillet (3D analyses)

Figure 3.14. Effect of loading and boundary conditions on radial bending principal stress distributions

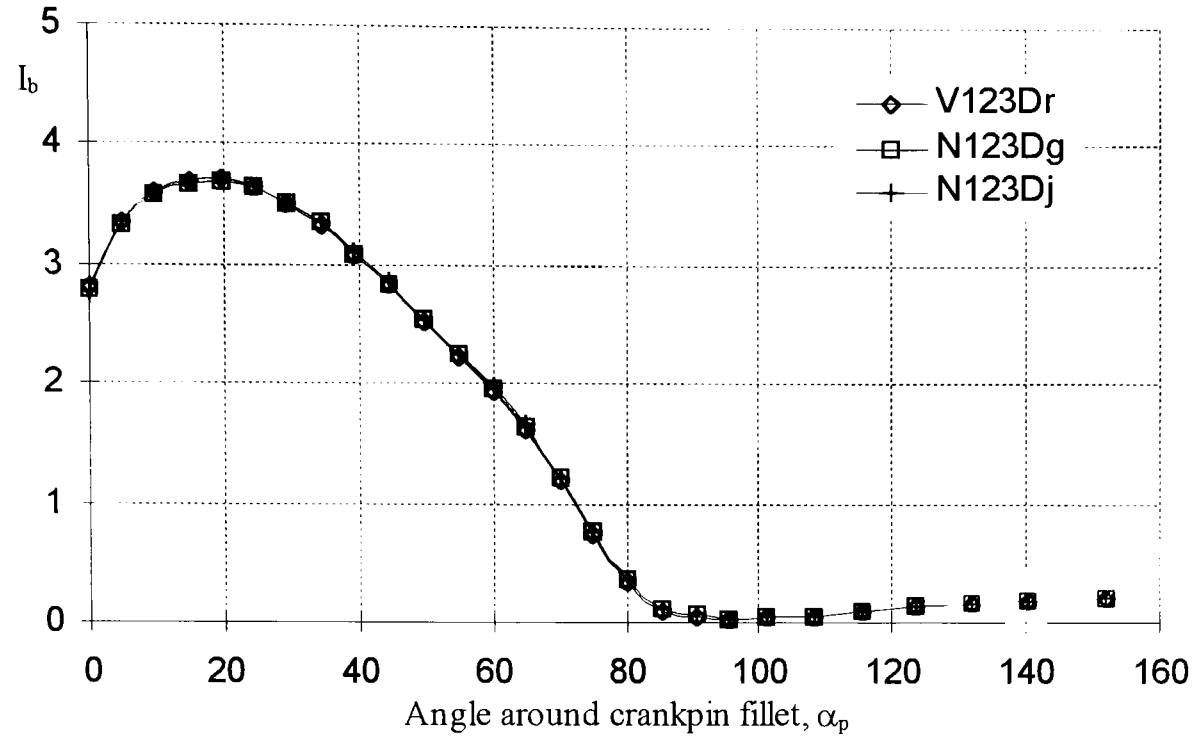

(a) Distribution around crankpin fillet (3D analyses)

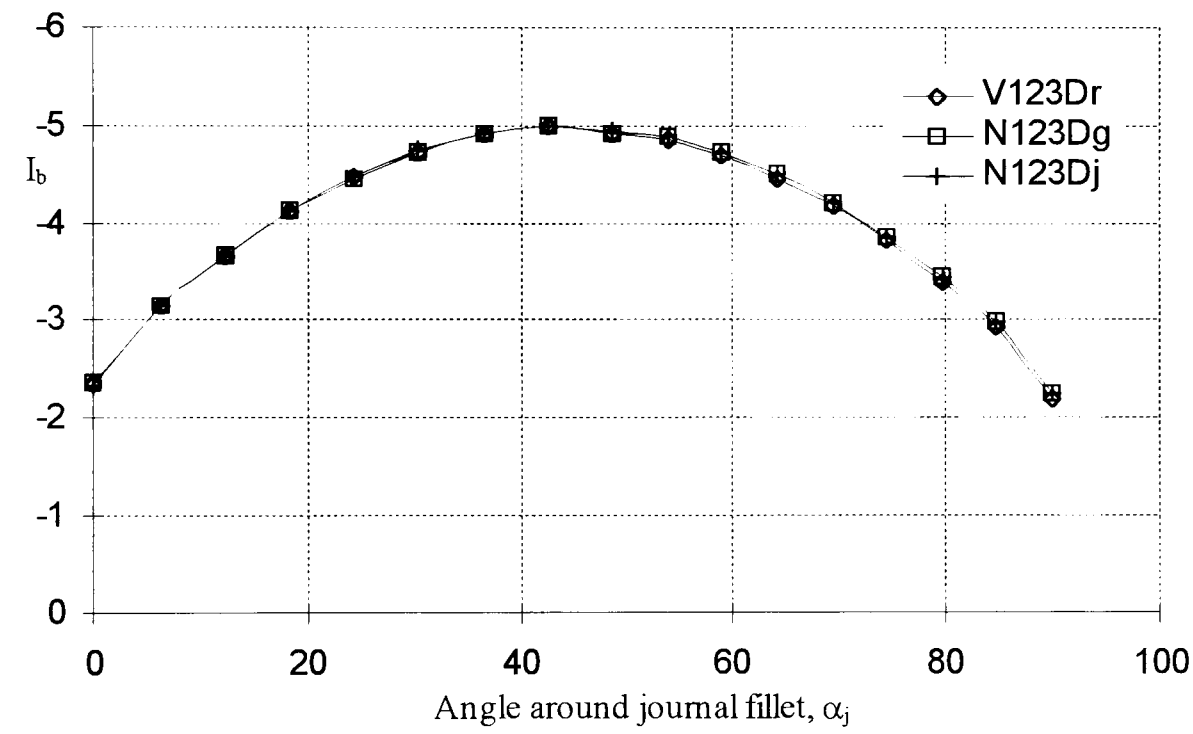

(b) Distribution around journal fillet (3D analyses)

Figure 3.15. Effect of symmetry conditions on radial bending principal stress distributions

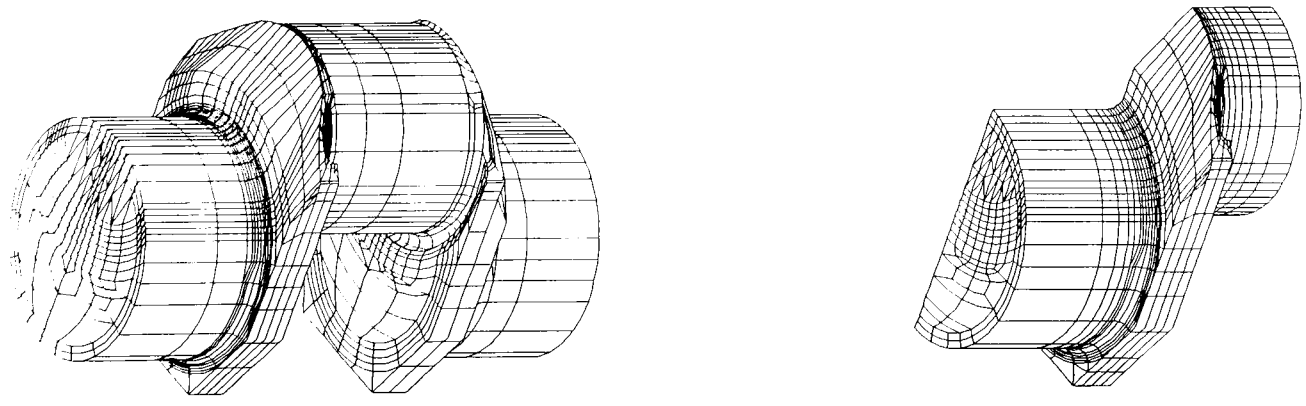

(a) Full crankthrow (b) Quarter crankthrow

Figure 3.16. The application of FE mesh symmetry

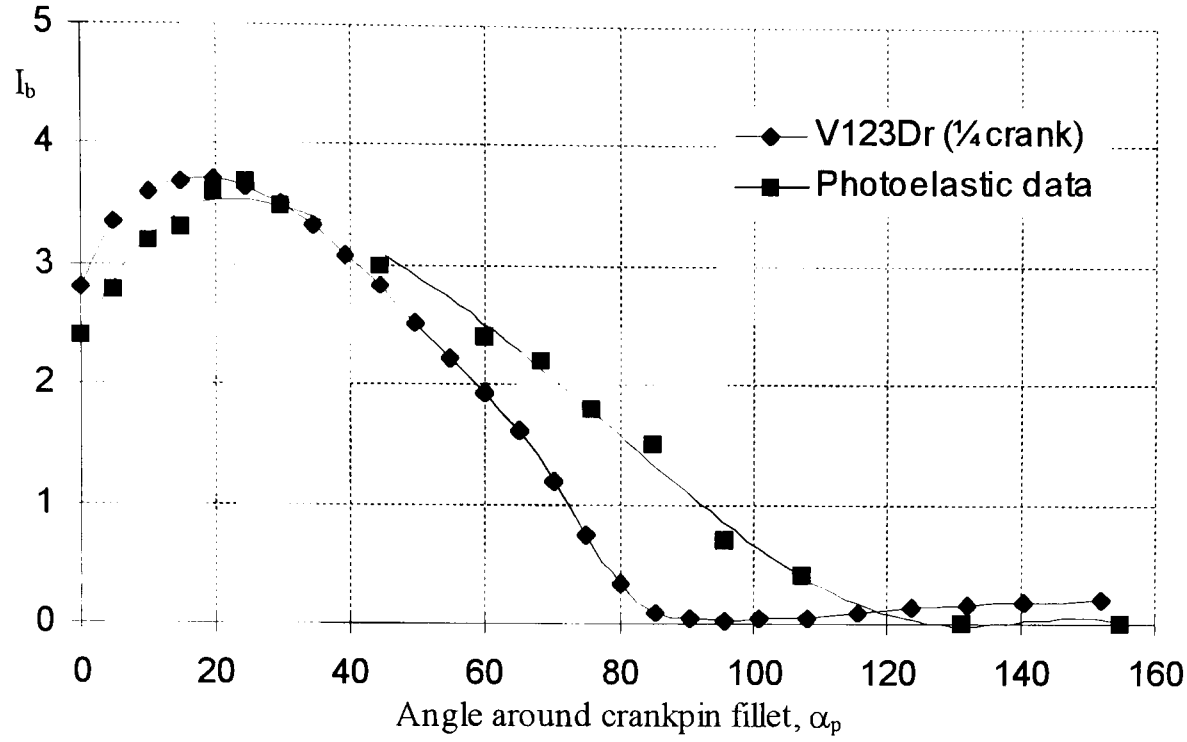

(a) Distribution around crankpin fillet (3D analyses)

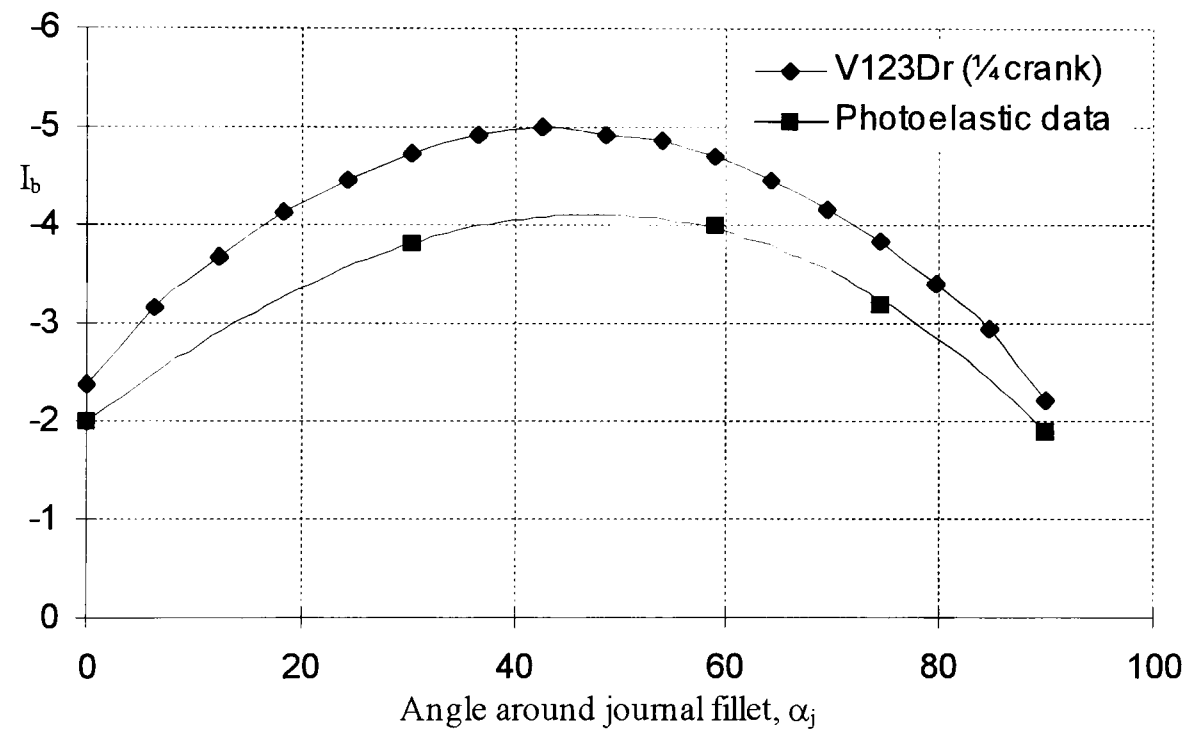

(b) Distribution around journal fillet (3D analyses)

Figure 3.17. Comparison of FE and photoelastic radial bending maximum principal stress distributions

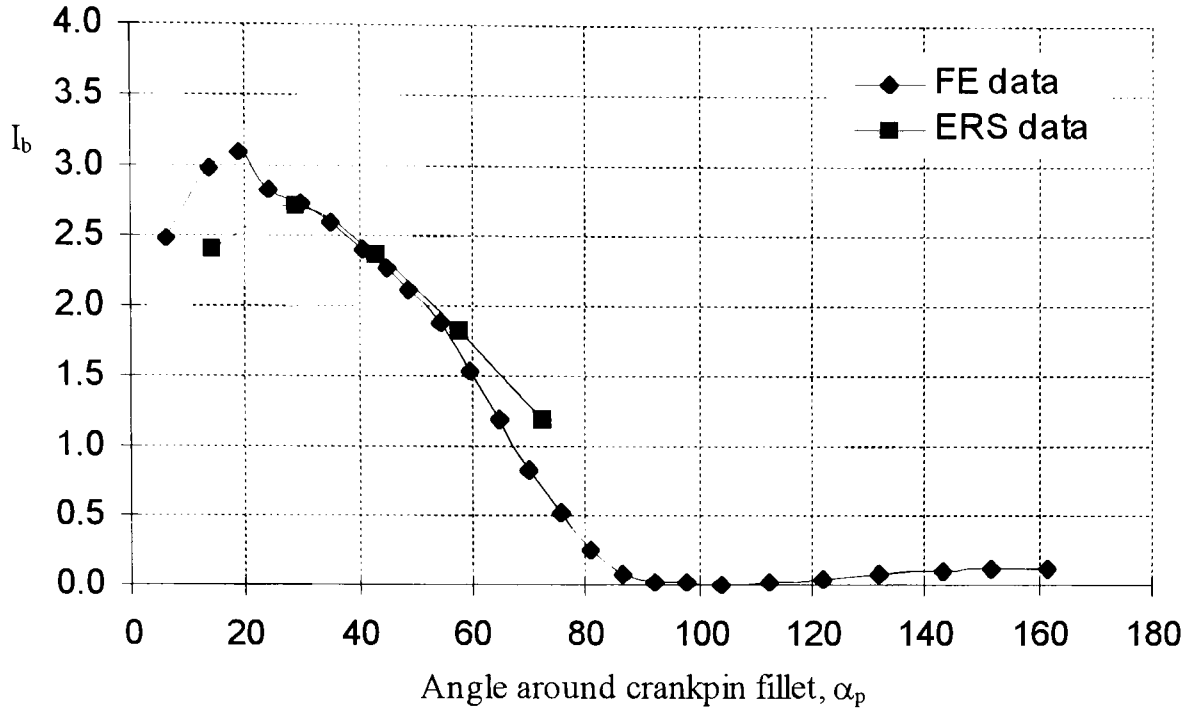

(a) Distribution around crankpin fillet (3D analyses)

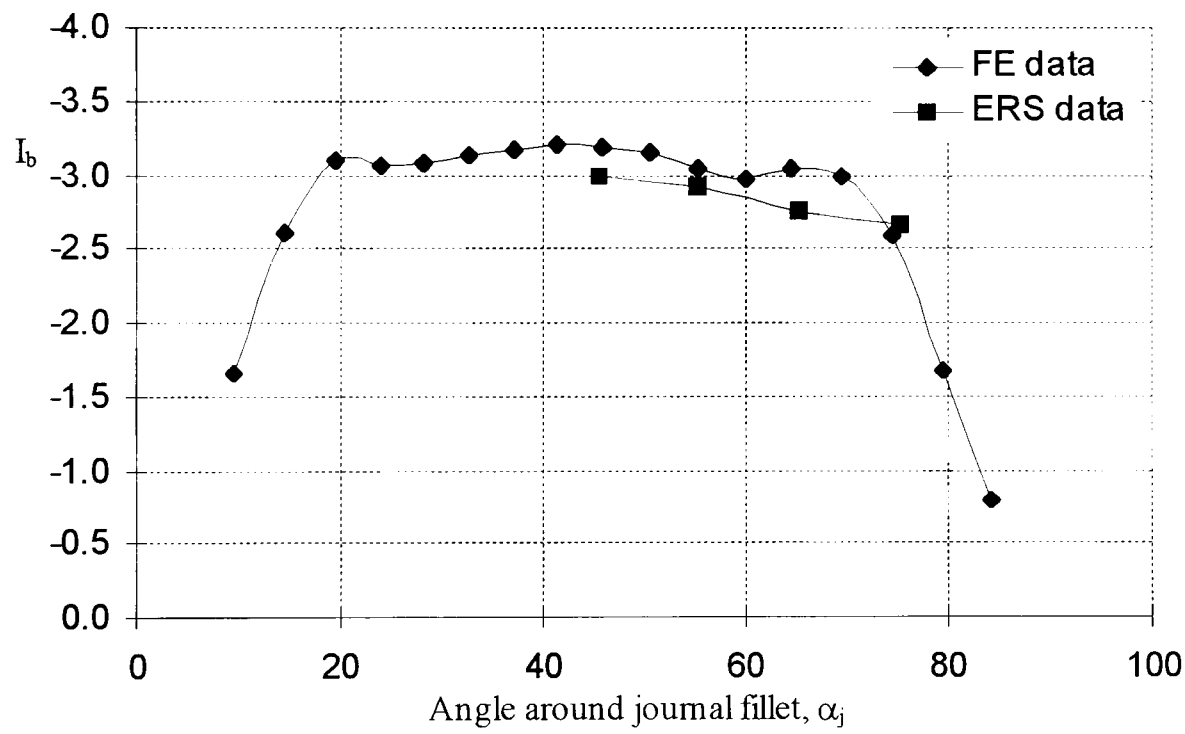

(b) Distribution around journal fillet (3D analyses)

Figure 3.18. Comparison of FE and ERS radial bending maximum principal stress distributions

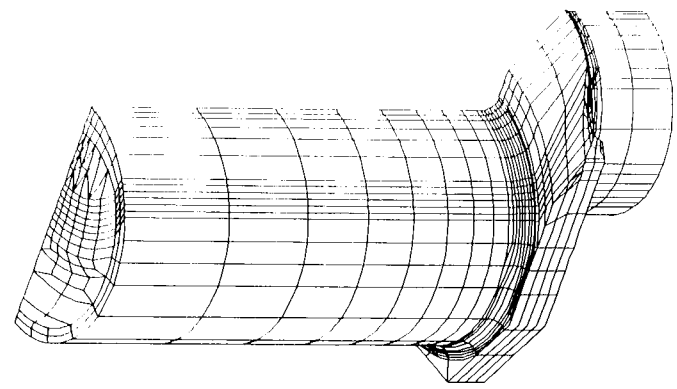

Figure 3.19. A typical FE mesh used for pure bending analyses

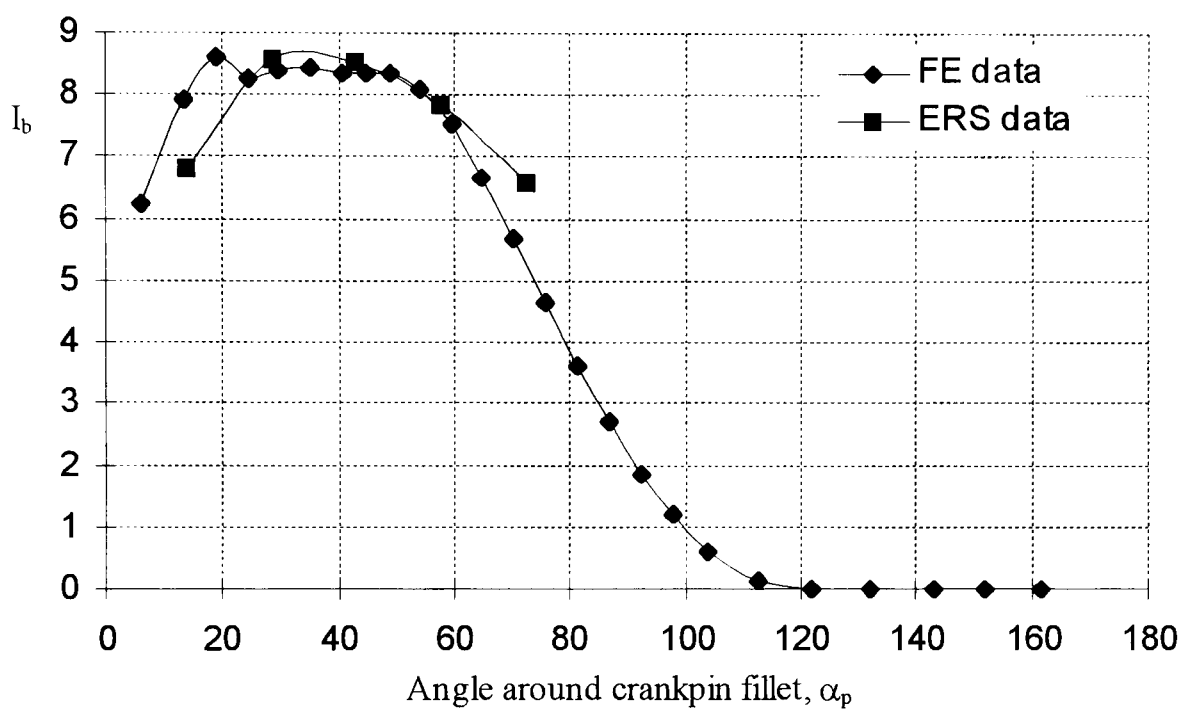

(a) Distribution around crankpin fillet (3D analyses)

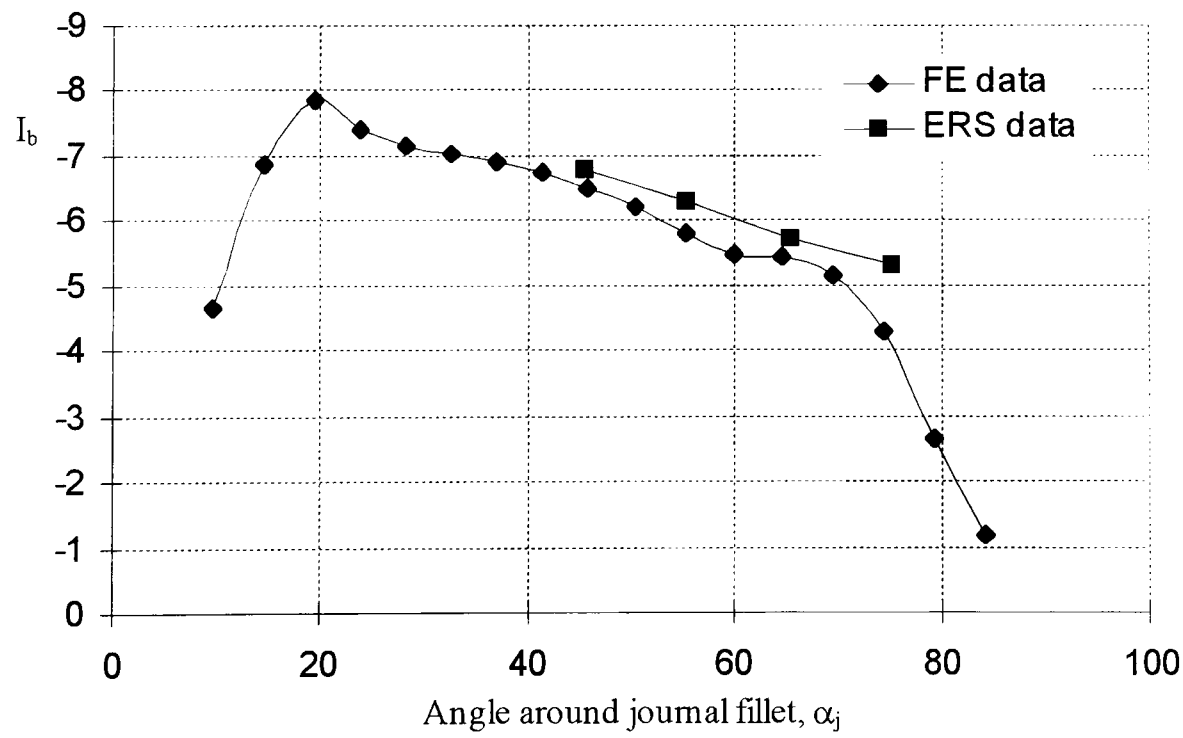

(b) Distribution around journal fillet (3D analyses)

Figure 3.20. Comparison of FE and ERS pure bending maximum principal stress distributions

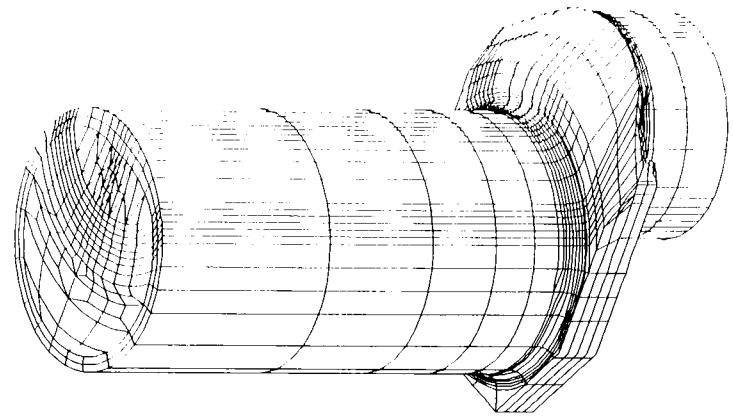

Figure 3.21. A typical FE mesh used for pure torsion analyses

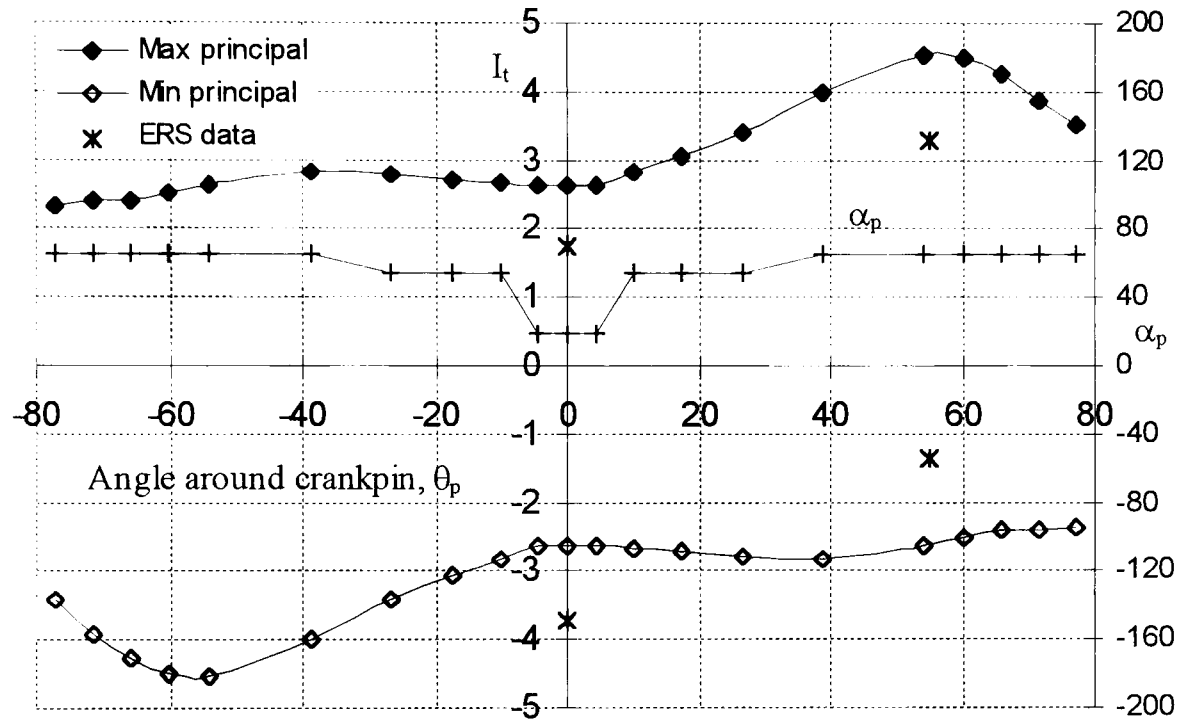

(a) Distribution around crankpin (3D analyses)

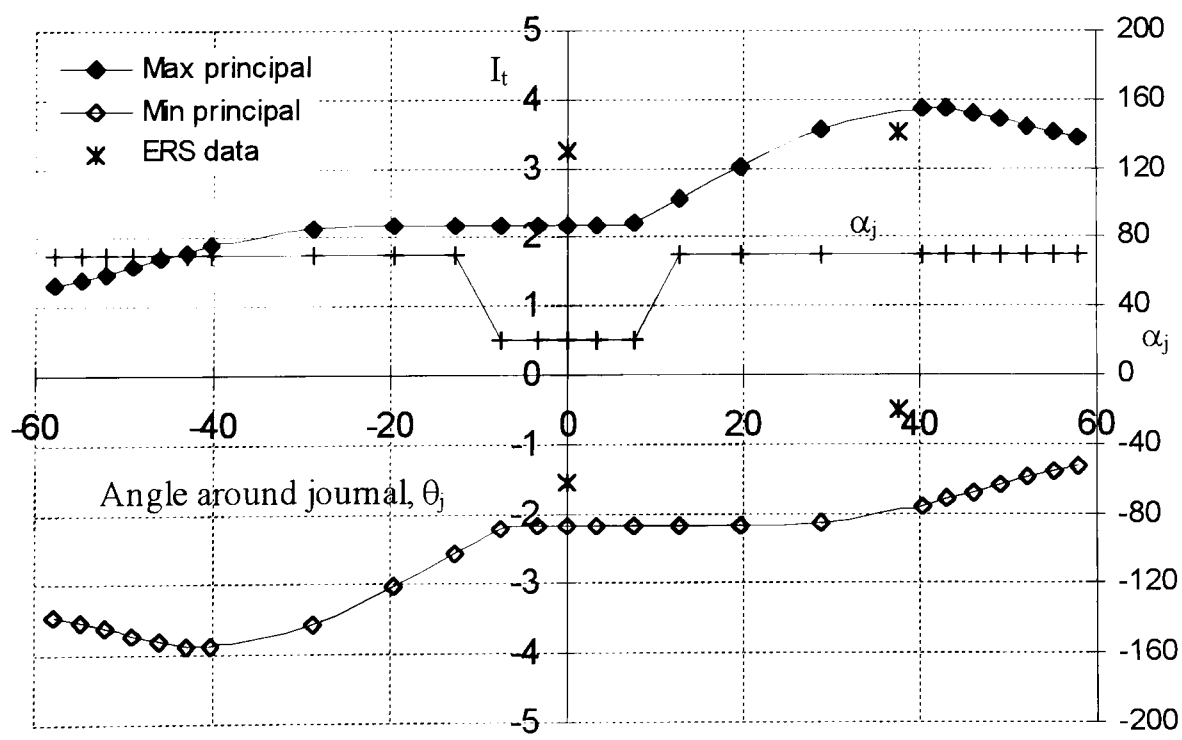

(b) Distribution around journal (3D analyses)

Figure 3.22. Comparison of FE and ERS pure torsion principal stress distributions

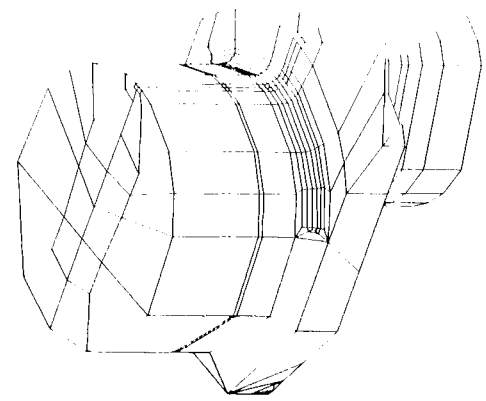

Figure 3.23. A typical half crankthrow BE mesh used for radial bending analyses

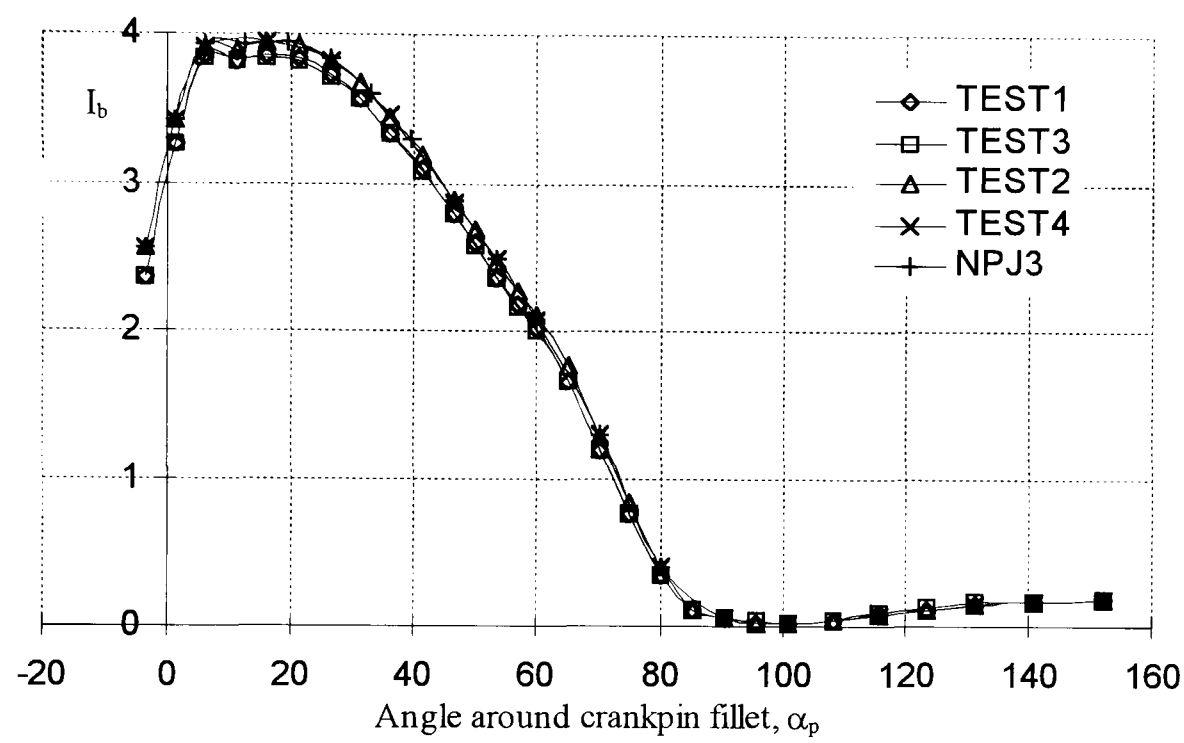

(a) Distribution around crankpin fillet (3D analyses)

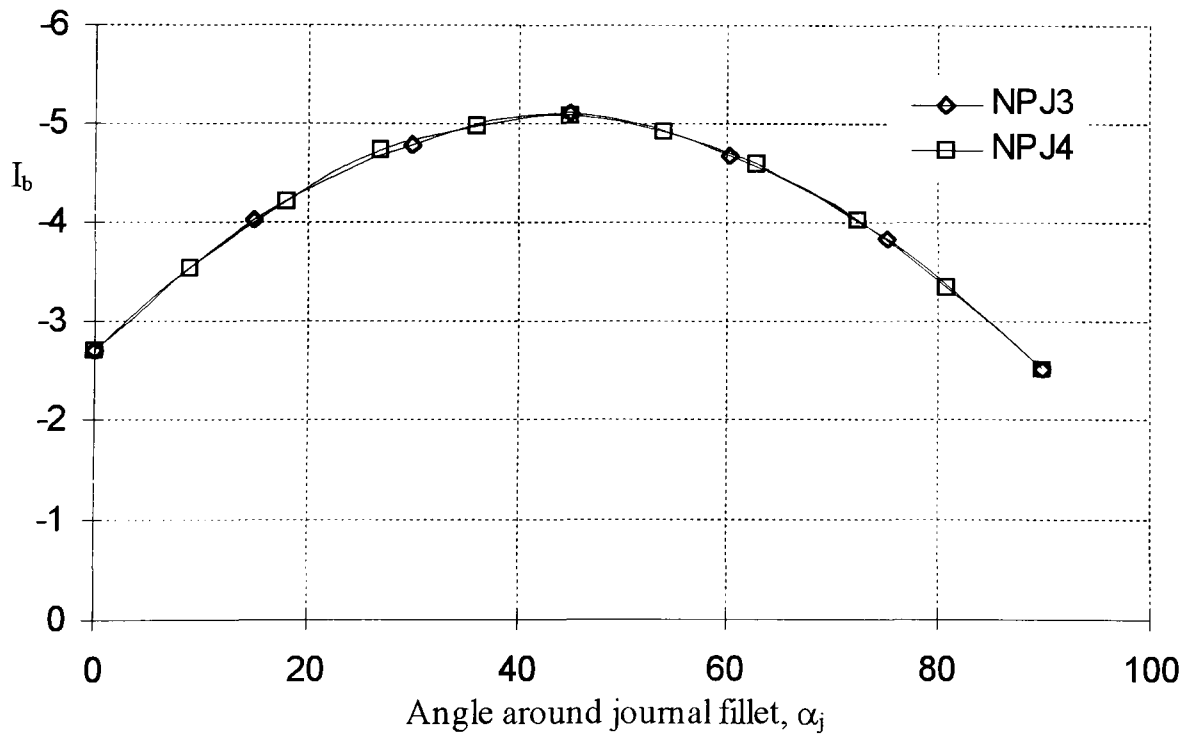

(b) Distribution around journal fillet (3D analyses)

Figure 3.24. Effects of fillet mesh refinement on radial bending maximum principal stress distributions

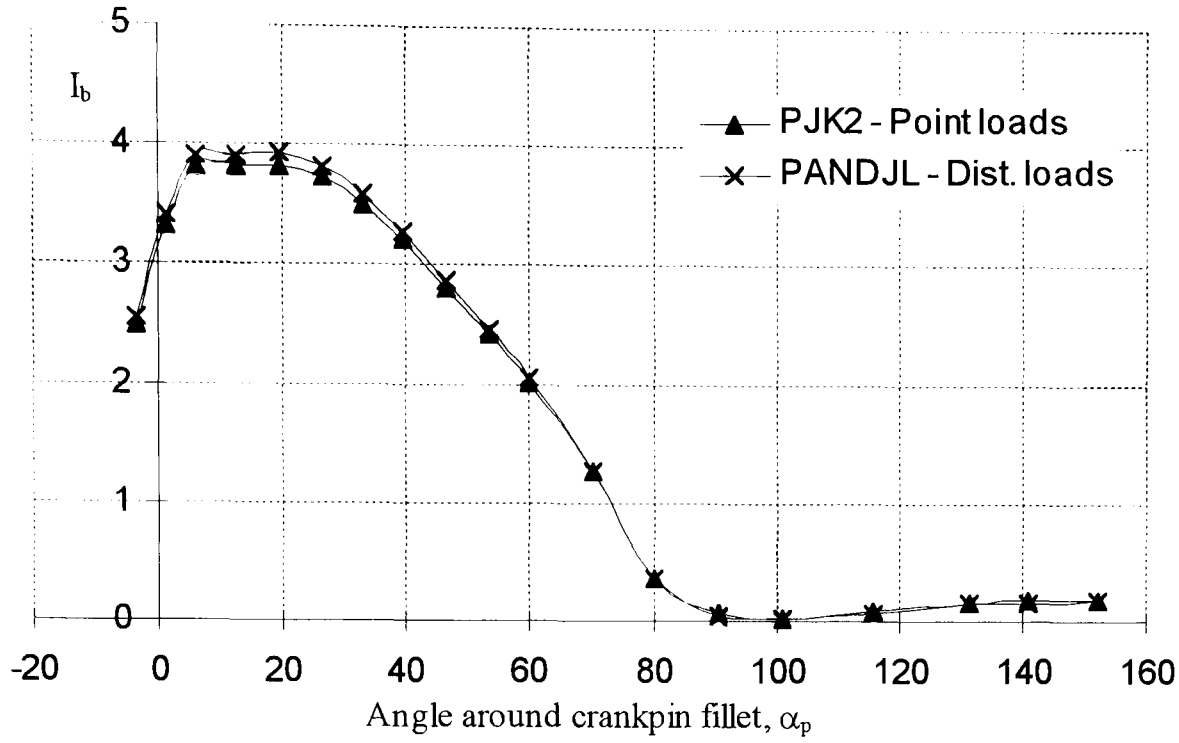

(a) Distribution around crankpin fillet (3D analyses)

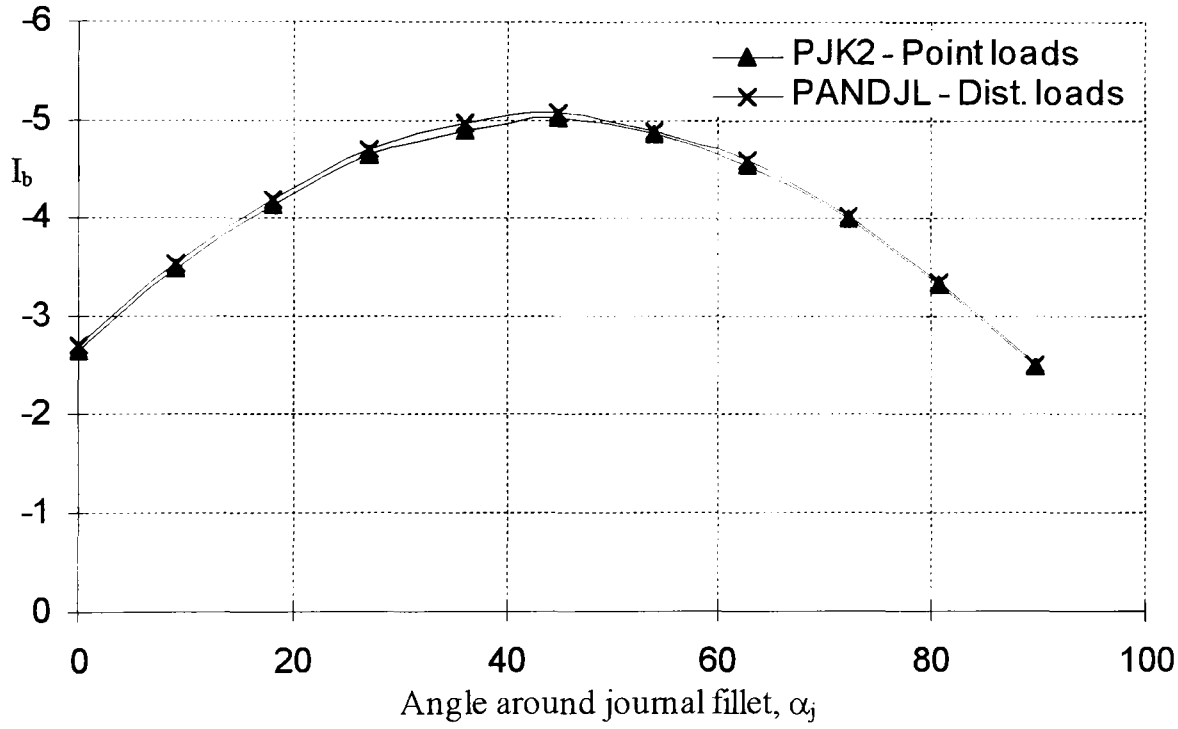

(b) Distribution around journal fillet (3D analyses)

Figure 3.25. Effect of loading conditions on radial bending principal stress distributions

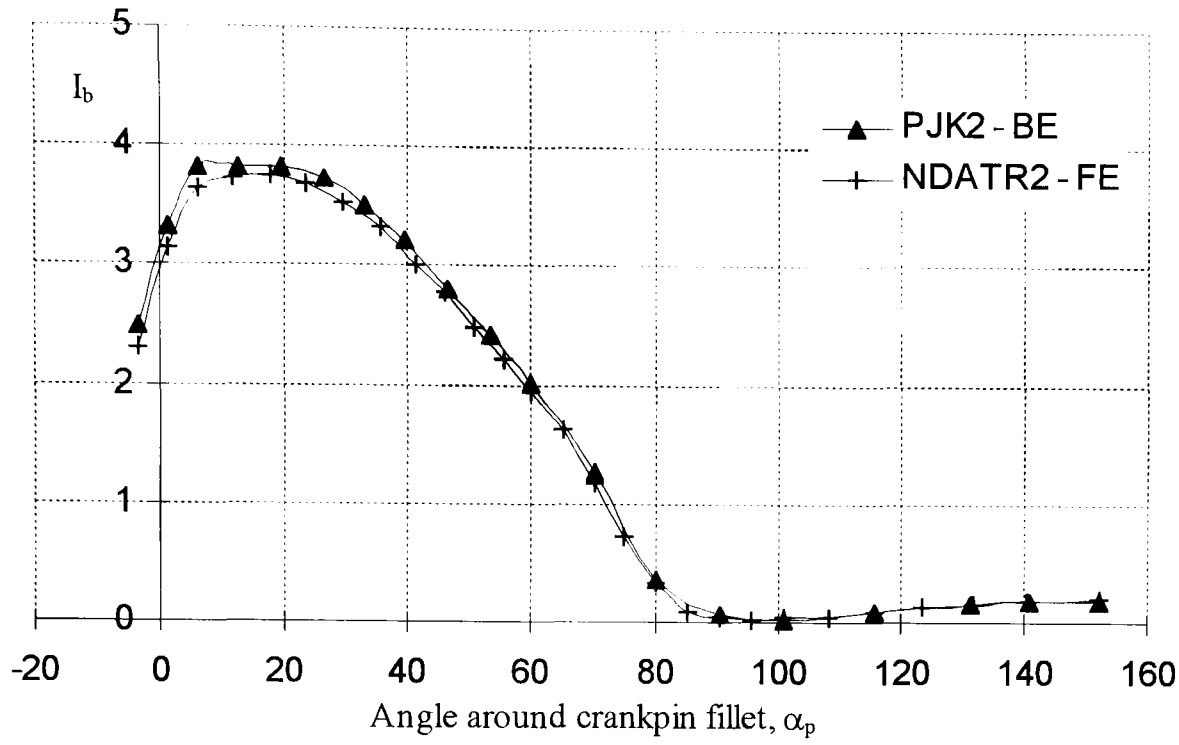

(a) Distribution around crankpin fillet (3D analyses)

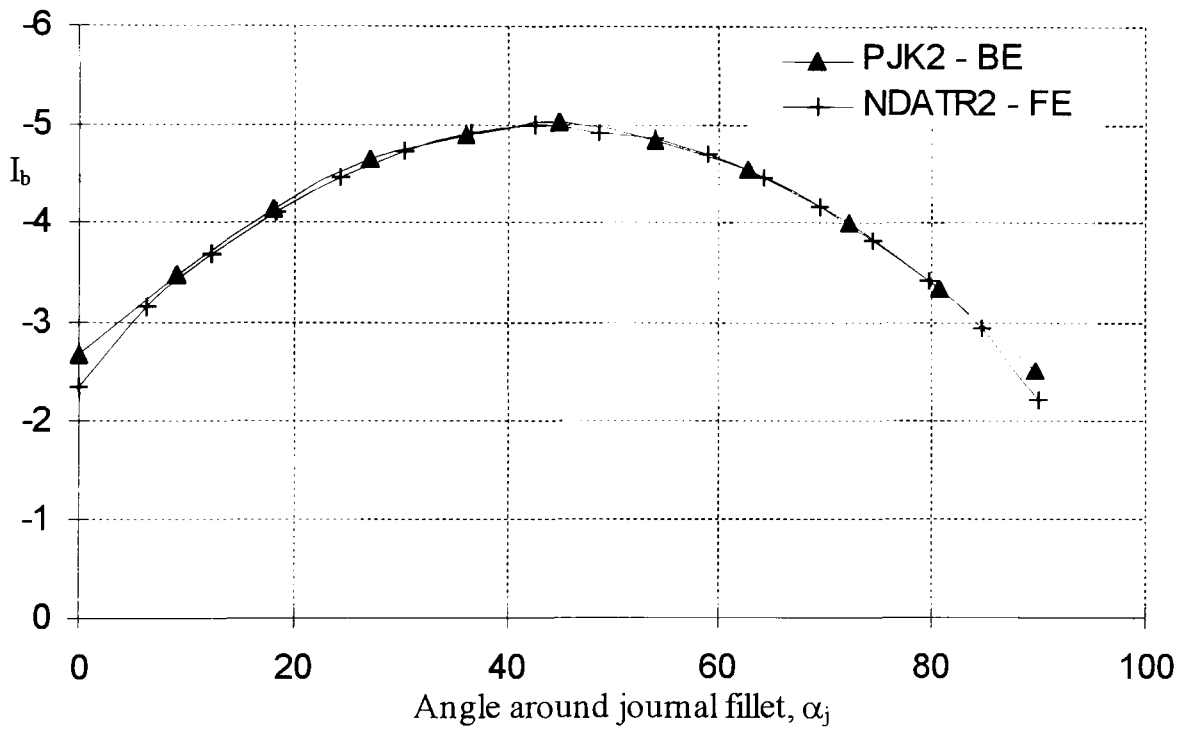

(b) Distribution around journal fillet (3D analyses)

Figure 3.26 Comparison of radial bending maximum principal stresses calculated by FE and BE methods

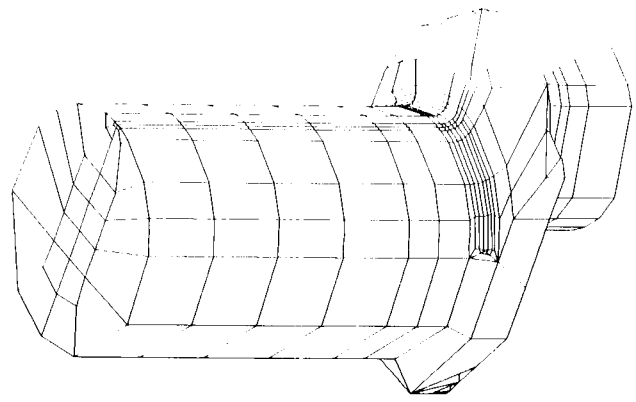

Figure 3.27. A typical half crankthrow BE mesh with extended journal used for pure bending analyses

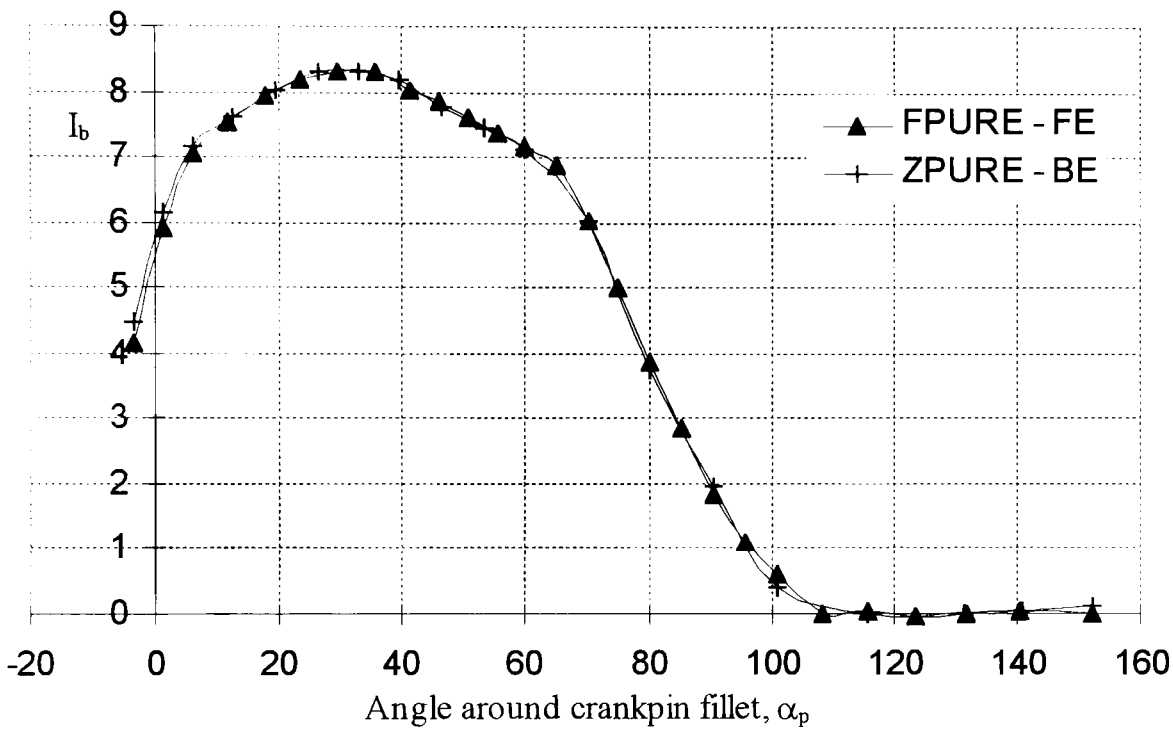

(a) Distribution around crankpin fillet (3D analyses)

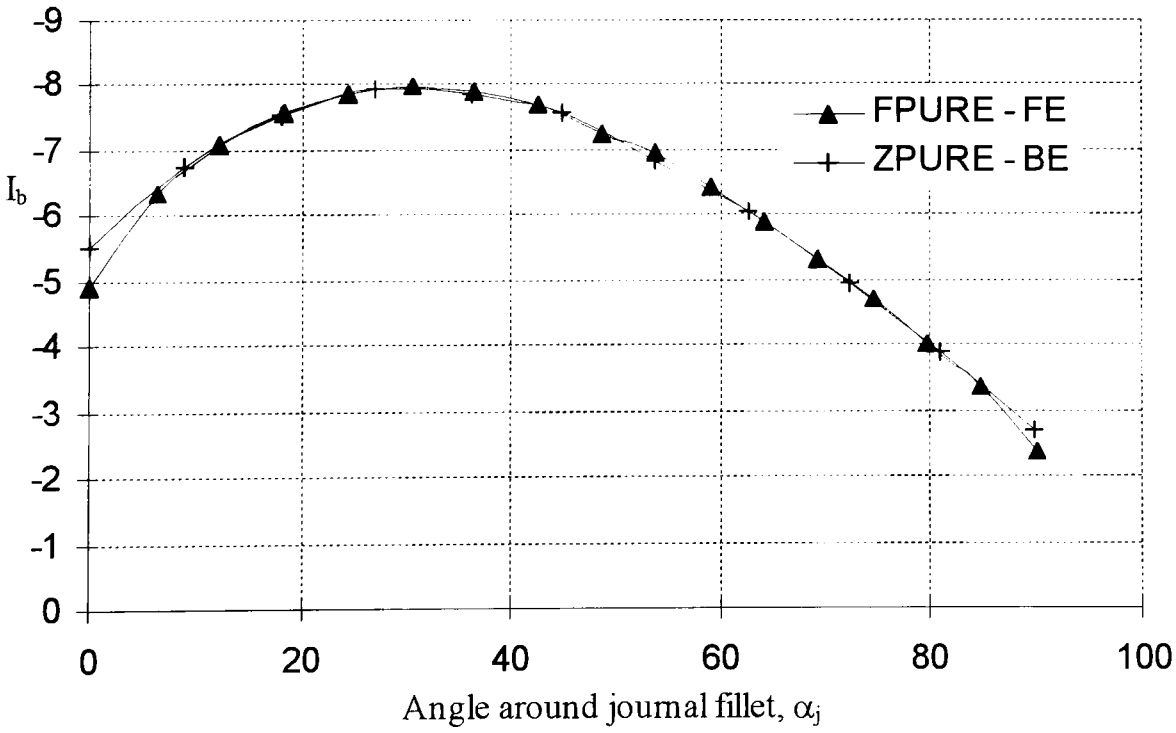

(b) Distribution around journal fillet (3D analyses)

Figure 3.28. Comparison of pure bending maximum principal stresses calculated by FE and BE methods

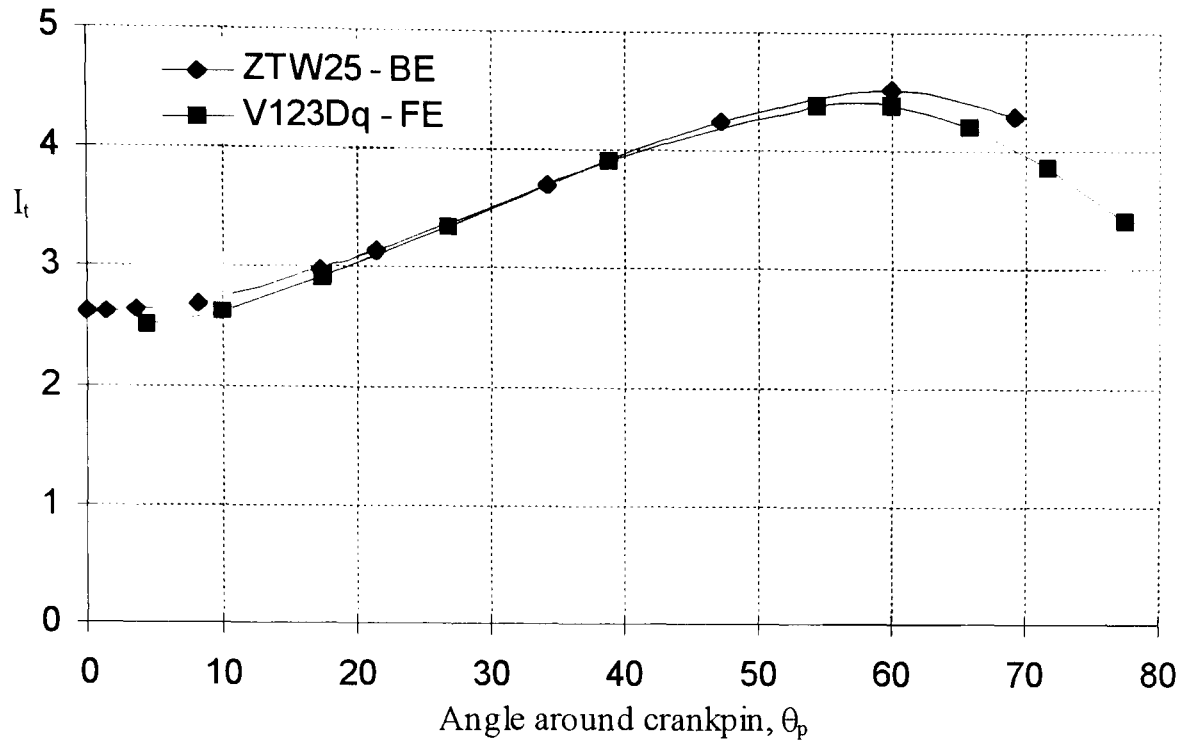

(a) Distribution around crankpin (3D analyses)

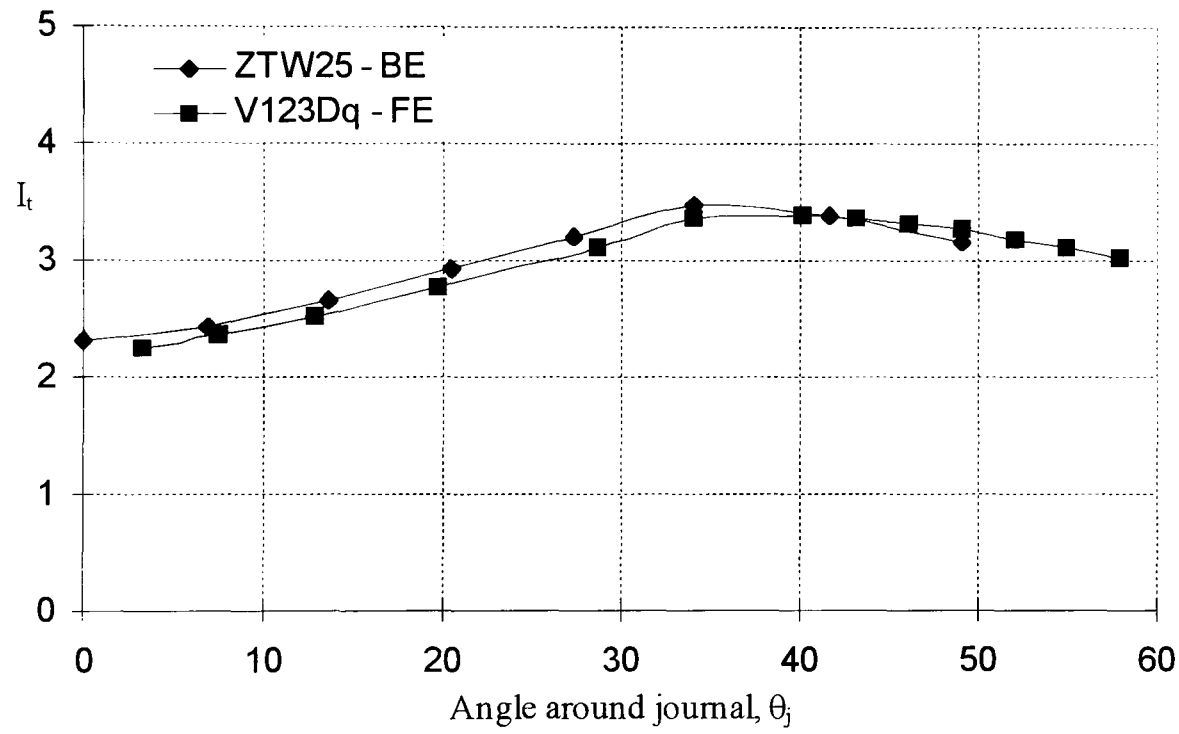

(b) Distribution around journal (3D analyses)

Figure 3.29. Comparison of pure torsion maximum principal stresses calculated by FE and BE methods

CHAPTER 4

NOMINAL STRESS BASIS

4.1 Introduction

The stress concentration factor is an indication of the magnitude of a local stress compared to a datum or nominal stress. Stress concentrations are usually of interest at stress raisers such as notches or holes in bars and plates. The accurate calculation of SCFs in crankshafts is an important design requirement. If the SCF is available for a particular crank geometry (from formulae or design curves), the designer can multiply this SCF by the appropriate nominal stress to calculate the maximum stress in the region of interest. This stress can be used to determine if the fatigue strength of the material will be exceeded.

However, a problem arises, because there is no universally accepted basis for these stress concentrations and nominal stresses. The review of available literature highlighted this problem, and shows the many different nominal stresses that have been used in the past as the basis for the stress concentration factor in the crankshaft (Section 2.5). The CIMAC M53 rules, for example, use three different prismatic bars to calculate nominal stresses; the crankpin for torsion at the crankpin fillet, the journal for torsion at the journal fillet and the web for radial bending. Ideally, one nominal stress basis should be accepted as standard. This nominal stress should be based around two important features;

1. It should be directly related to the region of the crank that is developing the fillet stresses. This will ensure that SCFs have reasonable and meaningful values.
2. It should be easily calculable, for the important loadcases of bending and torsion.

In order to demonstrate the advantages and disadvantages of different nominal stress methods, the crankthrow geometry from the photoelastic analyses will be used. This geometry has equal crankpin and journal fillet sizes (major radii = $0.064D_p$), which removes the unknown effect of fillet size from the analyses and aids the understanding of the nominal stress basis.

4.2 Nominal stress based in various bars

Several nominal stresses are investigated in Section 4.2. The stress concentration factors arising from the various nominal stress methods are tabulated in Tables 4.1, 4.2 and 4.3.

Table 4.1 Radial bending SCF values

Nominal stress	2D		3D	
	Crankpin fillet	Journal fillet	Crankpin fillet	Journal fillet
Crankpin section	3.3	5.1	3.7	5.0
H × B	1.6	2.6	4.0	5.3
Eye-shape	1.3	2.0	1.1	1.5
Slanted eye-shape	1.6	2.6	1.9	2.6
H × C	1.6	2.6	2.8	3.7
H × C + comp	1.8	2.3	3.1	3.4

Table 4.2 Pure bending SCF values

Nominal stress	3D	
	Crankpin fillet	Journal fillet
H × C	3.3	3.2

Table 4.3 Pure torsion SCF values

Nominal stress	3D	
	Crankpin fillet	Journal fillet
Crankpin section	4.4	3.4
H × C	3.6	2.8

4.2.1 Nominal stress in the crankpin

The maximum principal stresses in the fillets of the 3D model, occurring under radial bending, are normalised with respect to the maximum bending stress occurring in the crankpin (Figure 4.1). The nominal bending stress is calculated as follows,

$$\sigma_{nom} = \frac{M_c \times \frac{D_p}{2}}{\frac{\pi D_p^{\,4}}{64}}$$

$$\sigma_{nom} = \frac{32M_c}{\pi D_p^{\,3}} \qquad (4.1)$$

The SCFs at the crankpin and journal fillet are 3.7 and 5.0 respectively. A similar trend is seen in 2D (Figure 4.2), where the crankpin and journal fillet SCFs are 3.3 and 5.1 respectively. It is clear that for equal sized crankpin and journal fillet radii, the magnitudes of the two SCFs differ (see Section 4.3). It should also be noted that the SCF values are dependent on the dimensions of the crankpin, and can be significantly

altered by simply changing the crankpin diameter. This leads to the conclusion that the nominal stress should be directly related to the region that develops the fillet stresses, rather than some remote section.

Under the torsional loadcase, the principal fillet stresses are normalised with respect to the maximum shear stress occurring in the crankpin;

$$\tau_{nom} = \frac{T_c \times \frac{D_p}{2}}{\frac{\pi D_p^{\ 4}}{32}}$$

$$\tau_{nom} = \frac{16T_c}{\pi D_p^{\ 3}} \qquad (4.2)$$

The crankpin and journal fillet results (3D only) are presented in Figure 4.3, having SCFs of 4.4 and 3.4 respectively. The crankpin fillet SCF is higher than the journal fillet SCF purely because it occurs in the smallest radii of the compound fillet ($0.0358D_p$).

4.2.2 Nominal stress in a rectangular beam, H × B

It has been suggested that, of the many possible nominal stresses, one of the most appropriate is that based upon the bending moment at the web centre, making use of the sectional properties of a rectangular beam, H × B (Figure 4.4a). H is defined as the minimum distance between the crankpin and journal fillets (on the centreplane of the

crankthrow), and is inclined at an angle (90° - ϕ) to the crank axis. B is defined as the depth of the web.

$$\sigma_{nom} = \frac{M_w \times \frac{H}{2}}{\frac{BH^3}{12}}$$

$$\sigma_{nom} = \frac{6M_w}{BH^2} \qquad (4.3)$$

This idea is the application of the classical method of analysing stress concentrations in notched bars, which uses the two governing parameters H and R (fillet radius). Extensive research has been carried out in this field by Neuber and Peterson [21],[22], but the author is not aware of any publications where such a method has been applied to the analysis of overlapped crankshafts. The lack of a standard nominal stress basis (Section 2.5), would seem to support this conclusion. In the Neuber and Peterson work, stress concentrations are plotted against R/H. It is found that as R/H increases (increase in R or decrease in H) the stress concentration factors decrease (at a decreasing rate). Given that Neuber and Peterson are two of the most authoritative names in the stress concentration factor field of research, it is only natural to suggest that similar observations would be expected when calculating stress concentrations in crankshafts. Yet both Leikin [6] and Hoshino and Arai [5] found that as H was decreased (reducing positive overlap), stress concentrations increased. This is clearly contrary to Neuber's work, but may possibly be explained by Leikin's choice of nominal stress as that occurring in the web section T × B, and Hoshino and Arai's section which is based in the crankpin. Both of these methods allow for the increase in maximum stress due to the geometry change, but do not take into account the local

changes in nominal stress between the fillets. It would be certainly be wrong to assume that Leikin's and Hoshino and Arai's work is at fault because both methods produce valid, consistent SCFs, from which design curves and equations can be derived. However, as Lowell [20] observes, the bending plane developing the fillet stresses is in the web. A nominal stress based on a section between the fillets could perhaps be considered to produce more familiar trends in SCFs than a nominal stress based in the remote crankpin section.

Because bars in bending or torsion are usually considered to have their axes horizontal, it may be convenient to think of the dimension line H as vertical. This may assist in visualising half of a crankthrow as having complex projections on (and notches in) a rectangular section (Figure 4.4b).

The SCFs based on the H × B beam for the 3D model are similar in value to those calculated with the crankpin section nominal stress (4.0 - crankpin fillet, 5.3 - journal fillet). Although the section modulus of the beam H × B is far less than that of the crankpin, the bending moment, which is measured at the web centre, is also less, and this results in similar nominal stresses.

In this case, the 2D SCFs are less than half the values of the corresponding 3D SCFs (1.6 - crankpin fillet, 2.6 - journal fillet). However, this discrepancy does actually provide very useful information relating to how the nominal stress should be calculated. It has already been established that 2D models can produce similar SCFs to 3D models. Because of the uniform through thickness nature of the 2D model, the full

thickness ($0.0077D_p$) transmits the load from the point of application to reaction. This is true at every point on the 2D model and it therefore does not matter where the nominal stress is calculated. This implies that the 2D SCFs are more consistent than those calculated in the non-uniform 3D model. The 3D SCFs are higher than the 2D, which must mean that the nominal stress is lower than it should be. This is caused by the assumption that the full width of the 3D web uniformly carries load from the crankpin to the journal. In reality, because of the nature of the crank, there is a region where the crankpin and journal are overlapped, forming an 'eye-shape'. This provides a large common area between the crankpin and journal, through which most of the load will be transmitted. If this is the case, the nominal stress in this region will be higher, and the resulting stress concentrations at the fillets will be lower, theoretically showing an improved agreement with the 2D results.

4.2.3 Nominal stress in the eye-shape

The section modulus of this eye-shaped bar (which runs axially along the crankshaft) is calculated in Appendix 4 for the radial bending loadcase. It is found that the bar does not bend about an axis mid way across it's section - the neutral axis is now biased towards the crankpin (or to generalise, the smaller of the crankpin and the journal). In order to provide a 2D comparison for the 3D eye-shape normalised results, the 2D radial bending data was normalised with respect to the nominal stress occurring at the web centre in a rectangular section. The major dimension of this section is defined by the overlap of the crankpin and journal, and the minor dimension is the thickness assigned to the 2D elements ($0.0077D_p$). It was assumed that the neutral axis of this bar was half way across the section.

The SCFs from the 3D model are 1.1 and 1.5 at the crankpin and journal fillets. The 2D model produces SCFs of 1.3 and 2.0 at the crankpin and journal fillets. The agreement between 2D and 3D results is better than with the H × B method, but some problems do remain when using the eye-shape nominal stress.

1. The apparently important H (minimum section) term is neglected with this method.
2. The 3D non-dimensional stresses at both fillets are still lower than the 2D non-dimensional stresses, indicating that the nominal stress used for the calculations is too large, i.e. the eye-shape section is too small. This also has the effect of producing SCFs with a magnitude very close to unity, which is undesirable because it misleadingly indicates that there is virtually no stress concentration at the pin/web and journal/web intersections. Matters could be made worse if the SCFs actually fell below unity.

4.2.4 - Nominal stress in the slanted eye-shape

The proposals presented in this method are in keeping with the traditional methods of analysis of stress concentration factors in notched bars. The last two points in Section 4.2.3 suggest that the 'ideal' nominal stress would be based on a bar running perpendicular to the minimum section, taking the shape of the maximum common area between the crankpin and journal. The calculation of the section modulus of such a bar is based on that in Appendix 4 and is detailed fully in Appendix 5. The slanted eye-shape is defined by two elliptical overlapping curves, but the angles of overlap are not the same as for the standard eye-shape bar. This can be better visualised by referring

to Appendix 6. The radii, R_1 and R_2 are defined as the radii of the crankpin and journal at the points where the minimum section, H, touches each fillet. Therefore R_1 and R_2 are slightly larger than $D_p/2$ and $D_j/2$ respectively. The axial distance, V, between the two end-points of H must also be calculated.

The 3D radial bending SCFs, normalised with respect to this slanted eye-section, using the bending moment at the web centre, are presented in Table 4.1. They can be compared with the 2D radial bending results which are normalised with respect to the H × B section (the 2D equivalent of the slanted eye-shape).

The agreement between the 2D and 3D results is greatly improved when using the slanted eye-shape method. The SCFs at the crankpin fillet are 1.6 (2D) and 1.9 (3D), and at the journal fillet they are both 2.6 (2D and 3D). This method fulfils the objectives of achieving good agreement between 2D and 3D results, and also to relate the SCFs to a relevant section of the crank, and achieve SCFs of a reasonable magnitude. However, one of the original objectives was that the nominal stress be easily calculable for the important loadcases of bending and torsion. The calculation for the radial bending nominal stress (Appendix 5) is far from trivial, and that for the torsional nominal stress would be even less trivial. It is therefore necessary to refine the slanted eye-shape method in the interest of reducing calculation time and effort on the part of the designer.

4.2.5 Nominal stress in a rectangular beam, H × C

Essentially, the new method should have similar characteristics to the slanted eye-shape method, i.e.

1. Nominal stress based in a bar running perpendicular to the minimum section H.
2. The bar should have one of it's dimensions as H, and have an area similar to the slanted eye bar.

It has already been established that a similar method, the H × B beam, produces SCFs in the 3D models that are significantly higher than the 2D SCFs. Other than that, the method is a good one. It is a simple task to calculate bending and torsion nominal stresses in a rectangular beam, and if the area of the beam cross section can be reduced, the method would be ideal. This would increase the nominal stress and therefore reduce the 3D SCFs. It is necessary to choose a second dimension for the beam that is in some way related to the governing dimensions of the crankthrow. The most appropriate dimension would appear to be C, the maximum width of the overlap of the crankpin and journal. This produces a beam which is of similar dimensions to the largest dimensions of the slanted eye-shape, and therefore has a slightly larger area (Figure 4.5). This results in a lower nominal stress, and SCFs which are higher than those calculated by the slanted eye-shape, but not as high as with the H × B method. The nominal bending stress is calculated as follows;

$$\sigma_{nom} = \frac{6M_w}{CH^2} \tag{4.4}$$

The H × C method SCFs are presented in Table 4.1 and should be compared with the 2D results from the H × B method. The 3D SCFs are 2.8 at the crankpin fillet, and 3.7 at the journal fillet, compared to the 2D SCFs of 1.6 at the crankpin fillet, and 2.6 at the journal fillet.

The agreement between the 2D and 3D results is slightly worse than when using the slanted-eye shape method, but the H × C nominal bending stress is significantly easier to calculate, and importantly is based on the region of the crankthrow that develops the fillet stresses.

The torsional loadcase is complicated slightly by the H × C beam being inclined at angle ϕ to the crankthrow axis. It is necessary to split the vector representing torque (which is parallel to the crankthrow axis) into its components parallel to and perpendicular to the rectangular bar. The former causes the bar to twist about its axis, and the nominal shear stress is defined as

$$\tau_{nom} = \frac{T\cos\phi(3C + 1.8H)}{H^2C^2} \tag{4.5}$$

The latter component causes tangential bending in the bar, and the nominal stress can be defined as

$$\sigma_{\theta nom} = \frac{6T \sin \phi}{HC^2} \tag{4.6}$$

The nominal stress based on the tangential bending component of torque is used because the greatest torsional stresses in the crankthrow occur near the ends of the overlap, where the maximum nominal tangential bending values are.

The crankpin and journal fillet SCFs (Table 4.3) are 3.6 and 2.8 respectively, which is lower than those calculated with the crankpin section nominal stress, but still a reasonable magnitude.

Summarising, the H × C beam has many advantages over the other methods;

1. Only one bar is needed.
2. It touches the fillets near the positions of the maxima in the crankthrow due to radial bending and torsion.
3. The nominal stresses are easily calculable for radial bending and torsion.
4. It produces SCFs which are directly related to the region developing the fillet stresses.
5. The SCFs are therefore of a reasonable magnitude.

4.3 Compression in the web and pure bending

Up to this point, Section 4.2 has solely concentrated on comparisons between radial bending results in two and three dimensions, but it is also important to consider the pure bending results and to compare these with the radial bending data. This provides an insight into why (for this particular geometry) the magnitude of the journal fillet SCF is higher than the crankpin fillet SCF. The differences that exist between the radial and pure bending loadcases are presented in Figure 4.6.

The fundamental difference between the radial and pure bending loadcases is the extra compression in the web that occurs under radial bending (Appendix 7). Under radial bending, this extra compression will cause the nominal stress at the journal fillet (under compression) to increase, and the nominal stress at the crankpin fillet (under tension) to reduce. If this is not taken into account in the nominal stress calculation, then the journal fillet SCF will be higher than the crankpin fillet SCF.

Figure 4.7 shows a comparison of the 3D pure bending results with the 3D radial bending results. The results for both loadcases are normalised with respect to the maximum bending stress in the H × C beam at the web centre. The pure bending SCFs are 3.3 at the crankpin fillet and 3.2 at the journal fillet, which is reasonable for equal sized fillets. The radial bending SCF at the crankpin fillet is 16% lower than the pure bending SCF, but is 16% higher at the journal fillet. If the extra compressive stress that occurs in the H × C beam under radial bending is taken into account (Appendix 7), it is seen that the radial bending SCFs move towards each other, and by doing so, they

show improved agreement with the pure bending SCFs (within ~6%). This effect can be clearly observed in Figure 4.8.

The remaining difference between the radial bending and pure bending SCFs is inevitable. The process of adding the compressive stress component in the web is heavily dependent on the area of the cross section that the normal component of force is assumed to act over. The H × C section is known to be an approximation of the area carrying the majority of the load from the crankpin to the journal, and this affects the calculated magnitude of the compressive stress in the web.

It is interesting to note that for the pure bending loadcase, the peak stresses occur at different angles, α_p' and α_j', to the radial bending SCFs. For the pure bending case, the SCFs occur very close to the points where the minimum section, H, touches the crankpin and journal fillets. This is a further indication that H is a critical parameter.

4.4 Choice of nominal stress basis for geometric investigations

It may appear that instead of clarifying the issue of nominal stress basis, the author is simply adding to the numerous methods already in existence. However, the purpose of this chapter is to propose a reasonable and practical nominal stress basis, and the H × C method fulfils these criteria, under both radial bending and pure torsion. By relating the nominal stress to the critical H dimension, SCFs at different values of R/H should show good agreement with trends established by Neuber in simple notched beams and bars. This has the implication of simplifying the crankshaft design process by allowing the crankshaft to be analysed using existing formulae and curves.

The investigations detailed in this thesis are widely related to the geometric form of the crankshaft, including the extent of overlap, web thickness, fillet size, fillet shape and crankpin and journal diameters. By varying any one of these parameters, the R/H term will be changed. This will allow curves similar to Neuber's [21], [22] to be plotted - SCF v R/H. Whilst giving a good indication of how SCFs behave with geometry changes, this may mislead the reader in terms of stress variations. For example, an increase in overlap of crankpin and journal will inevitably stiffen the crankthrow and reduce the peak principal stresses in the crankpin and journal fillets. But as the overlap is increased, H increases and the R/H term decreases in value. According to Neuber [21], this leads to an increase in fillet SCFs. Simply viewing the SCF variation may lead the reader to assume that stresses also increase with overlap.

For this reason, it is most appropriate when analysing geometric changes to present the results via (at least) one of three methods;

1. Stresses (not normalised).
2. Stress normalised with respect to the maximum stress in the crankpin, which gives a good indication of actual stress levels since for most analyses this nominal stress remains constant.
3. Stress normalised with respect to the maximum stress in the H × C section, which highlights trends in a particularly relevant SCF for a range of R/H values.

The chosen method of presentation is clearly stated for each analysis.

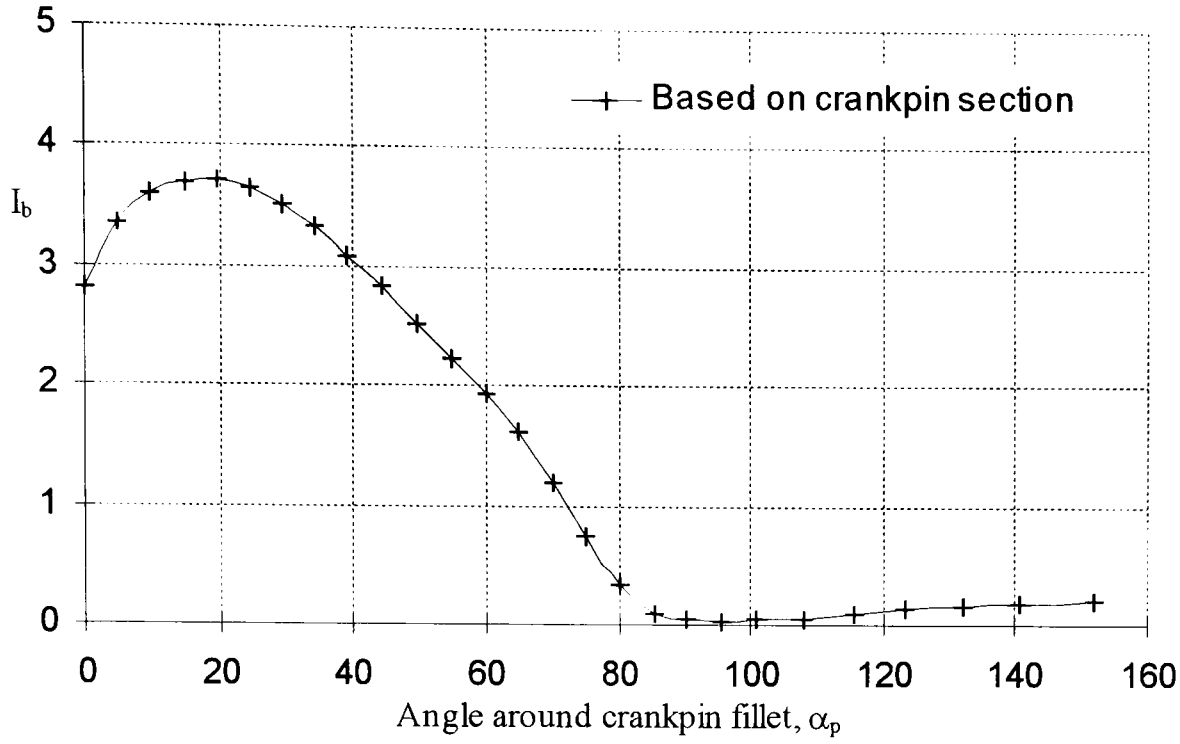

(a) Distribution around crankpin fillet (3D analysis)

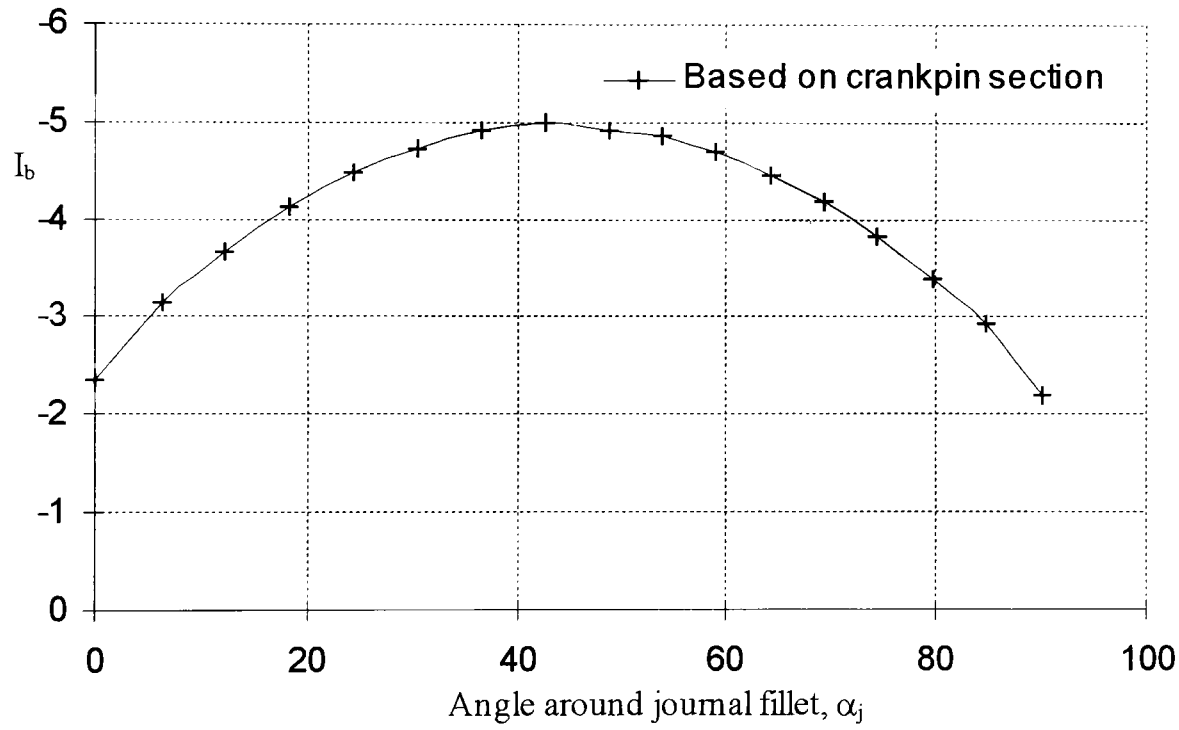

(b) Distribution around journal fillet (3D analysis)

Figure 4.1. Maximum principal stress indices under radial bending based on the maximum bending stress occurring in the crankpin (3D model)

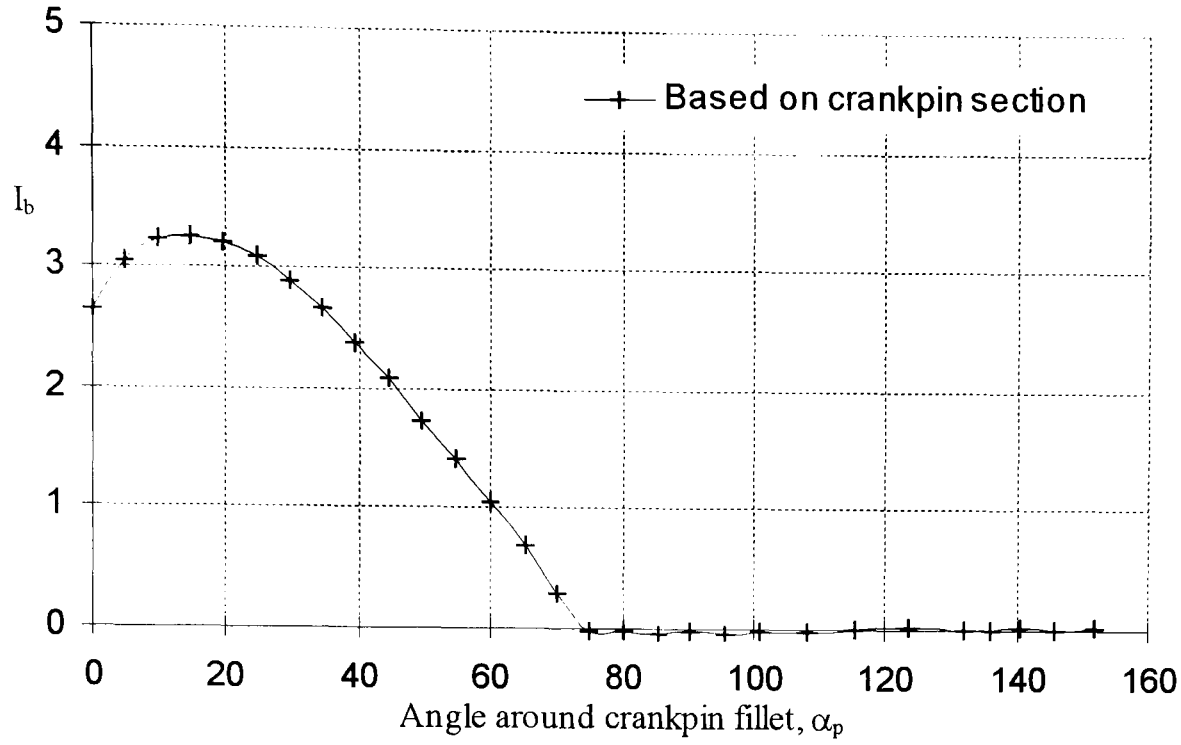

(a) Distribution around crankpin fillet (2D analysis)

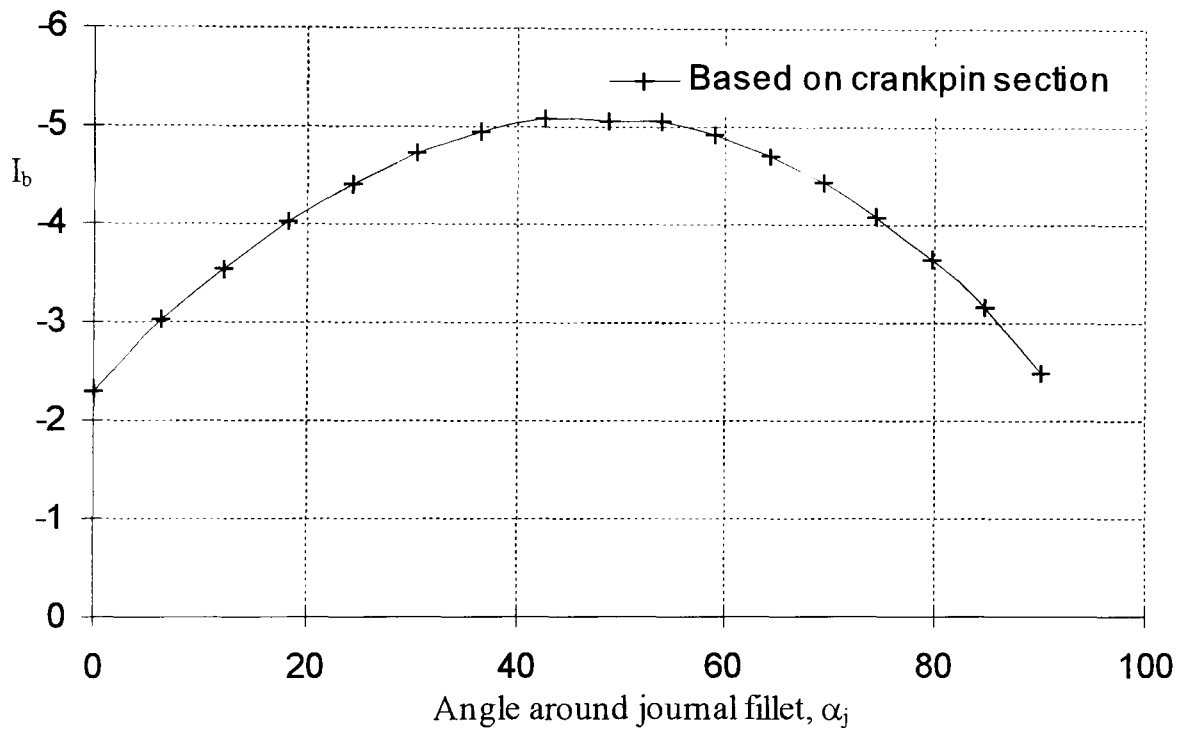

(b) Distribution around journal fillet (2D analysis)

Figure 4.2. Maximum principal stress indices under radial bending based on the maximum bending stress occurring in the crankpin (2D model)

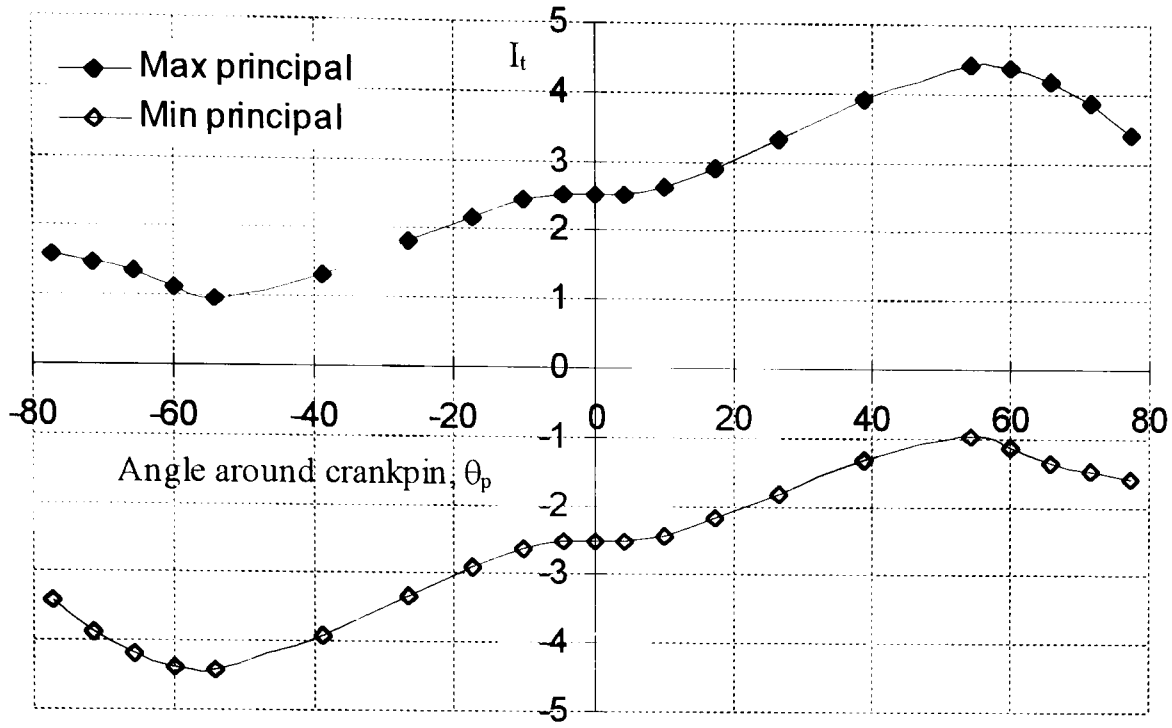

(a) Distribution around crankpin (3D analysis)

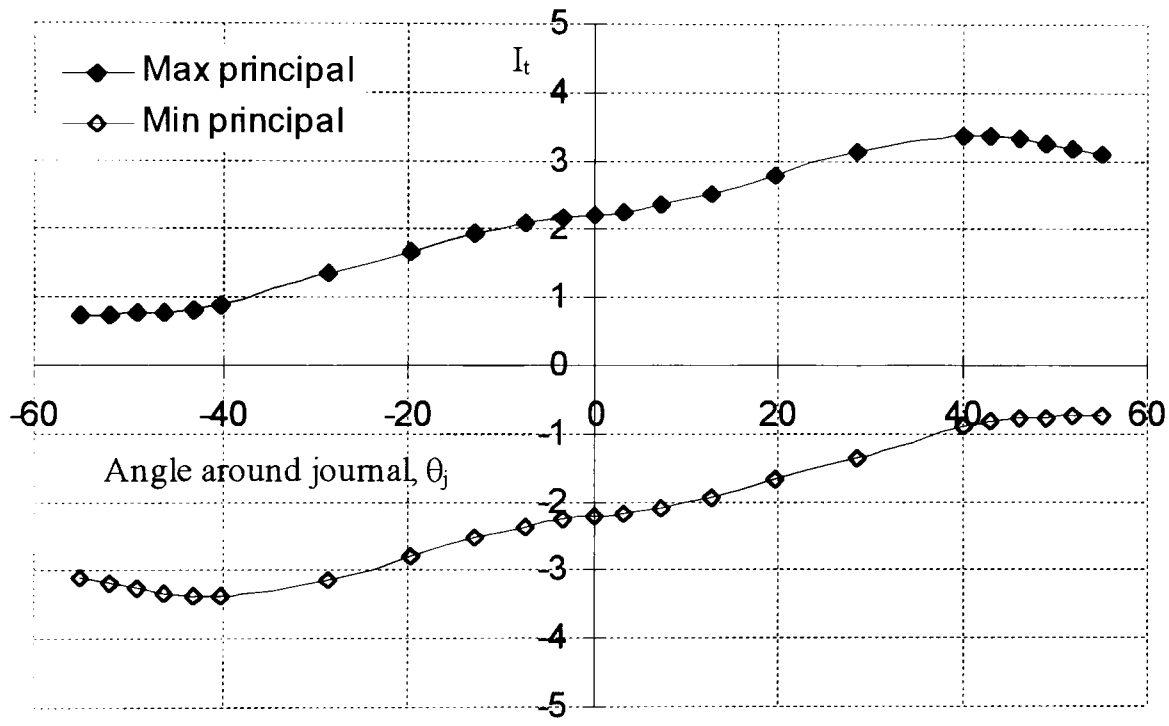

(b) Distribution around journal fillet (3D analysis)

Figure 4.3. Maximum principal stress indices under pure torsion based on the maximum shear stress occurring in the crankpin (3D model)

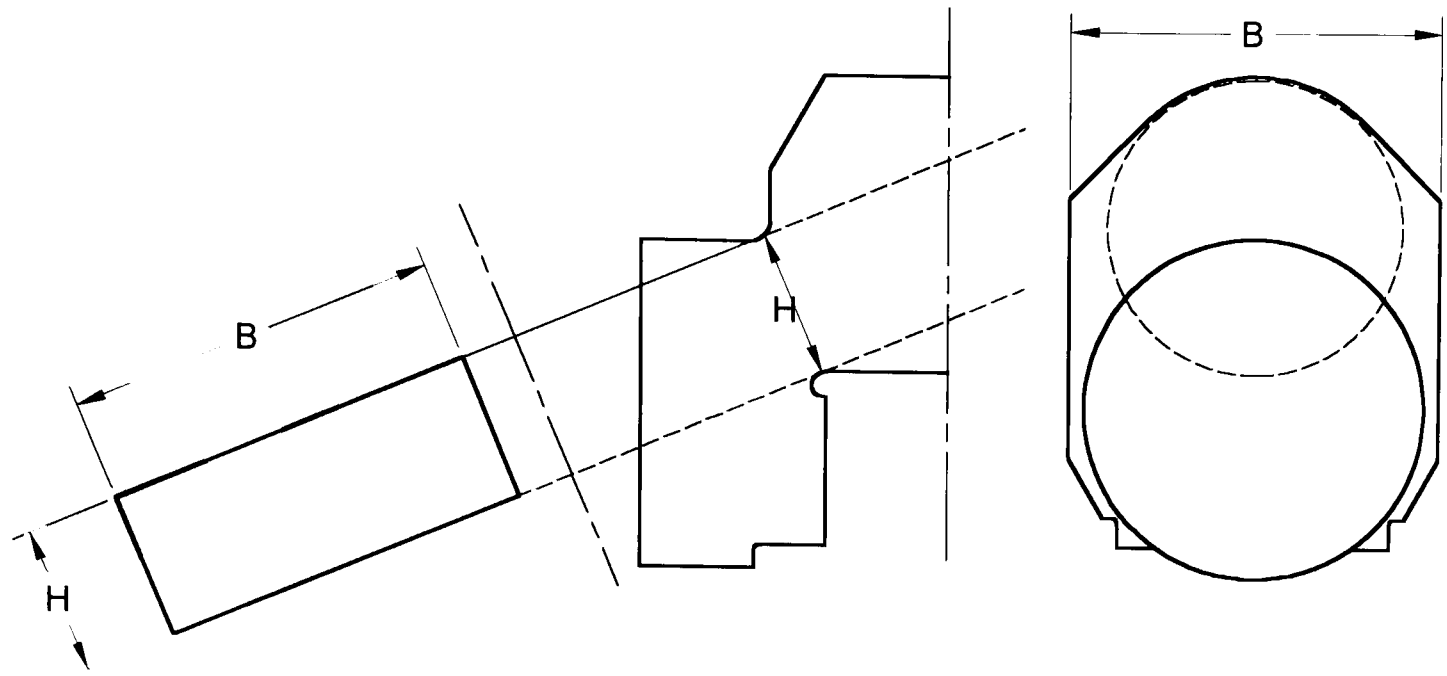

(a) Definition of H × B beam for nominal stress calculation

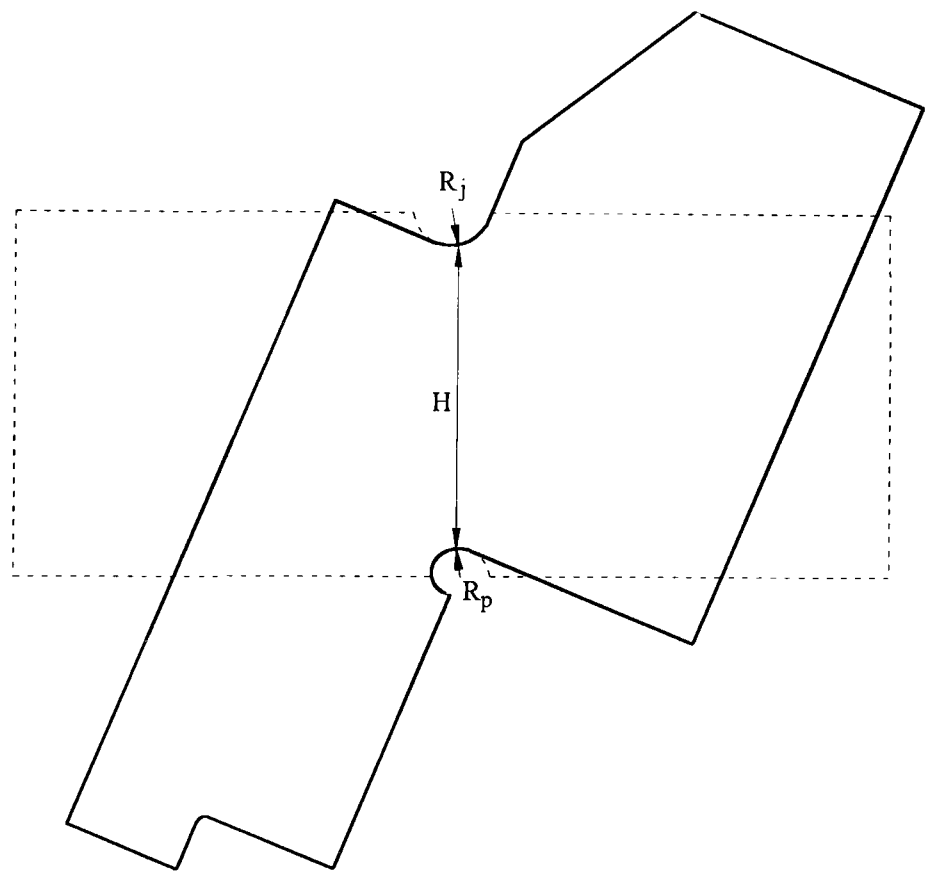

(b) A crankthrow considered as a notched rectangular beam

Figure 4.4. The application of classical stress concentration factor techniques

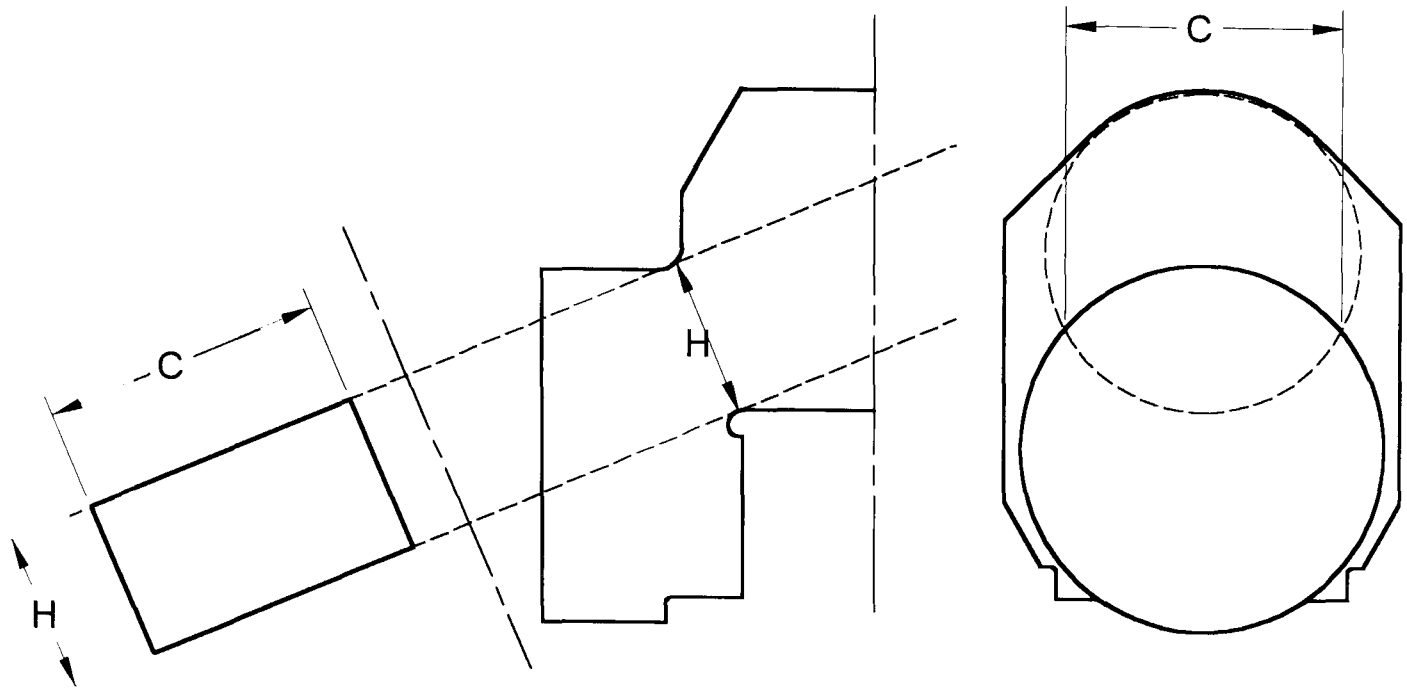

Figure 4.5. Definition of H × C beam for nominal stress calculation

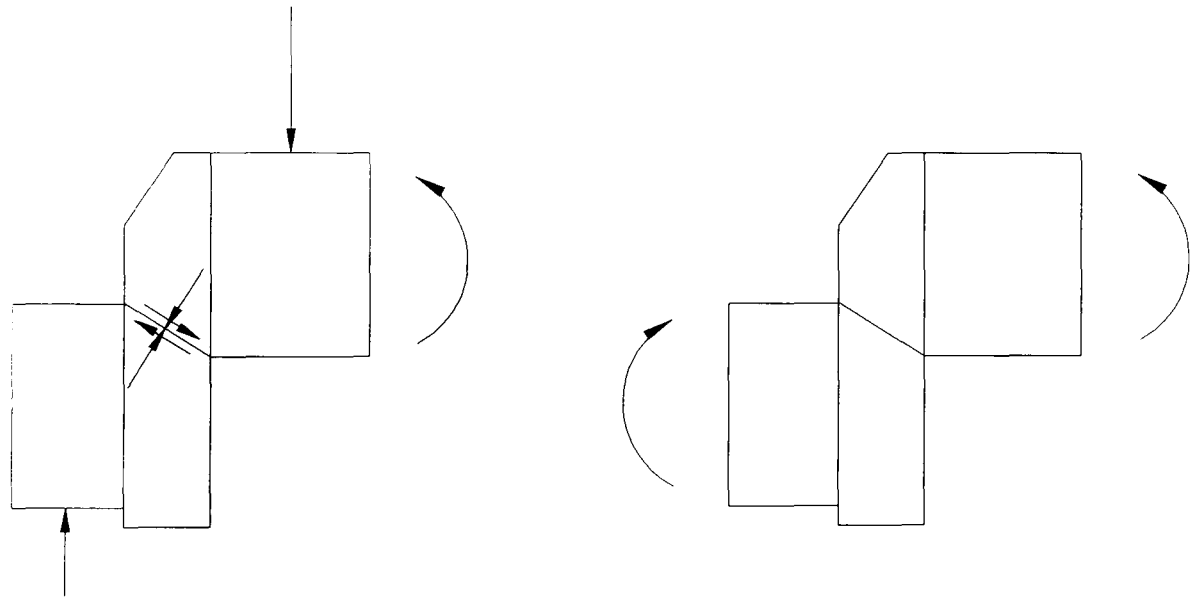

(a) Radial bending (b) Pure bending

Figure 4.6. A comparison of the radial and pure bending loadcases

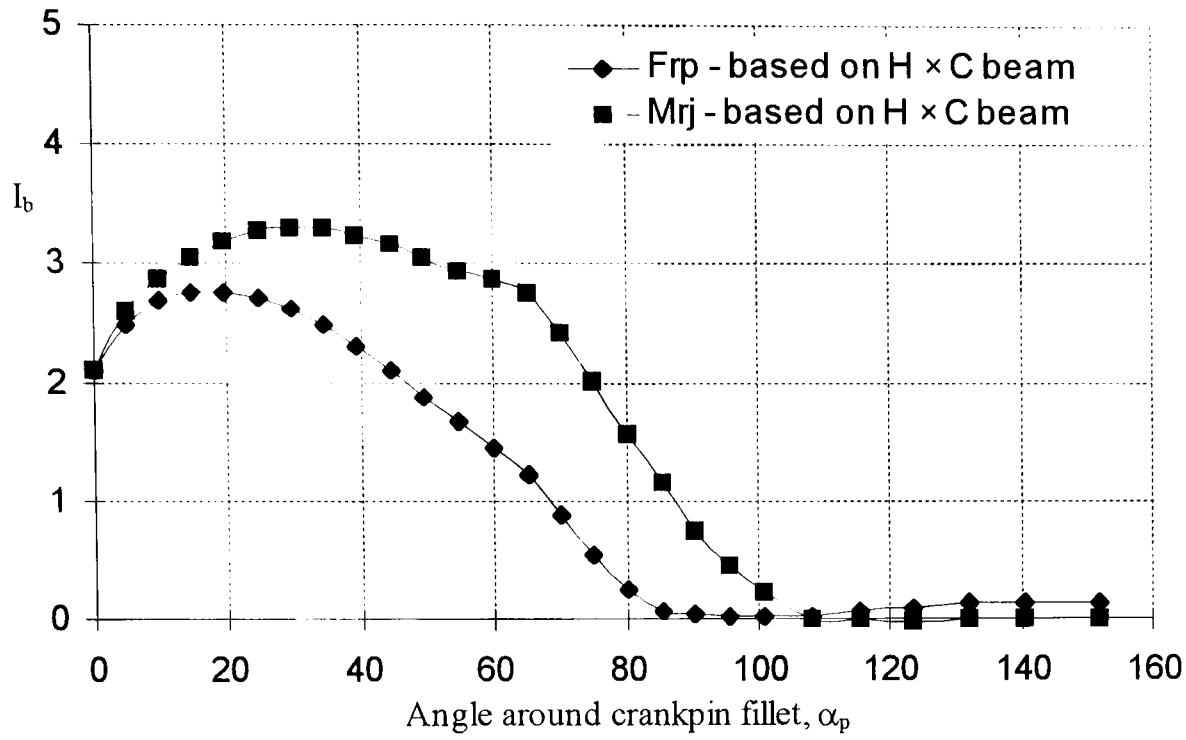

(a) Distribution around crankpin fillet (3D analyses)

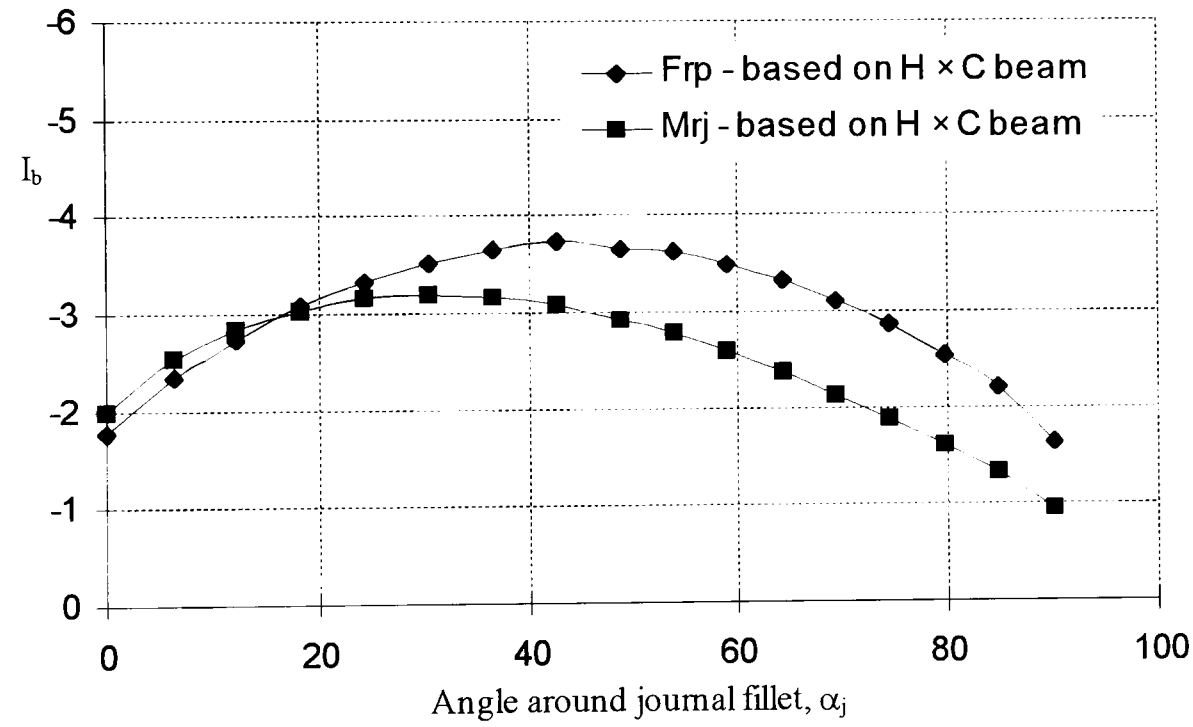

(b) Distribution around journal fillet (3D analyses)

Figure 4.7. Maximum principal stress indices under radial and pure bending based on the maximum bending stress occurring in the H × C beam

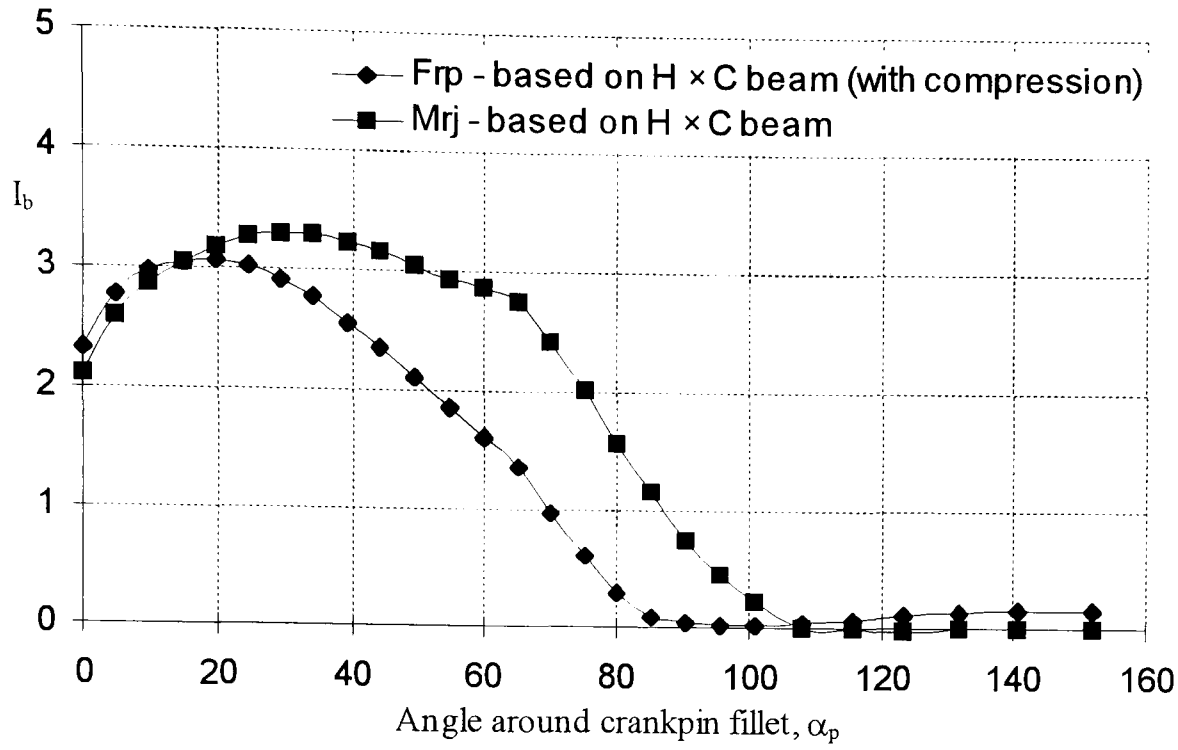

(a) Distribution around crankpin fillet (3D analyses)

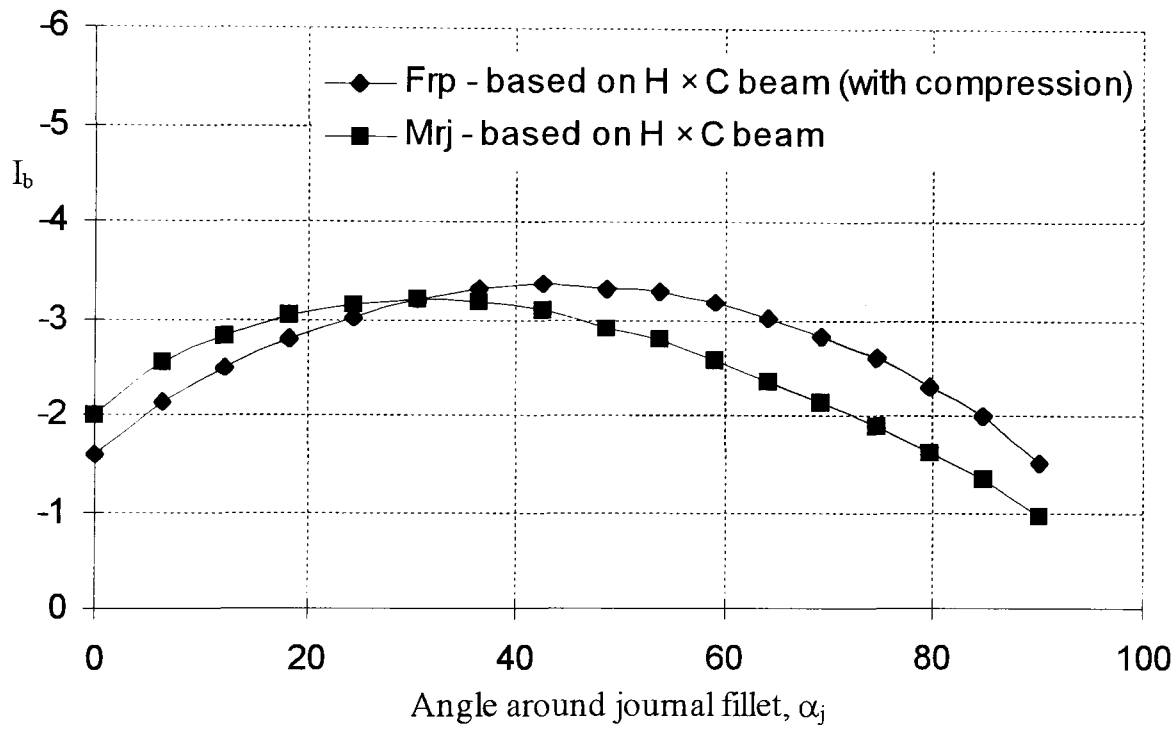

(b) Distribution around journal fillet (3D analyses)

Figure 4.8. Maximum principal stress indices under radial and pure bending based on the maximum bending stress occurring in the H × C beam (including web compression component in radial bending calculation)

CHAPTER 5

GEOMETRIC INVESTIGATIONS

5.1 Introduction

The basic form of the crankshaft can be defined by a relatively small number of parameters. These are the crankpin and journal diameters and lengths, the degree of overlap of the crankpin and journal and the web thickness and width. These are the governing dimensions of the crankshaft, and dictate the stroke and the overall length of the engine. The crankshaft dimensions are controlled, to some extent, by the capacity of the engine, as clearly the distance between the centres of adjacent cylinders must be greater than one cylinder diameter. This imposes a lower limit on the span of one crankthrow (the distance between journal centres). Previous authors have collectively investigated most of these parameters, but as discussed in Chapters 2 and 4, the use of different nominal stresses (and different crankshaft geometries) makes it difficult to unite these separate works.

Because the engine specification can impose such narrow limits on the governing dimensions of the crankshaft, instead of simply changing the overall stiffness of the crankshaft, the designer usually has to find other ways to control the operating stresses. Under the important loading modes of radial bending and torsion, the peak stresses occur at the crankpin/web and journal/web intersections. Fillets are used to reduce these stresses as far as possible. Often, compound fillets will be used to allow for grinding wheel run-out and to keep the fillet small, but the author is not aware of any detailed analyses of compound fillets in crankshafts.

There are other design details which must also be considered when analysing crankshaft stresses. These can include cut-back webs and bore holes to reduce the rotary out of balance mass of the crankshaft, and oil galleries which carry lubricant to the bearing surfaces. All of these features are likely to have an effect on the stiffness and peak stress levels of the crankshaft. However, they too are not widely investigated in the literature.

The FE and BE methods have potential for quick and simple analysis of all of the geometric parameters of the crankshaft. Both methods have been validated by various means, and the results under all the important loadcases are shown to be reliable and repeatable. This chapter presents investigations into all of these geometric parameters in order to provide a good understanding of how stresses and stress concentration factors can be influenced in overlapped crankshafts.

5.2 Crankpin fillet parametric study and optimisation

In order to maximise the life of the crankshaft, the designer strives to minimise the stress concentration factors which exist at the crankpin/web and journal/web intersections. This is achieved by the use of fillet radii, which may either be simple, or compound. The latter are more compact, and can offer the benefits of either increasing the bearing surface areas, or reducing the length of the crankshaft (which in turn reduces the length of the whole engine).

It has been shown in Chapter 3, that the FE method can be used to study the operating stresses in crankshafts. Here, the FE method is used to perform a parametric study of a compound fillet, in a single crankthrow loaded under the principal loading modes of radial bending and pure torsion. Stress concentration factors are calculated by normalising the maximum principal stresses in the fillet with respect to the maximum bending stress in the crankpin (radial bending) or maximum shear stress in the crankpin (pure torsion).

The compound fillet studied is that at the crankpin/web intersection - the crankpin fillet. The datum fillet consists of a major radius, R_{p2}, and two minor radii, R_{p1} and R_{p3}. The major radius and the minor radii are joined at the blend angles α_{p1} and α_{p2} (Figure 5.1). The axial and radial dimensions of the fillets, X and Y, are a function of these parameters.

The initial investigations into the effects of these parameters were carried with 2-dimensional FE models to reduce preprocessing and analysis time.

5.2.1 2D analysis - radial bending

The centreplane of one half of a crankthrow, consisting of half of a crankpin, one web, and half of a journal is modelled in 2D (Figure 5.2). The journal is extended by $0.4D_p$ past the mid point to ensure regular deformation of the web and journal under loading. The crankthrow is loaded with a point load at the quarter-point of the crankpin, to represent the gas load from one of the connecting rods, and a point load reaction is supplied at the bearing centre-line of the journal. The centre of the crankpin is encastré. These boundary condition approximations have been shown to produce the same results as a full crankthrow loaded with distributed forces (see Section 3.2). The 2D mesh is constructed from 590 8-noded quadratic plane strain elements and 1867 nodes. The fillet mesh presented in Chapter 3 was such that stresses did not change with successive refinement. However, the mesh used in this analysis was refined to a greater extent so that the subtle effects of changing the defining parameters of the fillet could be accurately observed. The maximum principal stresses are normalised with respect to the maximum bending stress in the crankpin. Running on a DEC Vax-Alpha, a 2D analysis required less than one minute CPU time.

Each of the parameters defining the compound fillet is varied according to Table 5.1;

Table 5.1 2D radial bending analyses of fillet parameters

Model	r_{p1}	r_{p2}	r_{p3}	α_{p1}	α_{p2}	Summary of changes
R01-2D	0.036	0.064	0.036	5.95	60	Datum
R02-2D	0.029	0.064	0.029	5.95	60	Reduce r_{p1}, r_{p3} by 20%
R03-2D	0.036	0.051	0.036	5.95	60	Reduce r_{p2} by 20%
R04-2D	0.036	0.077	0.036	5.95	60	Increase r_{p2} by 20%
R05-2D	0.036	0.090	0.036	5.95	60	Increase r_{p2} by 40%
R06-2D	0.036	0.103	0.036	5.95	60	Increase r_{p2} by 60%.
R07-2D	0.036	0.064	0.036	5.95	48	Reduce α_2 to 48°
R08-2D	0.036	0.064	0.036	15	60	Increase α_1 to 15°

The dimensions Ω_x and Ω_y are maintained as $0.015D_p$ and $0.64\times10^{-3}D_p$ respectively. Consequently, the position of the 'centre' of the fillet changes as the radii and blend angles are changed. It is found that the I_b distributions for different fillet shapes can be most meaningfully compared if the angle they are plotted against is measured about a notional centre, which remains in a fixed position for all fillets. The notional centre is defined in Figure 5.3, and the angle measured about this point is β_p. Where appropriate, the blends between adjacent radii are marked on the stress distribution curves to assist in the interpretation of results.

5.2.1.1 Effect of minor radii

Figure 5.4 shows the effect of reducing the minor radii by 20%. The SCF, which occurs in the minor radius, R_{p1}, of both fillets, increases by 1.5%. However, there is no difference between the two stress distributions in the minor radius R_{p3}, which begins at $\alpha_{p2} = 60°$.

5.2.1.2 Effect of major radius

Figure 5.5 shows the effect of changing the major radius by -20%, 20%, 40% and 60%. As the size of the major radius increases, the SCF reduces, but at a decreasing rate. This can be seen in Figure 5.6. It should also be noted that the SCF, which generally occurs in the minor radius R_{p1}, decreases at a slower rate than the peak stress index in the major radius R_{p2}. This results in an increasing spike in the stress curve as the major radius is decreased.

5.2.1.3 Effect of blend angles

Figure 5.7 shows the effects of changing the blend angles. Increasing α_{p1} to 15° has a significant effect on the SCF, increasing it by some 10%, but reducing α_{p2} to 48° has no effect on the SCF and simply changes the stress distribution slightly from the blend onwards.

5.2.2 Observations

The analysis of the parameters which define the compound fillet highlights important points that should be taken into account when designing such a fillet.

1. Increasing the size of the major radius by fixed intervals has a decreasing effect on the reduction of stress levels in the fillet. It is therefore important to investigate the optimum size of major radius, taking into account peak stress levels and the implications for total fillet size. The second point is important because this can affect the size of the bearing and thrust areas

available, and can also, in the case of an undercut fillet, influence the stiffness of the crankweb and therefore the stiffness of the whole crankshaft.

2. The compound fillet, by definition, consists of several differently sized radii which are blended together at particular angles. It is apparent from the analyses that as discontinuities in size between adjacent radii increase, the resulting spike in the stress distribution curve also increases. Taking, the results from model R06-2D as an example (Figure 5.5), and following them from the start of the fillet - the initial radius, R_{p1}, is relatively small and the stress index reaches a peak of 3.1. The next radius, R_{p2}, however is far larger than the first and it is clear that the stresses over this radius will be lower. In order to preserve the continuity of the stress plot, the stresses in the first radius now fall to the level determined by the major radius, and continue to be determined by radius R_{p2} until radius R_{p3} nears. These discontinuities can be minimised by ensuring that lengths of adjacent radii do not differ too much.

3. The use of a large initial blend angle can also have a detrimental effect on the peak stress level. Model R08-2D (Figure 5.7) produces the highest SCF of all the fillets analysed because the initial radius, R_{p1}, is carried over too great an angle. The small radius determines the peak stress level in the fillet, rather than the major radius.

5.2.3 Fillet optimisation

It is advantageous when designing a crankshaft to create a fillet that is both small, to allow large bearing surfaces to accomodate increased firing pressures, and one that produces stresses that are as low as possible. Having a basic understanding of the effects of each parameter in the fillet, and using the FE method, the designer can iterate towards an optimum fillet shape.

The approach taken in this analysis is to produce an optimum fillet for the 2D case, and then use a combination of 2D and 3D modelling to find the optimum fillet for the 3D crankshaft, in as short a time as possible. The criteria for the study are

- the axial and radial dimensions of the optimum fillet must be similar to, if not smaller than the those of current fillet, to avoid a reduction in crankthrow stiffness.
- the optimum fillet must reduce the peak stress by distributing the high stresses over a wider area (thus producing a flatter stress curve).

5.2.3.1 2D analysis - radial bending

Figure 5.8 shows the 2D optimisation process, with the parameters of each fillet shown in Table 5.2. The major radius is increased by 60% because this gave the greatest stress reduction in the parametric study. It is found that the SCF can be moved from minor radius, R_{p1}, to major radius, R_{p2}, by either increasing radius R_{p1} or reducing the blend angle α_{p1}. Similarly, the SCF can be moved from the minor radius, R_{p3}, to major radius, R_{p2}, by increasing radius R_{p3}, or increasing the blend angle α_{p2}. It is also worth

noting that the second blend angle can be reduced considerably before the peak stress is increased. This reduces the axial and radial dimensions of the fillet, and compensates for the increase in size of the major radius.

Table 5.2 2D radial bending fillet optimisation analyses

Model	r_{p1}	r_{p2}	r_{p3}	α_{p1}	α_{p2}	x	y
R01-2D	0.036	0.064	0.036	5.95	60	0.049	0.085
R09-2D	0.043	0.090	0.021	5.95	40	0.052	0.056
R10-2D	0.050	0.103	0.021	2	30	0.052	0.051
R11-2D	0.036	0.103	0.036	2	30	0.058	0.080
R12-2D	0.036	0.103	0.036	2	25	0.053	0.077

5.2.3.2 2D and 3D analysis - radial bending

R11-2D was chosen as the optimum 2D fillet and was then tested under radial bending in 3D (R11-3D). The 3D mesh used for this analysis is shown in Figure 5.9. The 3D model makes full use of symmetry to reduce the number of elements and nodes. The mesh discretisation around the fillet is approximately half that used in the 2D models, because it was impractical to model such a fine mesh in 3D. The datum mesh (R01-3D) has 10982 nodes and 2384 elements. The boundary conditions are the symmetric ones, and the loading is the same as in the 2D analyses. The resulting stress distribution is shown in Figure 5.10. In the first minor radius and the major radius, the stress distribution is very similar to the 2D case, but a sharp peak is observed in the second minor radius of the 3D model (at node 9). This peak is at the same point in the fillet as node 23 in the optimum 2D fillet, where a sharp change in stress level is observed.

2D modelling is used to test new fillet shapes to remove the peak from radius R_{p3}. In the two models tested (detailed in Table 5.3) slight changes are made to radii R_{p2} and R_{p3}, and a radius, R_{p4}, is added to tighten the fillet in the low stress region. These refinements produce a relatively smooth stress curve near node 23 (Figure 5.11).

Table 5.3 2D radial bending fillet optimisation analyses

Model	r_{p1}	r_{p2}	r_{p3}	r_{p4}	α_{p1}	α_{p2}	α_{p3}	x	y
R13-2D	0.036	0.095	0.054	0.023	3	30	45	0.054	0.060
R14-2D	0.036	0.095	0.060	0.023	3	31	43	0.054	0.060

Testing the better of these two fillets (R14-2D) in 3D (R14-3D), reveals a very flat stress distribution (Figure 5.12), with the exception of a slight peak in the minor radius R_{p1}. This has arisen because α_{p1} was increased to 3° to keep the fillet small. Reducing α_{p1} to 2° eliminates this peak. The parameters of the datum and optimum 3D fillets under radial bending are shown in Table 5.4. The fillet in model R15-3D produces an SCF which is some 11% lower than that occurring in the datum fillet.

Table 5.4 3D radial bending fillet optimisation analyses

Model	r_{p1}	r_{p2}	r_{p3}	r_{p4}	α_{p1}	α_{p2}	α_{p3}	x	y
R01-3D	0.036	0.064	0.036	-	5.95	60	-	0.049	0.085
R15-3D	0.036	0.095	0.060	0.023	2	31	43	0.055	0.060

5.2.3.3 3D analysis - torsion

The datum and optimum fillet shape (under radial bending) are tested under torsion (models T01-3D and T15-3D). The models used for the torsion analyses have the same fillet mesh discretisation, loading and boundary conditions as those described in

Section 3.2.4. The datum model (T01-3D) is constructed from 22048 nodes and 5026 elements. The results are presented in Figure 5.13. Unfortunately, it is found that the optimum radial bending fillet increases the torsional SCF by 22%. The SCF occurs in smallest minor radius, R_{p4}. Increasing this radius, and adding a further minor radius, R_{p5}, at 100° produces results which can also be seen in Figure 5.13 (model T16-3D). Although the SCF is around 9% higher than the datum SCF, it has been shown in Section 2.4.1 that radial bending stresses are generally acknowledged to be greater than torsional stresses, and it is therefore more important to reduce the peak stresses for the radial loadcase.

The optimum fillet under torsion is then retested under radial bending as model R16-3D. The results can be seen in Figure 5.14. The SCF is not affected by the addition of R_{p5}, and the size of the fillet is only increased slightly. The dimensions of the datum fillet and the optimum fillet for radial bending and torsion are given in Table 5.5.

Table 5.5 Dimensions of the datum fillet and optimum fillet for radial bending

Model	r_{p1}	r_{p2}	r_{p3}	r_{p4}	r_{p5}	α_{p1}	α_{p2}	α_{p3}	α_{p4}	x	y
R01-3D	0.036	0.064	0.036	-	-	5.95	60	-	-	0.049	0.085
R16-3D	0.036	0.095	0.060	0.036	0.018	2	31	43	100	0.059	0.068

The fillet in model R16-3D is 22% larger in the axial direction, but 21% smaller in the radial direction than the datum fillet. This reduces the stiffness of the crankthrow by around 2% under radial bending and torsion. The SCF is 11% lower under radial bending, and 9% higher under torsion.

5.2.4 The spiral fillet

The parametric study highlights the fact that stress peaks can be caused by ill positioned blends between major and minor radii, and as the discontinuity between radii increases, so too does the resulting peak. The ideal fillet would be one with virtually zero discontinuity, but with a smaller radius at the end of the fillet than at the start. A suggested solution is to use a radius that varies linearly between specified start and end radii, r_i and r_f, over a given angle, α_s, commonly referred to as a spiral.

The linear equation defining the radius of a spiral fillet at any angle is as follows;

$$r = A\alpha + B \tag{5.1}$$

where

$$A = \frac{r_f - r_i}{\alpha_s} \qquad B = r_i$$

As an example, a study is performed with three 2D models, which were created with variations of the parameters r_i, r_f and α_s. The dimensions of these fillets are presented in Table 5.6. The 'centre' of each fillet is positioned such that a small undercut is created in the crankpin at the start of each fillet to allow for the grinding wheel run-out. An example of the spiral fillet shape is presented in Figure 5.15.

Table 5.6 2D radial bending analyses of spiral fillets

Model	r_i	r_f	α_s	r
SP012D	0.089	0.019	163.48	$-0.00043\alpha + 0.089$
SP022D	0.106	0.008	120.71	$-0.00081\alpha + 0.106$
SP032D	0.118	0.002	124.24	$-0.00093\alpha + 0.118$

The results from these three analyses are presented in Figure 5.16, and are plotted against angle β_p, measured about the notional centre described previously. In every model the stress plot around the fillet appears continuous with no stress peaks as seen in the compound fillet. As the initial radius is increased, the peak stress in the fillet is reduced. Each increase of initial radius is accompanied by a reduction of the final radius so as to keep the fillet as small as possible.

The spiral fillet which resulted in the lowest SCF (SP032D) was also modelled in 3D (SP033D). The crankpin fillet principal stress indices are presented in Figure 5.17. The resulting stress distribution is very similar to that occurring in 2D.

The stress reduction in the second half of all of the spiral fillets is very rapid, indicating that the fillets could be tightened. However, it is difficult to do this with linearly varying radii because they must have a large initial radius in order to keep the stresses low, and tend not to rapidly reduce in size, which in turn leads to a larger fillet than absolutely necessary. The smallest spiral fillet, SP012D, has dimensions x = 0.086 and y = 0.094, compared to the datum fillet where x = 0.049 and y = 0.085.

This problem can be partially solved by using a radius variation of higher order (quadratic, cubic...). However, as the order increases, the fillet radius can change very rapidly over small angles of B_p, and this effectively introduces discontinuities which result in spikes in the stress distribution. An alternative method of keeping the fillet small is to use a back to back spiral with the largest radius placed in the area of the peak stress. Both of these points are illustrated with the aid of a 3D model with a back

to back cubic spiral fillet (NM273D). The fillet shape is presented in Figure 5.18, and the results are shown in Figure 5.17.

5.2.5 Analysis of different fillet constructions

So far, the fillets considered have been either compound (datum and optimised) or spiral. The clearest way of showing how effective these fillet constructions are at reducing stresses, is to compare them with a simple, single radius fillet, which is detailed in Table 5.7.

Table 5.7 3D radial bending analyses of different fillet constructions

Model	r_{p1}	r_{p2}	r_{p3}	r_{p4}	r_{p5}	α_{p1}	α_{p2}	α_{p3}	α_{p4}	x	y
Datum (R01-3D)	0.036	0.064	0.036	-	-	5.95	60	-	-	0.049	0.085
Optimum (R16-3D)	0.036	0.095	0.060	0.036	0.018	2	31	43	100	0.059	0.068
Spiral (SP033D)	$r_i = 0.118$			$r_f = 0.002$		$\alpha_s = 124.24$				0.077	0.103
Simple (SIMP3D)	-	0.043	-	-	-	-	-	-	-	0.043	0.086

5.2.5.1 Radial bending

The simple fillet is modelled so that it has virtually the same Y dimension as the datum fillet. Because of this, the radius of the simple fillet is 33% smaller than the major radius, and 19% larger than the minor radii in the datum fillet. Accordingly, the stresses in the simple fillet (Figure 5.19) are lower than those at the start and end of the datum fillet, but are higher in the middle. The SCF occurring in the datum fillet is 12%

lower than the simple fillet SCF, whereas the optimised fillet shows a 22% reduction in SCF.

The stress distribution in the spiral fillet is similar to that in the optimised compound fillet, being slightly lower in places, but with an SCF which is virtually equal. However, it is clear from Table 5.7, that the spiral fillet is significantly larger than the optimised compound, for little further reduction in SCF.

5.2.5.2 Torsion

It is noteworthy, however, that under the torsional loadcase, the simple fillet out-performs the datum and optimised compound fillets, as well as the spiral fillet (Figure 5.20). At the point of maximum stress, the simple fillet has a larger radius than any of the other fillets, and this results in a lower stress in this region.

5.2.6 Effect of fillet size on web spread

Changing the size of the crankpin fillet, which is cut into the web, will have an impact on the overall stiffness of the web. Depending on the extent of the change in stiffness, bearing alignment and torsional vibration characteristics may be significantly affected.

In order to establish the magnitude of this effect, the web deformation was measured for the four fillet types under both radial bending and torsion.

5.2.6.1 Radial bending

The results indicate that as the fillet axial and radial dimensions are increased, the web spread of the corresponding model also increases because the section modulus of the web is reduced. However, the change in web spread as the fillet size is increased is relatively small. The greatest reduction in stiffness, compared to datum fillet, occurs in the spiral fillet model (the largest fillet analysed), which shows an increase in web spread of only 2.9%.

5.2.6.2 Torsion

Under the torsional loadcase, similar effects are observed. An increase in the fillet dimensions leads to a reduction in crankthrow stiffness. The spiral fillet model has the greatest web deformation of the models analysed (5.5% increase in deformation compared to the datum compound fillet).

5.3 Crankpin and journal diameter

It is reported in Section 2.4.2 that few investigations have been made into the effects on peak stress of crankpin and journal diameter. Here, the FE method is used to investigate a crankpin and journal regrind. The bearing surface diameters are reduced by 5%, which is a typical value for a regrind. Subsequently, the overlap is reduced and the fillet shapes are changed (Figure 5.21). Four crankthrow shapes are analysed;

1. standard crankpin and standard journal, called SS
2. standard crankpin and reduced journal, called SR
3. reduced crankpin and standard journal, called RS
4. reduced crankpin and reduced journal, called RR

Each shape was tested under radial bending, pure bending and pure torsion. For the bending loadcases, quarter crankthrows were used to reduce the analysis time. For the torsional loadcase, a half crankthrow was analysed. The results from the FE analyses are compared with results obtained previously from strain gauge analyses of the four crankthrow shapes. The strain gauge tests were carried out with two full crankthrows. One model had a standard crankpin and the other a reduced crankpin ($0.95D_p$), whilst both had one standard and one reduced journal ($0.95D_j$). This meant that from these two models, all twelve sets of results could be obtained (four geometries under three loadcases). The dimensions of the fillets in the former crankthrow are defined in Figure 5.21.

5.3.1 Experimental technique

Warrior and Hyde [28] carried out experimental tests on strain gauged epoxy resin models. The Young's modulus, E, for the material was determined by four-point bending tests on 10mm × 10mm section strips, cast at the same time as the crank halves. Seven batches of material were tested; the average Young's modulus was 3550 MPa. For bending, the results were converted to stresses using a Poisson's ratio $\nu = 0.4$ for the epoxy resin, loaded at room temperature.

Previous work [30] had shown that the greatest bending stresses occur at $\alpha' \approx 25°$. Strips of electrical resistance strain gauges were applied to the fillet radii and were used to measure bending strains. Three-gauge rosettes were used to determine torsional strains. Details are shown in Table 5.8.

Table 5.8 Strain gauge types used

Type	Strip	Strip	Rosette
Gauges per strip	10	5	3
Gauge length	0.79mm	1.0mm	1.0mm
Grid centreline spacing	2.03mm	2.0mm	-

For radial bending, the models were loaded in an Instron Universal Testing Machine 1195 (Figure 5.22). The crankpin support was attached to the upper universal joint of the loading frame. Identical stirrups, which were located under the moving crosshead, were used to load the journals through epoxy resin blocks which were encased in steel frames.

For pure bending, sprocket wheels were rigidly attached to the steel frames and the models were loaded through chains (Figure 5.23). All components of the loading rigs were pin-jointed to ensure that the rigs were self-aligning.

The arrangement for torsion loading of the strain-gauged models is shown in Figure 5.24, mounted in an Avery torsion testing machine. The joint at the right hand end of the model was intended to permit movement of the right hand end relative to the left hand end. This was simulate free torsion, as occurs in a running engine where the crankshaft journals are free to move within the bearing clearances. Flats were machined on the model journals to prevent rotation relative to the journal clamps.

5.3.2 Radial bending

5.3.2.1 3D analysis

The strain gauge models were loaded with a cradle positioned at the centre of the crankpin. In order that reasonable comparisons could be made, the FE models were also loaded at the crankpin centre (with a point load). A simple support was applied at the centre of each journal. The quarter models were otherwise restained in the same manner as those used in the validation of the FE method.

It is seen that for all models, the maximum principal stresses occur in the crankpin and journal fillets on the centre-plane of the crankthrow ($\theta_p' = 0$, $\theta_j' = 0$). In addition to reducing crankpin and journal diameters, regrinding reduces the neck section, distance H, in the overlap region. It has already been discussed that this area should be considered to control the fillet stresses, and as such, the peak stresses are plotted

against dimension H in Figure 5.25. It is apparent that there is an inverse linear relationship between the peak stress and H at both fillets. As the crankpin or journal is reground, section H reduces and the peak stress increases. It is noted that the crankpin fillet peak stress increases at a faster rate than that in the journal fillet.

The maximum principal stresses are normalised with respect to the nominal stress occurring in the H × C beam (including the web compression component), so that trends in meaningful SCFs can be established. The stress indices, based on the H × C beam, are presented in Figures 5.26 and 5.27, along with the corresponding strain gauge results.

Good agreement is obtained between the FE and strain gauge data for the four model shapes analysed under radial bending. The maximum principal stress distributions agree well over most of the strain gauge measurement range, but the strain gauges do not detect the absolute peak stress. This is discussed further in Section 3.2.2.6 and is probably due to the nature of the strain gauges which detect strains at discrete intervals. The strain gauge results are generally within a few percent (+ or -) of the FE results. This indicates that they can be used to determine an approximate stress level, but are not accurate enough for conclusions to be drawn about the effects of regrinding the crankpin and journal. Possible reasons for these slight errors may include imperfect bonding of strain gauges to the models, slight inaccuracies in model fillet shapes, or friction at the pivots in the loading system.

The radial bending SCFs from the FE method and experimental (shown in parenthesis) method are presented in Table 5.9.

Table 5.9 3D radial bending SCF values

SHAPE	Crankpin	Journal
SS	3.42 (2.99)	2.87 (2.67)
SR	3.33 (3.21)	2.76 (2.83)
RS	3.33 (2.98)	2.73 (2.58)
RR	3.22 (3.44)	2.62 (2.86)

The FE results highlight the fact that differences occur in the stress distributions near the webs between models with standard and reduced diameters on that side of the web. This is due to the change in fillet shapes caused by regrinding. There is almost coincidence of pairs throughout. This can be seen more clearly in Figure 5.28. For example, in Figure 5.28b, the journal fillet stress distributions for shapes SR and RR are the same. The magnitudes are slightly different because of the reduction in both H and the crankthrow stiffness due to the reground crankpin. However, it is clear that the fillet stress distributions remain virtually unaffected when minor changes are made to the position of the fillet on the other side of the web.

5.3.2.2 2D analysis

The four crankthrow shapes were modelled in 2D in order to see if 2D modelling predicts similar trends in SCFs to 3D modelling when the crankpin and journal are reground. Half crankthrows with journals extended $0.38D_p$ are modelled in 2D, and are loaded under radial bending at the crankpin centre. The boundary conditions and

mesh are the same as those used in the 2D FE validation, except with the strain gauged fillet shapes.

The results are presented in Figure 5.29. The general trend of the 2D results agrees with the 3D trends. As the crankpin and journal are reground, the SCF at both fillets is reduced. The reduction is not as great as that in the 3D models for a regrind of 5%, and the magnitudes of the SCFs are also not as large (this is consistent with the observations in Section 4.2.5). The 2D SCFs are presented in Table 5.10.

Table 5.10 2D radial bending SCF values

SHAPE	Crankpin	Journal
SS	1.98	1.99
SR	1.97	1.95
RS	1.95	1.93
RR	1.94	1.88

It is interesting to note, however, that the shapes of the 3D and 2D stress distributions are very similar. It can clearly be seen at the journal, that both 3D and 2D predict very similar changes in the stress distribution as the fillet shape is changed.

5.3.3 Pure bending

A pure bending moment was applied to the strain gauge models via sprocket wheels and chains (Figure 5.23). The FE quarter crankthrow models were constructed with a journal which extended $1.86D_p$ past the journal midpoint. A point load couple was applied in the plane $z = 0$ to the free face of the journal to create a pure bending

moment in the crankthrow. The quarter models were constrained on the planes of symmetry.

As was the case under radial bending, the maximum principal stresses occur in the crankpin and journal fillets on the planes $\theta_p' = 0$ and $\theta_j' = 0$. The change in peak stress as H is varied is presented in Figure 5.30. The peak stresses at the two fillets are seen to increase linearly as H is reduced, at the same rate. Figures 5.31 and 5.32 show the fillet stress distributions normalised with respect to the nominal stress in the H × C beam. Because of the pure bending loadcase, the nominal stress is calculated with a constant bending moment, and there is no web compression component to include in the calculation. Again, agreement between the FE and strain gauge results is very good. It is noticeable that for all the radial and pure bending data, the worst agreement between the numerical and experimental results is obtained at the reground crankpin fillet. It is suggested that this is because the crankpin fillet is undercut into the web, and is practically the most difficult fillet to access and regrind accurately which may have led to inaccuracies of fillet shape. The SCFs obtained by both methods are shown in Table 5.11, again with the strain gauge data in parenthesis.

Table 5.11 3D pure bending SCF values

SHAPE	Crankpin	Journal
SS	3.48 (3.46)	3.17 (2.74)
SR	3.36 (3.14)	3.06 (2.59)
RS	3.34 (3.18)	3.04 (2.59)
RR	3.21 (3.55)	2.91 (2.39)

As was observed under radial bending, when the FE stress distributions for the different crankthrow shapes are compared, the stress distributions in the fillets change little as the fillet position on the opposite side of the web is changed (Figure 5.33).

There is a marked difference between the stress distributions for radial and pure bending. In the crankpin fillet, the stress between $\alpha_p = 20°$ and $\alpha_p = 60°$ under pure bending is notably higher than that under radial bending. Conversely, at the journal fillet, the stress between $\alpha_j = 10°$ and $\alpha_j = 30°$ under pure bending is lower than that under radial bending. This may be due to the extra compressive stress that exists in the web under radial bending, which causes higher journal fillet stresses and lower crankpin fillet stresses than under pure bending. This compressive stress is taken into account in the nominal stress calculation in order to improve agreement between radial and pure bending SCFs, but the shapes of the stress distributions cannot be changed by it's inclusion.

5.3.4 Pure torsion

Free torsion was applied to the strain gauged models as described in Section 5.3.1. The finite element models were of one half crankthrow (one end) because under torsion there is only one plane of symmetry. The centre of the crankpin is encastré, and the journal is extended $1.86D_p$ past the journal midpoint. A torque was applied to the free surface of the journal as four forces in the $+\theta_j$ direction at $\theta_j = 0°$, 90°, 180° and 270°.

Unlike radial and pure bending, the θ position of the maximum stress is not well documented. The maxima may occur anywhere in the toroidal surfaces formed by the fillets. Figure 5.34 shows the positions of the nodes in the crankpin fillet on the various θ=constant planes. The maximum and minimum principal stresses on these planes, as well as their positions, α', were recorded. It is interesting to note that the peak fillet stresses recorded remain virtually constant as the crankpin and/or journal are reground (Figure 5.35). The one exception to this rule is at the journal fillet for the SR and RS models.

It has been discussed in Section 4.2.5 that the most appropriate basis for the torsional nominal stress is that based on the tangential bending component occurring in the beam H × C. The principal stresses which were recorded were normalised with respect to this nominal stress and are presented in Figure 5.36, along with the α' positions at which they occur.

At both fillets, the minimum principal stresses are found to be the double mirror image of the maximum principal stresses. It is seen that the stresses decrease outside the overlap region, $\theta_p > 60°$, $\theta_j > 48°$. Figure 5.36 also shows that over most of the fillets ($|\theta| > 10°$) the maximum stresses occur at large values of α, i.e. near the web, as would be expected if bending of the web were important. Small values of α' are limited to the vicinity of the plane of symmetry ($|\theta| < 10°$), where torsion predominates because it is near to the neutral surface of the rectangular bar in tangential bending. This region is effectively in torsion because the two principal stresses are equal and opposite in

magnitude. The predominantly torsional stresses occur at small α' values, i.e. near the crankpin and journal which are also in torsion.

The maximum I values, K_t, are shown in Table 5.12.

Table 5.12 3D torsional SCF values

Shape	Crankpin	Journal
SS	3.64	3.13
SR	3.23	2.60
RS	3.05	2.79
RR	2.69	2.32

The strain gauge torsion data is not presented because of inconsistencies in results, i.e. measurements taken at $\theta_j=0$ when the crank is twisted firstly in $+\theta_j$, and secondly in $-\theta_j$ are substantially different (in some cases > 100% different). It is clear that both readings should be equal, so it is therefore meaningless to compare the FE and strain gauge torsion data. The scatter of the strain gauge results is probably due to inconsistent measurements caused by friction in the loading systems at various pivots.

5.3.5 Summary of the effects of regrinding

By considering the crankthrow as a complicated shape, which is notched to touch the rectangular bar H × C, it is clear that the dimensions which most influence the magnitude of the stress concentration factor are the fillet radii, R, and the thickness, H.

As the crankpin and/or journal are reground, under radial and pure bending, the peak stress in the crankthrow rises linearly as H is reduced. Under torsion however, there is little change to the peak stress.

Figure 5.37 shows the SCFs for all loading conditions, plotted against H/R, so that the effect of reducing H is obvious. For radial and pure bending, these are virtually linear relationships,

$$K = \frac{AH}{R} + 1$$

Values of A are presented in Table 5.13.

Table 5.13 Values of A (slope of line, A = (K-1)R/H)

	Crankpin	**Journal**
$\mathbf{F_{rp^*}}$ radial bending with web compression	0.290	0.318
$\mathbf{F_{rp}}$ radial bending without web compression	0.248	0.370
$\mathbf{M_{rj}}$ pure bending	0.293	0.372

The SCFs due to torsion decrease much more than proportionately with H. Plotting K_t against C/R gives similarly steep curves. Non-linear relationships between SCFs and the most relevant shape parameter are usual; the linear ones are the remarkable exception.

5.4 Overlap of crankpin and journal

The overlap region of the crankshaft can be changed in two ways, one of which (regrinding) has been discussed in Section 5.3. The other method is to change the throw of the crankshaft (which also alters the stroke of the engine). Increasing the throw reduces the overlap of crankpin and journal and vice versa. At the design stage, it would be useful to know what magnitude of peak stress might be expected for a given throw, and how peak stresses vary over a range of overlap values.

Here, the BE method is used to investigate the effect of varying the crankthrow overlap. This method is used in preference to FE because modelling only the boundary elements allows the relatively major structural changes to the geometry to be made in a matter of minutes. A typical BE mesh used in the overlap investigations is presented in Figure 5.38. The range of overlap investigated is $0.31 \leq S/D_p \leq 0.62$. The loadcases of radial and pure bending, as well as torsion are examined.

Peak stresses are initially plotted against S/D_p so that the effects of changing the overlap are obvious. They are then normalised with respect to the nominal stress occurring in the H × C beam (taking into account the web compression component).

5.4.1 3D radial and pure bending

A half crankthrow, with equally sized major radii in the crankpin and journal fillets, is modelled with the BE method to enable loading under bending (radial and pure) and torsion. It is also more convenient to model a half crankthrow instead of a quarter crankthrow. A quarter crankthrow would require a boundary mesh on the plane of

symmetry (z = 0), but this is not necessary with the half crankthrow. The half crankthrow requires more elements, which increases the analysis time, but this is partly offset by the reduction in modelling time. The mesh disretisation at the fillets is the same as that which produced the best results in the BE validation.

Under radial bending, the half crankthrow is modelled encastré at the crankpin centre, and has a journal extension of $0.4D_p$ to ensure regular deformation of the journal. The loads are applied as pressures over small areas (at the crankpin quarter point and journal centre) to approximate point loads.

Under pure bending, the crankthrow is again encastré at the crankpin centre, and has a journal extension of $0.81D_p$ past the journal midpoint. Pressure loads are applied as a couple to the free face of the journal in the +x and -x directions.

The overlap is increased from $0.31D_p$ in four steps of $0.077D_p$ to $0.62D_p$. The datum overlap value is $0.46D_p$. The peak bending stresses are presented in Figure 5.39, although the radial and pure bending results should not be directly compared because each has a different load applied. As might be expected, as the overlap is increased, dimension H increases, the crankthrow is stiffened, and the maximum principal stresses decrease. The rate of stress reduction with overlap slows at higher values of overlap, which gives rise to a non-linear relationship between peak stress and overlap. It is noteworthy that under both radial and pure bending, the crankpin and journal fillet stresses change by an equal amount for a given change in overlap.

Normalising these peak stresses with respect to the nominal stress occurring in the H × C beam, results in slightly more linear relationships (Figure 5.40). The normalised radial and pure bending curves are also now more aligned. It is apparent that as the overlap is increased, the SCFs increase at both fillet, under both loadcases. This highlights the fact the the trend in SCFs can mislead the reader into assuming that the peak stress changes accordingly, which, as has been shown, is not the case.

If the peak stresses are normalised with respect to the nominal stress occurring in the slanted eye beam (Figure 5.41), the relationship between the SCF and overlap becomes linear for the range investigated. The pure bending results at both fillets are virtually equal, by virtue of the eye beam neutral axis being slightly closer to the journal fillet, thus slightly increasing the journal fillet SCF and reducing the crankpin fillet SCF. The radial bending results increase at different rates to the pure bending results as overlap in increased. The crankpin fillet SCFs increase at a lower rate, and the journal fillet SCFs increase at a higher rate, but at each value of overlap they are virtually equidistant from the pure bending results. The linear relationships seen here are an excellent indication that the slanted eye method is the most relevant of the nominal stress bases investigated, although it has already been discussed that it is impractical for the torsion loadcase.

It is also clear that the inclusion of the web compressive stress in the radial bending nominal stress calculation helps to increase the alignment of the radial and pure bending results. For example, if it were not included, the journal nominal stress (compressive) would be lower, resulting in higher SCFs at each value of overlap. The

opposite is true at the crankpin fillet, and the radial bending curves would thus move away from the pure bending curves.

The angles within the fillets at which the peak stresses occur, α', are also seen to change as the overlap is increased. The values of α' are tabulated below in Table 5.14.

Table 5.14 Values of α' for the range $0.31 \leq S/D_p \leq 0.62$ (3D BE)

	Radial bending		Pure bending	
S/D_p	Crankpin	Journal	Crankpin	Journal
0.31	26.2°	44.8°	32.6°	36.1°
0.38	19.6°	44.8°	32.6°	36.1°
0.46	19.6°	44.8°	26.3°	27.0°
0.54	6.2°	44.8°	26.3°	27.0°
0.62	6.2°	44.8°	26.3°	27.0°

These changes in α' can be explained by considering what happens to the shape of the crankthrow as the S/D_p ratio is increased. As the overlap is increased, the point at which the minimum section, H, touches each fillet moves further towards the start of the fillet, i.e. a smaller angle α. It has already been discussed that this section controls the peak stress, and therefore the peak stress moves towards the point where H touches the fillets.

5.4.1.1 2D Radial and Pure Bending

The same range of analyses was carried out with the FE method in 2D. The findings correspond very well with the 3D BE results. The peak stresses at each value of overlap are normalised with respect to the nominal stress in the 2D H × B beam, and are presented in Figure 5.42. Agreement between these results and those in Figure

5.41, is excellent. Similar trends in the position of α' are noted, and these are detailed in Table 5.15.

Table 5.15 Values of α' for the range $0.31 \leq S/D_p \leq 0.62$ (2D FE)

	Radial bending		Pure bending	
S/D_p	Crankpin	Journal	Crankpin	Journal
0.31	19.6°	53.8°	34.3°	36.4°
0.38	14.7°	53.8°	34.3°	30.4°
0.46	14.7°	42.6°	34.3°	30.4°
0.54	9.8°	42.6°	34.3°	30.4°
0.62	9.8°	42.6°	29.4°	24.3°

5.4.2 Pure torsion

The final loadcase investigated is torsion. A BE mesh of a half crankthrow is created, with a journal extension of $0.81D_p$. The crankpin centre is encastré, and four pressure loads are applied as two couples to the free face of the journal, to put the journal in torsion.

For torsion, three shapes are analysed, the datum and the two cranks at the extremes of the overlap range which was investigated under bending, i.e. $S/D_p = 0.31$, 0.46 and 0.62. The peak stresses at the crankpin and journal fillets are presented for the three models in Figure 5.43. At both fillets, as the overlap is increased, the peak stress is linearly reduced over the range investigated, but at a faster rate in the crankpin fillet. As the ratio S/D_p is increased from 0.31 to 0.62, the peak crankpin fillet stress is reduced by 45%, and the peak journal fillet stress is reduced by 39%.

The maximum principal stresses, normalised with respect to the H × C beam nominal stress, at various angles, θ, around the crankpin and journal are presented in Figure 5.44. The SCFs are seen to increase as the overlap is increased, and occur in the regions $50° < \theta_p < 70°$, and $30° < \theta_j < 45°$.

5.4.3 Web stiffness

Under radial bending, there is a significant increase in web deformation as the crankpin and journal overlap is decreased (Figure 5.45a). Measuring the web displacement at $J/D_p = 1.1$, it is found that reducing the overlap, S/D_p, by 33% from the datum value of 0.46 to 0.31 results in an 80% increase in web deformation. Increasing S/D_p by 33% to 0.62 has the effect of reducing the web deformation by 36%. It is therefore clear that as the overlap is increased, the rate of increase in web stiffness slows.

Additionally, the web displacements are measured for the pure torsion loadcase. It is obvious from Figure 5.45b that the value of overlap has less effect on the web stiffness when the crankthrow is under torsion than when under radial bending. Again, measuring the web displacement at $J/D_p = 1.1$, reducing S/D_p by 33% increases the web deformation by 15%. Increasing S/D_p by 33% reduces the web deformation by 14%.

5.5 Web thickness

The web thickness has a significant influence on the characteristics of the crankshaft, affecting the overall length, stiffness and torsional vibration characteristics. The designer strives to produce an engine as compact as possible, whilst ensuring acceptable stress and vibration levels. Clearly the crankshaft (and also the whole engine if cylinder spacing permits) can be shortened by reducing the web thickness, but this is likely to be accompanied by a stress increase at the fillets. In addition, the capability of the crankshaft to carry sufficient balance weights is reduced, since the (reduced) area at the bottom of the web is the only position where they can be attached.

It has already been established in Sections 5.3 and 5.4 that a reduction in H results in an increase in peak stress, and it is suggested that a reduction in web thickness will produce similar results. In order to test this hypothesis, five models are analysed with web thicknesses in the range $0.12 \leq T/D_p \leq 0.38$. As was the case in the overlap analyses, the BE method was used. This was to allow the relatively major structural changes involved in changing the web thickness to be made relatively easily. The loadcases of radial bending and torsion are investigated.

5.5.1 3D radial bending

A half crankthrow, with a journal extension of $0.4D_p$ and equally sized major radii in the crankpin and journal fillets, is modelled with the BE method to enable loading under radial bending and torsion. The mesh discretisation and boundary conditions are the same as those in the overlap analyses. The load applied to the crankpin is also the

same, but the reaction at the journal is scaled to allow for the increase or decrease in web thickness. The reaction applied is the same as that which would occur if the whole crankthrow was loaded at the quarter point of the crankpin and simply supported at the two journal centres. The procedure for calculating the new journal reaction is described in Appendix 8.

The peak principal stresses at the two fillets are plotted against T/D_p and are presented in Figure 5.46, for the five values of web thickness analysed. As the web thickness is increased, the stresses fall linearly, but at a higher rate in the journal fillet. Over the range investigated ($0.12 \leq T/D_p \leq 0.38$) the reduction in the crankpin fillet peak stress is 12%, whereas the reduction in the journal fillet is 34%.

Normalising the maximum principal stresses measured at each of the different values of web thickness, with respect to the H × C nominal stress (including web compression), results in the curves presented in Figure 5.47. As has been observed in investigations into other crankshaft parameters, normalising the stresses with respect to a section which is dependent on the local geometry means that the stress and SCF distributions do not necessarily agree. This is because as H is changed, not only do the peak stresses, but so too does the nominal stress. However, the stresses and nominal stress rarely change at the same rate. This can clearly be seen in Figure 5.47, where the SCFs in the crankpin fillet increase with the web thickness, but the journal fillet SCFs decrease. The curves for both fillets are almost linear over the range investigated, but do appear to become less so at higher values of T/D_p. The point at which the curves cross (T/D_p=0.25) is the optimum value of web thickness for the fillet dimensions and

overlap used in these models. However, the value of T/D_p at which the two curves cross is dependent not only on fillet radii and overlap, but also the nominal stress chosen. This is because the crankpin and journal fillet curves may move up and down relative to each other. Some nominal stress methods assume the neutral axis of the nominal beam to be at H/2 (H × B, H × C), and others do not (eye-shape, slanted eye-shape). This changes the relative magnitudes of the crankpin and journal fillet curves, thus changing the crossover point. A similar effect can be achieved by the choice of whether to include or exclude the web compression component. The former point regarding the value of overlap is also an important consideration. It has been shown in Section 5.4 that the as the overlap is changed, the SCFs at the crankpin and journal fillets change at different rates. So the crossover point on the web thickness SCF graph will change depending on what value of overlap is chosen.

It is interesting to note that, unlike the overlap study, with the exception of the model with the smallest web thickness, the angular position of the greatest stress in the fillets, α', remains constant over the range investigated. This is illustrated in Table 5.16.

Table 5.16 Values of α' for the range $0.12 \leq T/D_p \leq 0.38$ (3D BE)

	Radial bending	
T/D_p	Crankpin	Journal
0.12	13.3°	44.8°
0.19	19.9°	44.8°
0.27	19.9°	44.8°
0.35	19.9°	44.8°
0.38	19.9°	44.8°

5.5.2 Pure torsion

A BE mesh of a half crankthrow with a journal extension of $0.81D_p$ is used to investigate the torsion loadcase. The crankpin centre is encastré, and four pressure loads are applied as two couples to the free face of the journal, to put the journal in torsion.

As was the case in the overlap analysis, three shapes are modelled; the datum ($T=0.19D_p$), a thinner webbed crank ($T=0.12D_p$) and a thicker webbed crank ($T=0.27D_p$). The peak stresses at the crankpin and journal fillets are presented for the three models in Figure 5.48. As the web thickness is increased, the peak fillet stresses exhibit a non-linear reduction. Although the crankpin fillet stresses are higher than those in the journal fillet, the peak stresses in both fillets reduce at approximately the same rate.

The maximum principal stresses, normalised with respect to the H × C beam nominal stress, at various angles, θ, around the crankpin and journal are presented in Figure 5.49. The SCFs are seen to decrease as the web thickness is increased, and occur in the regions $\theta_p' = 60°$ and $34° < \theta_j' < 42°$.

Generally, using the H × C beam as the nominal stress basis, the trend has been for the SCFs to increase as H is increased. This is not true for the web thickness analyses, and is probably because the C term (maximum width of overlap region) remains constant as the web thickness is changed. This perhaps highlights a limitation of the H × C method, because the equivalent of C in the slanted eye beam would change

significantly as the web thickness was varied. In this case, the slanted eye beam would be a much more accurate reflection of the area over which stress is carried.

5.5.3 Web stiffness

The web deformation is measured under radial bending, and the results are presented in Figure 5.50a. It is immediately obvious that the web thickness affects the web stiffness to a lesser extent than the overlap. Reducing T/D_p by 40% from 0.19 to 0.12, only increases the web deformation by 9%. Increasing T/D_p by 100% from 0.19 to 0.38 reduces the web deformation by only 15%.

Similar observations are made when the web deformation is measured under torsion (Figure 5.50b). Reducing T/D_p by 40% increases the web deformation by 15%. Increasing T/D_p by 40% reduces the web deformation by 9%.

This indicates that it is the size of the common eye-shaped region formed by the crankpin and journal overlap that determines, to a large extent, the stiffness of the crankthrow.

5.6 Crankpin bores and dimples

Here, the effects of crankpin bores and dimples are investigated (Figure 5.51), where the term bore refers to a hole passing completely through the crankthrow, parallel to the crankthrow axis. The term dimple refers to a drilling into (but not completely through) the crankthrow. A dimple may be drilled parallel to, or at an angle to the crankthrow axis. Journal dimples are investigated in Section 5.7.

For many years now, in order to reduce the out-of-balance mass as the crankshaft rotates, crankpins have been axially bored. The balance weights which are required are therefore smaller, and the crankshaft can have a higher rotation speed. These advantages are clear, but what is less well documented is the effect of such holes on peak stresses in the fillets. Leikin [6] and Arai [10] investigated (in no great detail) crankpin bores, the latter concluding that the journal fillet stress distribution changes, but the peak stress remains at approximately the same value. Pfender, et al. [7] and Fessler and Sood [8] made more rigorous investigations into the bore hole effect. Fessler and Sood investigated the loadcases of radial bending and torsion and noted significant changes in fillet stress distributions and peak stress magnitudes when bore holes are present. However, they only investigate a limited number of crank geometries, which gives no indication of the effect of the size and position of the bores. Here, a range of parameters which define crankpin bores and dimples are investigated, in order to assist the crankshaft designer in making the best use of these features.

The BE method is chosen as the most appropriate for all of the bore hole and dimple analyses, because the task of adding holes to crankthrow geometry is greatly simplified by the surface only modelling. Half crankthrows (one end) are created to allow both radial bending and torsion to be analysed. Under radial bending, it was found that if point loads were applied to the crankpin and journal, high stress regions at either side of the bore holes and dimples were created. The high stress regions occur at the surfaces of the holes, just below the surface of the chamfered web. For this study therefore, it is therefore not appropriate to approximate the distributed oil film loads as point loads. Distributed loads were applied over a relatively large area at the crankpin and journal to spread the load more realistically around the holes. There is a significant reduction in the magnitude of the high stress at the holes when distributed loads are applied. The resulting fillet stresses are normalised with respect to the nominal stress occurring in the H × C beam (including web compression). The models created and analysed are described in Table 5.17. The terms diameter, depth, angle and radial position are explained in Figure 5.51.

Table 5.17 Models created to investigate crankpin bores and dimples

Name	Bore	Dimple	Diameter	Radial position	Depth	Angle
ZBHOL1	✓		0.231	0.956	Through	0°
ZBHOL2	✓		0.231	0.846	Through	0°
ZBHOL3	✓		0.308	0.846	Through	0°
ZD1-D		✓	0.231	0.956	0.423	30°
ZDIMP2		✓	0.308	0.956	0.423	30°
ZDIMP3		✓	0.231	0.956	0.231	30°
ZDIMP4		✓	0.231	0.956	0.538	30°
ZDIMP5		✓	0.231	0.956	0.423	15°
ZDIMP6		✓	0.231	0.956	0.423	45°
ZDIMP7		✓	0.231	0.846	0.423	30°

Three models with crankpin bores are used to carry out a basic investigation into the effect of the hole diameter and radial position. For a bore hole, these are the only parameters that can be changed. Seven models are created with dimples with variations of each of the four defining parameters. A typical mesh of a crankthrow with a crankpin dimple is presented in Figure 5.52. The results from all of these analyses are compared with a standard non-bored crankthrow, ZNDAT.

5.6.1 Radial bending

Under radial bending, it is observed that holes in the crankpin have the greatest effect on the journal fillet stress distribution. In the solid crankpin model, the peak stresses are known to lie on the planes θ_p' and $\theta_j' = 0°$. When a hole is introduced to the crankpin (bore or dimple), the peak stress moves from this central plane. Two peaks are observed, positioned symmetrically about the centreplane of the crankthrow, generally at angles $\pm 15° < \theta_j' < \pm 20°$. It is important to note that the peak stresses occurring with a bored or dimpled crankpin are lower than the single peak that occurs with a solid crankpin. This indicates that as well as reducing the out of balance mass, holes in the crankpin can be used to reduce peak stress levels under bending. However, care must be taken because the crankthrow stiffness is reduced, and crankpin fillet stresses are seen to rise as crankpin holes are introduced. The following sections summarise the effect of changing each of the defining parameters of the bores and dimples.

5.6.1.1 Diameter

For bore holes (Figure 5.53), as the diameter is increased, the stress in the journal fillet on the plane $\theta_j = 0°$ decreases and the SCF position moves to an increasing value of θ_j. The SCF is around 10% lower than that which occurs in the unbored model, but there is little further reduction in SCF as the hole diameter is increased from $0.231D_p$ to $0.308D_p$. At the crankpin fillet, the stress distribution does not change around the crankpin, but the SCF increases as the diameter of the crankpin bore is increased. A maximum SCF increase of 3% is noted at the crankpin fillet. It is also important to note that the stiffness of the crankthrow is reduced by around 8% when the larger diameter bore is present.

Similar effects are noted as the diameter of a dimple in the crankpin is increased (Figure 5.54). The basic dimple (angle = 30°, depth = $0.423D_p$, radial position = $0.956D_p$) with a diameter of $0.231D_p$, produces a virtually flat stress curve in the range $0° < \theta_j < \pm 14°$. As the diameter is increased to $0.308D_p$, the stress on the plane $\theta_j = 0°$ reduces further, and there is also a further slight decrease in the SCF at $\theta_j' = \pm 17°$, so that compared to the solid crankpin model, the SCF is reduced by 11%. Again, the SCF at the crankpin fillet increases as the diameter of the dimple is increased (3% maximum), and accordingly the stiffness of the crankthrow is reduced by around 8%.

5.6.1.2 Radial position

The bore hole has a greater effect on stress reduction as it is moved closer to the journal fillet (Figure 5.55). At a radial position of $0.956D_p$, compared to the solid crankpin model, the SCF is reduced by 5% and lies on the plane $\theta_j' = 0°$. When the

radial position is reduced to $0.846D_p$, the SCF is reduced by 9% and moves to the plane $\theta_j' = \pm 14°$. The bore hole closest to the journal fillet causes the crankpin fillet SCF to increase by 2%, and the stiffness of the crankthrow is reduced by 4%.

Conversely, the most beneficial dimple is that with the greater radial position value (Figure 5.56). The journal fillet SCF with this dimple is 9% lower than that in the solid crankpin model. Reducing the radial position of the dimple to $0.846D_p$ causes a further reduction in stress on the plane $\theta_j = 0°$, but the SCF (on the plane $\theta_j' = \pm 17°$) increases by 2%. The dimple with the radial position of $0.956D_p$ causes the crankpin fillet SCF to increase by 2% and the crankthrow stiffness to reduce by 4%.

5.6.1.3 Depth

The depth of the dimple is seen to have a slight effect on the journal fillet SCF (Figure 5.57). A dimple depth of $0.231D_p$ does not reduce SCFs as much as a dimple depth of $0.423D_p$, but increasing the depth to $0.538D_p$ does not reduce stresses any further.

5.6.1.4 Angle of inclination

The greatest reduction in SCF for the three dimple angles analysed (Figure 5.58) is achieved with the largest angle of inclination (45°). As the angle is increased, the stresses in the region $14° < \theta_j$ fall, but rise in the region $\theta_j > 14°$. Therefore, for this particular dimple diameter and angle of inclination, the journal fillet SCF occurs at $\theta_j' = 14°$ and is some 9% lower than that in the solid crankpin model. In addition, the crankpin fillet SCF increases slightly and the crankthrow stiffness is reduced as the angle of inclination is increased.

5.6.2 Pure torsion

The bore and dimple giving the greatest reduction in SCF under radial bending are analysed under the torsion loadcase. These models are ZBHOL3 and ZDIMP2, and are renamed TBHOL3 and TDIMP2 for the torsion analyses. The results from these analyses are compared with a solid crankpin model loaded under torsion. The BE models are constrained and loaded in the same way as previous BE torsion analyses. The results are presented in Figure 5.59. It is clear that the holes give rise to significantly different stress distributions around the journal fillet. The solid crankpin produces one peak at $\theta_j' = 38°$, while the bored and dimpled models both produce peaks at $\theta_j' = -7°$ & $42°$ (SCF). The dimpled model produces a slightly flatter stress distribution than the bored model in the region $-20° < \theta_j < 20°$, but the SCFs are the same, with both being around 2% lower than the SCF in the solid crankpin model. At the crankpin fillet, the stress distributions are all similar, but the SCFs in the bored and dimpled models are 2% higher than the SCF in the crankpin fillet of the solid crankpin model.

5.6.3 Discussion

Agreement with the trends noted by Fessler and Sood [8] is excellent, for both radial bending and torsion. They too observed the two peaks which are symmetrical about the centreplane of the crankthrow under radial bending at approximately $\theta_j' = \pm 20°$. They also detected the two peaks which appear under torsion, one near to $\theta_j = 0°$, and the other (the SCF) near to $\theta_j' = 45°$.

5.7 Journal dimples

Two journal dimple analyses are carried out with the intention of achieving a stress reduction at the crankpin fillet. The results from the crankpin dimple investigations are used as a guide to aid the initial choice of journal dimple dimensions, and then to improve it's design. The models created are described in Table 5.18.

Table 5.18 Models created to investigate journal dimples

Name	Bore	Dimple	Diameter	Radial position	Depth	Angle
ZJDIM1		✓	0.308	0.947	0.423	30°
ZJDIM2		✓	0.308	0.947	0.538	45°

5.7.1 Radial bending

The model ZJDIM1 is created with the same diameter, depth and angle of inclination and a similar radial position to the optimum crankpin dimple (ZDIMP2). These parameters are redefined for a journal dimple in Figure 5.60. The results obtained from analyses ZJDIM1 are presented in Figure 5.61. The expected change in stress distribution in the crankpin fillet does not occur. There is also no change in the journal fillet stress distribution or the overall stiffness of the crankthrow.

The crankpin dimple analyses highlighted the fact that the effect of the dimple can be increased if the depth and angle of inclination are increased. Both of these changes gave rise to lower stresses on the centreplane of the crankthrow ($\theta = 0°$). In order to achieve a similar effect, the depth of the journal dimple is increased to $0.538D_p$ and the angle of inclination is increased to 45° (ZJDIM2). The resulting stress distributions can also be seen in Figure 5.61. At the crankpin fillet, there now exists a very flat

stress distribution in the region $0° < \theta_p < 17°$, with the SCF being 6% lower than the solid journal model. There is a very slight increase of SCF at the journal fillet, due to the slight reduction in stiffness of the crankthrow, but these changes are neglible.

The effect of the journal dimple appears to be notably less than the crankpin dimple. It is suggested that this may be because the journal, which is larger than the crankpin, deforms less under bending than the crankpin. A similarly dimensioned hole in the crankpin and journal will therefore have a greater effect on stress redistribution in the less stiff crankpin. It is also clear that the bending moment in the crankpin is greater than in the journal and this may also cause the journal dimple to have a smaller effect.

5.7.2 Pure torsion

Model ZJDIM2 is also analysed under torsion (TJDIM2) and the results are compared with those from the solid journal model. The results at both fillets are presented in Figures 5.62. As was observed with the crankpin dimple torsion analysis, the journal dimple causes two peaks in the stress distribution curve. One peak occurs at $\theta_p = -4°$, whilst the other occurs at $\theta_p' = 60°$. The latter is the SCF and is 4% higher than the SCF occurring in the solid journal model. The stress distribution in the journal fillet is similar to that in the solid journal model for angles $\theta_p < 20°$, but is slightly higher at angles $\theta_p > 20°$.

5.7.3 Discussion

The second journal dimple modelled (ZJDIM2) gives rise to a 6% peak stress reduction under bending and a 4% peak stress increase under torsion. The increased

angle of inclination makes the machining access to the hole easier because of the restriction imposed by the opposite web. Because the hole is located near to the axis of rotation of the crankshaft, it is unlikely that it will have a great effect on the balance of the crankshaft. It is possible though that such a dimple might interfere with the balance weight fixing holes which are drilled into the base of the web. However, the results are presented because in some circumstances the benefits of stress and weight reduction may outweigh the added complications of alternative fixings or one piece crankthrow and balance weight construction.

5.8 Cut-back web

Section 5.6 dealt with a method of reducing the out of balance mass of the crankshaft by designing holes into the crankshaft. Here, another method is analysed, which involves cutting away the web adjacent to the crankpin (Figure 5.63). The datum crankthrow design already has a chamfered web to achieve the same goal, but the cut-back takes this a stage further. This design is already used in some commercially available crankshafts, but it's effects on stress distributions in the crankthrow are not well documented.

The BE method is used to analyse a typical cut-back web design under radial bending and torsion. The mesh used for the bending loadcase is presented in Figures 5.64. The loading and boundary conditions for the radial bending and torsion analyses are the same as those applied to other BE models. The maximum principal stresses are normalised with respect to the nominal stress occurring in the H × C beam (including web compression).

5.8.1 Radial bending

Compared to the results from the full-web datum crankthrow, the stress distribution around the journal fillet is flattened slightly when the cut-back web is used (Figure 5.65a). The SCF is reduced by 8%, but remains on the plane $\theta_j' = 0°$. The stresses in the cut-back fillet are also measured and presented in Figure 5.65a. They too peak on the plane $\theta_j' = 0°$, but the magnitude of this peak stress is only 0.67 times the SCF. This is probably partially due to the journal fillet radius being 0.56 times the size of the cut-back fillet radius.

At the crankpin fillet, as was observed in the bore/dimple analyses, the stress distribution does not change, but the SCF increases slightly (3%), and the stiffness of the crankthrow is reduced (5%).

5.8.2 Pure torsion

The results at the crankpin and journal fillets for the torsional loadcase, presented in Figure 5.66, are not unexpected, exhibiting similar trends to those seen in the dimple analyses. Compared to the results from the datum crankthrow, the stress distribution at the journal fillet, shifts slightly so that the SCF moves from $\theta_j' = 42°$, to $\theta_j' = 48°$. The SCF is also reduced by 6%. At the crankpin fillet, the cut-back web results in an increase in SCF 5%, but there is little change in the distribution of the stresses.

However, the stress distribution in the cut-back fillet is quite unexpected (Figure 5.67). Here, the principal stresses rise gradually as θ_j increases until $\theta_j = 28°$ (where $I_t = 3.6$), at which point there is a sharp rise in stress. The SCF in the cut-back fillet is around 5.4 (twice as high as the journal fillet SCF) and occurs at $\theta_j' = 31°$. By the next point of measurement at $\theta_j = 36°$, I_t has fallen to 3.3. This small region of very high stress is at the thinnest point of the web, where the cut-back is on one side of the web and the recessed crankpin fillet is on the other. It is suggested that this may be the cause of the very high SCF values. It should also be noted that in this analysis, the crankthrow is twisted in the $+\theta_j$ direction, which results in a tensile peak at $\theta_j' = +31°$, but there is also an equal and opposite compressive peak at $\theta_j' = -31°$. It is therefore advisable that the designer takes great care when removing material from this position on the web, even when using a generous fillet radii.

5.9 Oil holes

The oil holes in a crankshaft transport oil to the bearings to provide lubrication between the small/large end bearings and the crankpin/journal. The crankshaft investigated has a main oil hole, running from the crankpin (passing through the crankpin centre), through the web between the fillets, and into the journal (terminating at the journal centre). Smaller holes run from the main oil hole to the crankpin/journal surfaces. The main oil hole is bored from the opposite web, and the opening in that web is plugged to prevent oil loss. It is interesting to note that the centre of the drilling into the web almost coincides with the centre of the optimum crankpin dimple investigated in section 5.6 (ZDIMP2). This indicates that it may be possible to combine the two features by simply increasing the diameter of the entrance of the main oil hole.

It is of interest to the crankshaft designer to know how close to the fillets the main oil hole can be placed, before fillet stress distributions are significantly affected. A brief investigation is carried out here, whereby the main oil hole described above is modelled (ZOIL1). In addition, a second model is created where the main hole is placed so that at the centre of the crankpin, it passes through a point which is $0.1D_p$ below the crankpin axis (see Figure 5.68), thereby moving the hole closer to the crankpin fillet (ZOIL2). The BE method is used to carry out this investigation because, as with the bore and dimple analyses, it greatly simplifies the task of putting holes through the structure. Investigations are carried out under radial bending in order to observe the effect on the fillet stress distributions and the overall stiffness of the crankthrow. The

standard BE half crankthrow with extended journal is used in the analyses, encastré at the crankpin centre and loaded at the crankpin quarter point and journal centre.

5.9.1 Radial bending

Compared to a similarly loaded model with no oil holes (PJK2), the first model, ZOIL1, produces a stress increase of 1% at both the crankpin and journal fillet (Figure 5.69). The stress distribution around the crankpin and journal is unchanged, showing that the main oil hole does not have a similar effect to bores and dimples, probably because it follows rather than interrupting a load path. The stiffness of the crankthow remains unchanged by the hole, which has a relatively small diameter ($0.087D_p$) compared to a bore or dimple ($\sim 0.231D_p$).

The second model, ZOIL2, increase that crankpin fillet SCF by a further 2%, but has no further effect on the journal fillet SCF (Figure 5.69). The stiffness of the crankthrow also remains unaffected compared to the model with no oil holes.

It is suggested that because there is no change in crankthrow stiffness, the fillet stresses increase because the nominal stress in the neck region between the fillets has increased. This is due to the main oil hole reducing the cross-sectional area of the already highly stressed material in the neck.

Crankshaft designers are often also concerned with the stress concentrations at the breakouts of oil holes at the crankpin and journal bearing surfaces. Some authors have investigated stresses at crankshaft oil hole breakouts e.g. [18], [19]. However,

significantly more research has been carried out into oil hole breakouts in flat plates [17], [31], [32] and cylinders [33]. It would therefore be a relatively simple task to apply these findings to the analysis of crankshaft oil hole breakouts.

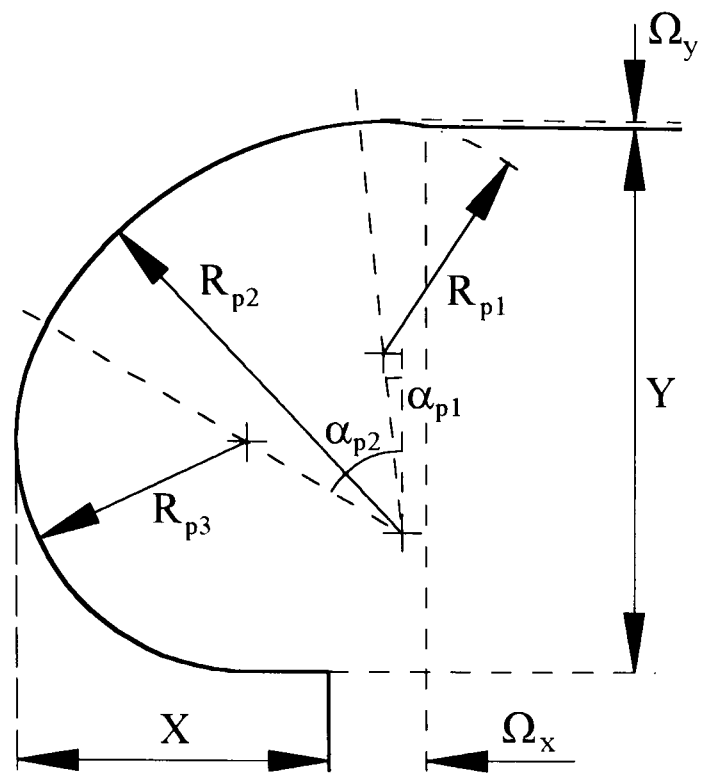

Figure 5.1. Definition of the compound crankpin fillet

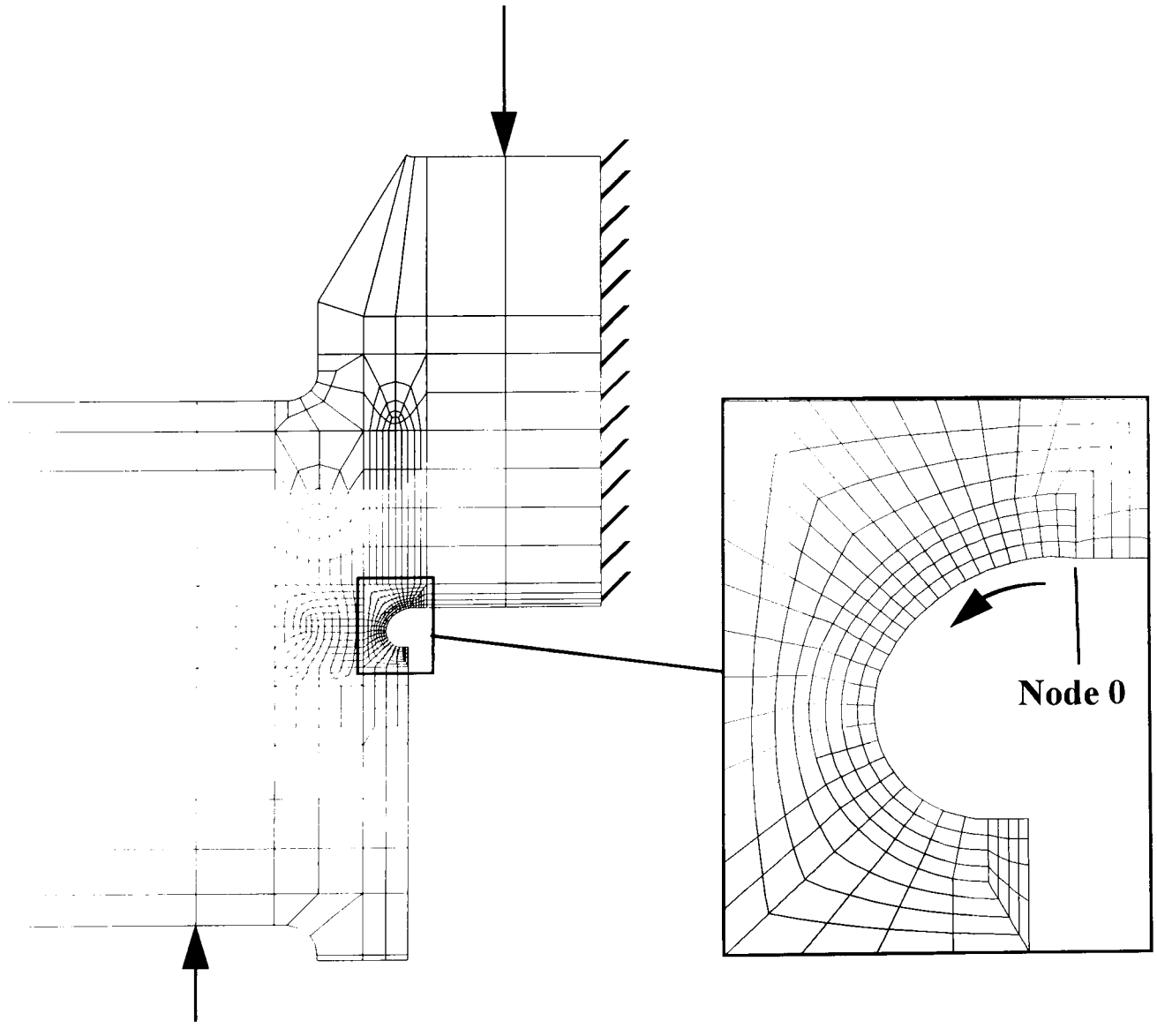

Figure 5.2. 2D crankpin fillet mesh

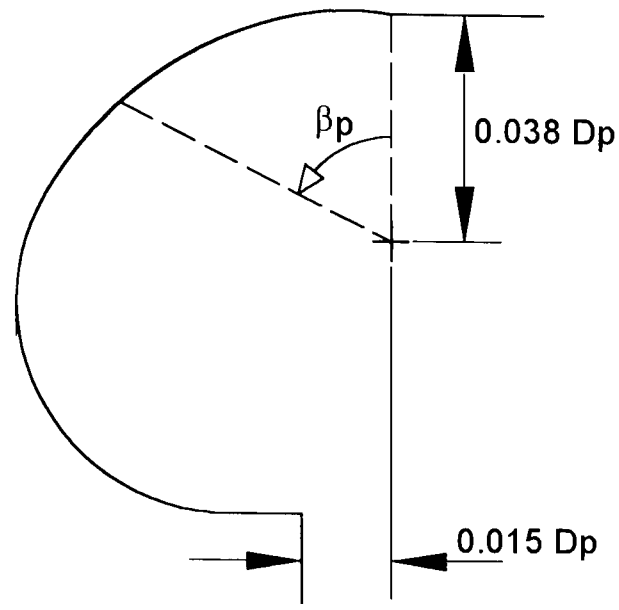

Figure 5.3. Definition of the notional centre of the crankpin fillet

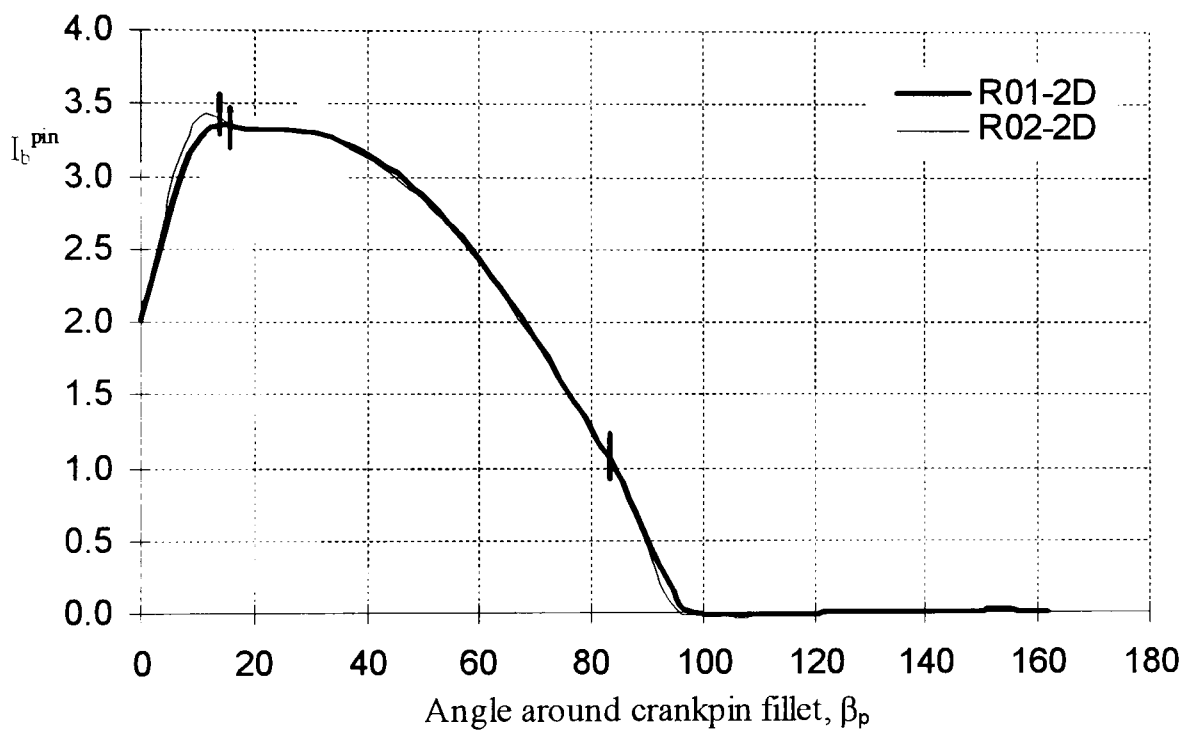

Figure 5.4. 2D investigation into the effect of minor radii under radial bending

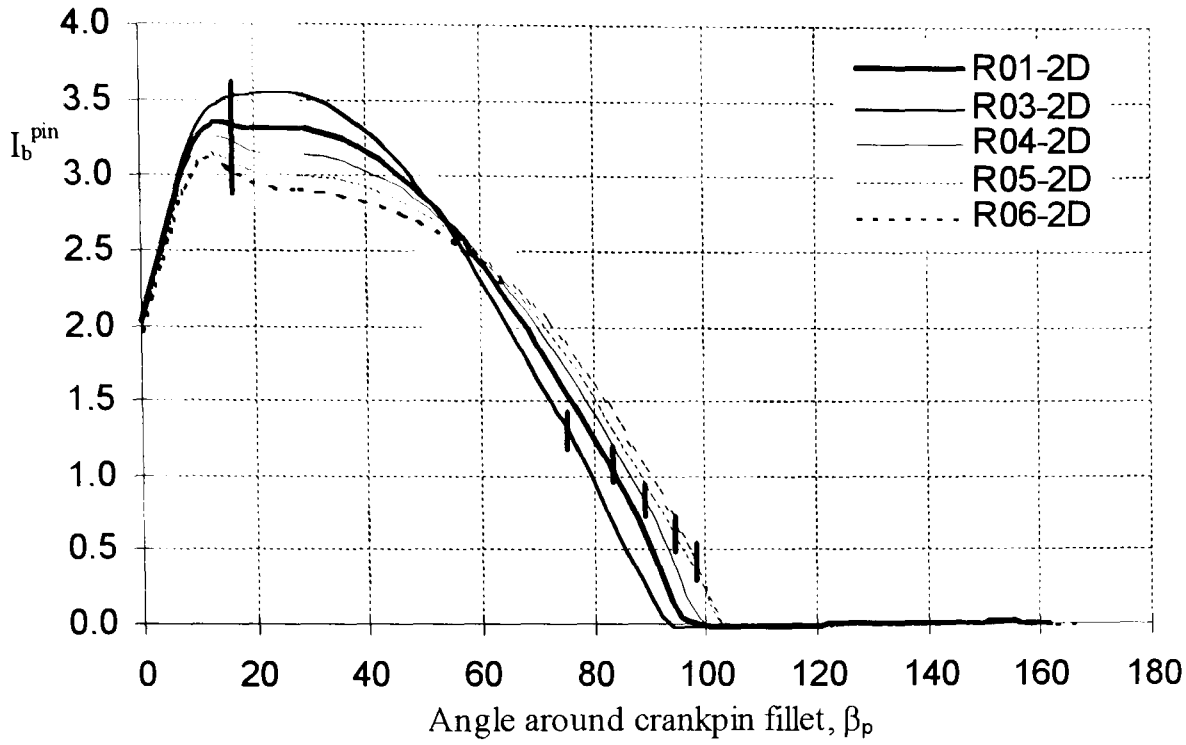

Figure 5.5. 2D investigation into the effect of major radius under radial bending

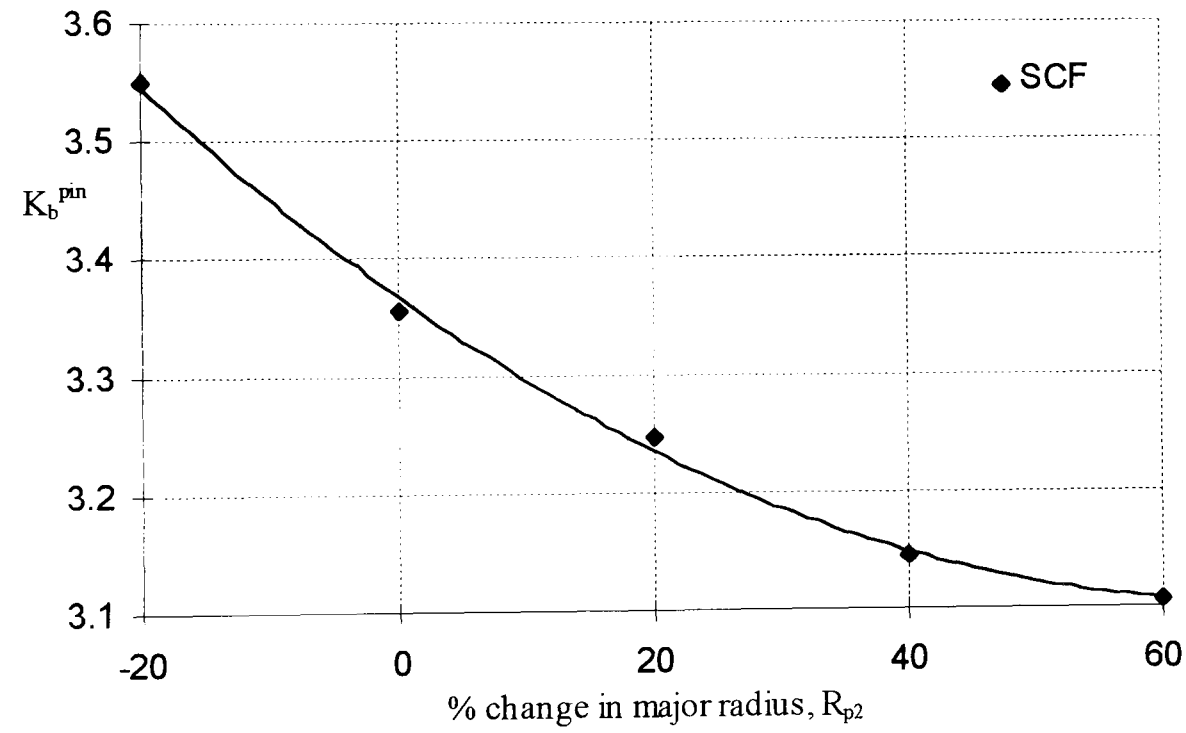

Figure 5.6. Variation in K_b as the major radius is changed

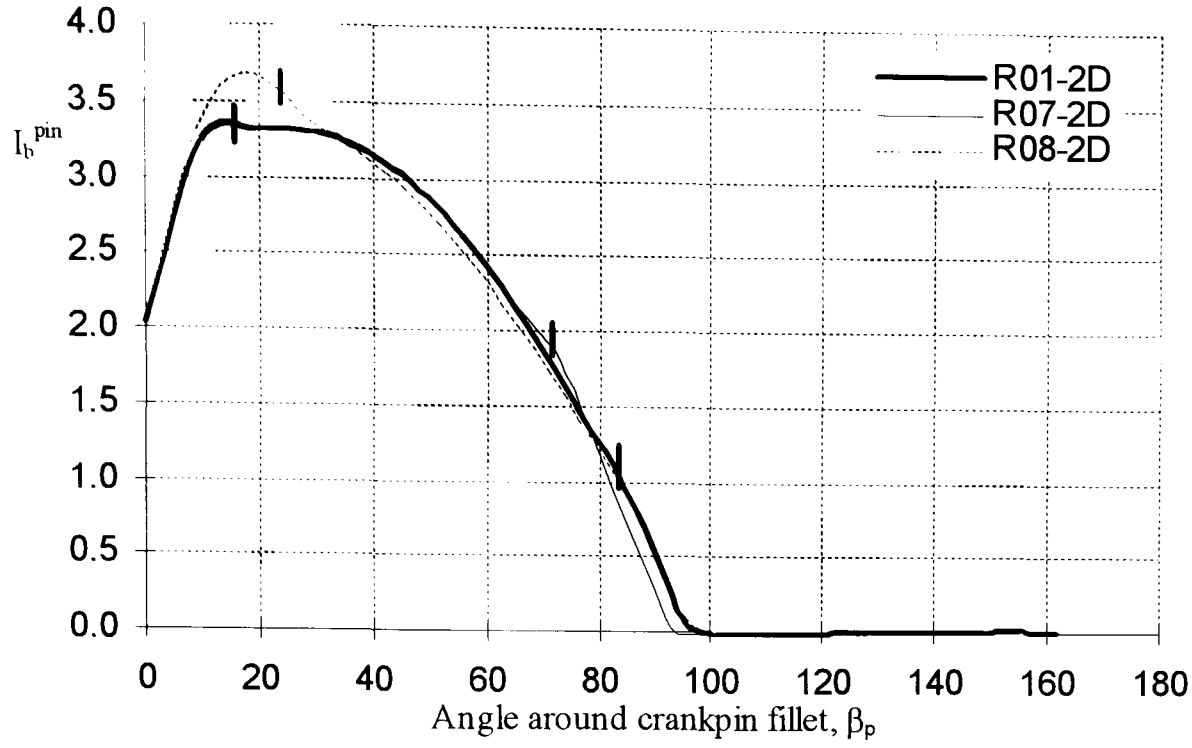

Figure 5.7. 2D investigation into the effect of blend angles under radial bending

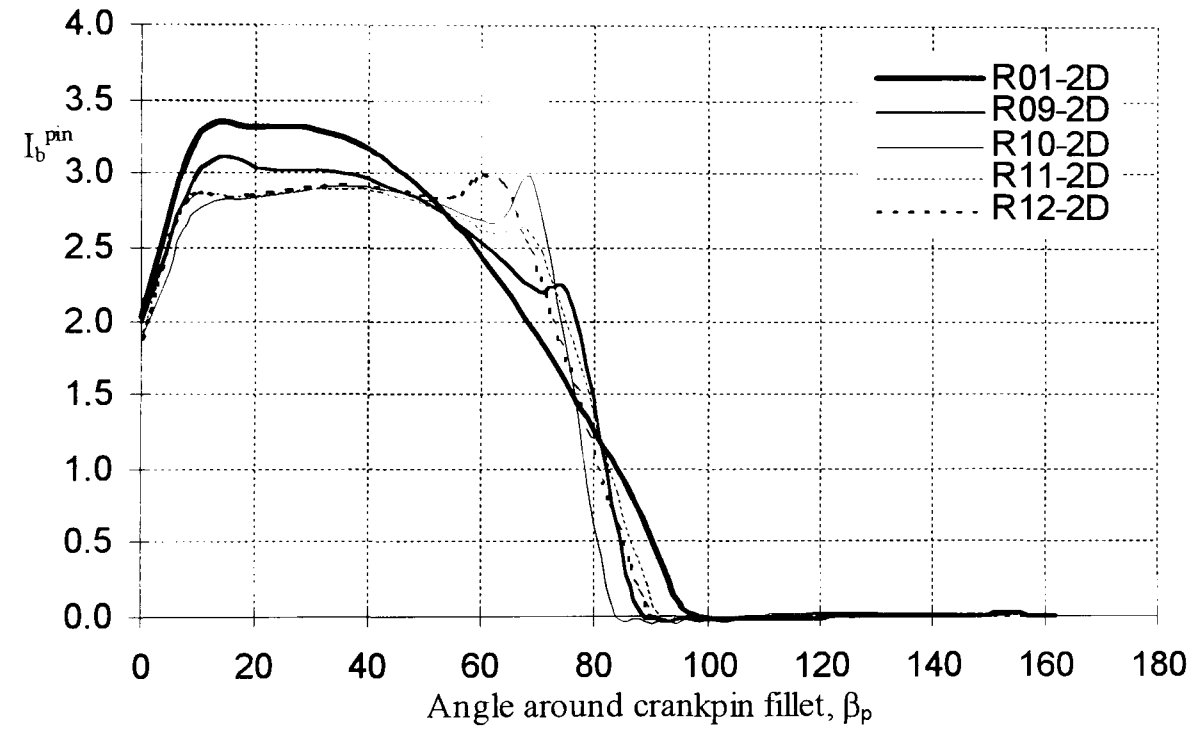

Figure 5.8. Optimisation of 2D crankpin fillet under radial bending

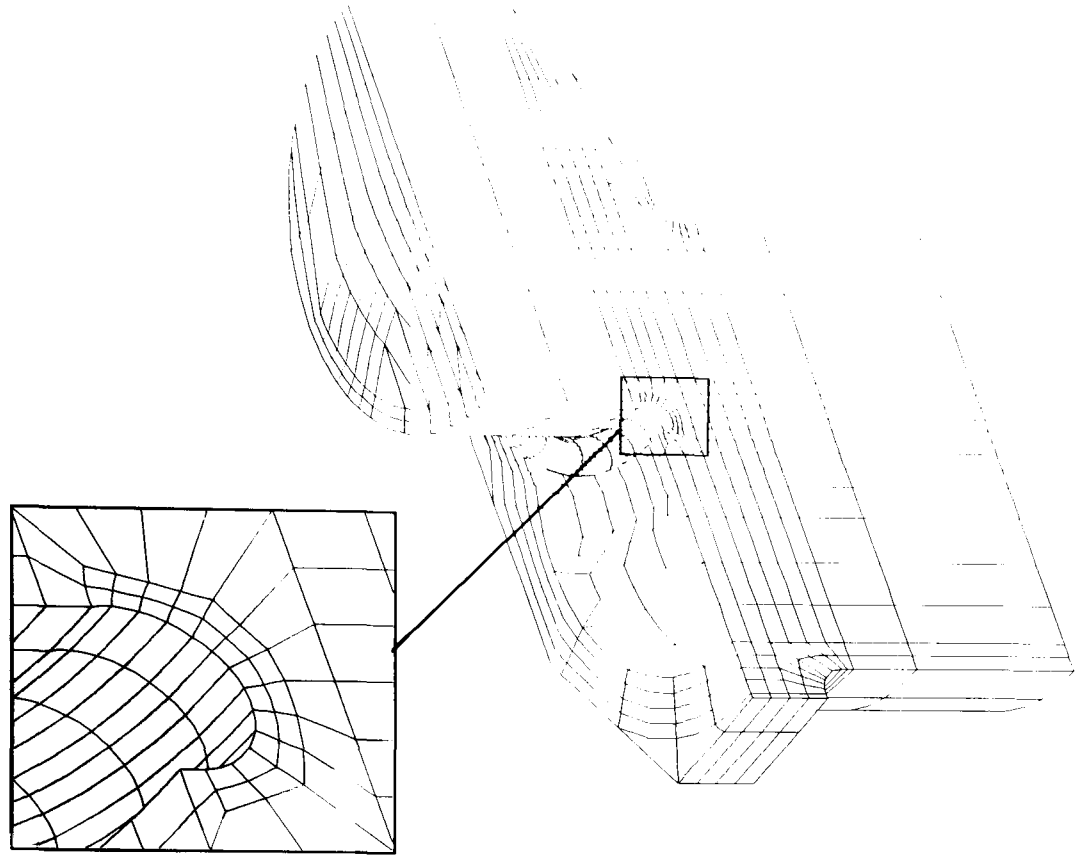

Figure 5.9. 3D crankpin fillet mesh used in crankpin fillet optimisation

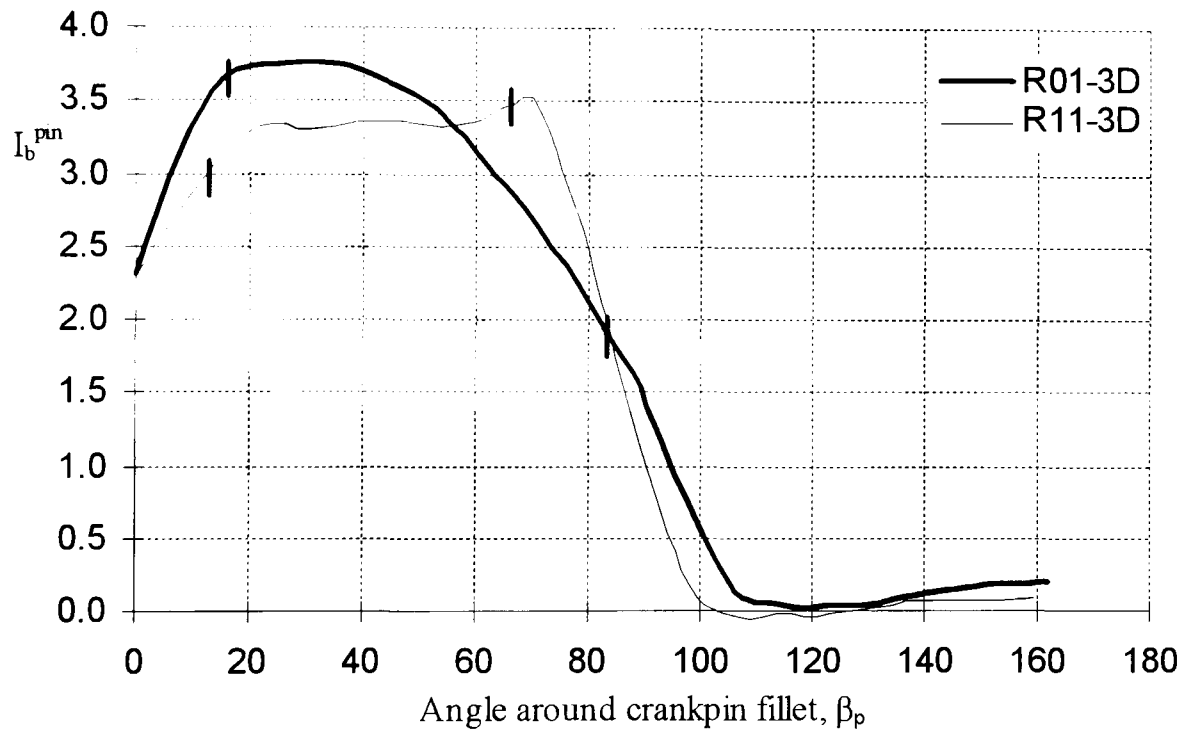

Figure 5.10. Optimum 2D crankpin fillet tested in 3D under radial bending

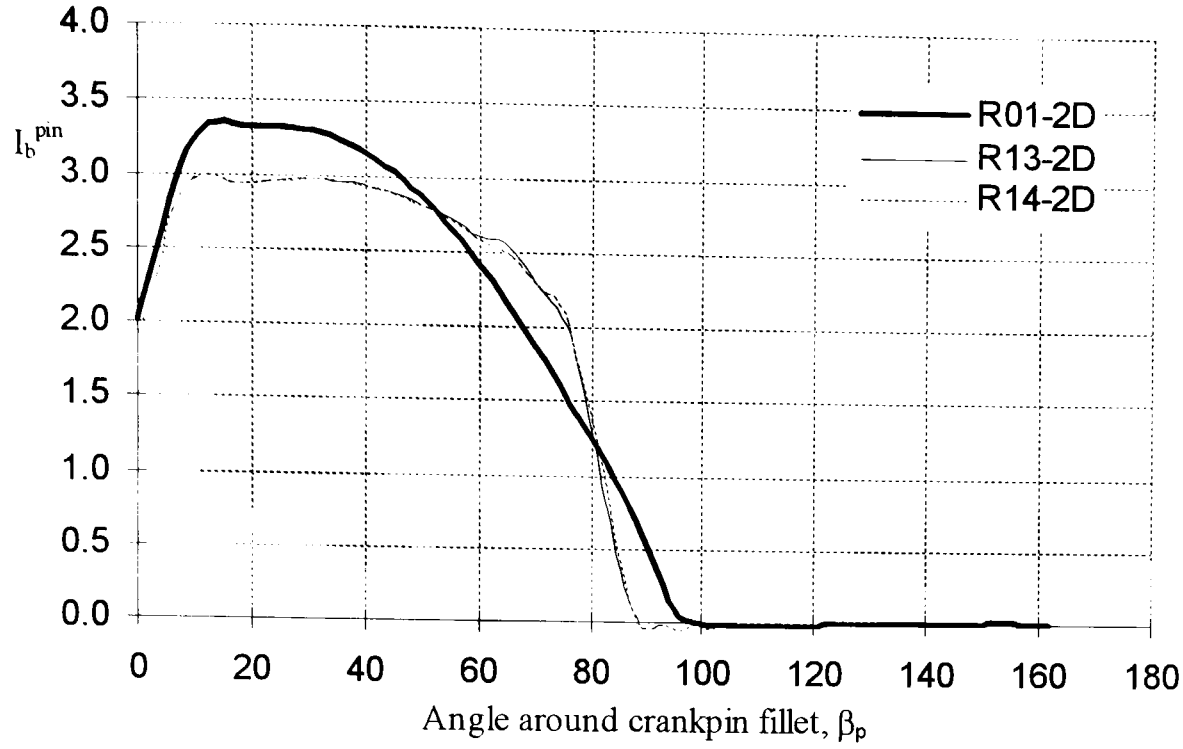

Figure 5.11. The use of 2D modelling to optimise the 3D crankpin fillet under radial bending

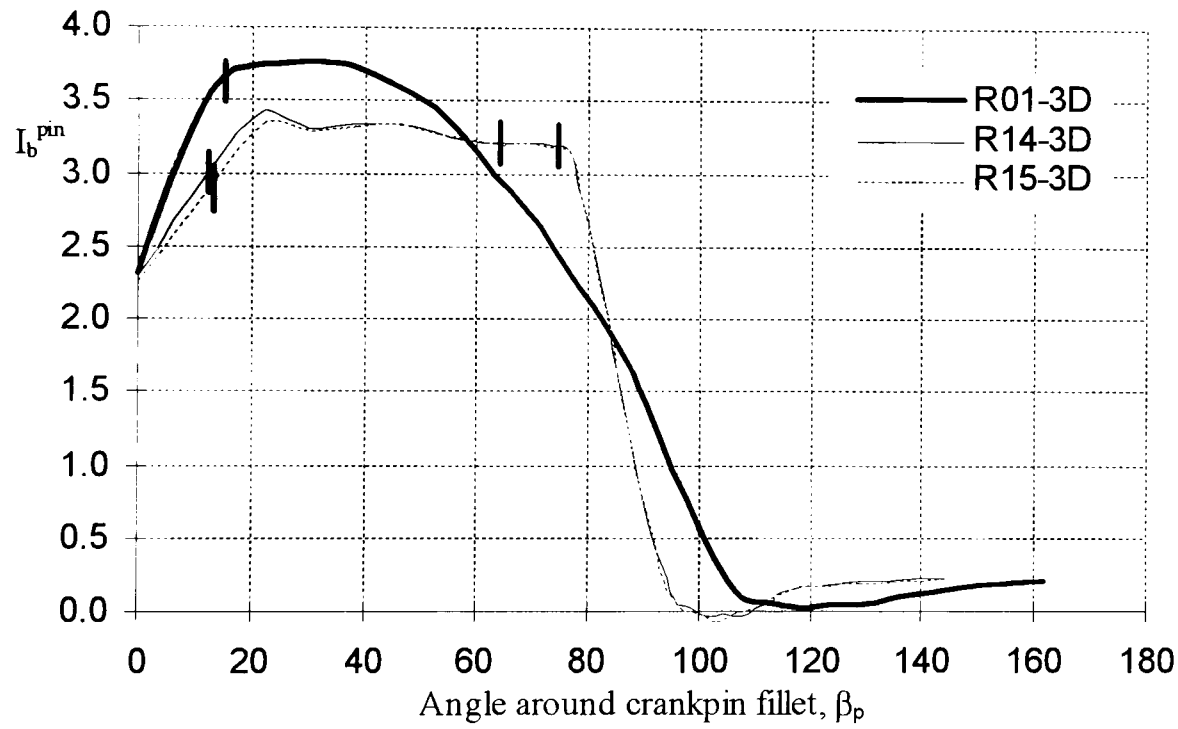

Figure 5.12. Optimisation of 3D crankpin fillet under radial bending

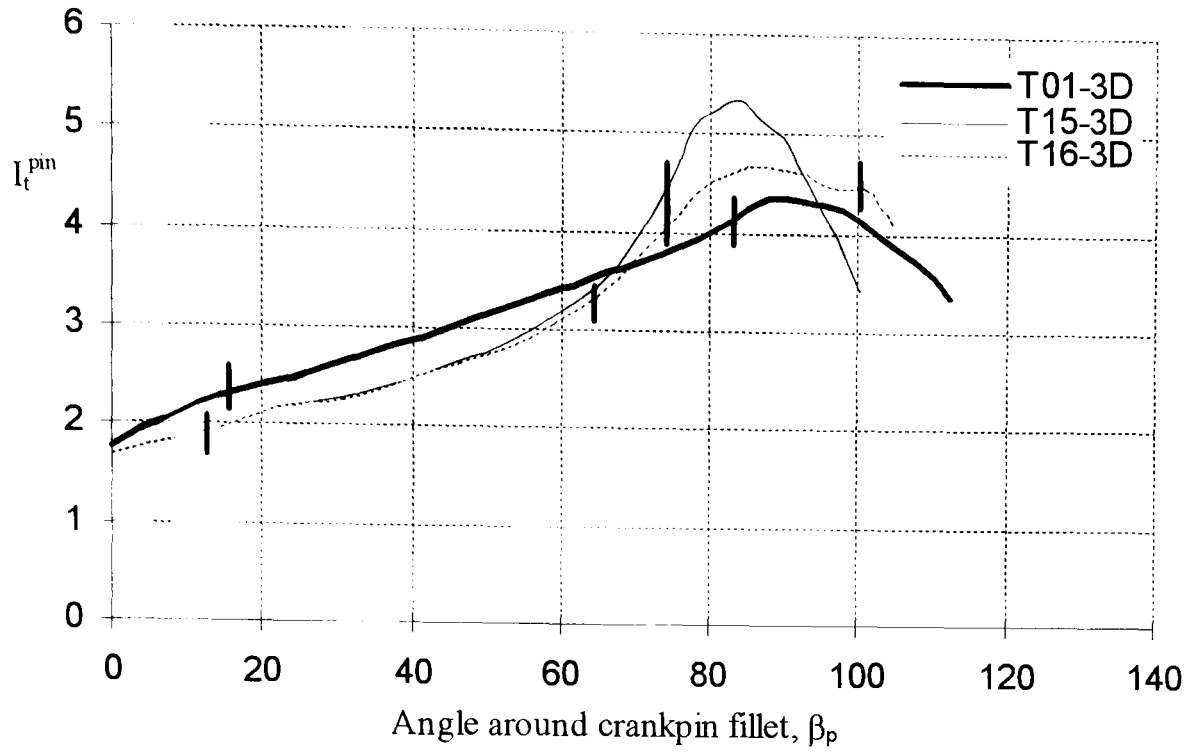

Figure 5.13. Optimisation of 3D crankpin fillet under pure torsion

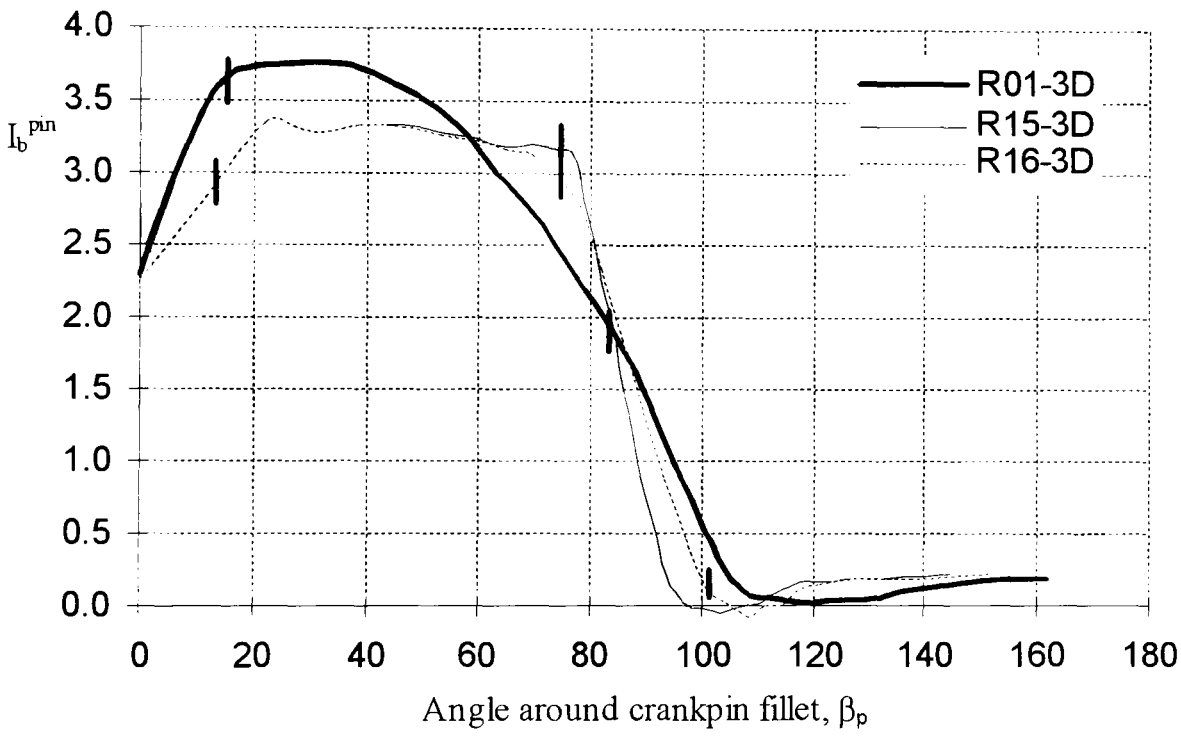

Figure 5.14. Investigating the optimum pure torsion 3D crankpin fillet under radial bending

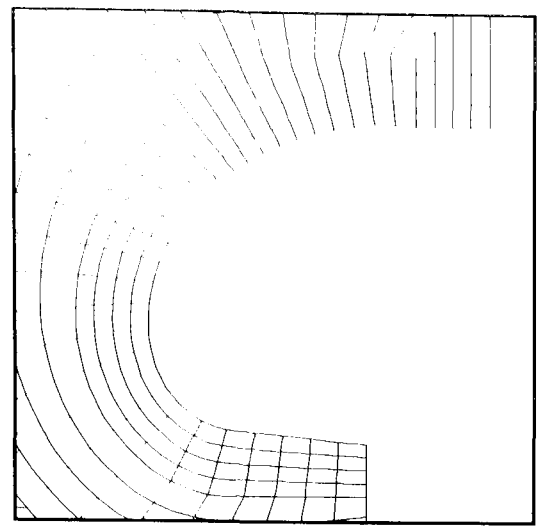

Figure 5.15. A typical spiral shaped fillet (linear reduction of radius)

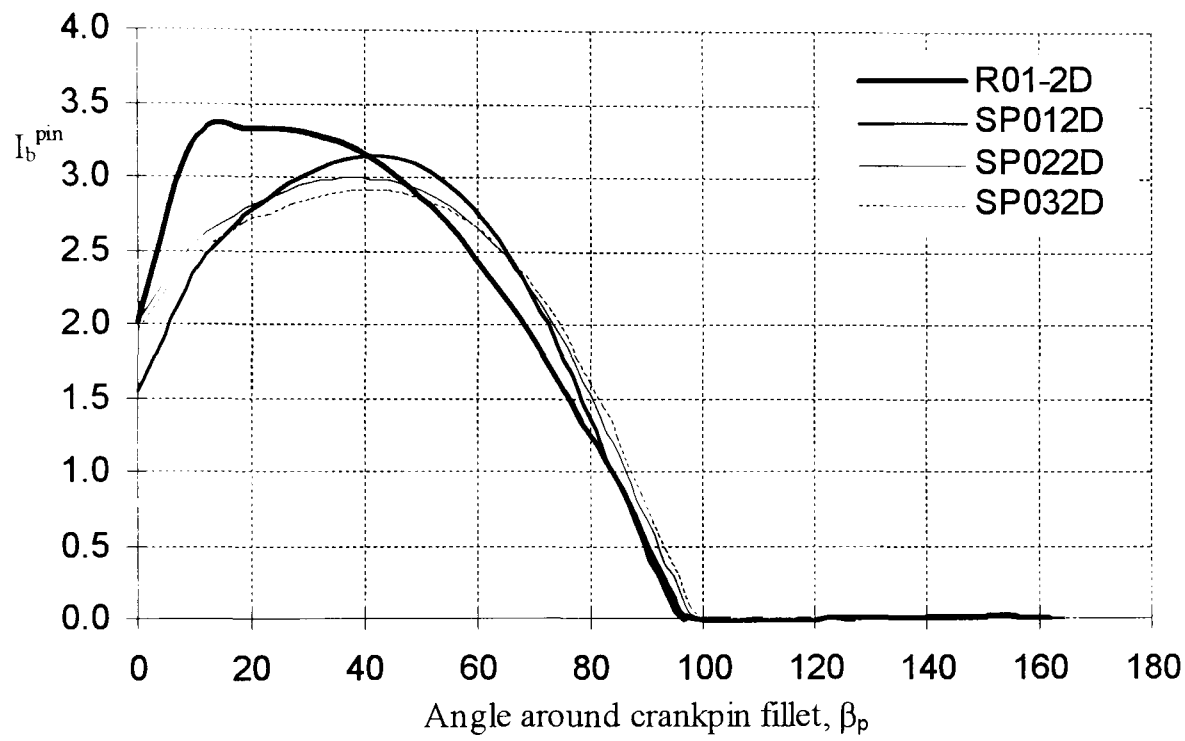

Figure 5.16. Investigation into the effects of varying the 2D spiral fillet shapes under radial bending

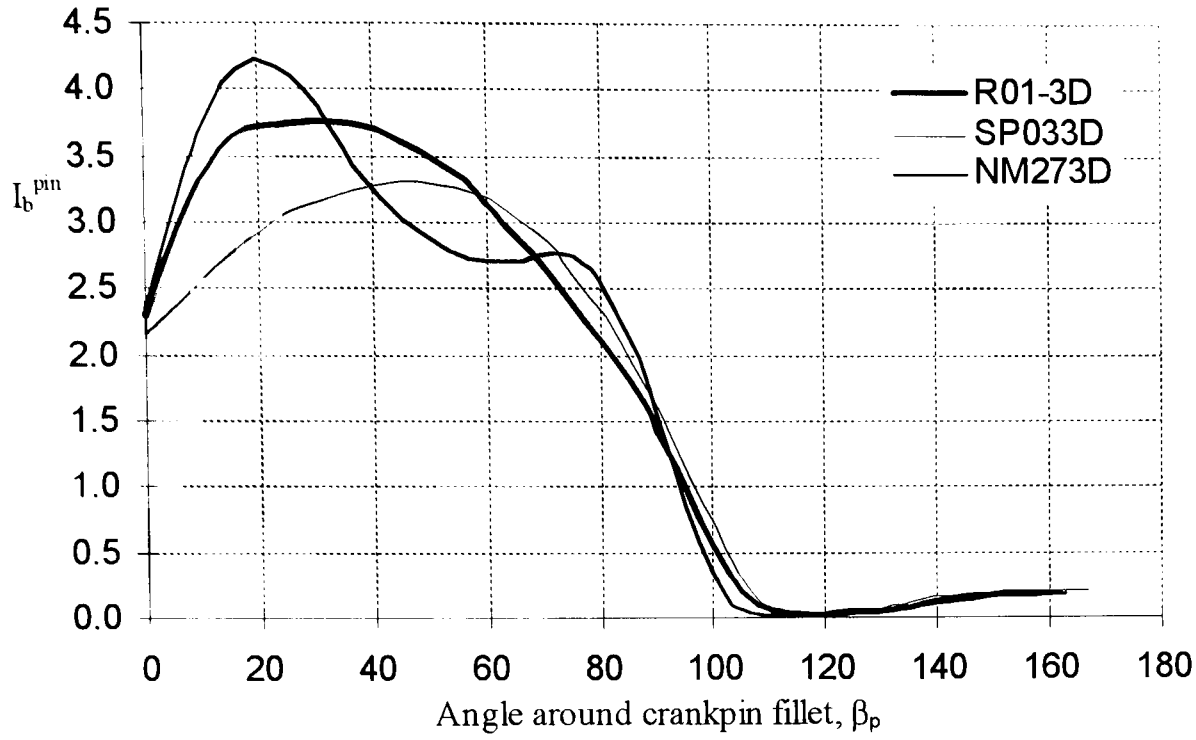

Figure 5.17. Investigation into the effects of linear and cubic spiral fillets in 3D under radial bending

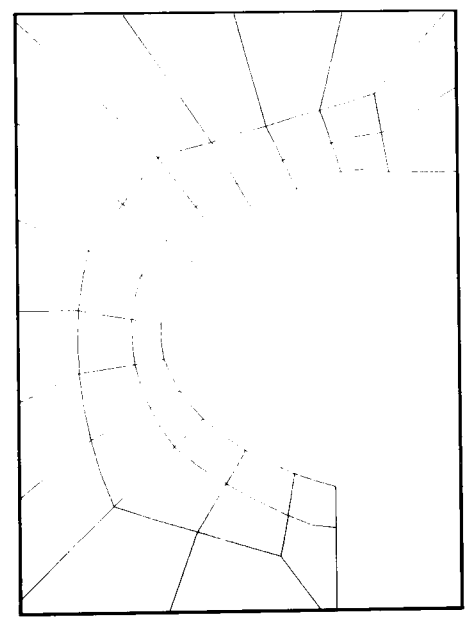

Figure 5.18. Crankpin fillet mesh used in the 3D modelling of a back to back cubic spiral fillet

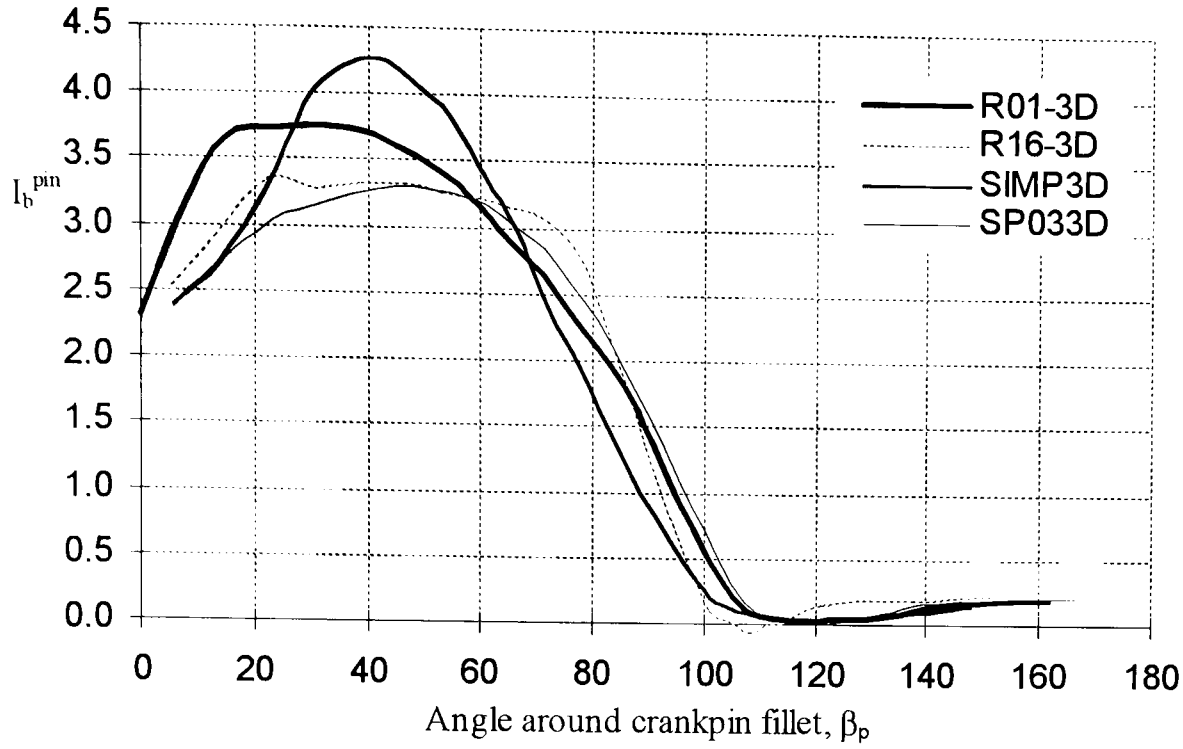

Figure 5.19. Investigation of various 3D fillet constructions under radial bending

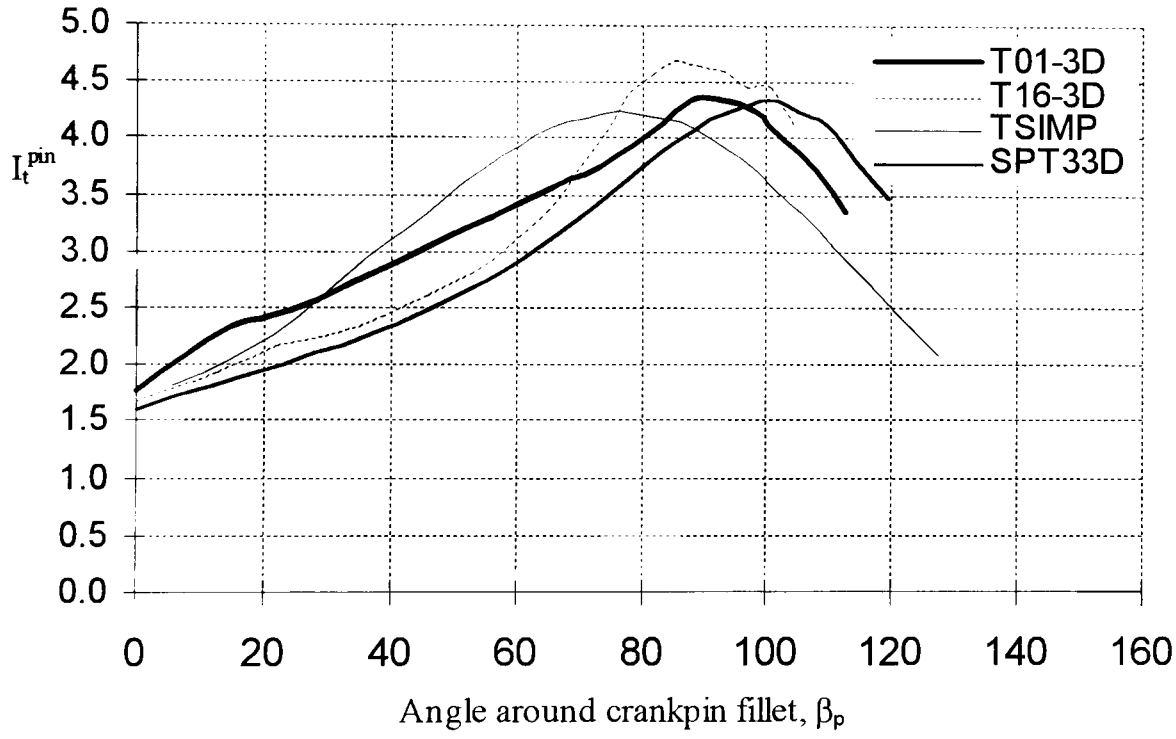

Figure 5.20. Investigation of various 3D fillet constructions under pure bending

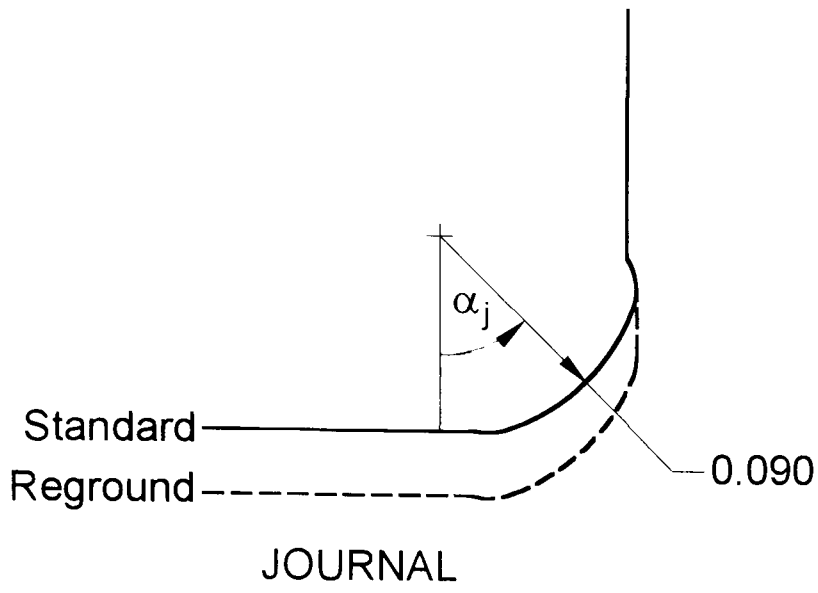

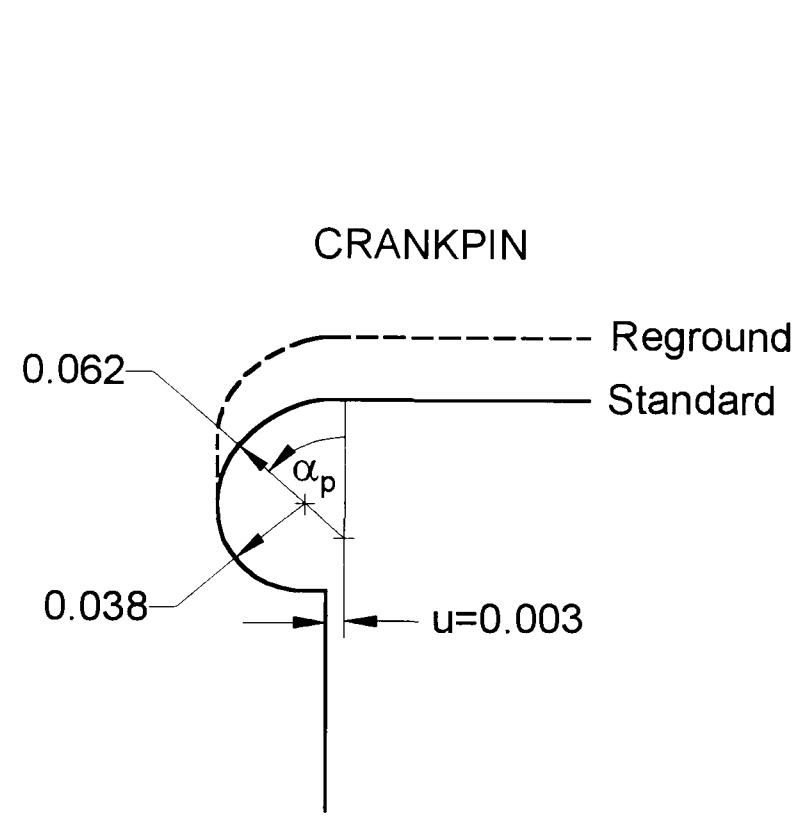

Figure 5.21. Standard and reground crankpin and journal fillet shapes

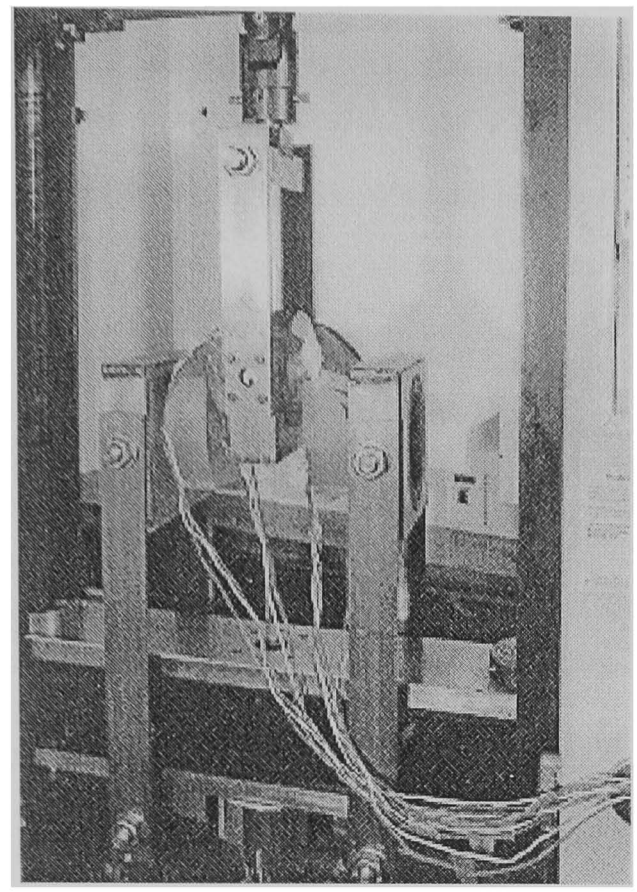

Figure 5.22. Experimental loading arrangement for ERS measurements under radial bending

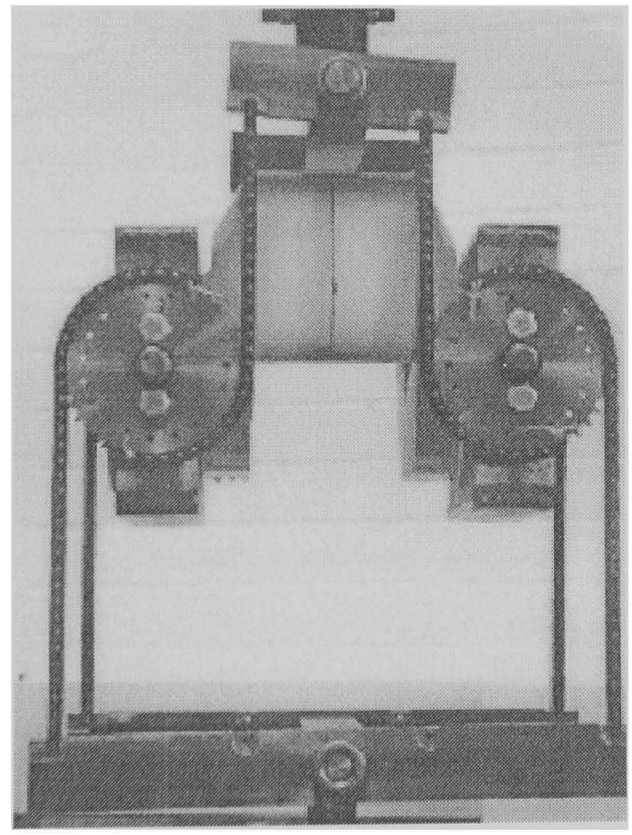

Figure 5.23. Experimental loading arrangement for ERS measurements under pure bending

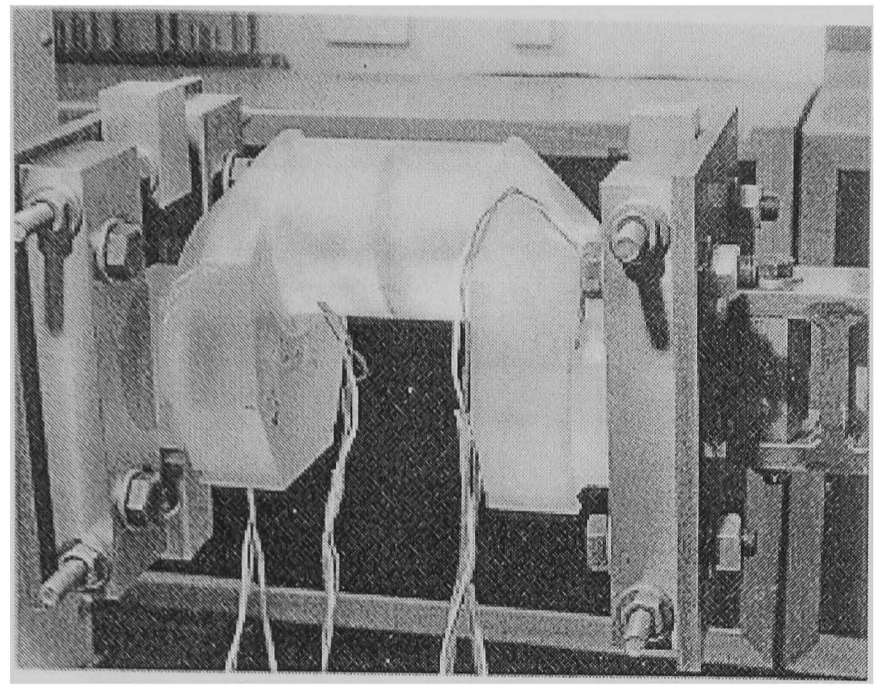

Figure 5.24. Experimental loading arrangement for ERS measurements under pure torsion

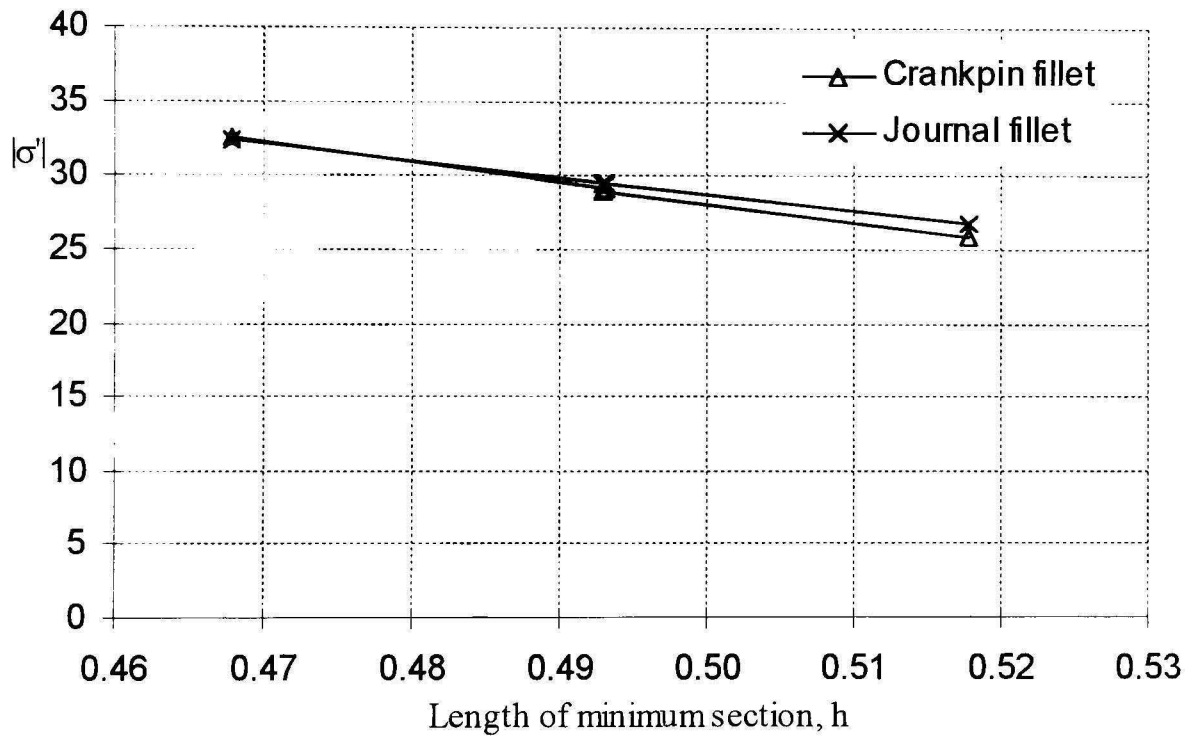

Figure 5.25. Peak fillet stresses under radial bending for various crankpin and journal diameters

(a)

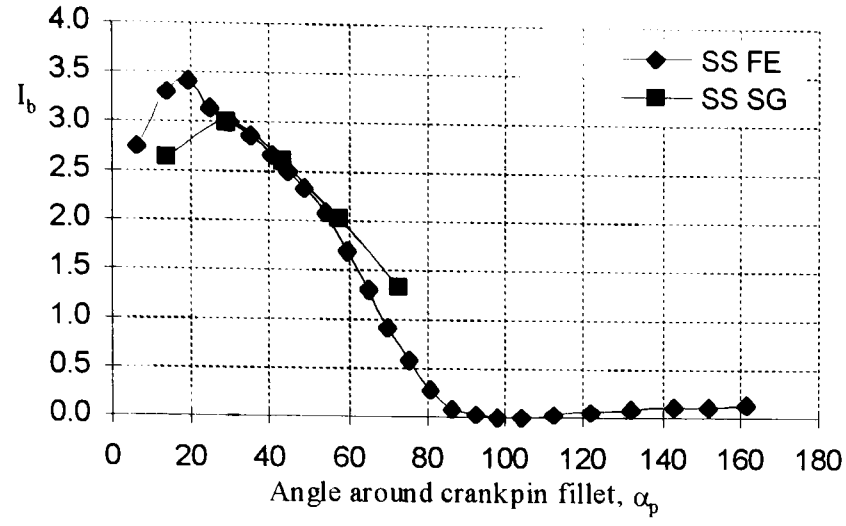

(b)

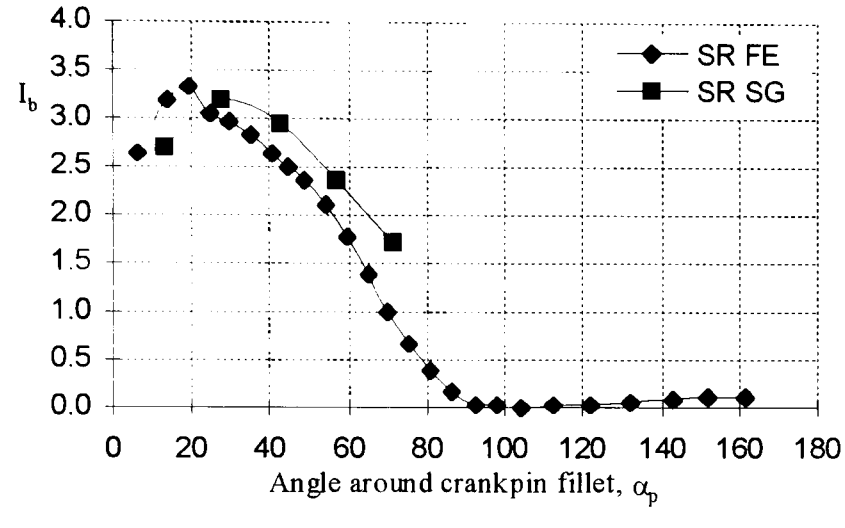

(c)

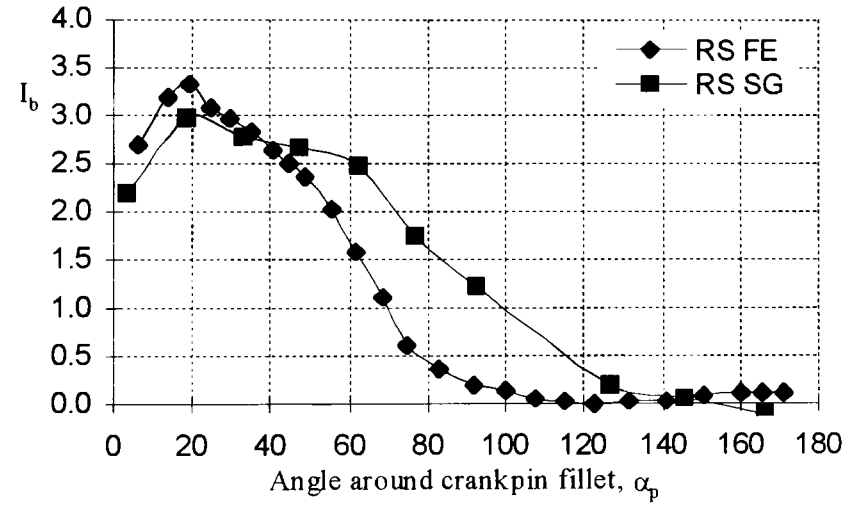

(d)

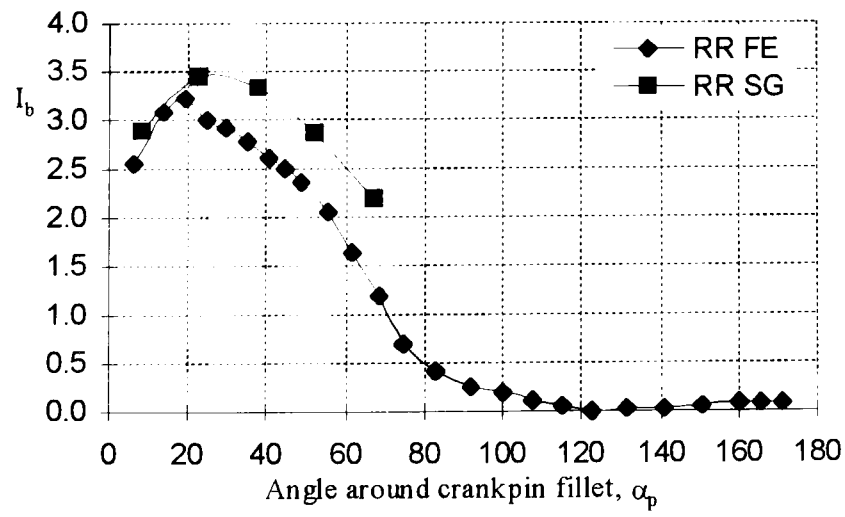

Figure 5.26. Comparison of 3D FE and ERS crankpin fillet data under radial bending

(a)

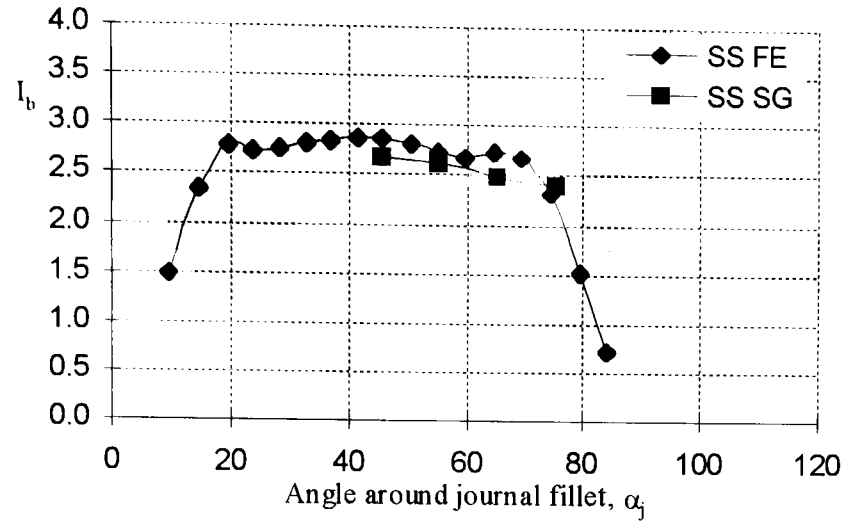

(b)

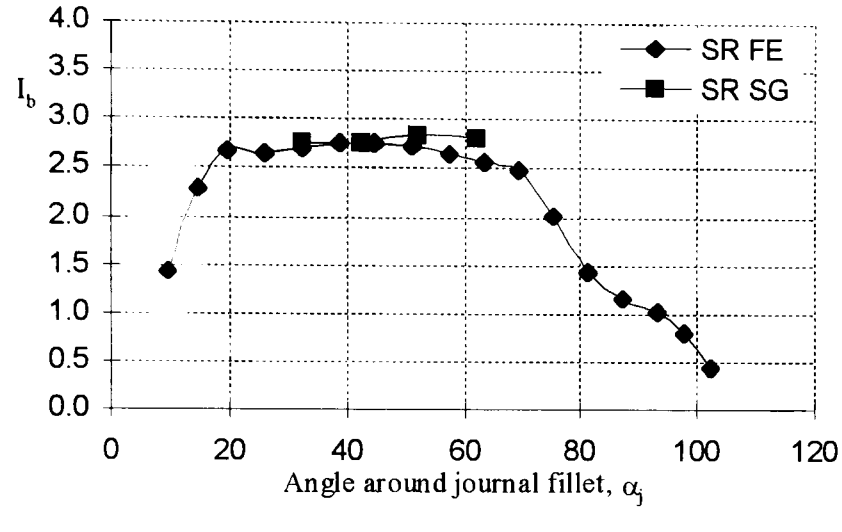

(c)

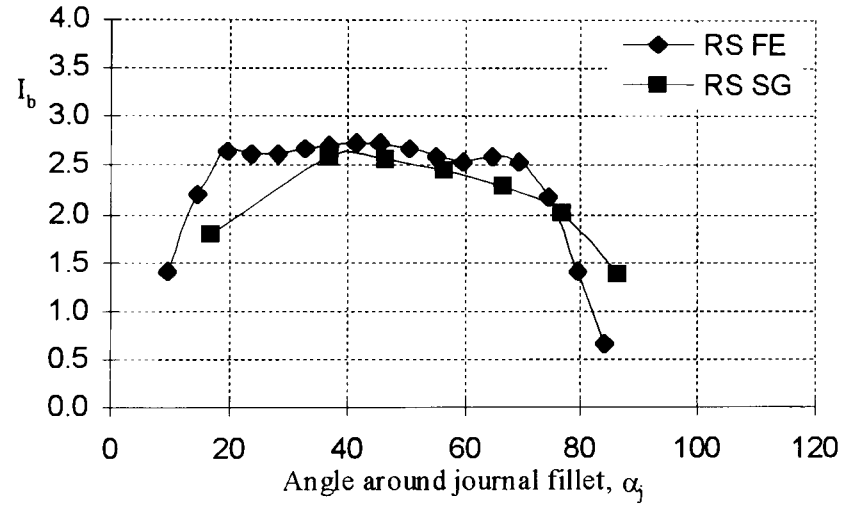

(d)

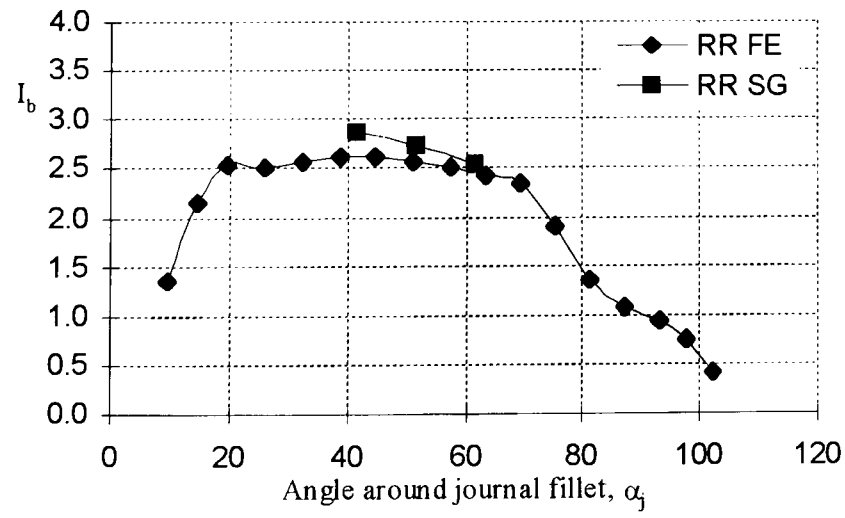

Figure 5.27. Comparison of 3D FE and ERS journal fillet data under radial bending

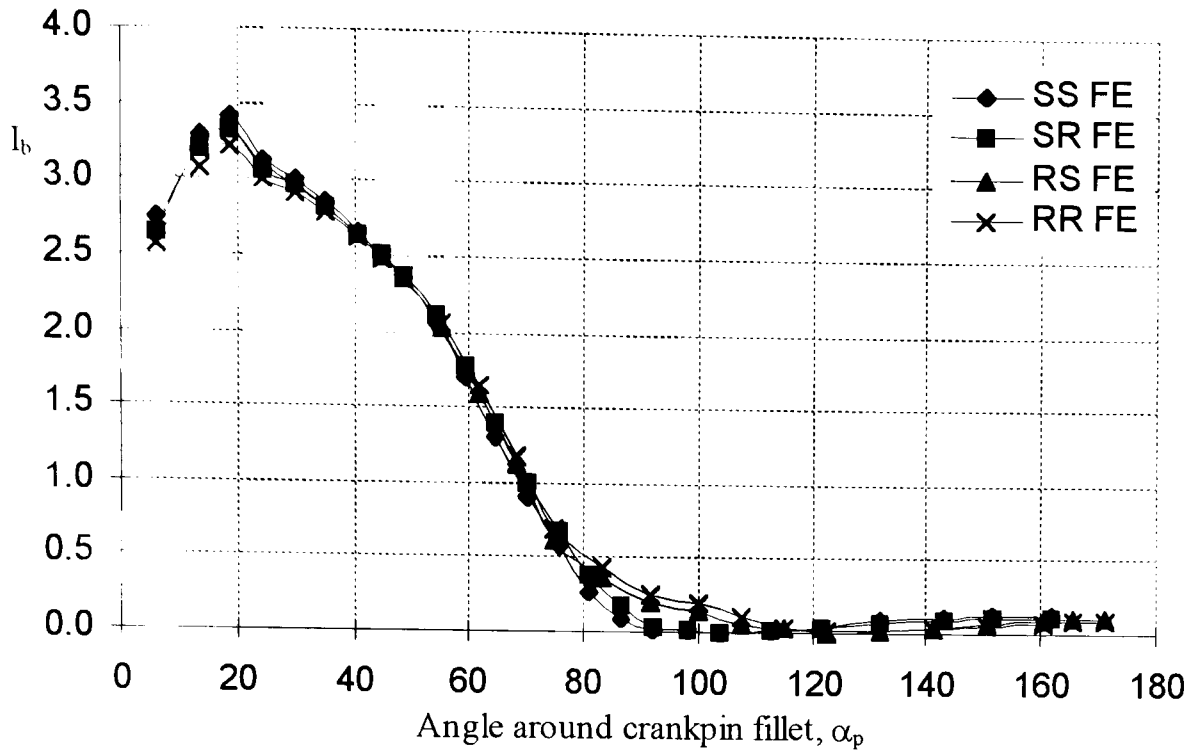

(a) Distribution around crankpin fillet (3D analyses)

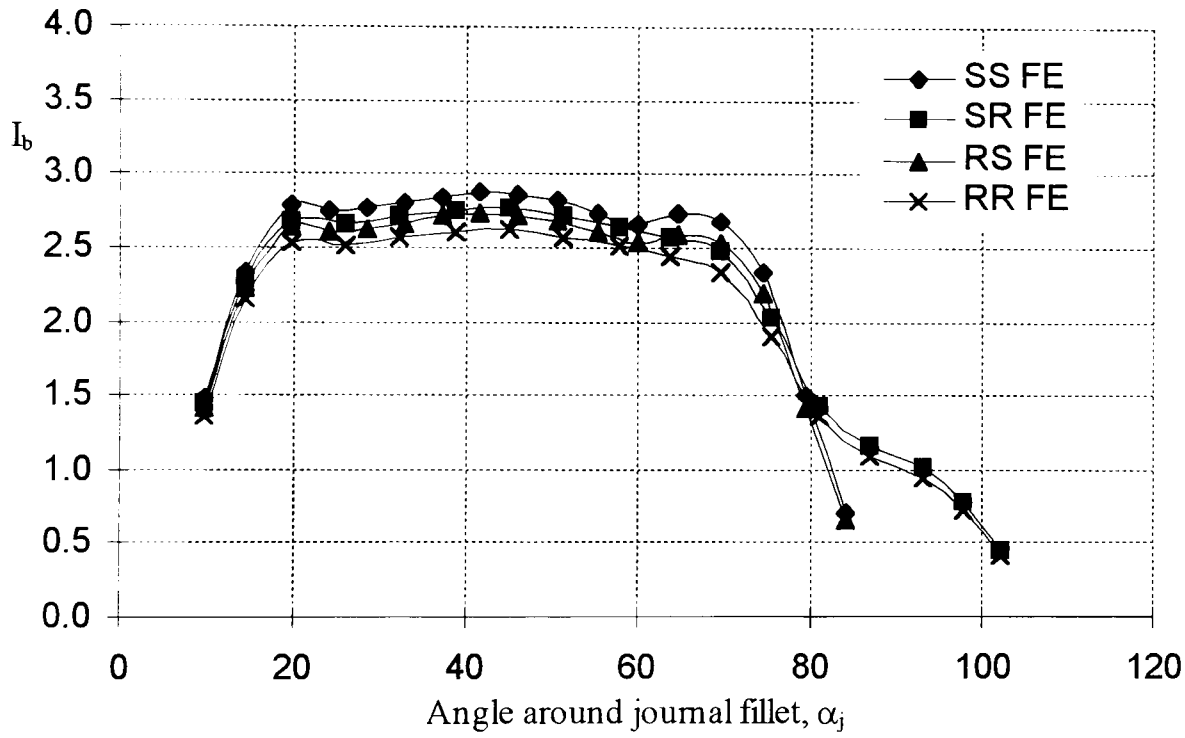

(b) Distribution around journal fillet (3D analyses)

Figure 5.28. 3D FE maximum principal fillet stress distributions under radial bending for various combinations of crankpin and journal diameter

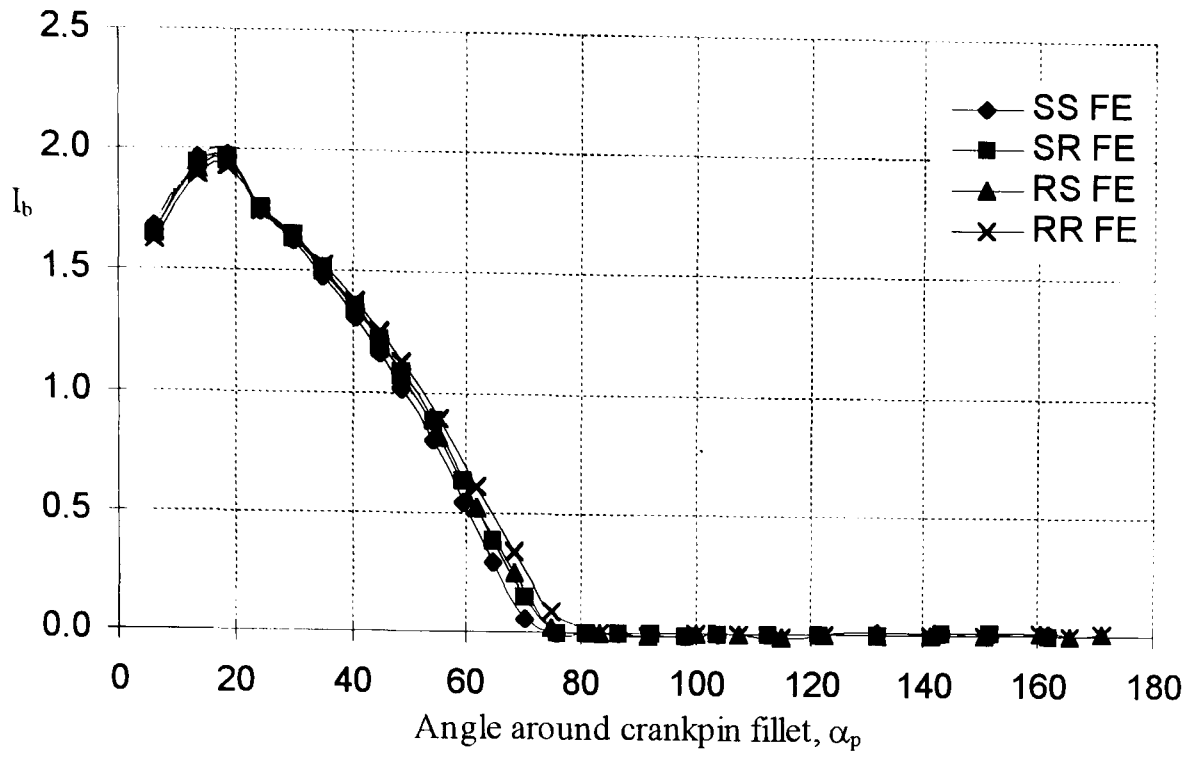

(a) Distribution around crankpin fillet (2D analyses)

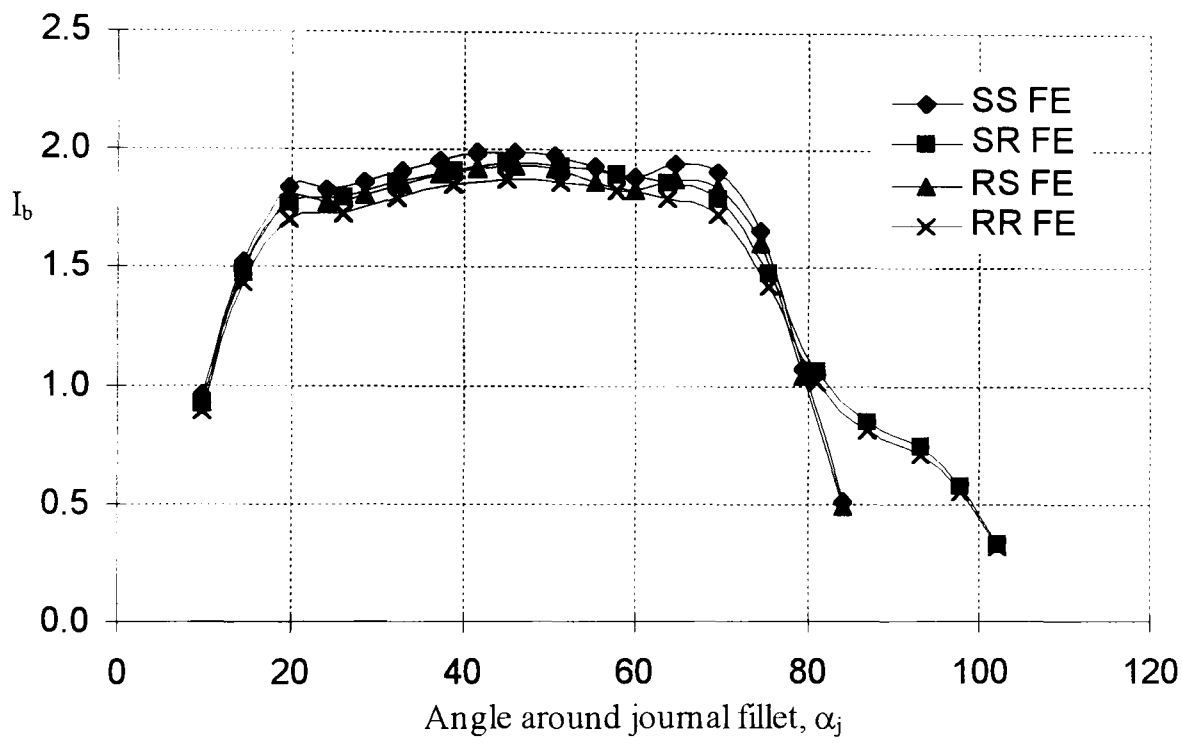

(b) Distribution around journal fillet (2D analyses)

Figure 5.29. 2D FE maximum principal fillet stress distributions under radial bending for various combinations of crankpin and journal diameter

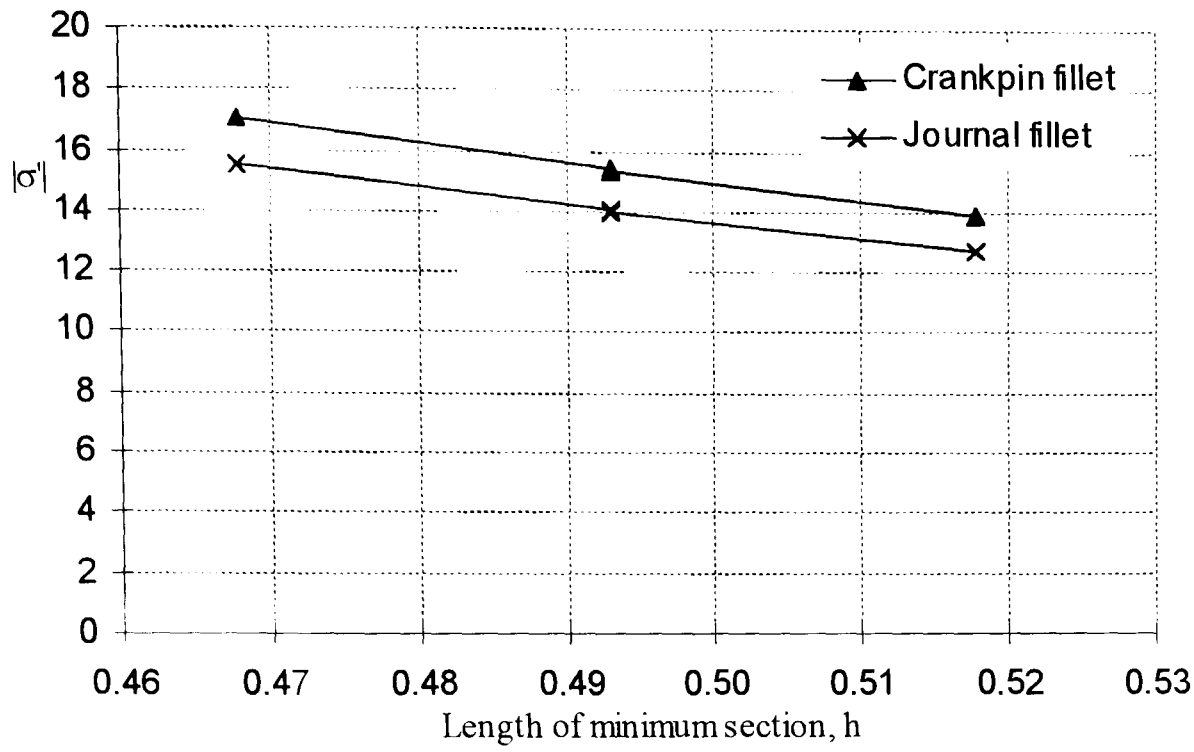

Figure 5.30. Peak fillet stresses under pure bending for various crankpin and journal diameters

(a)

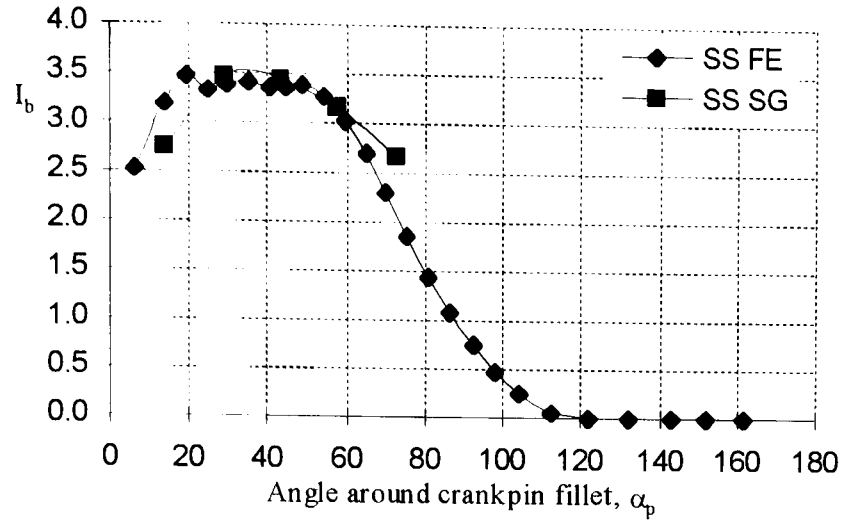

(b)

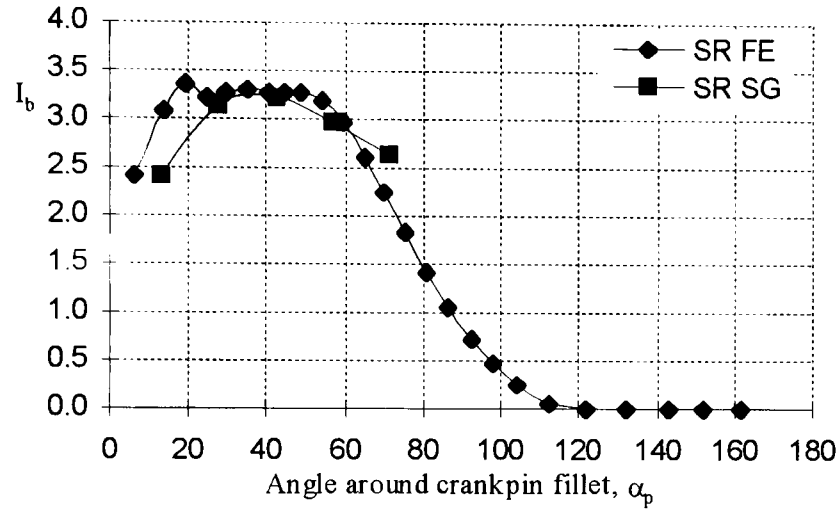

(c)

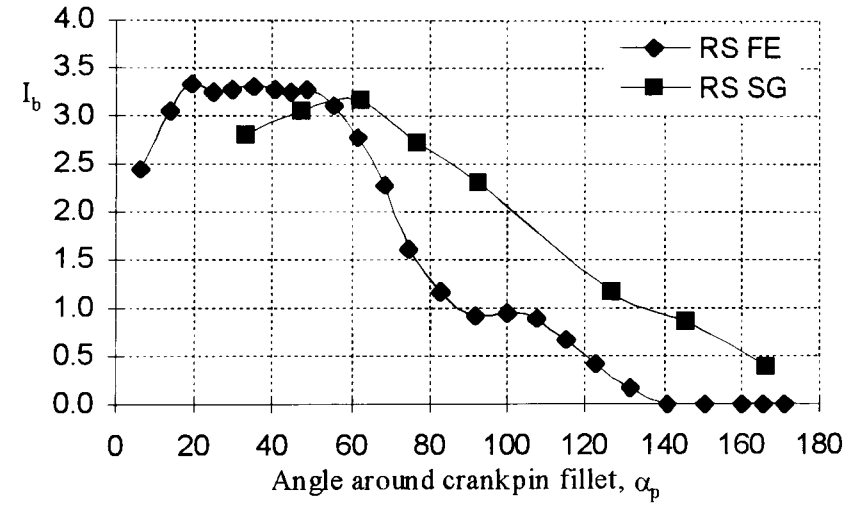

(d)

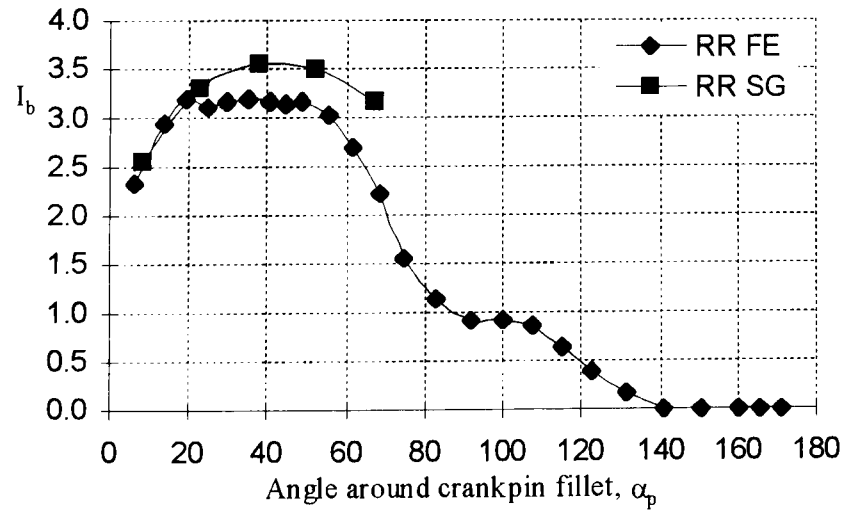

Figure 5.31. Comparison of 3D FE and ERS crankpin fillet data under pure bending

(a)

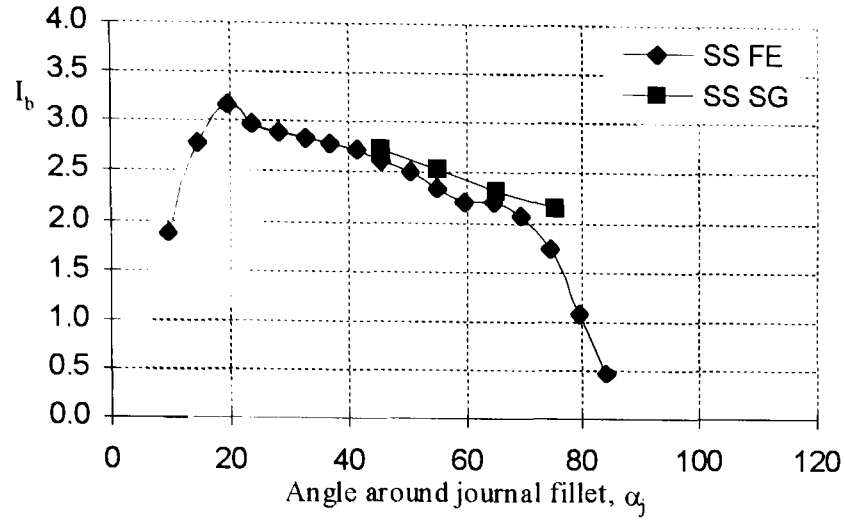

(b)

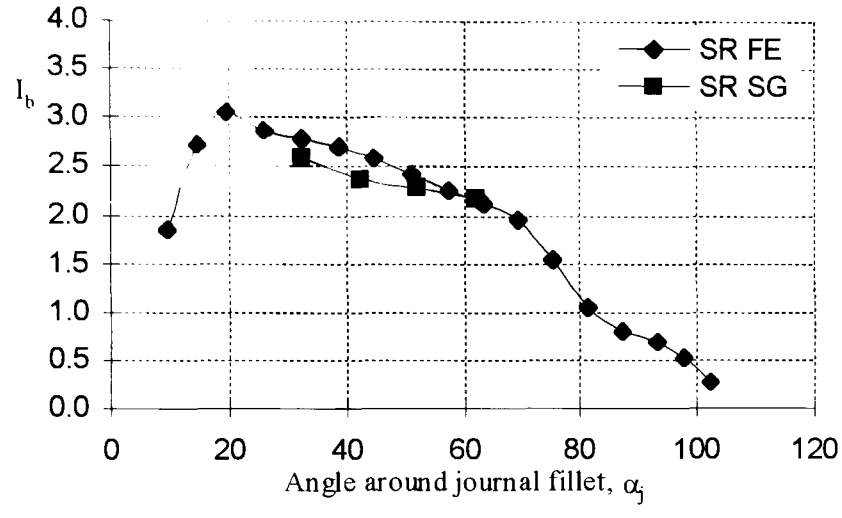

(c)

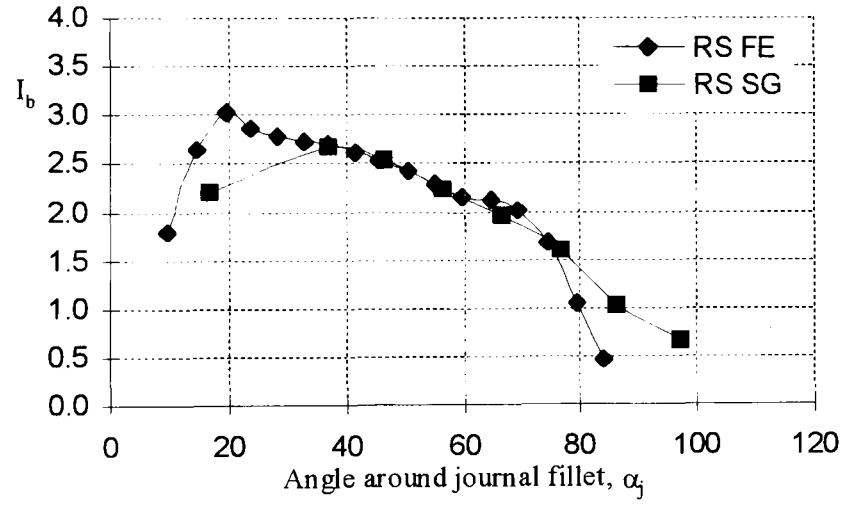

(d)

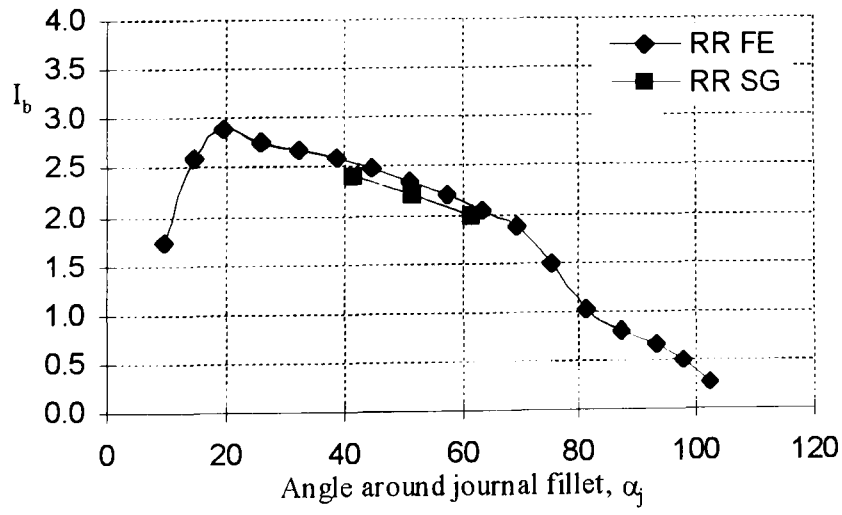

Figure 5.32. Comparison of 3D FE and ERS journal fillet data under pure bending

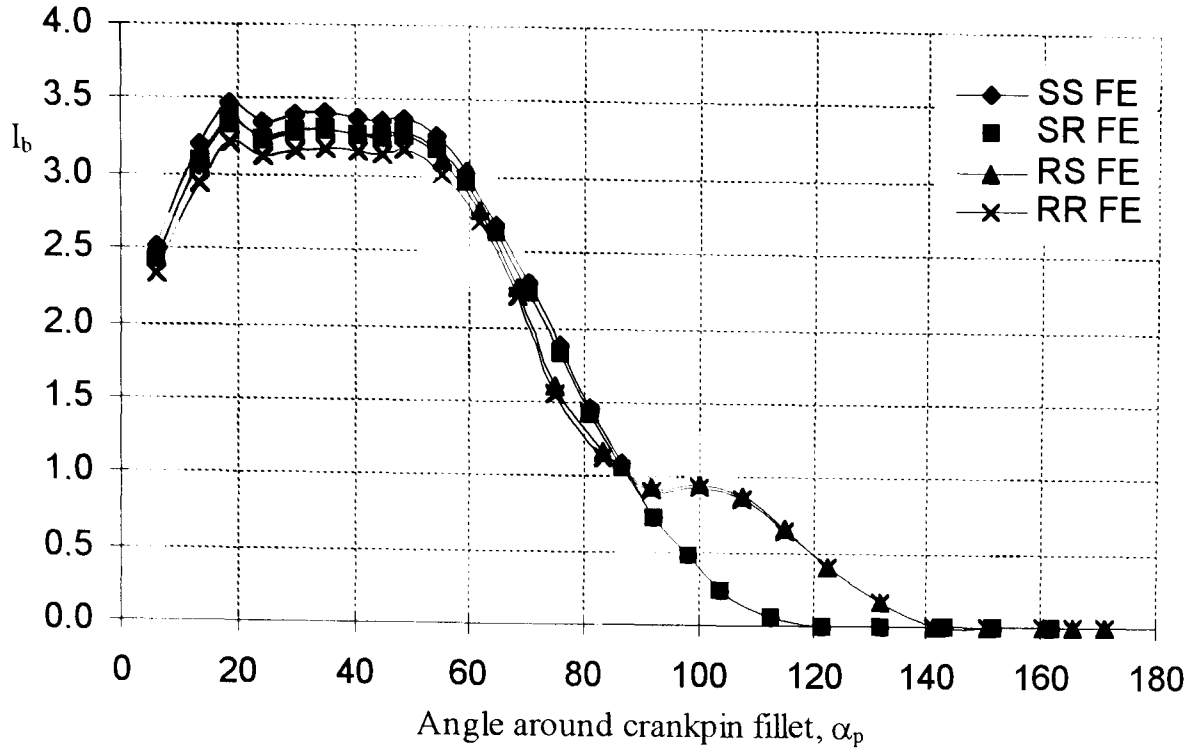

(a) Distribution around crankpin fillet (3D analyses)

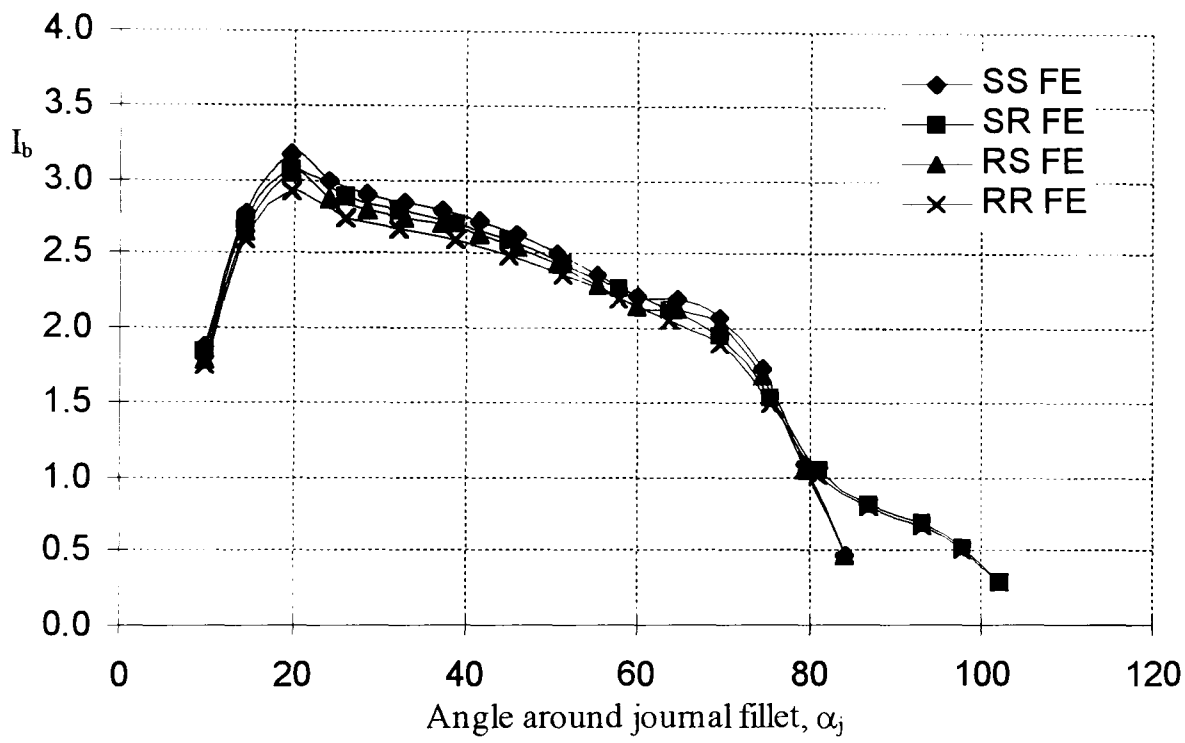

(b) Distribution around journal fillet (3D analyses)

Figure 5.33. 3D FE maximum principal fillet stress distributions under pure bending for various combinations of crankpin and journal diameter

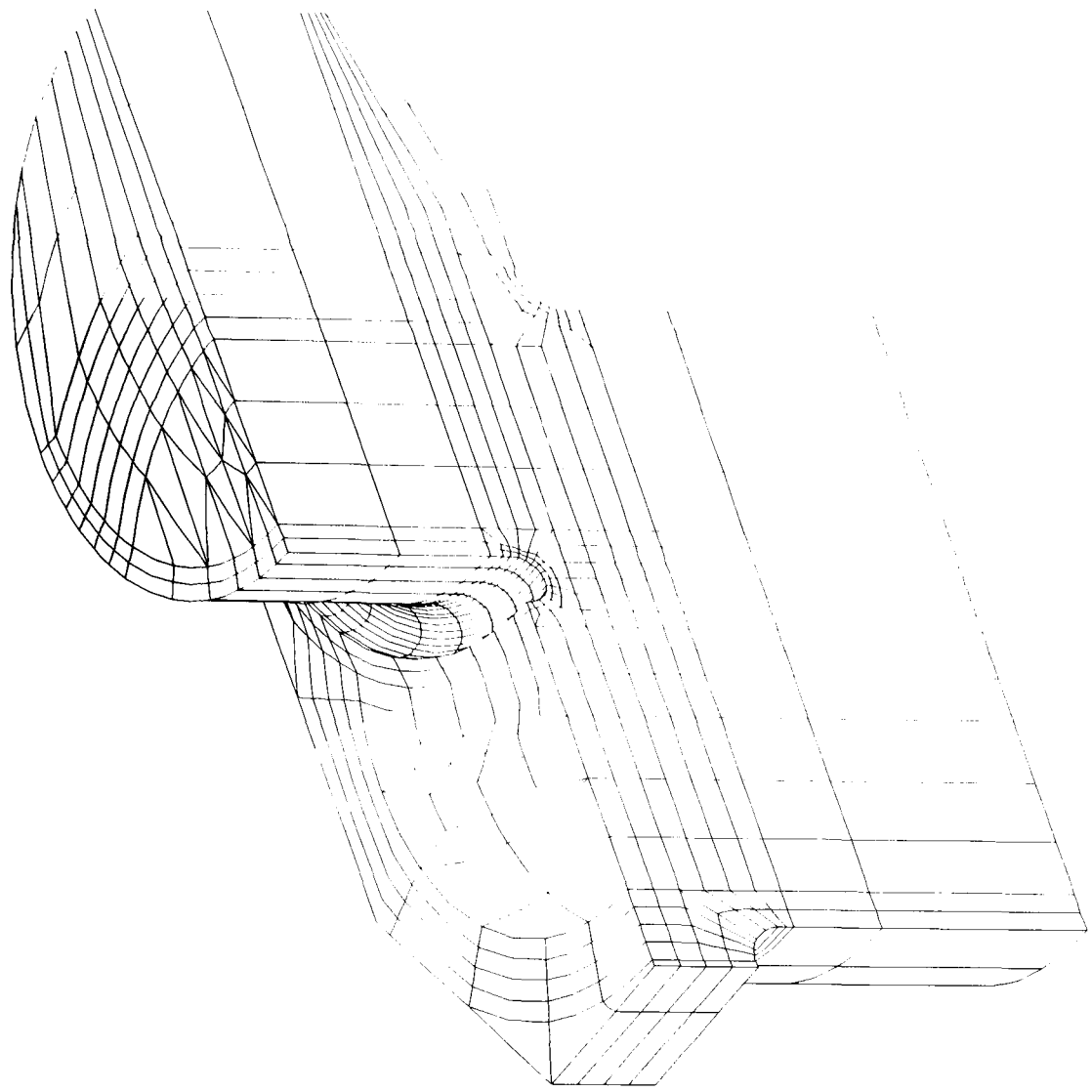

Figure 5.34. Nodes in crankpin fillet positioned on several constant θ_p planes

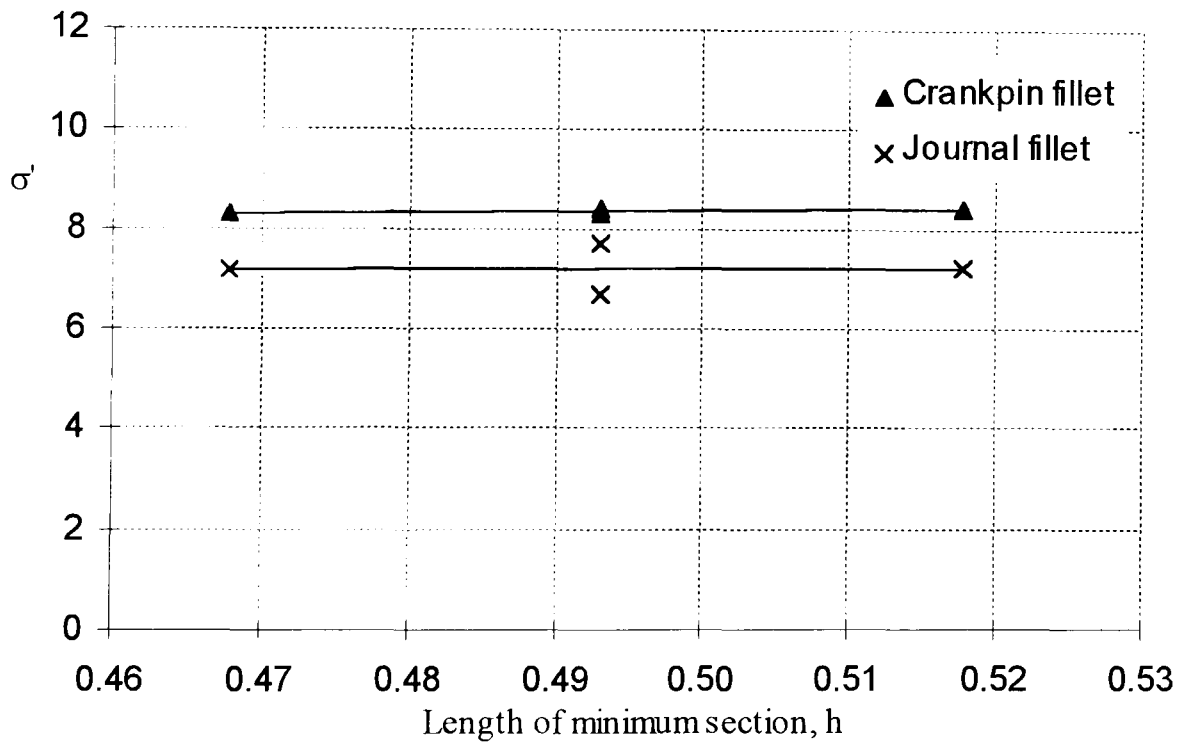

Figure 5.35. Peak fillet stresses under pure torsion for various crankpin and journal diameters

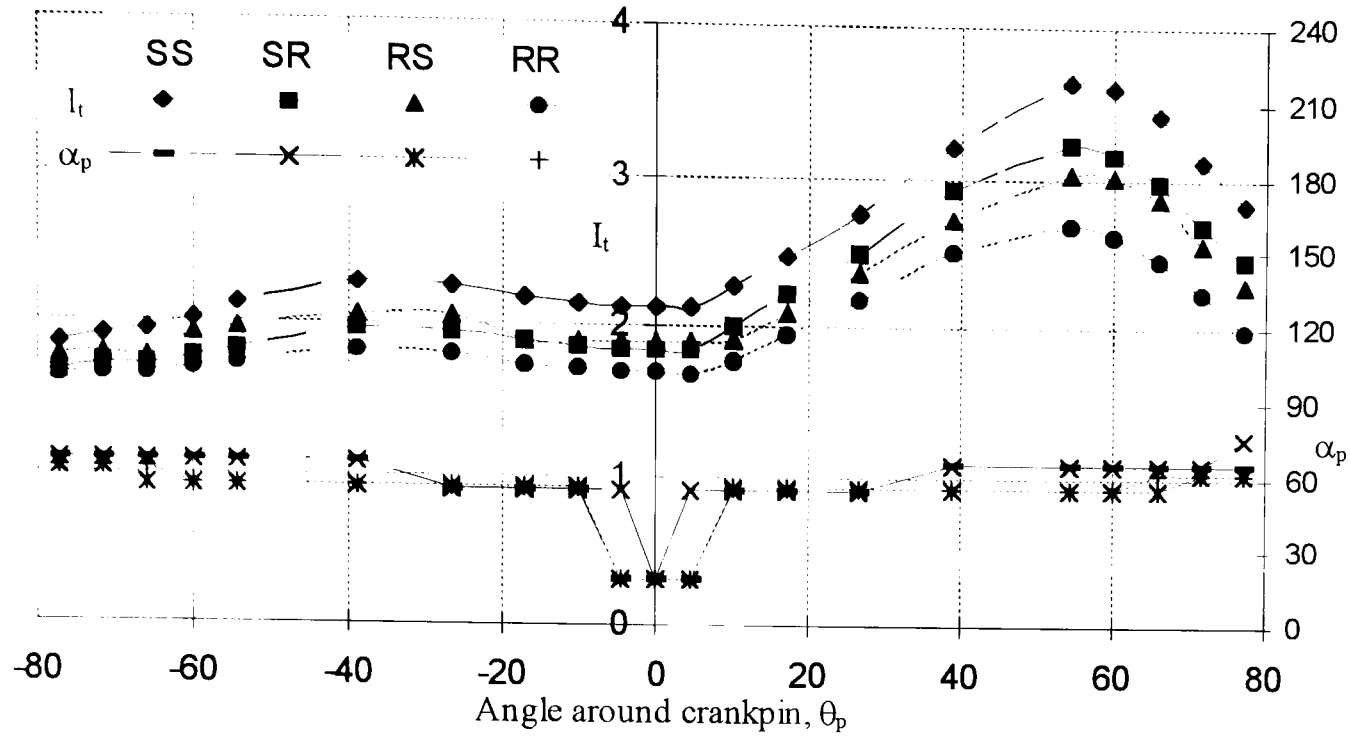

(a) Distribution around crankpin (3D analyses)

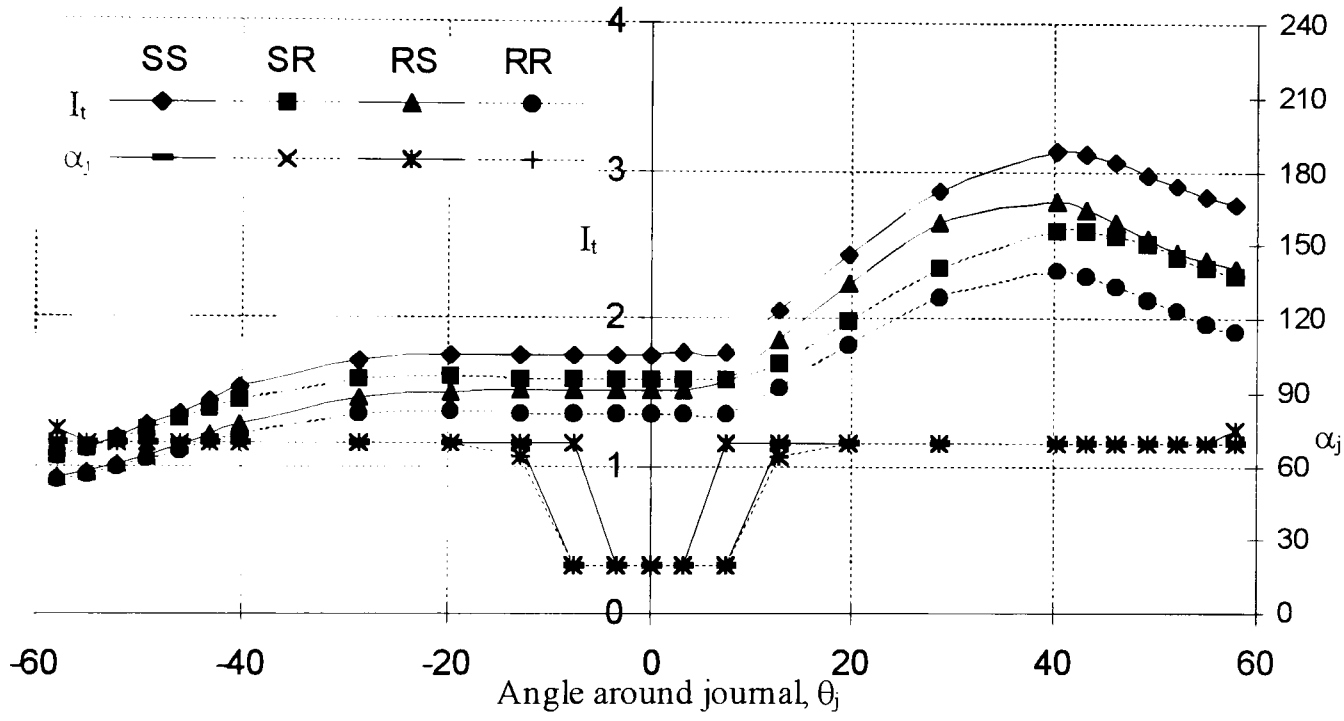

(b) Distribution around journal (3D analyses)

Figure 5.36. 3D FE maximum principal fillet stress distributions under pure torsion for various combinations of crankpin and journal diameter

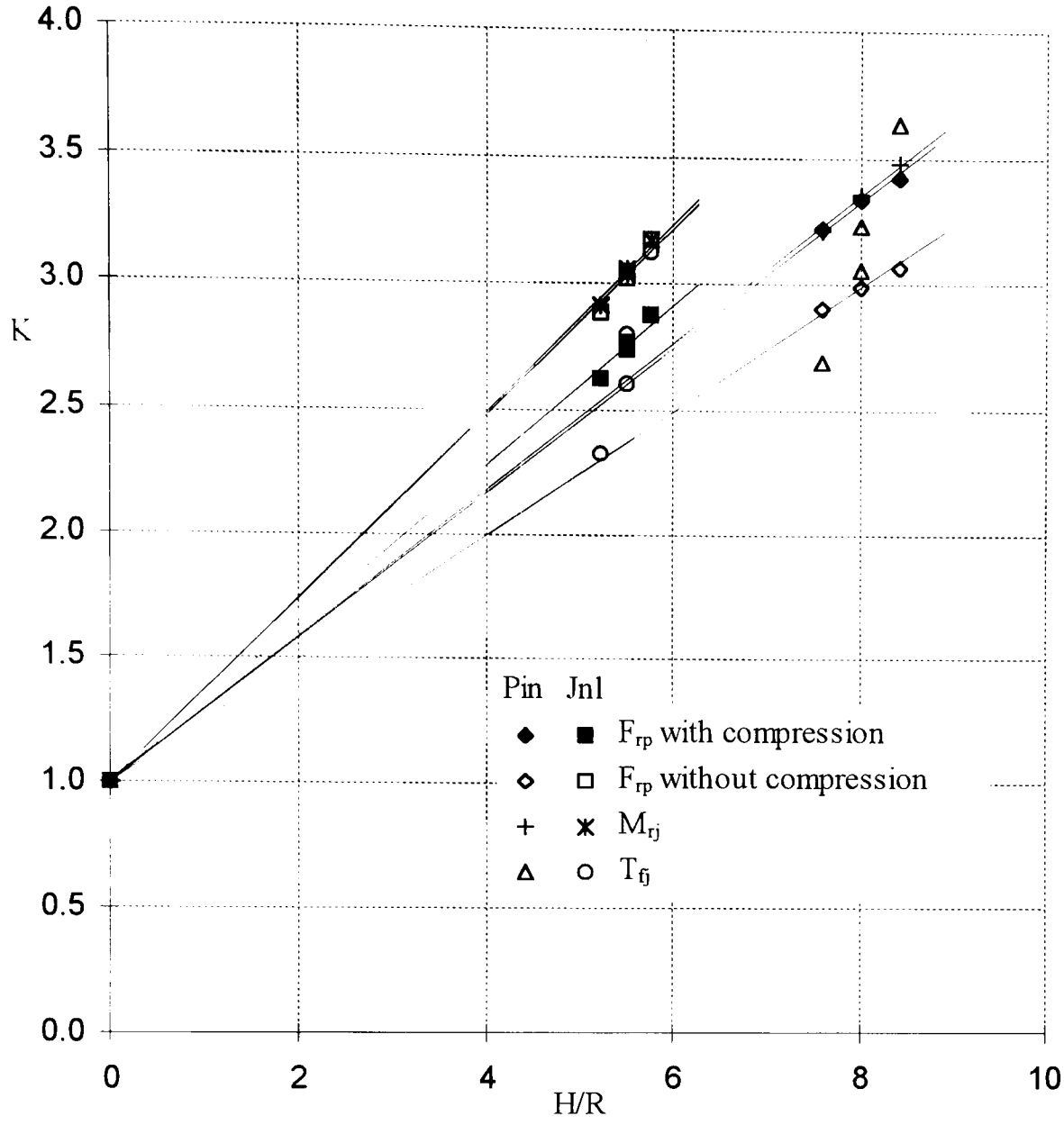

Figure 5.37. The relationship between K and H/R for crankshaft bending and torsion

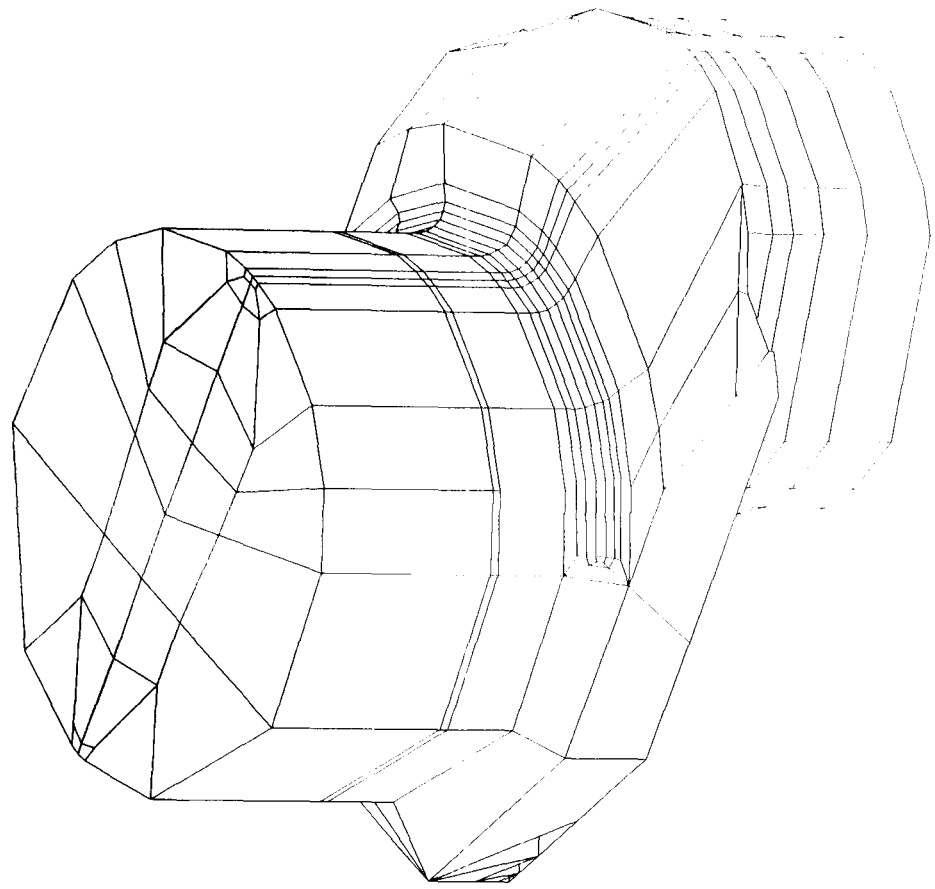

Figure 5.38. A typical BE mesh used for investigations into crankpin and journal overlap

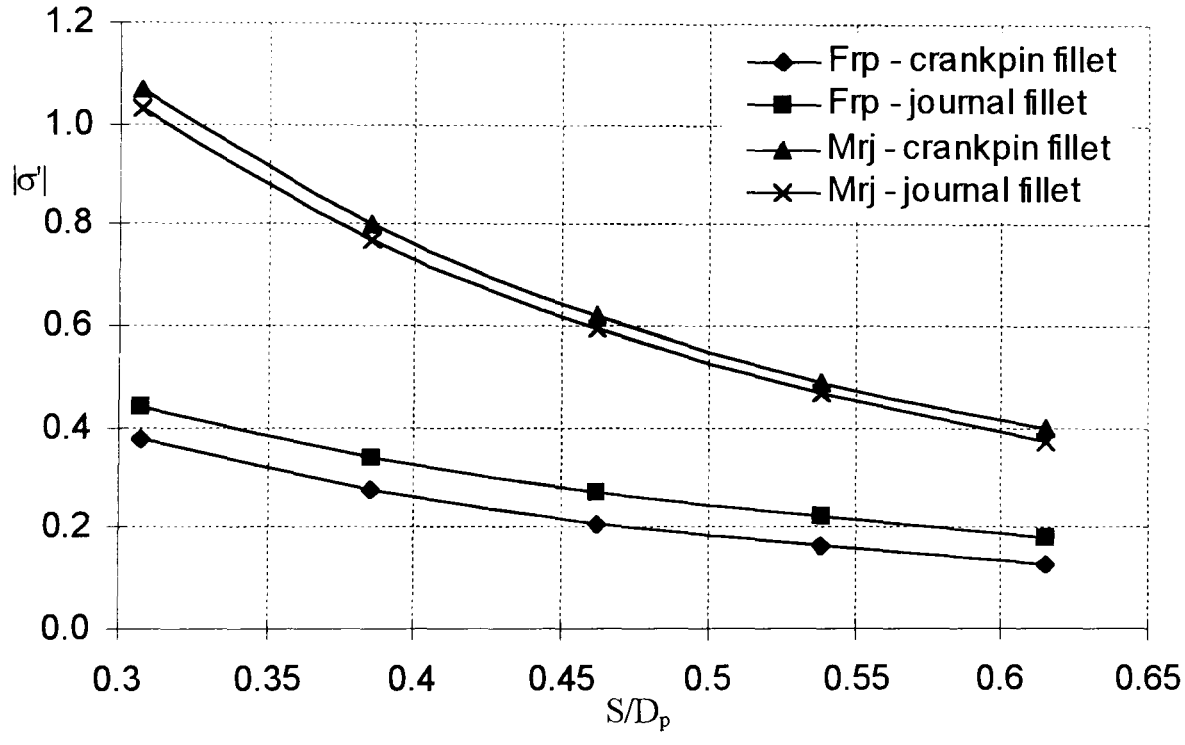

Figure 5.39. Peak principal fillet stresses under radial and pure bending for a range of crankpin and journal overlap (3D analyses)

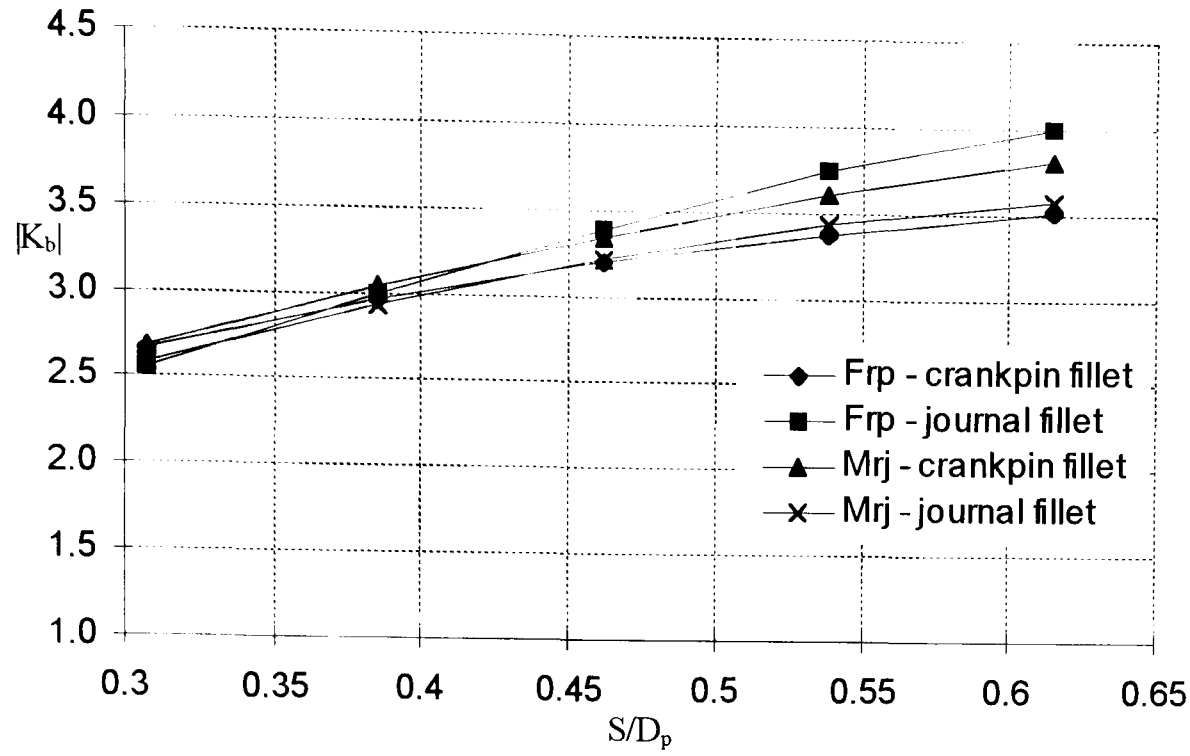

Figure 5.40. Stress concentration factors under radial and pure bending for a range of crankpin and journal overlap (3D analyses), based on the H × C nominal stress

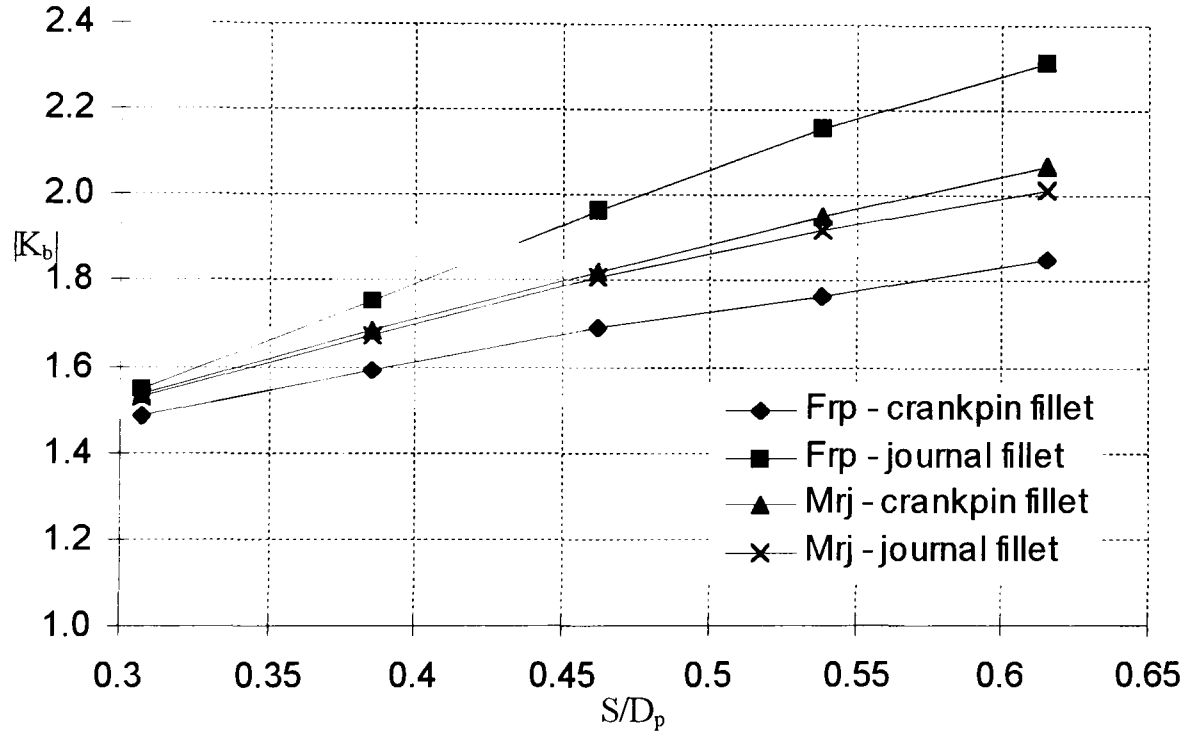

Figure 5.41. Stress concentration factors under radial and pure bending for a range of crankpin and journal overlap (3D analyses), based on the slanted eye-shape nominal stress

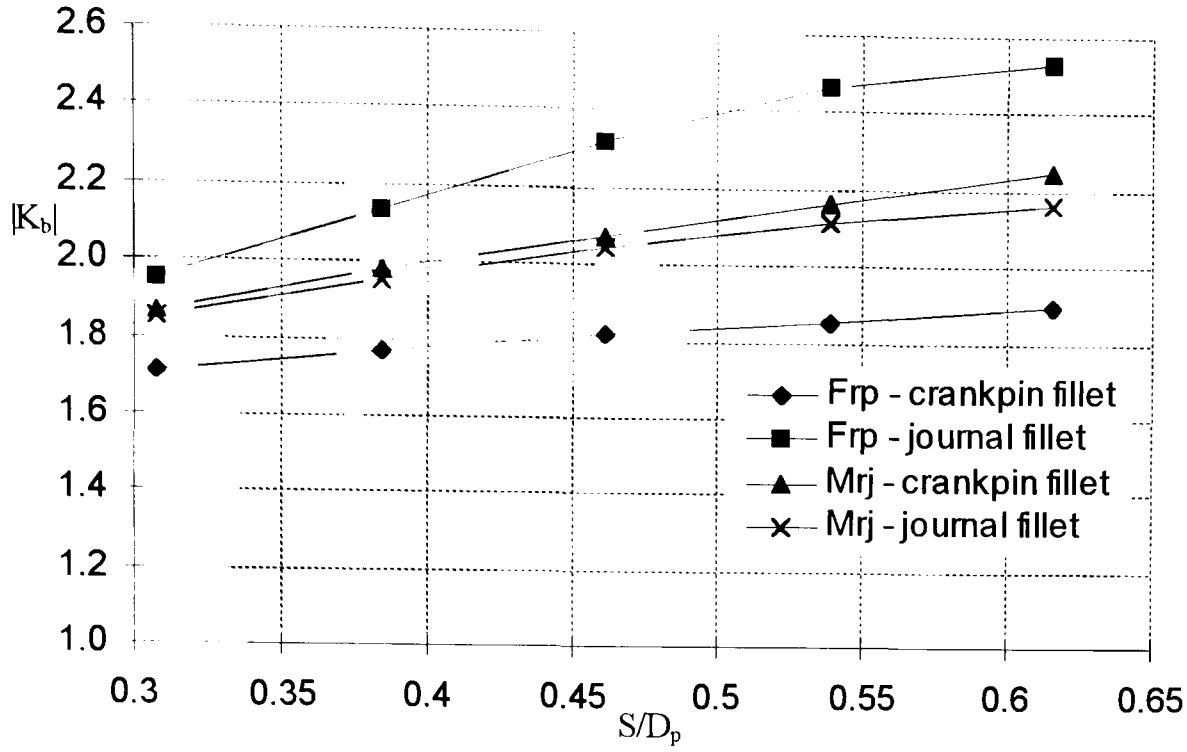

Figure 5.42. Stress concentration factors under radial and pure bending for a range of crankpin and journal overlap (2D analyses), based on the H × C nominal stress

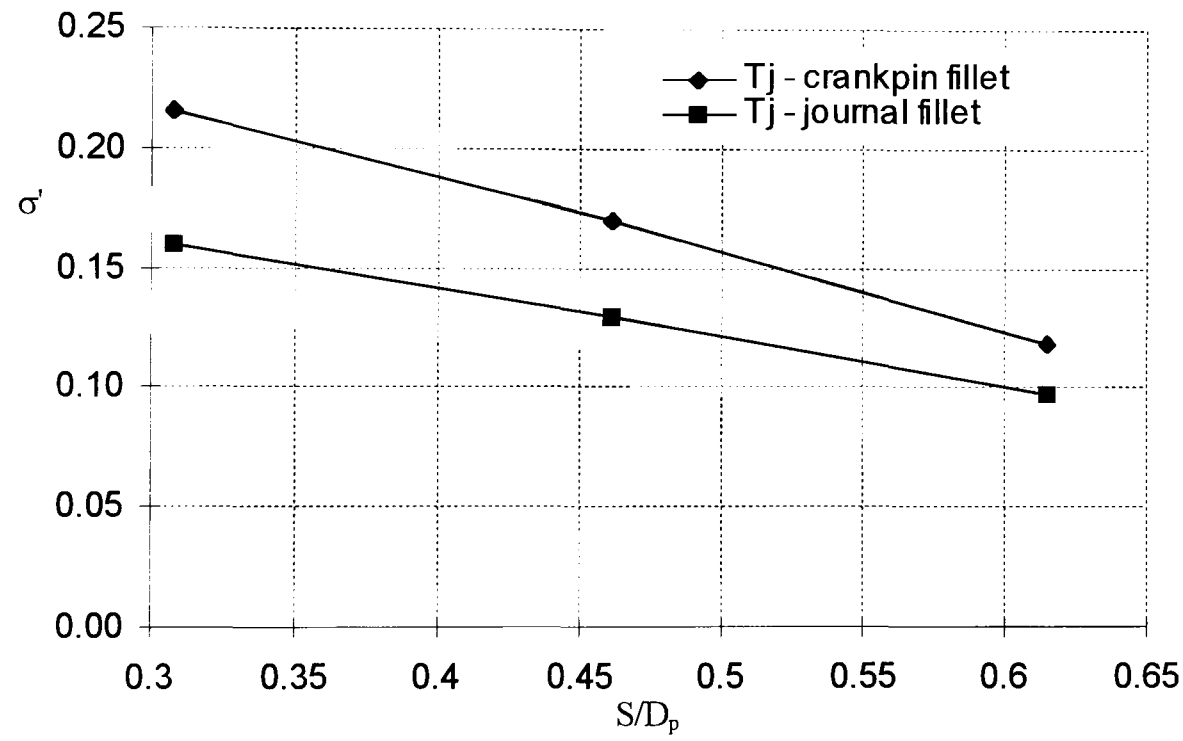

Figure 5.43. Peak principal fillet stresses under pure torsion for a range of crankpin and journal overlap (3D analyses)

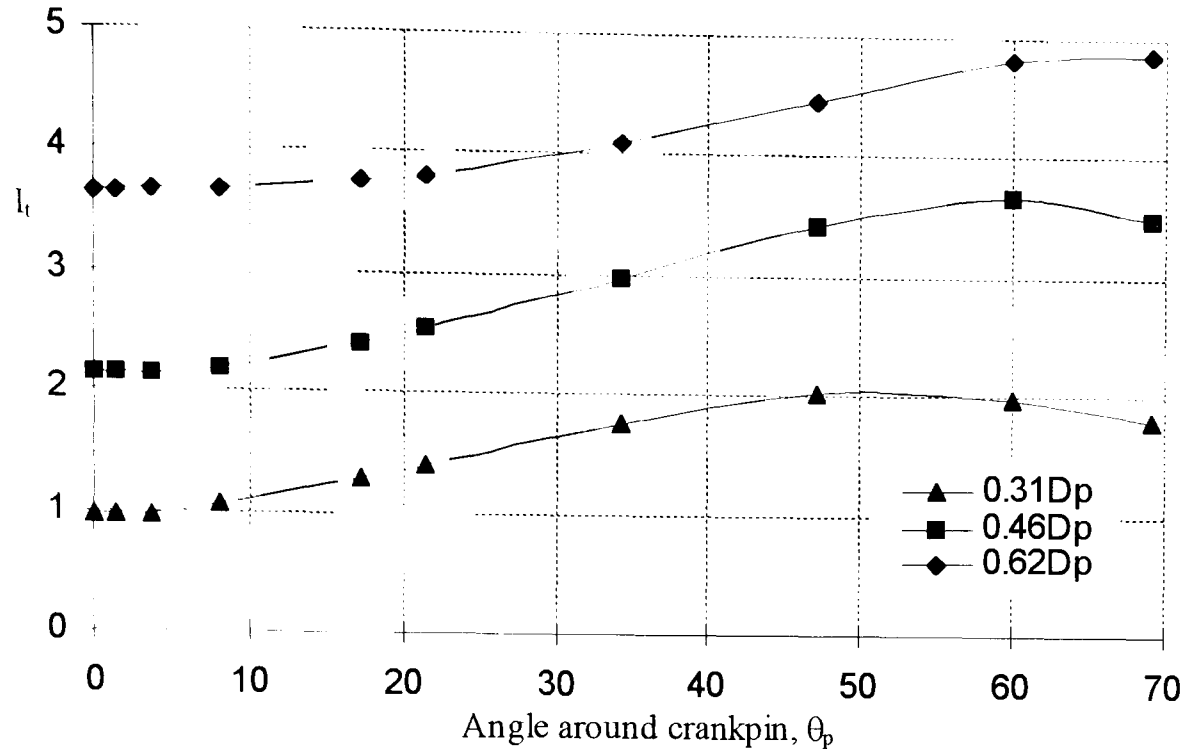

(a) Distribution around crankpin (3D analyses)

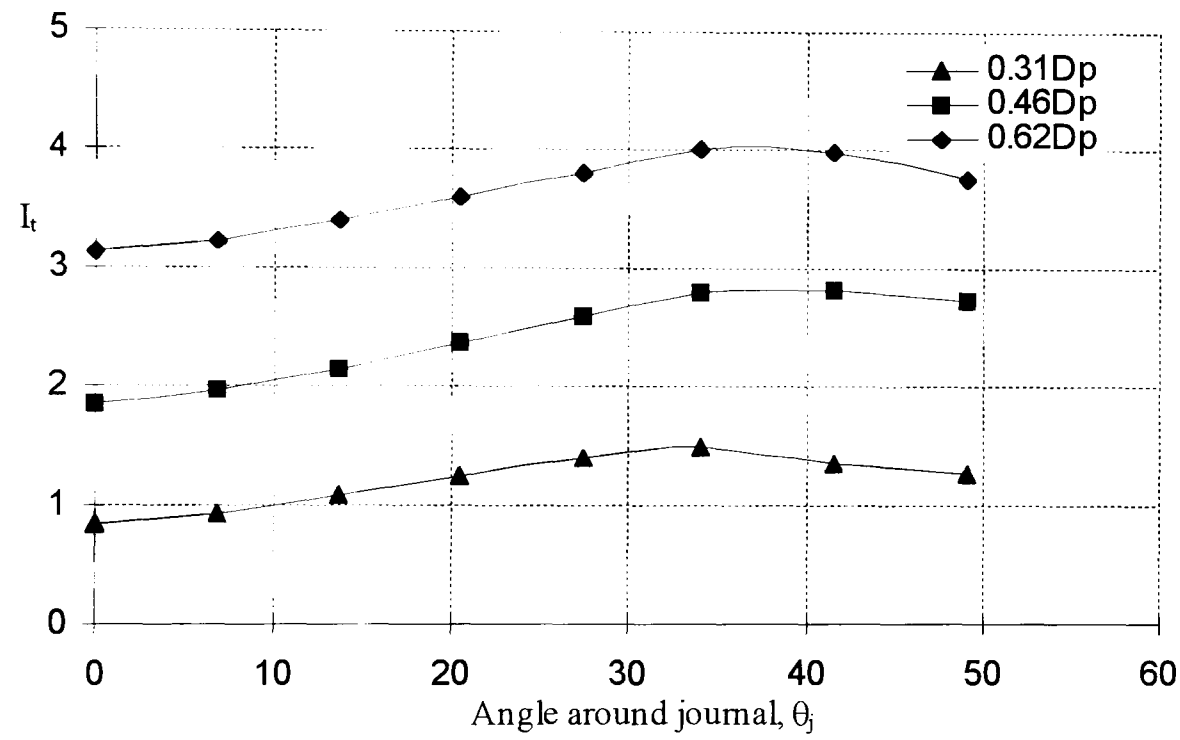

(b) Distribution around journal (3D analyses)

Figure 5.44. Maximum principal stress indices due to torsion for three values of crankpin and journal overlap

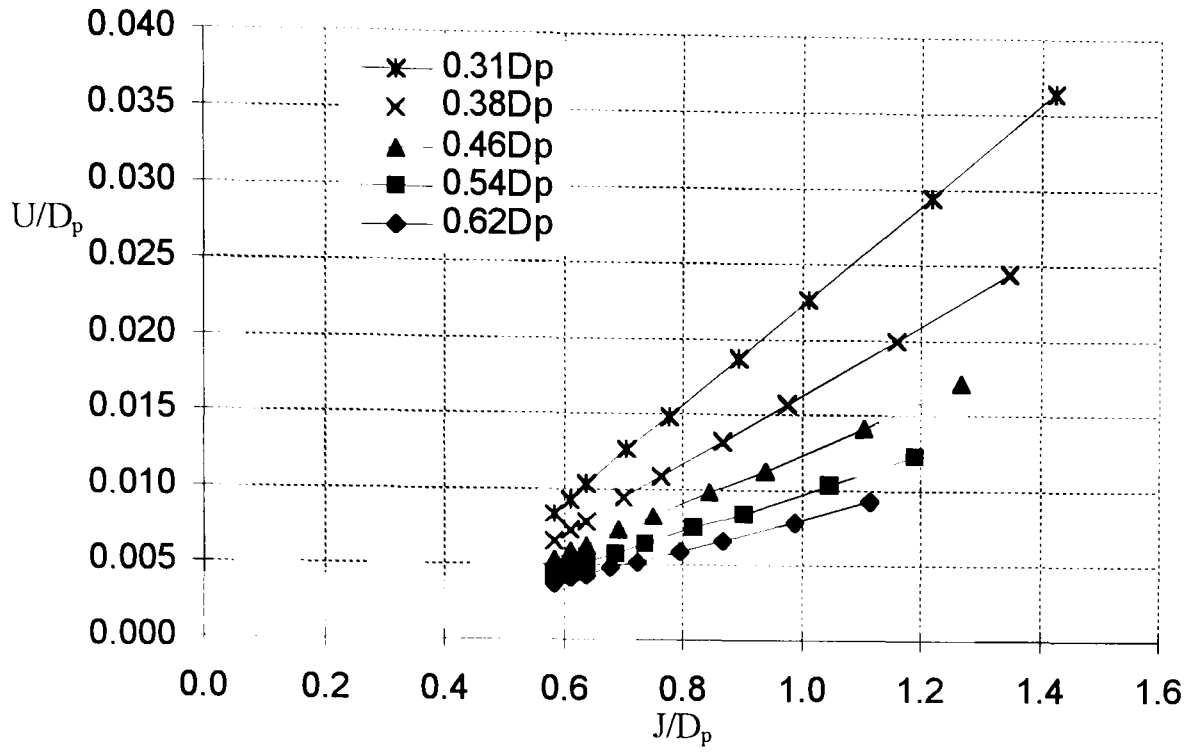

(a) Radial bending

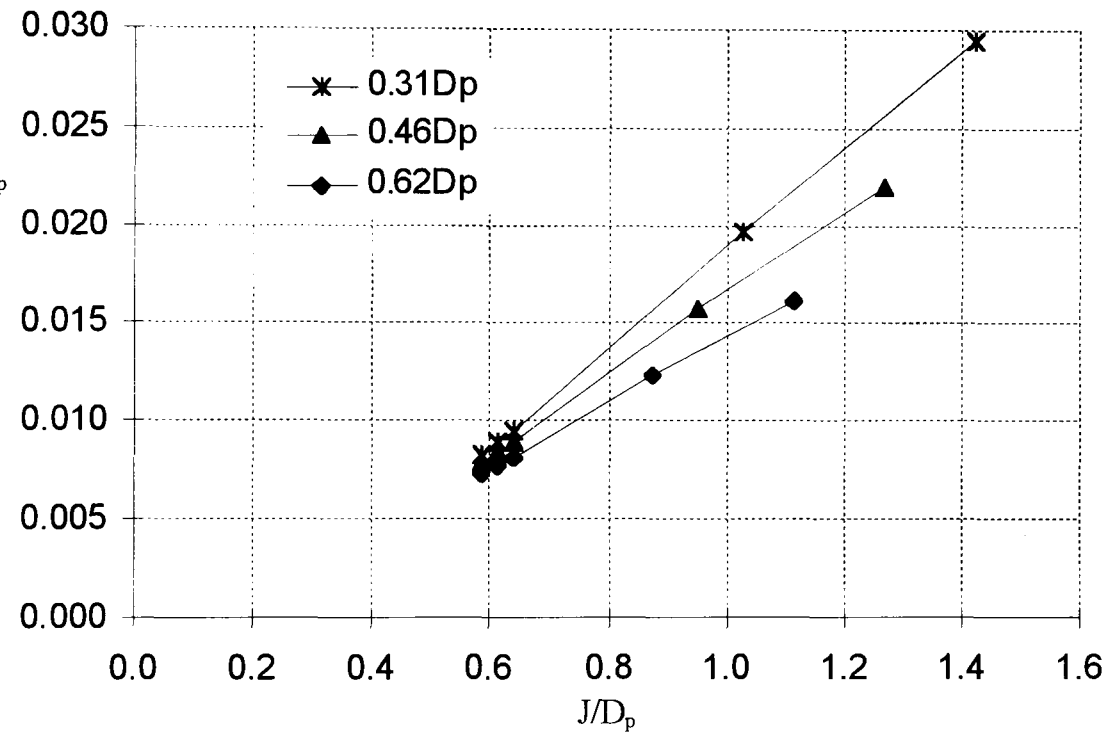

(b) Pure torsion

Figure 5.45. Web deformation due to radial bending and pure torsion for a range of crankpin and journal overlap values

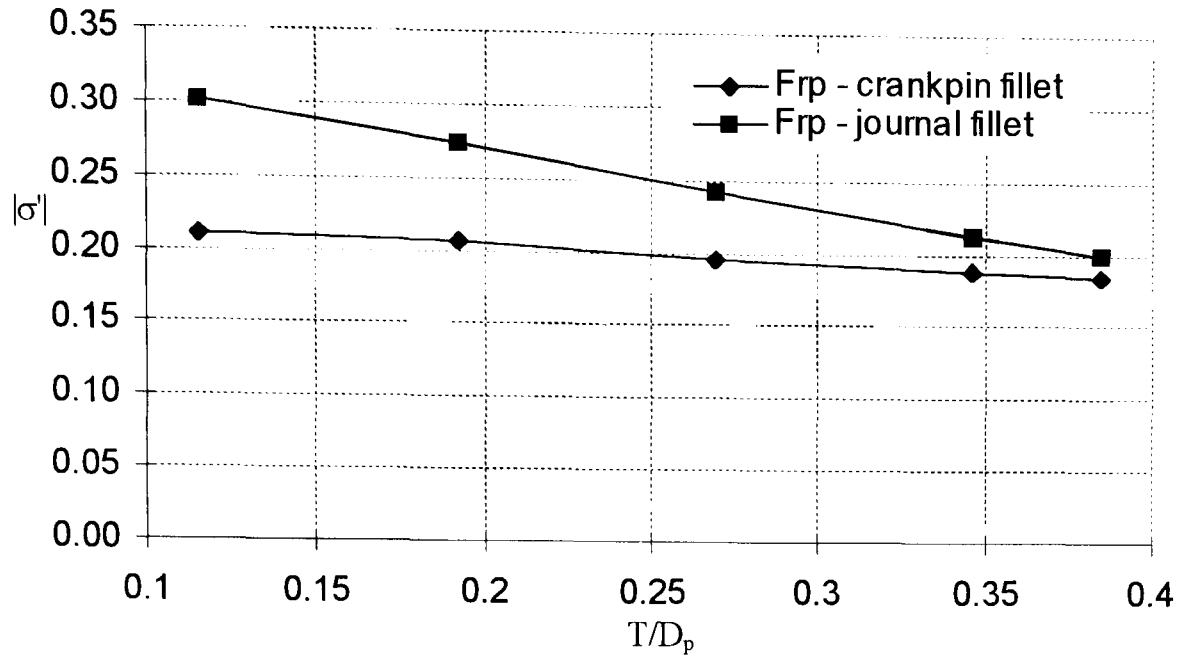

Figure 5.46. Peak principal fillet stresses due to radial bending for a range of web thickness (3D analyses)

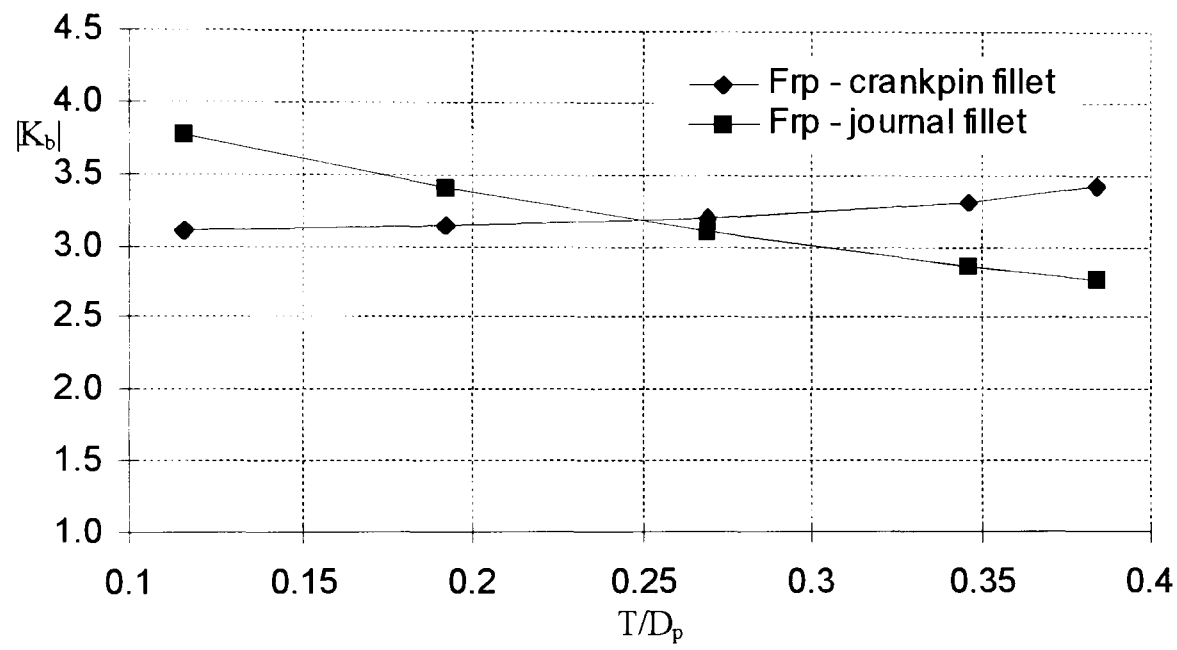

Figure 5.47. Stress concentration factors due to radial bending for a range of web thickness (3D analyses)

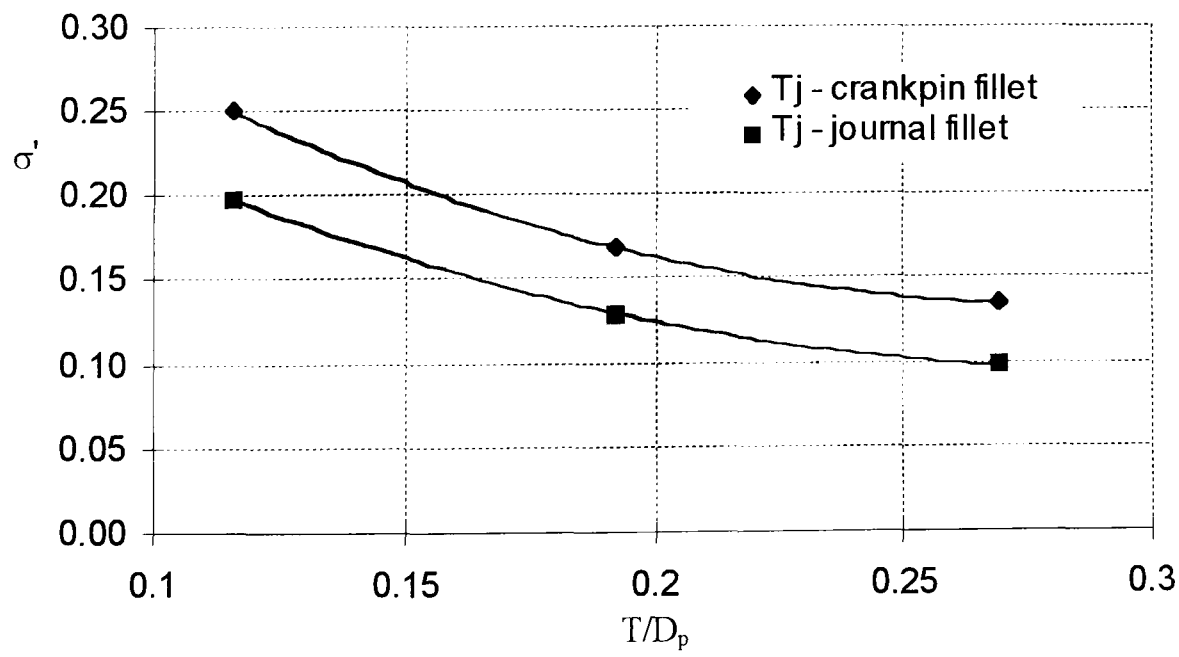

Figure 5.48. Peak principal fillet stresses due to pure torsion for a range of web thickness (3D analyses)

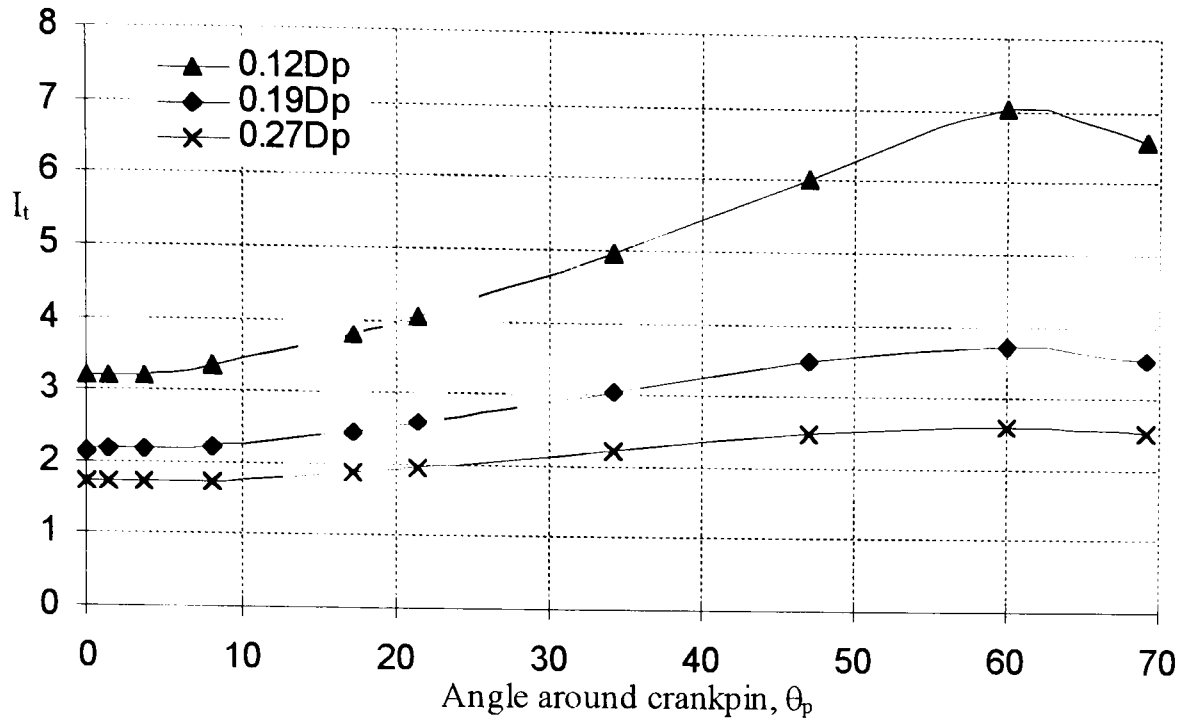

(a) Distribution around crankpin (3D analyses)

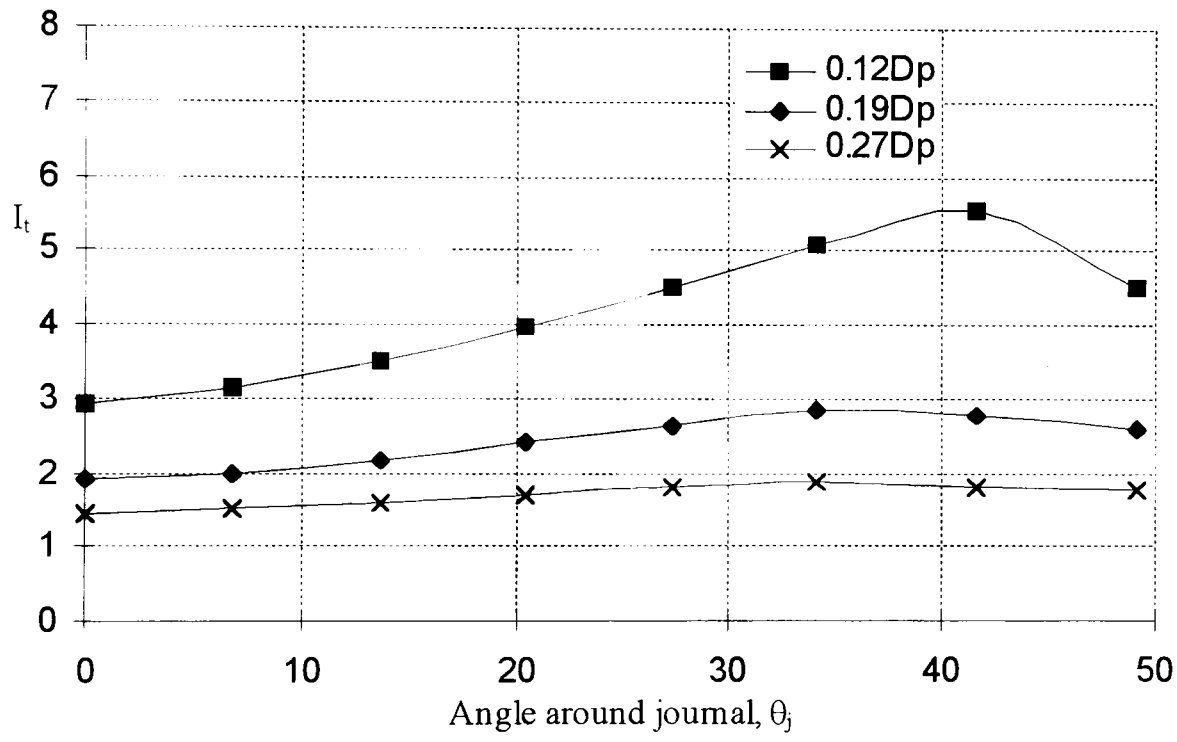

(b) Distribution around journal (3D analyses)

Figure 5.49. Maximum principal fillet stress indices due to torsion for three values of web thickness

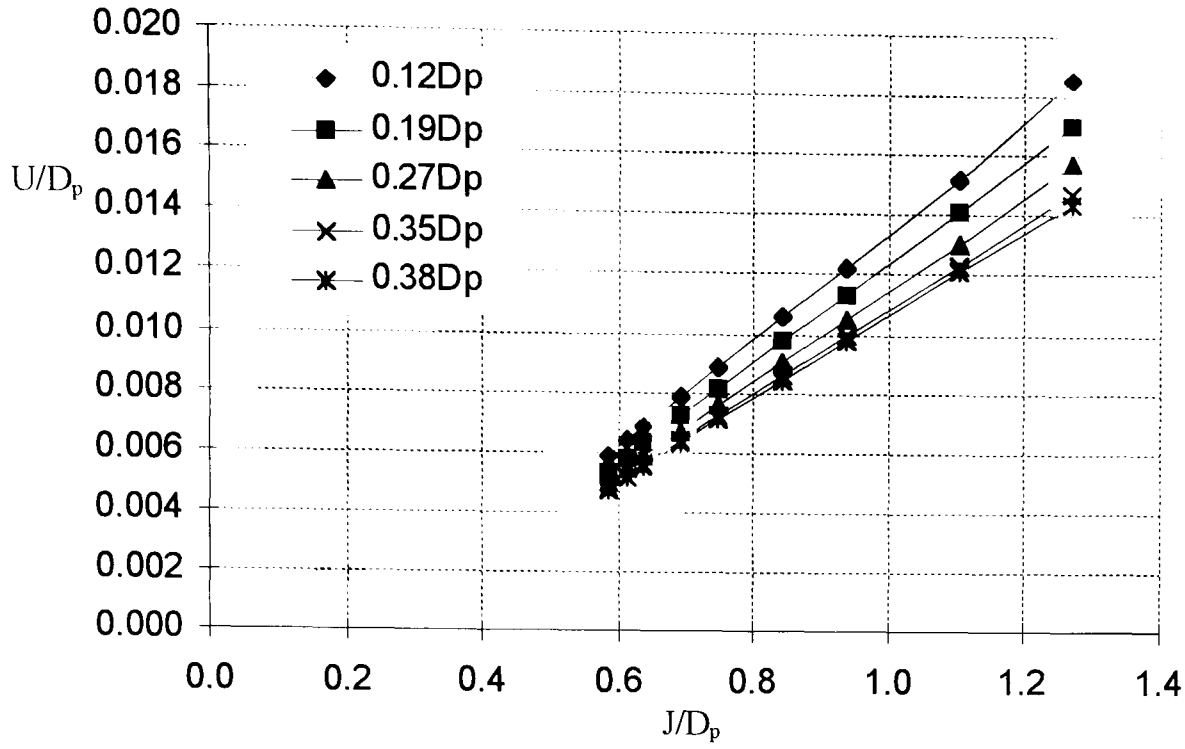

(a) Radial bending

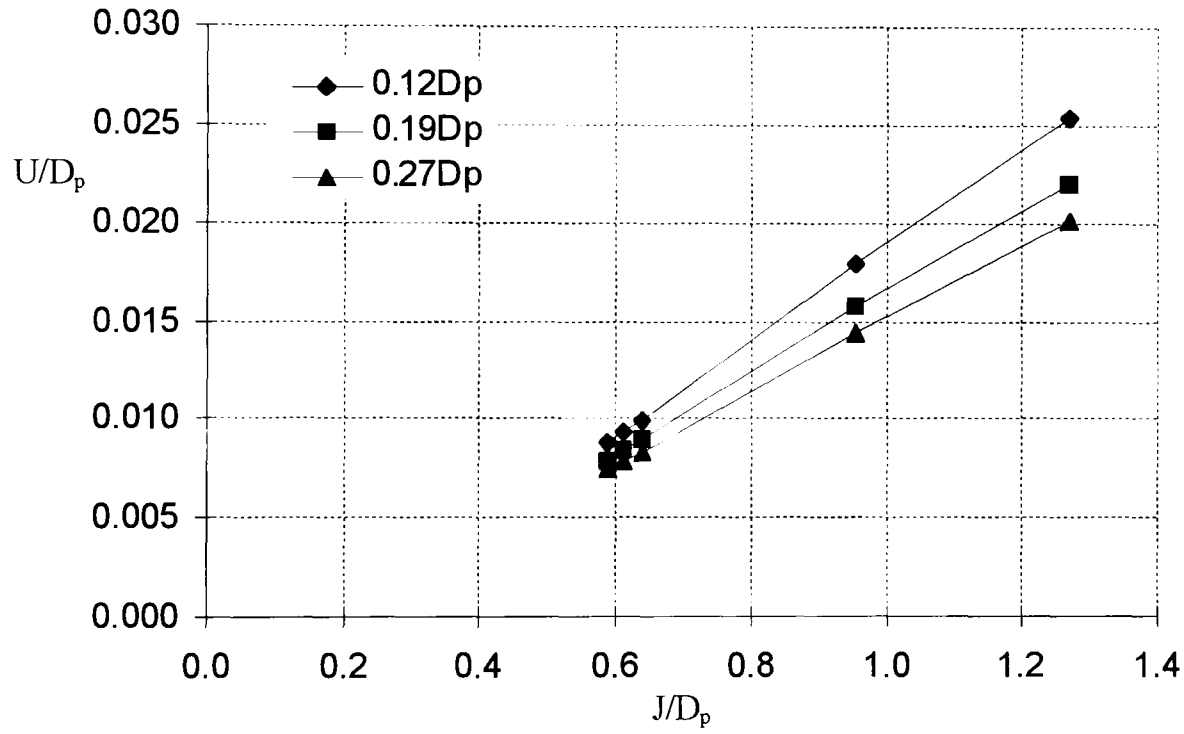

(b) Pure torsion

Figure 5.50. Web deformation due to radial bending and pure torsion for a range of web thickness

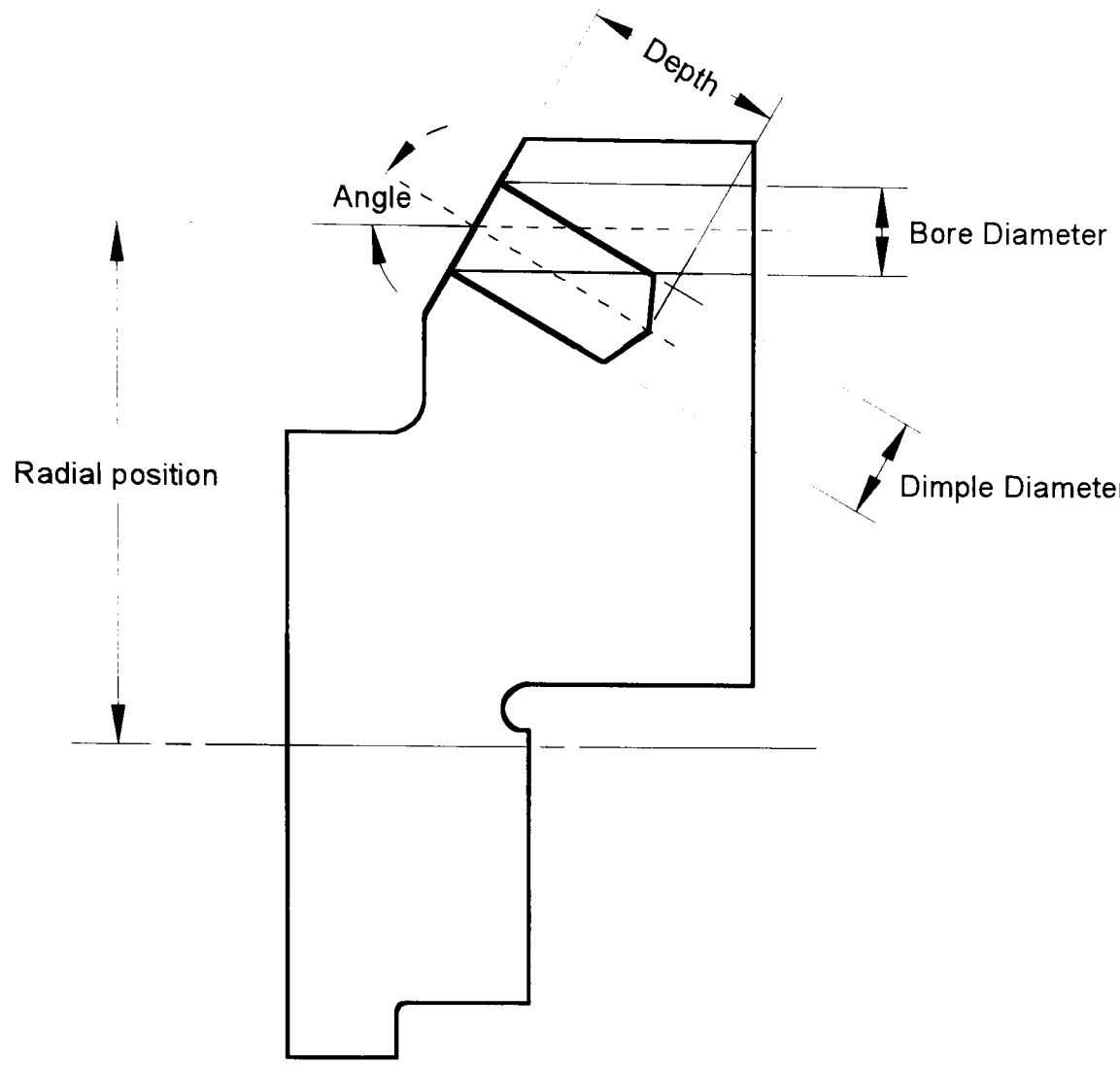

Figure 5.51. Definition of terms relating to crankpin bore holes and dimples

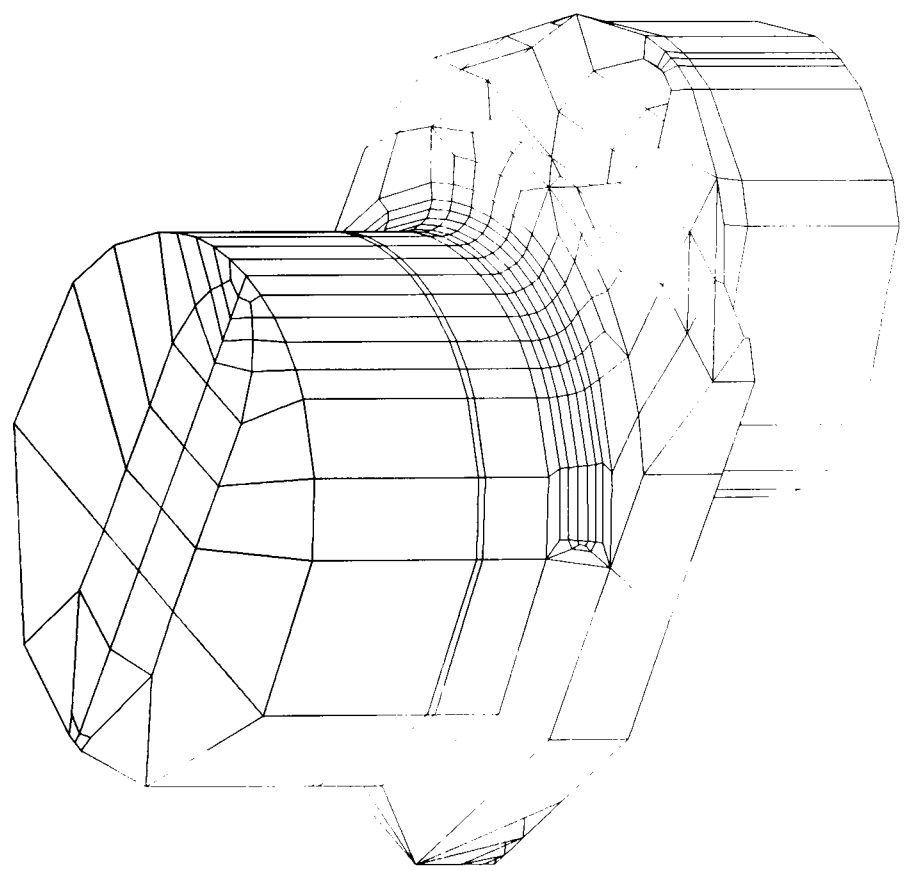

Figure 5.52. A typical BE mesh of a crankthrow with a crankpin dimple

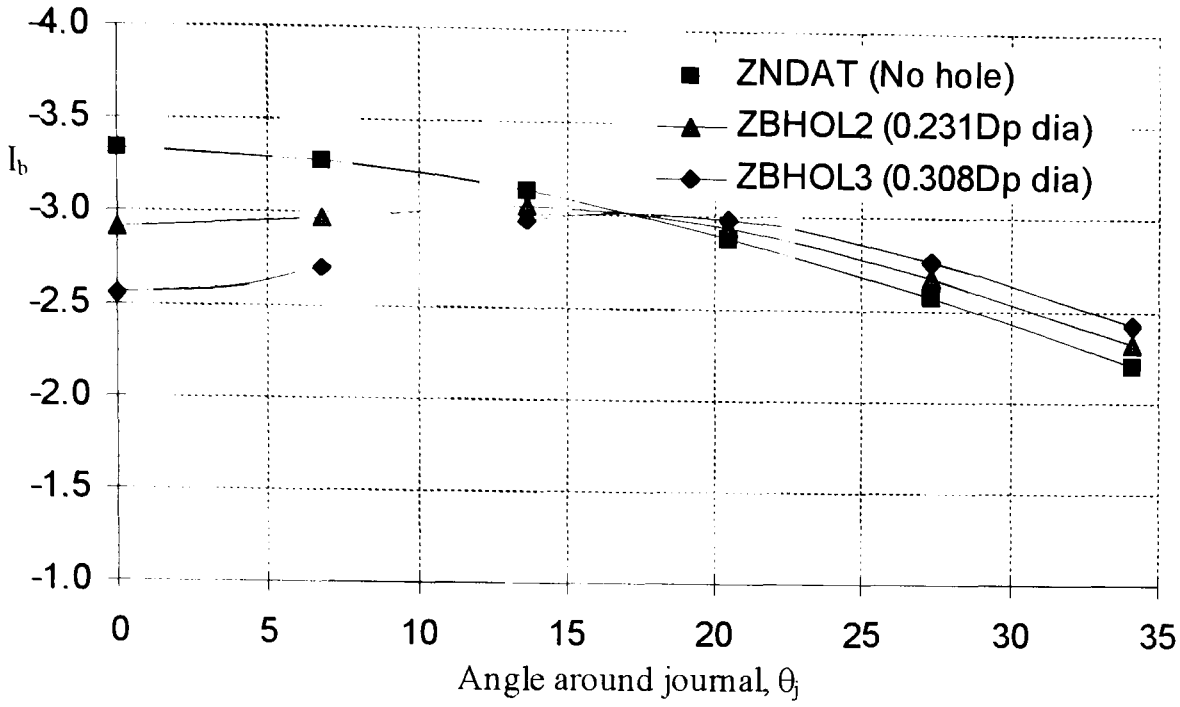

(a) Distribution around journal (3D analyses)

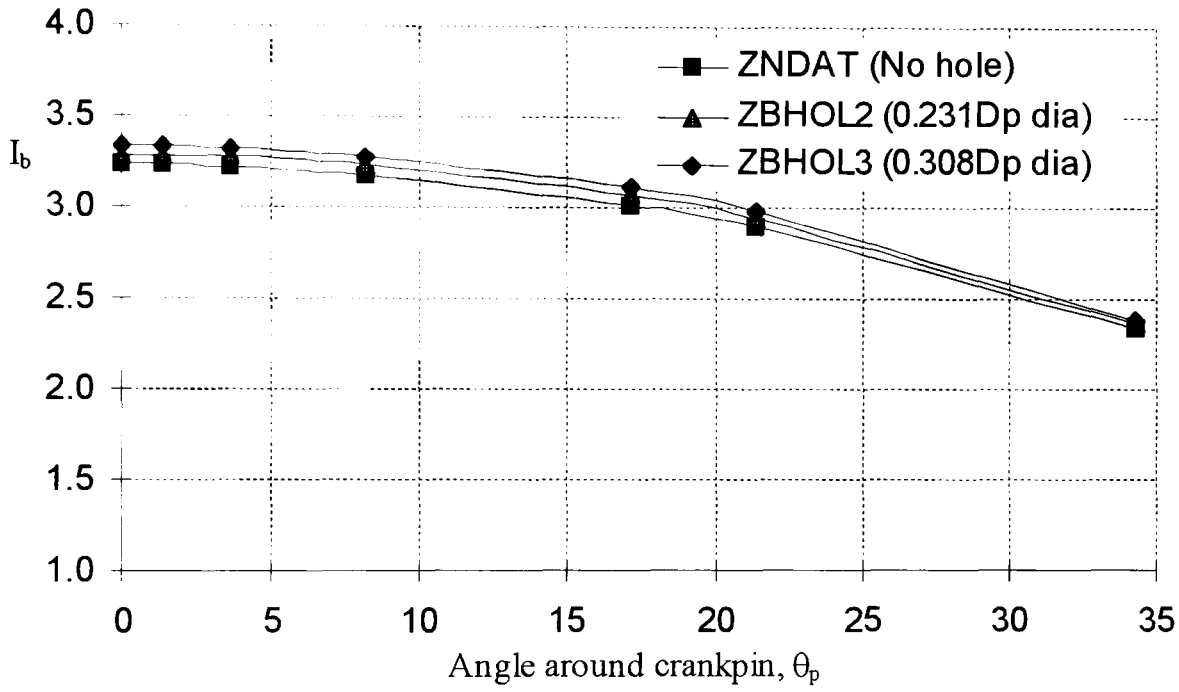

(b) Distribution around crankpin (3D analyses)

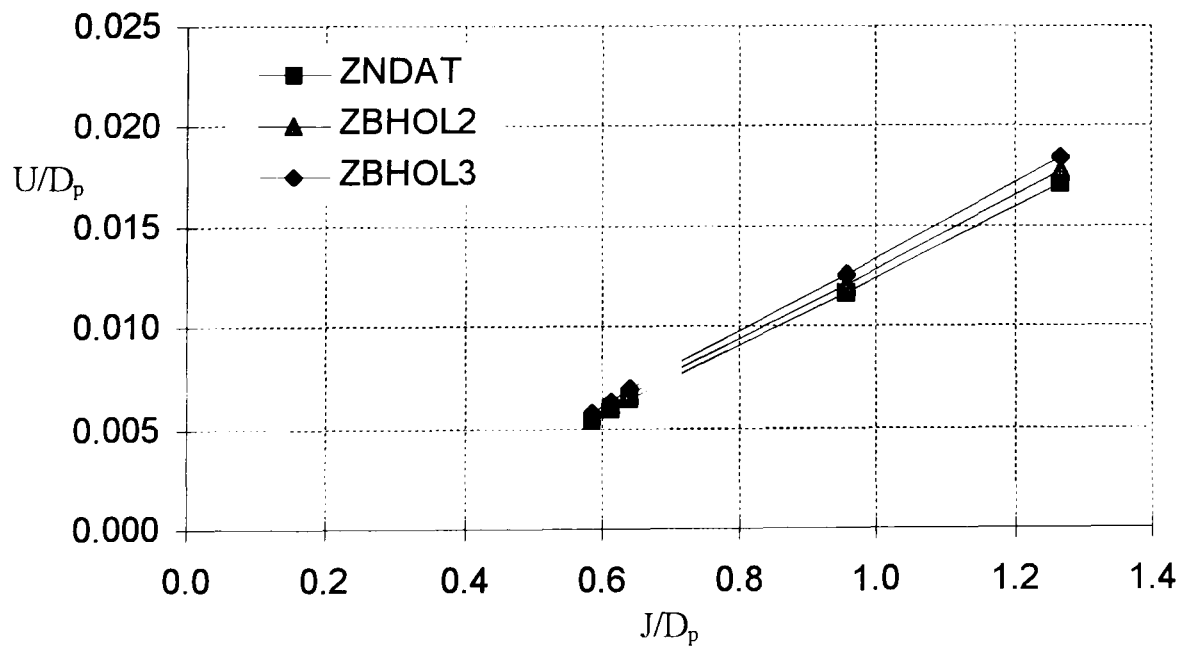

(c) Web deformation

Figure 5.53. Investigation into the effects of crankpin bore hole diameter under radial bending

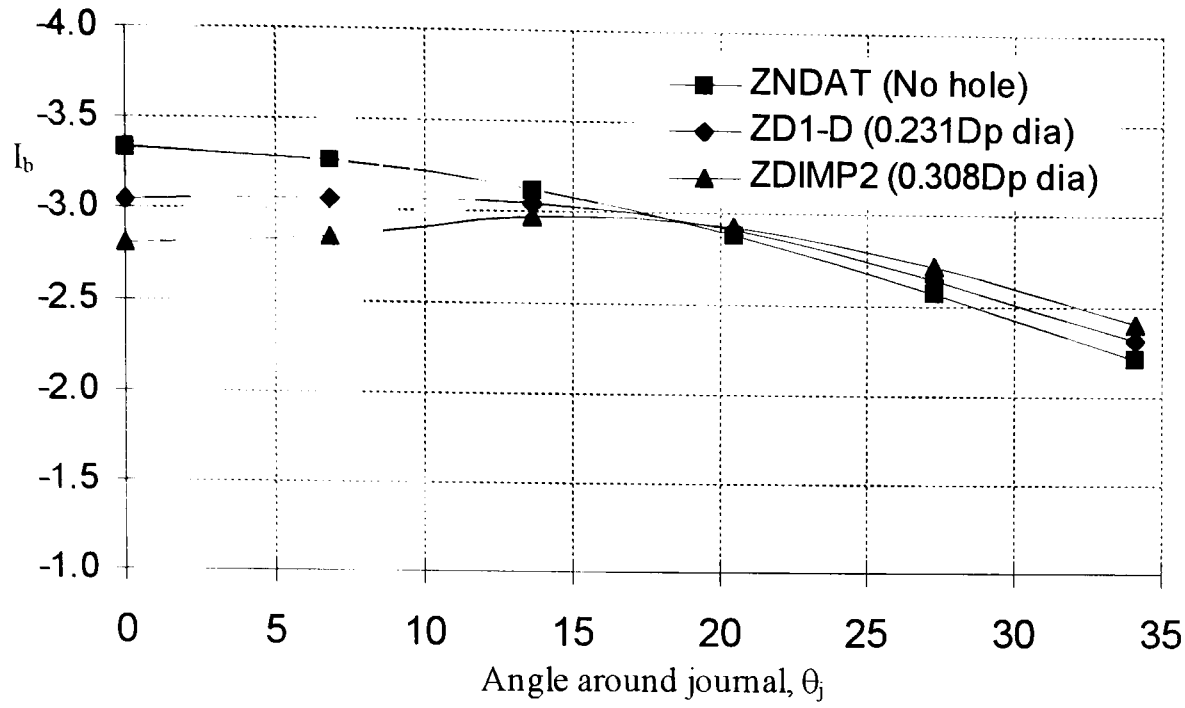

(a) Distribution around journal (3D analyses)

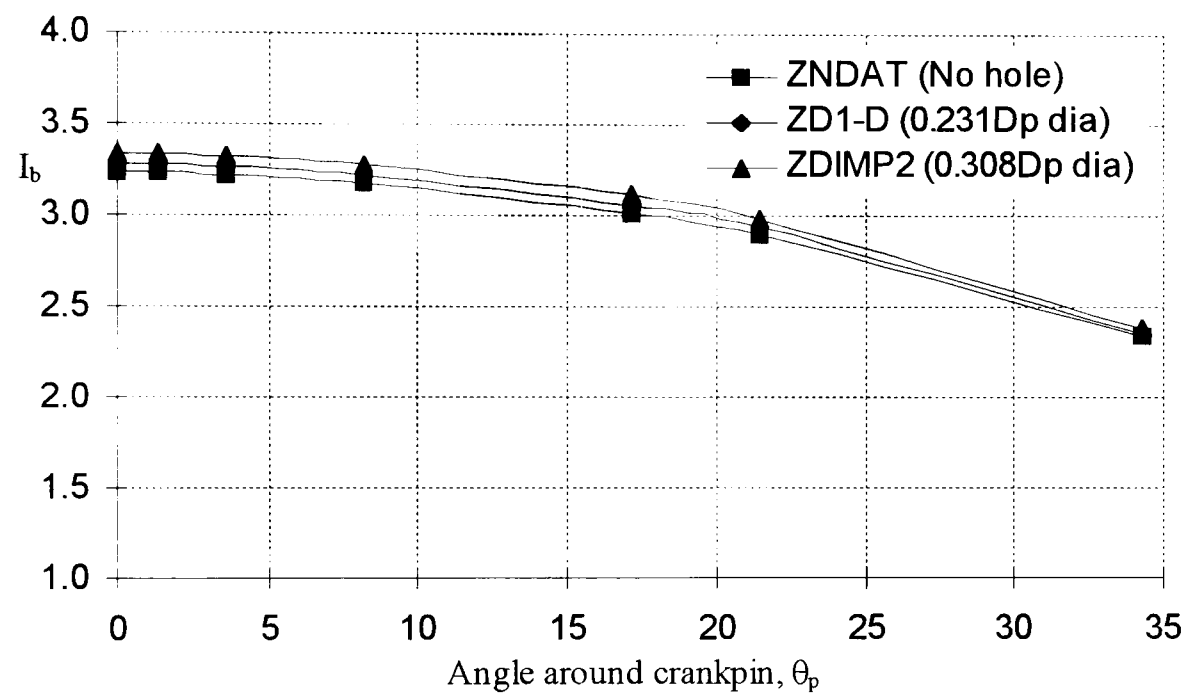

(b) Distribution around crankpin (3D analyses)

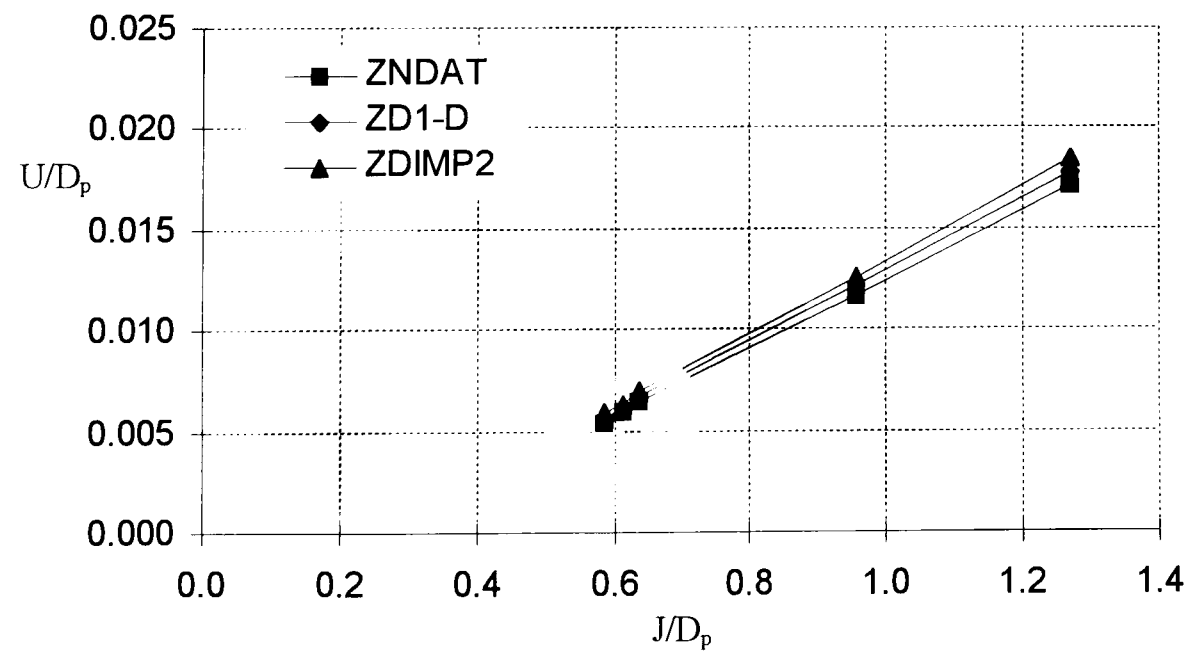

(c) Web deformation

Figure 5.54. Investigation into the effects of crankpin dimple diameter under radial bending

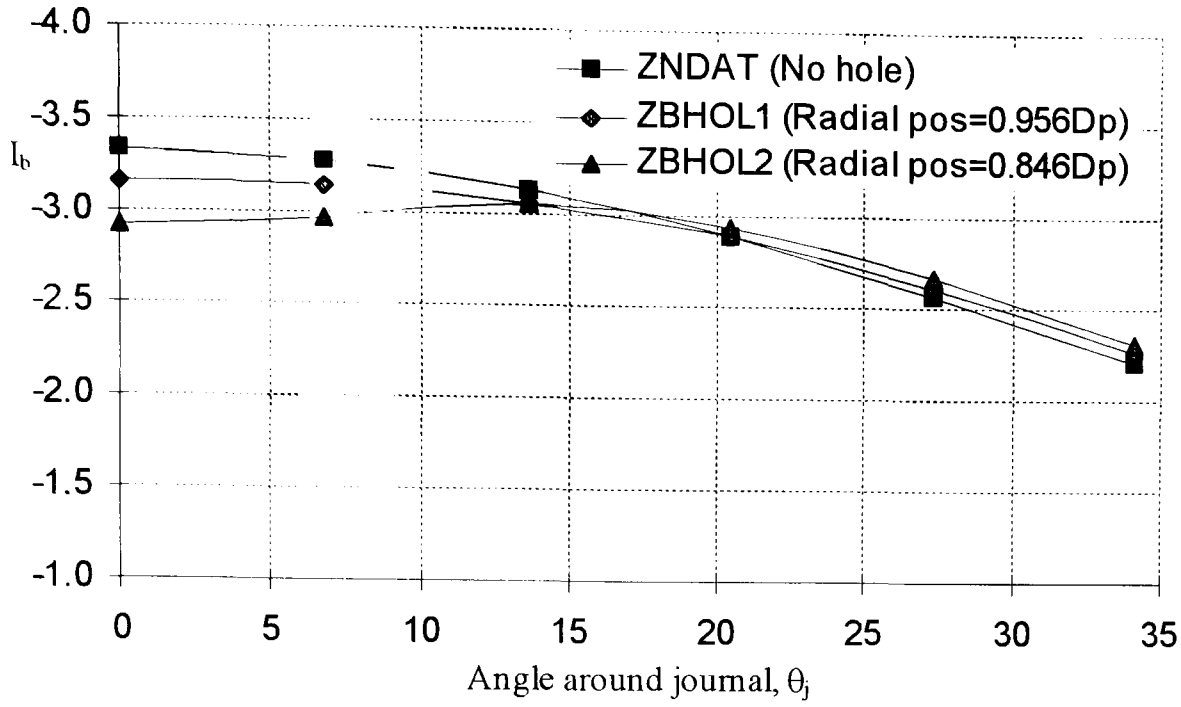

(a) Distribution around journal (3D analyses)

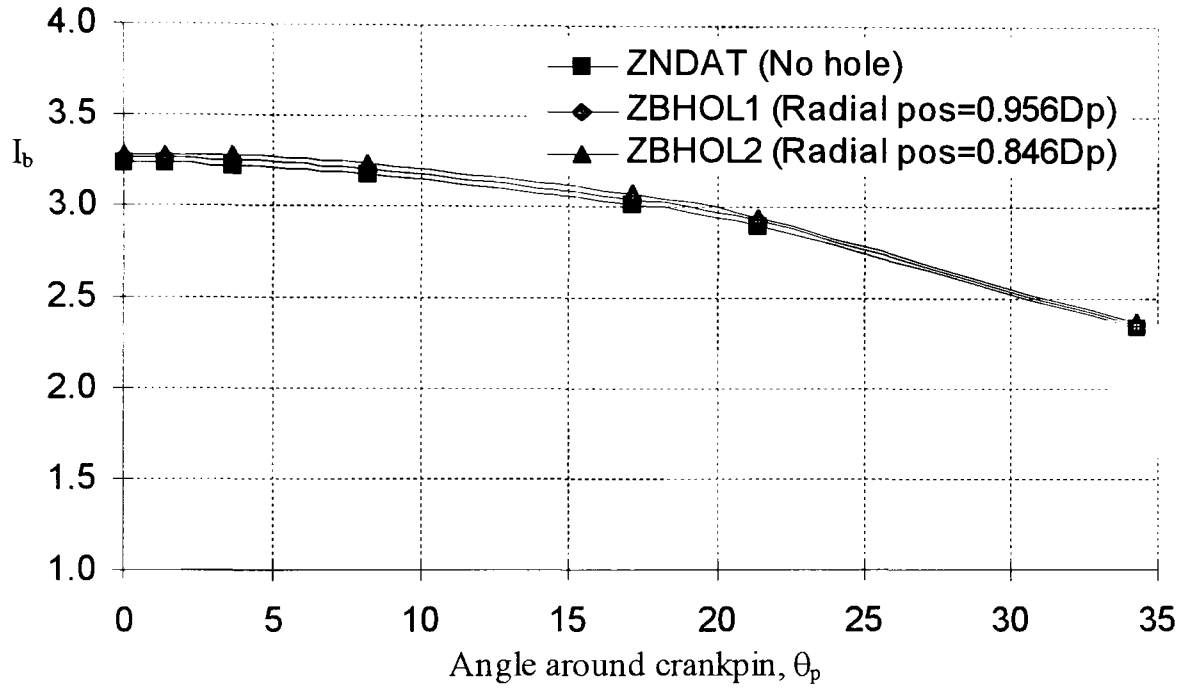

(b) Distribution around crankpin (3D analyses)

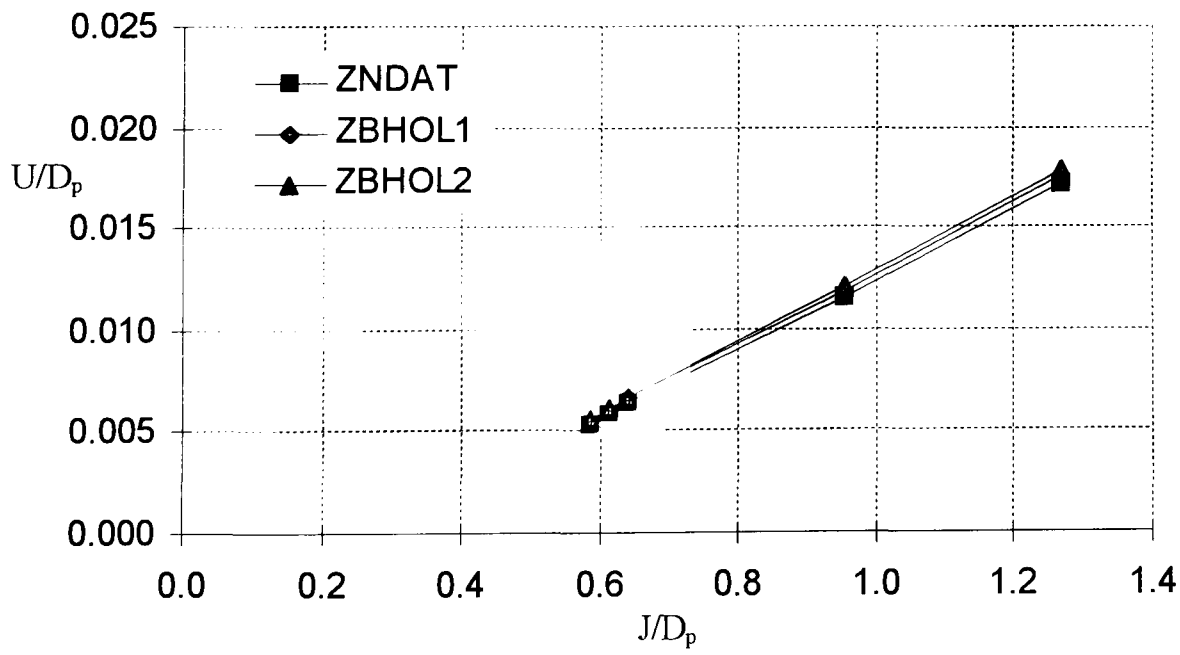

(c) Web deformation

Figure 5.55. Investigation into the effects of crankpin bore radial position under radial bending

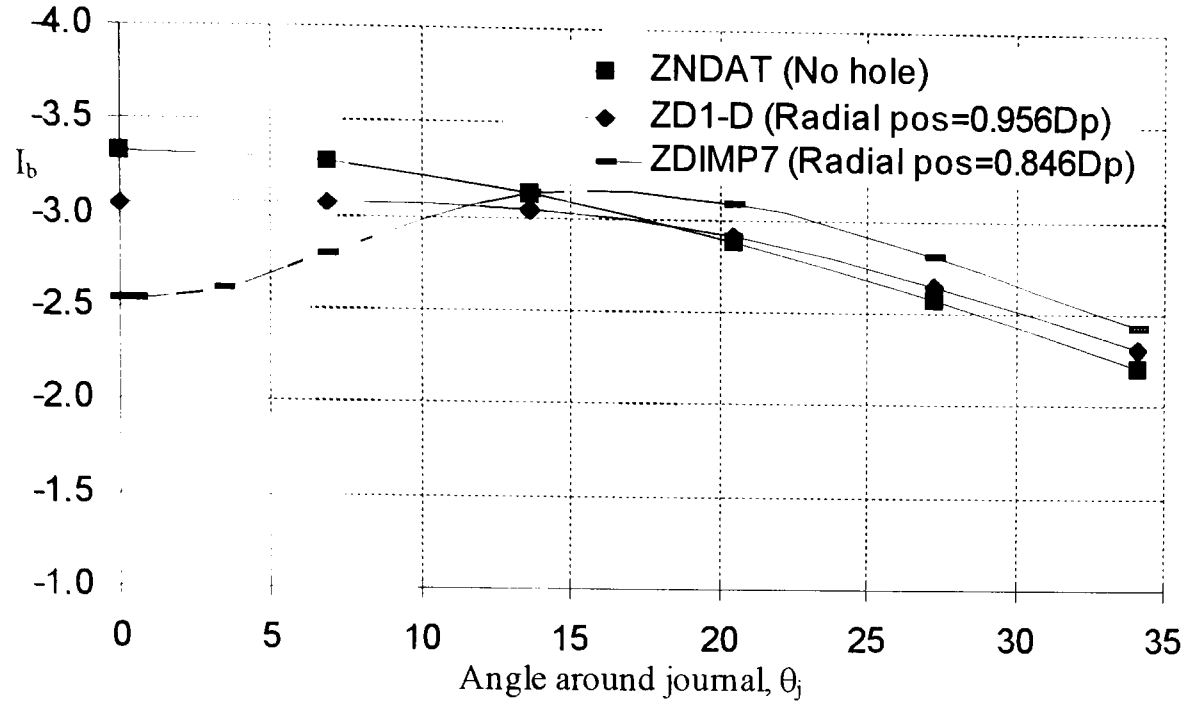

(a) Distribution around journal (3D analyses)

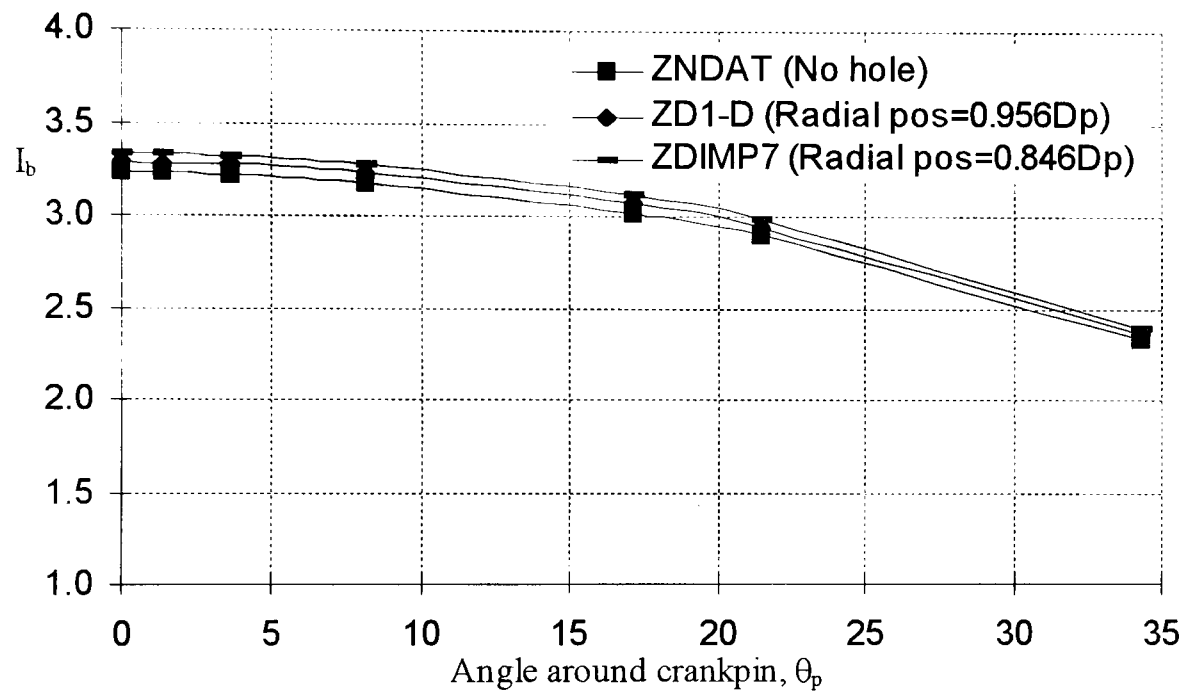

(b) Distribution around crankpin (3D analyses)

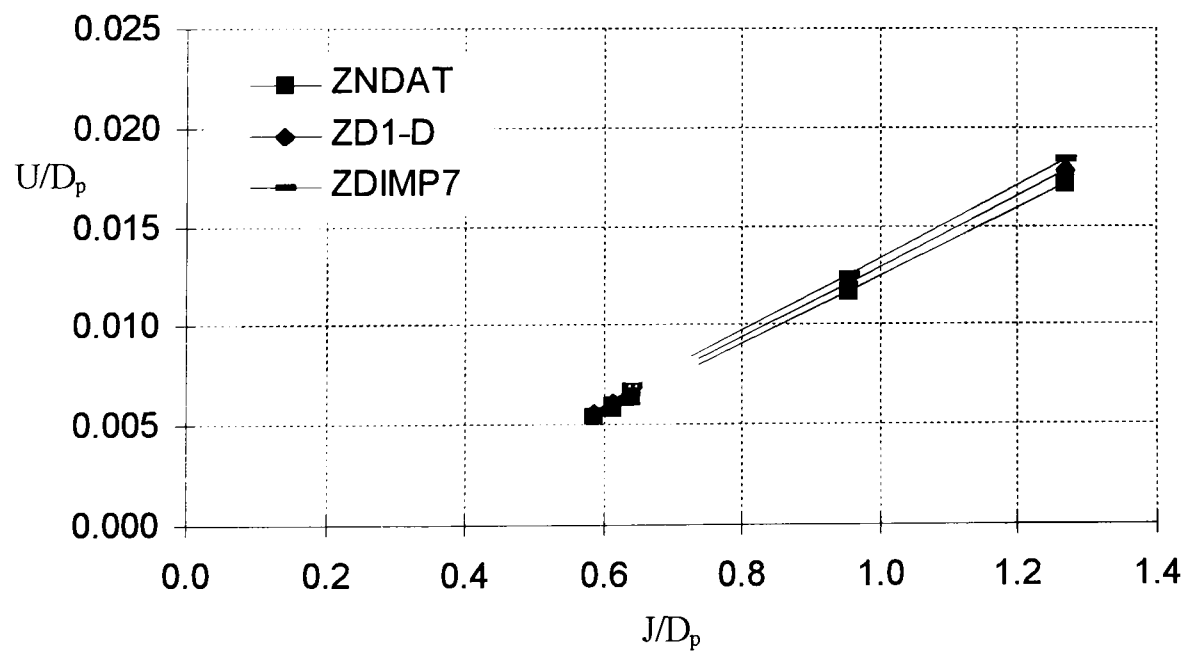

(c) Web deformation

Figure 5.56. Investigation into the effects of crankpin dimple radial position under radial bending

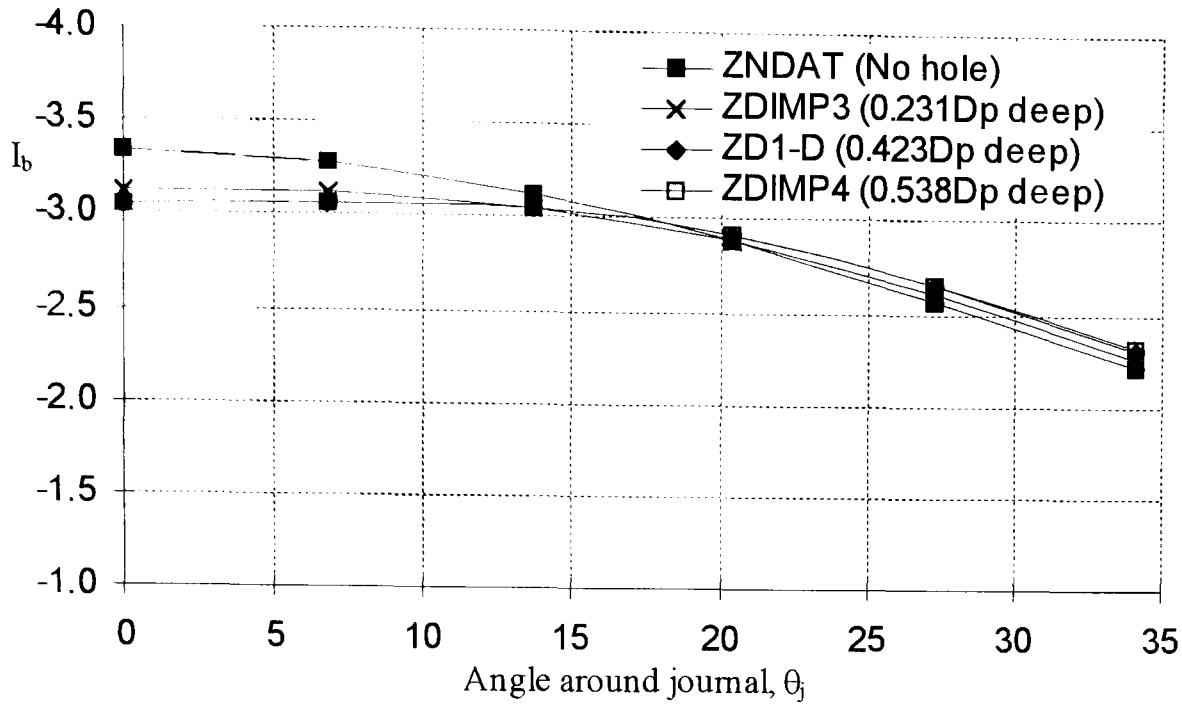

(a) Distribution around journal (3D analyses)

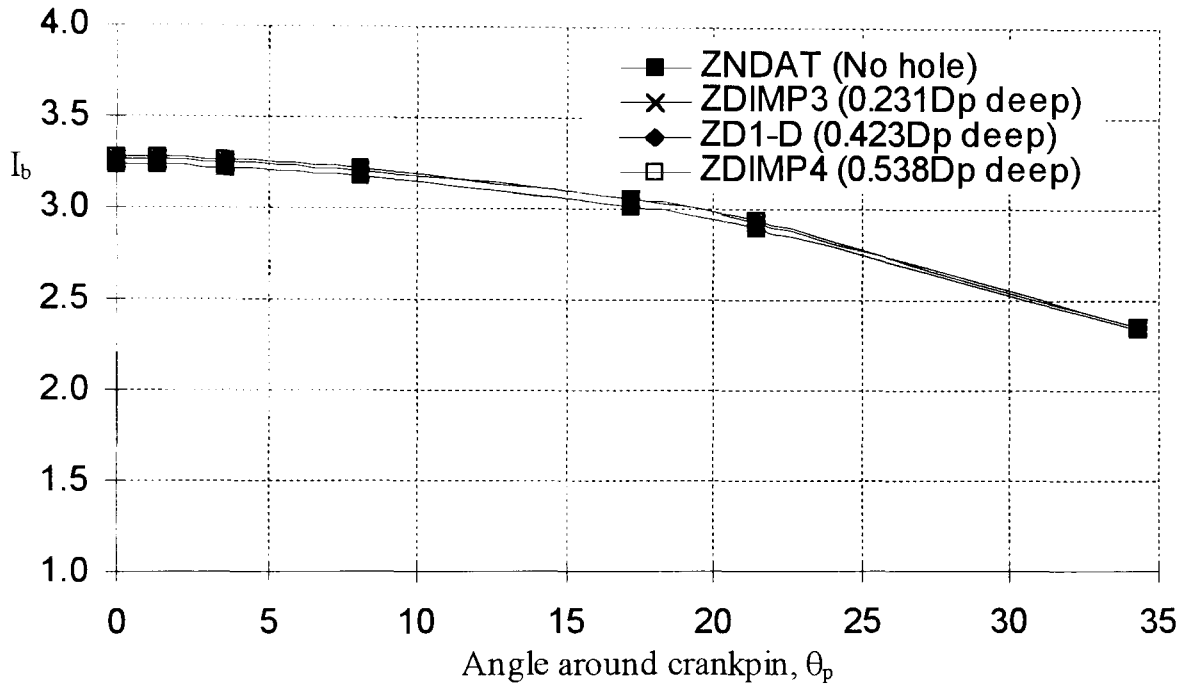

(b) Distribution around crankpin (3D analyses)

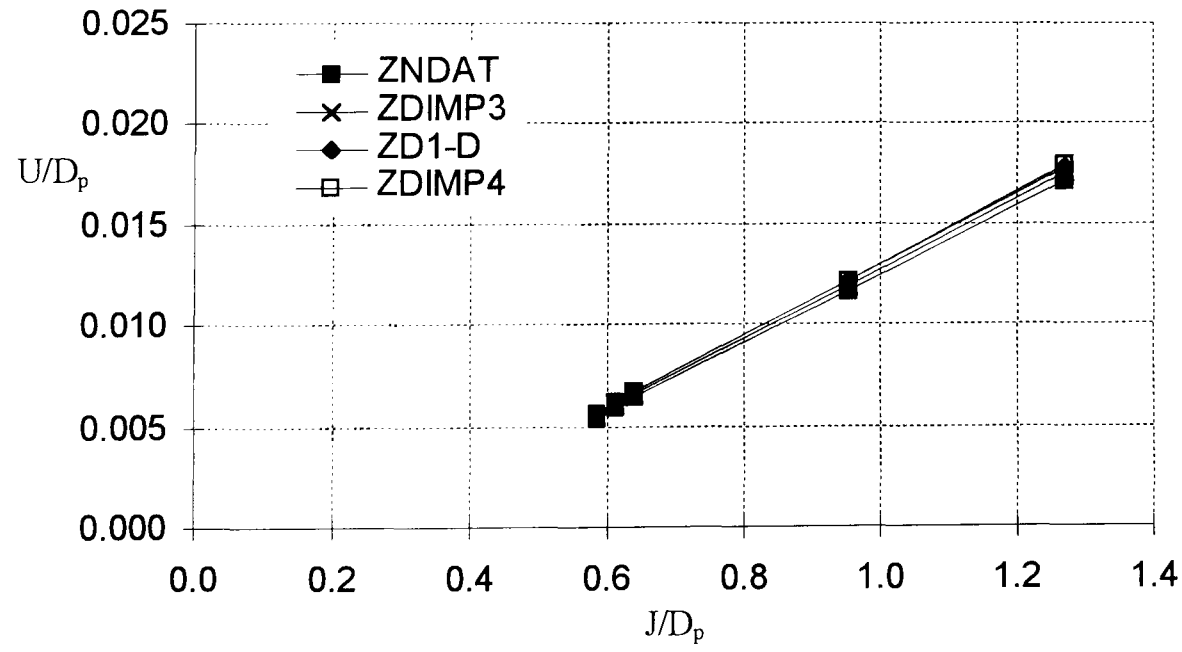

(c) Web deformation

Figure 5.57. Investigation into the effects of crankpin dimple depth under radial bending

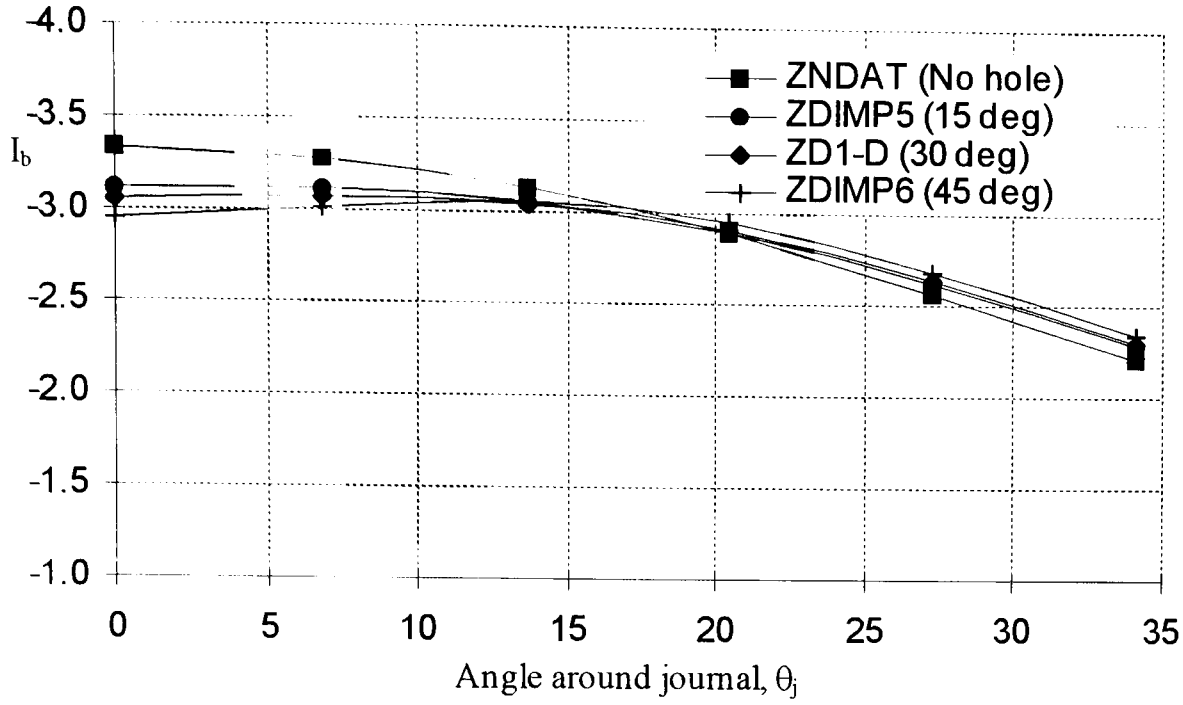

(a) Distribution around journal (3D analyses)

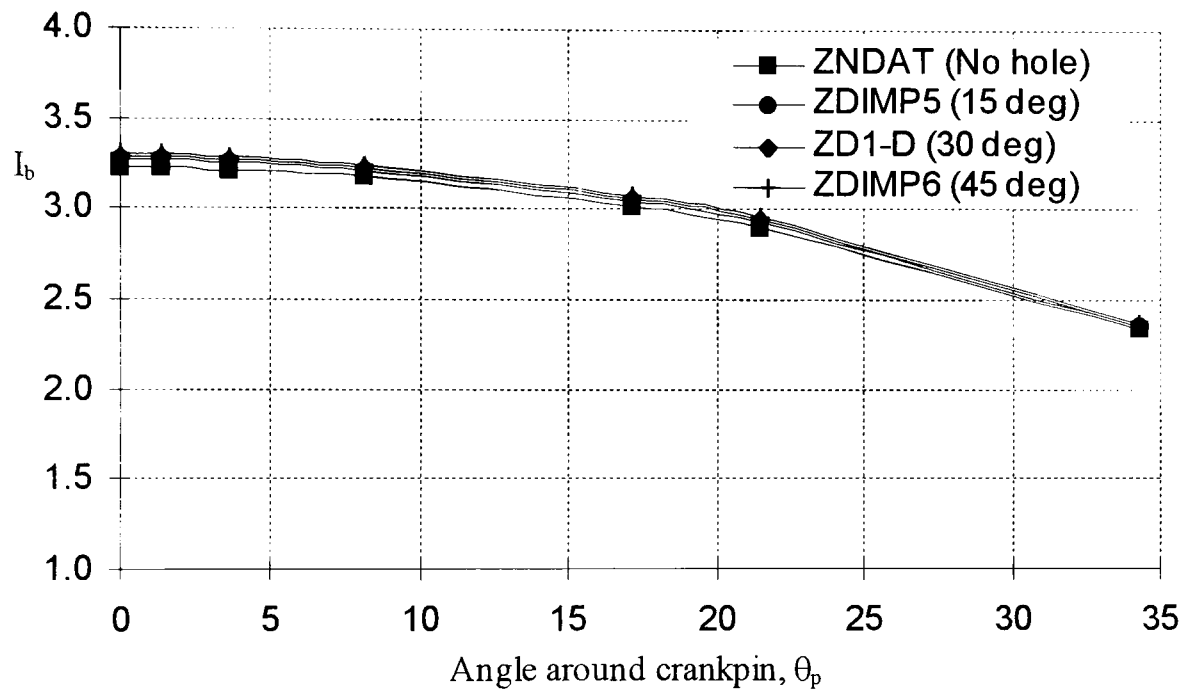

(b) Distribution around crankpin (3D analyses)

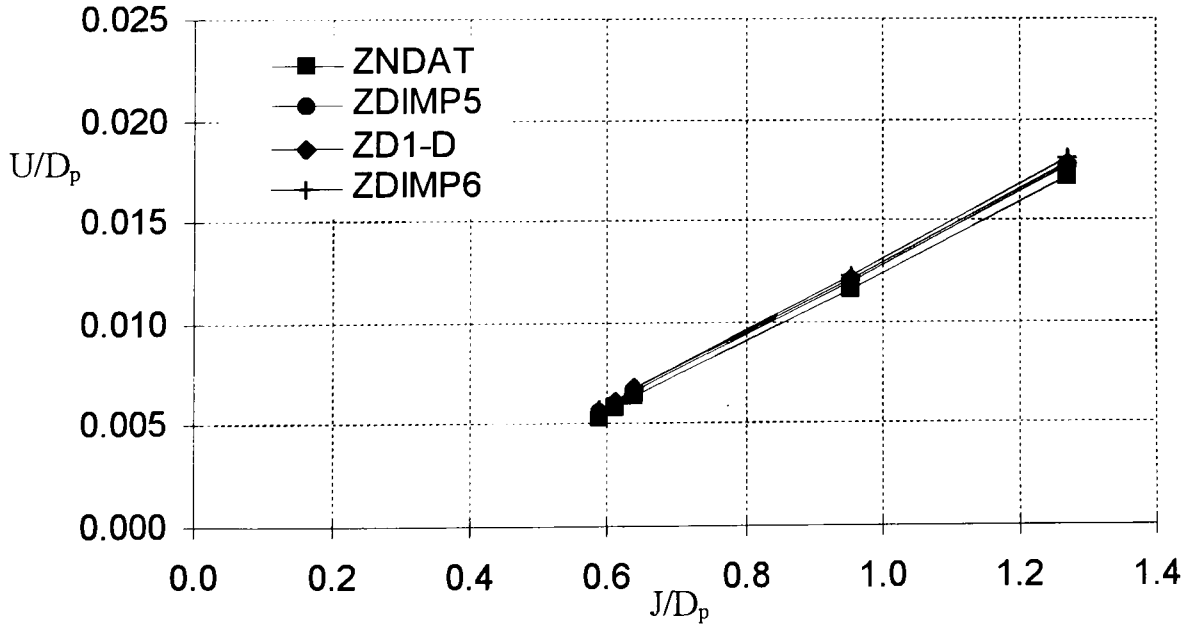

(c) Web deformation

Figure 5.58. Investigation into the effects of crankpin dimple angle under radial bending

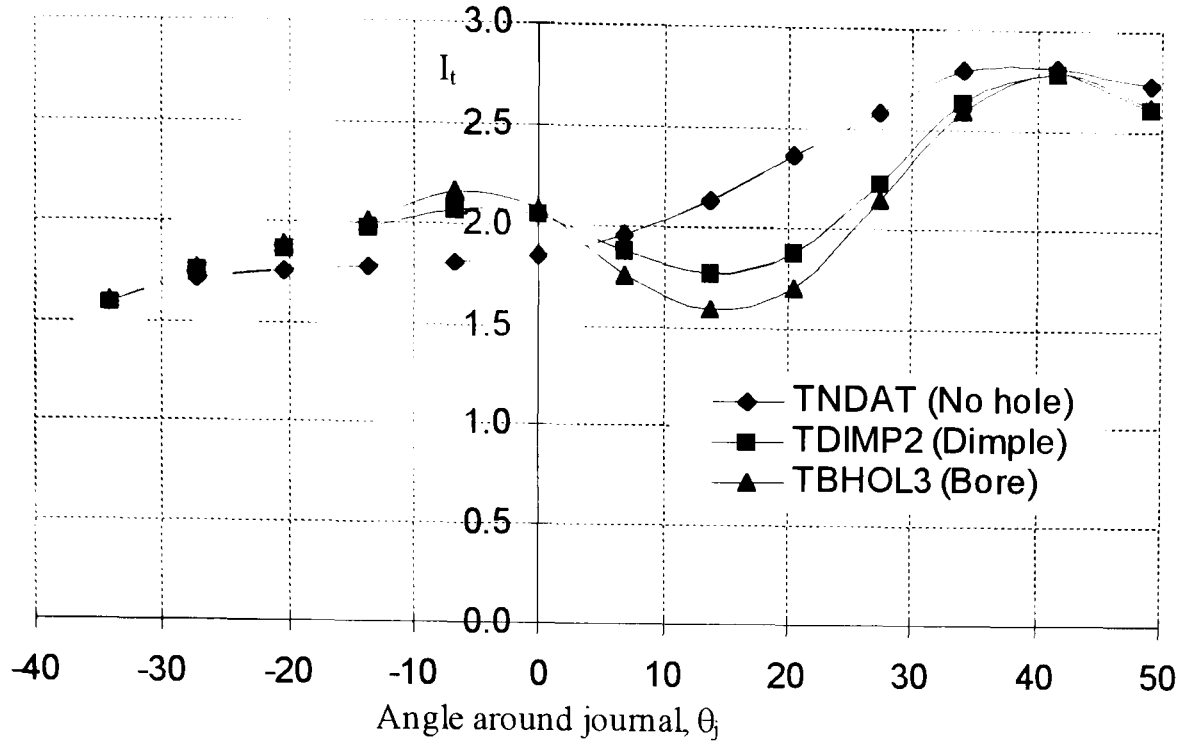

(a) Distribution around journal (3D analyses)

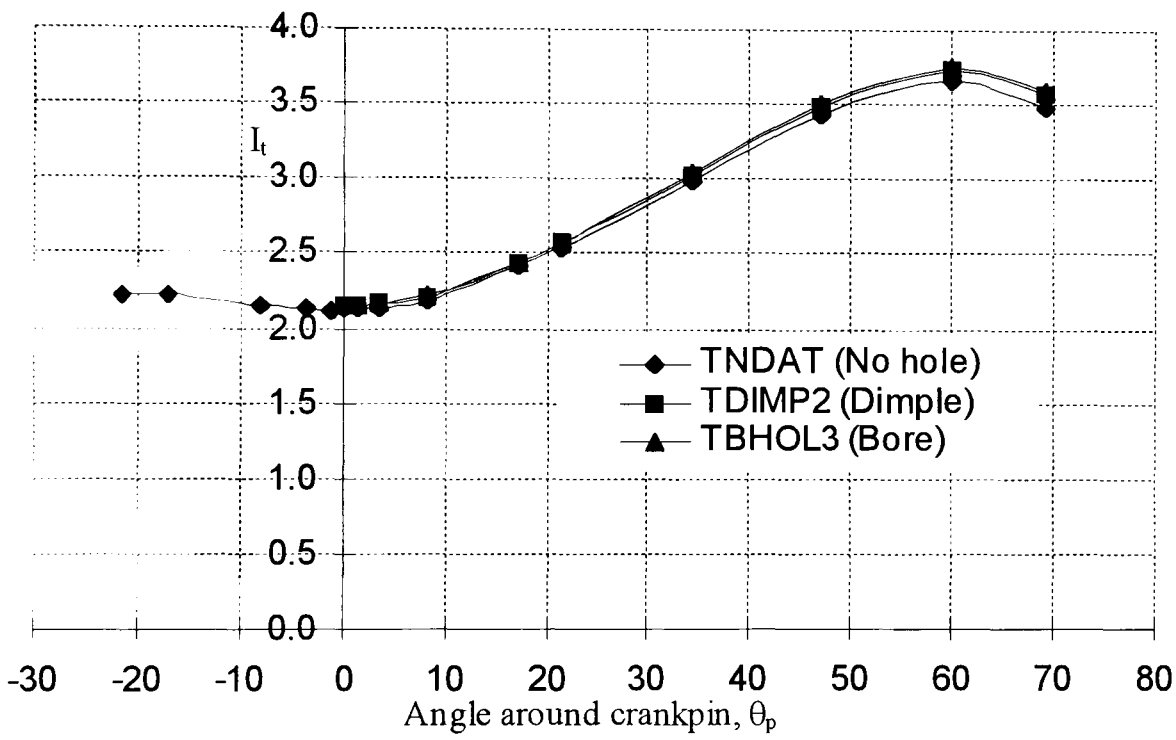

(b) Distribution around crankpin (3D analyses)

Figure 5.59. Investigation into the effects of crankpin bore holes and dimples under pure torsion

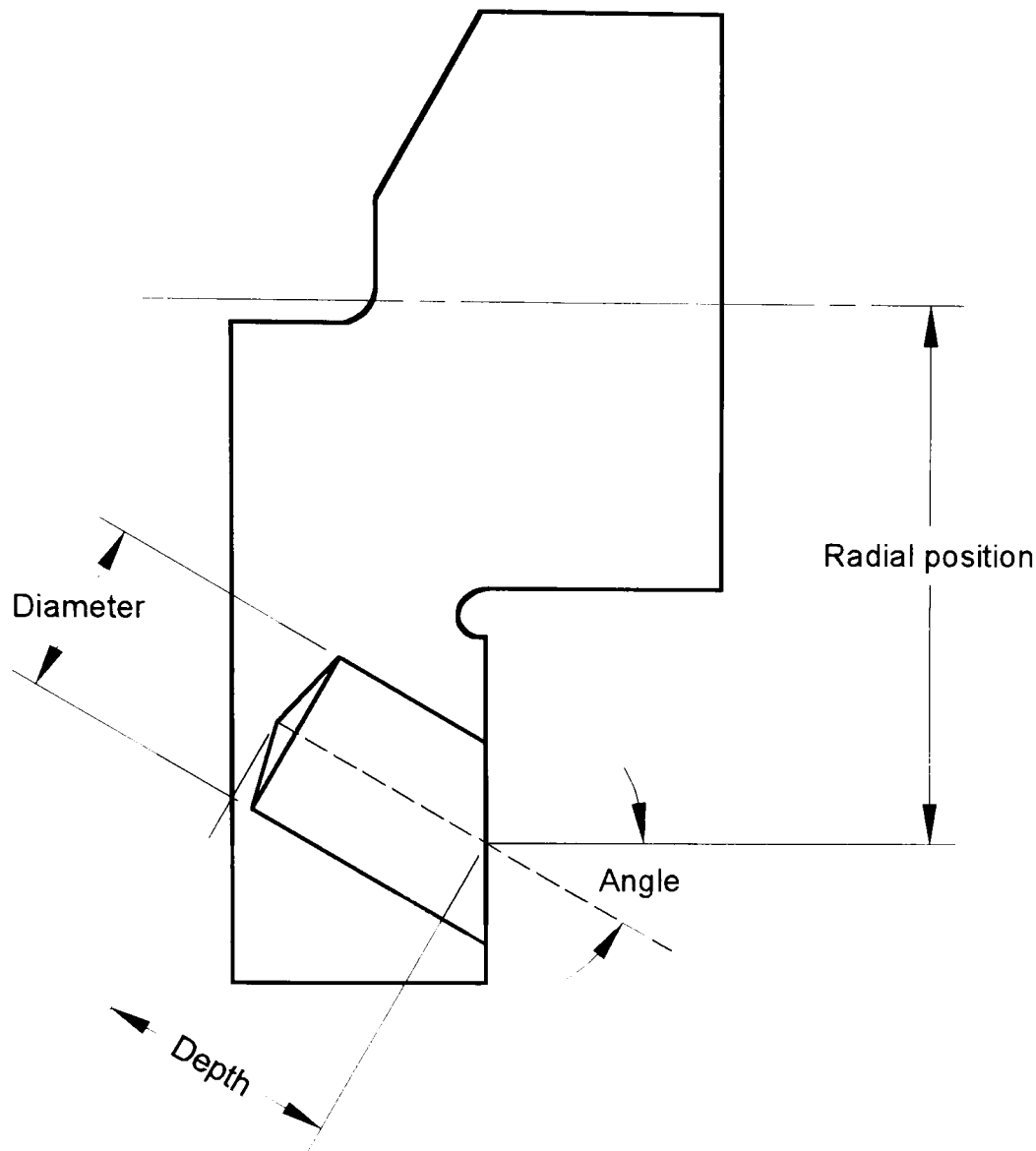

Figure 5.60. Definition of terms relating to journal dimples

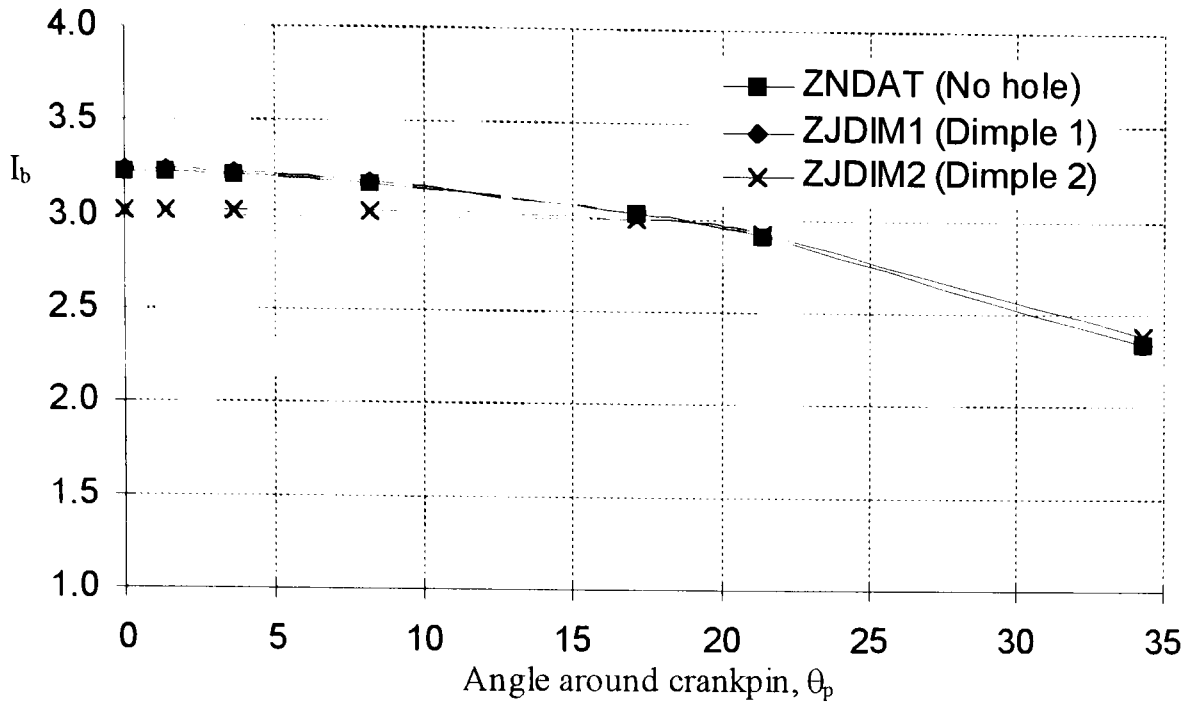

(a) Distribution around crankpin (3D analyses)

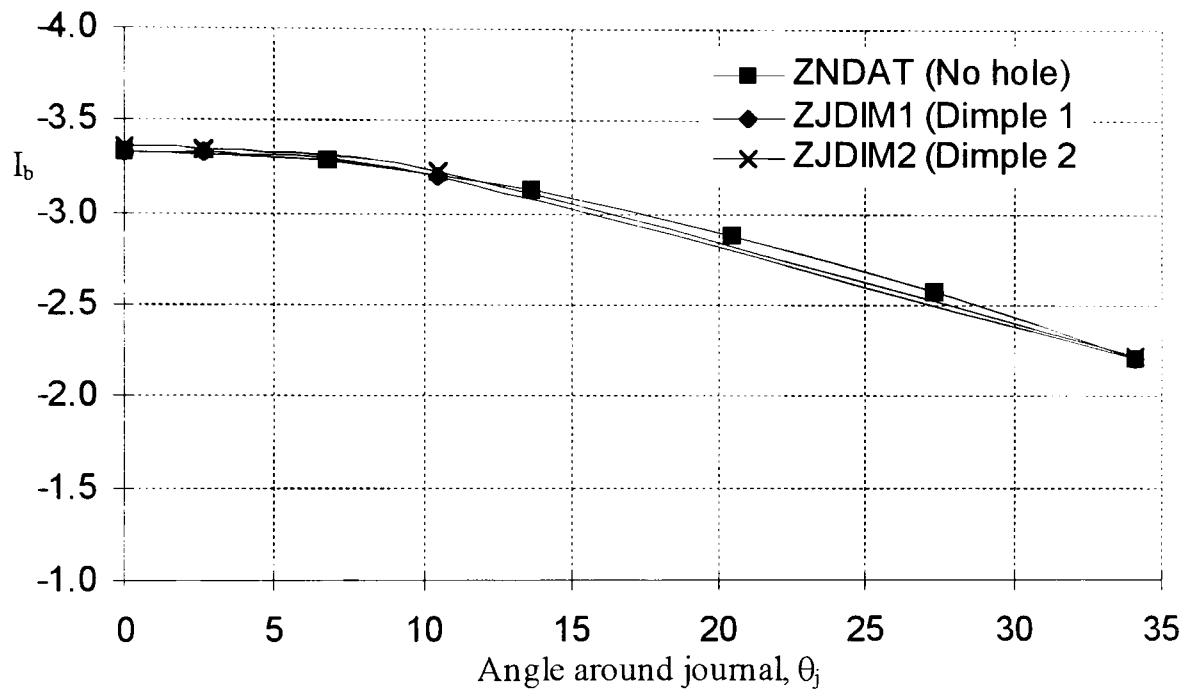

(b) Distribution around journal (3D analyses)

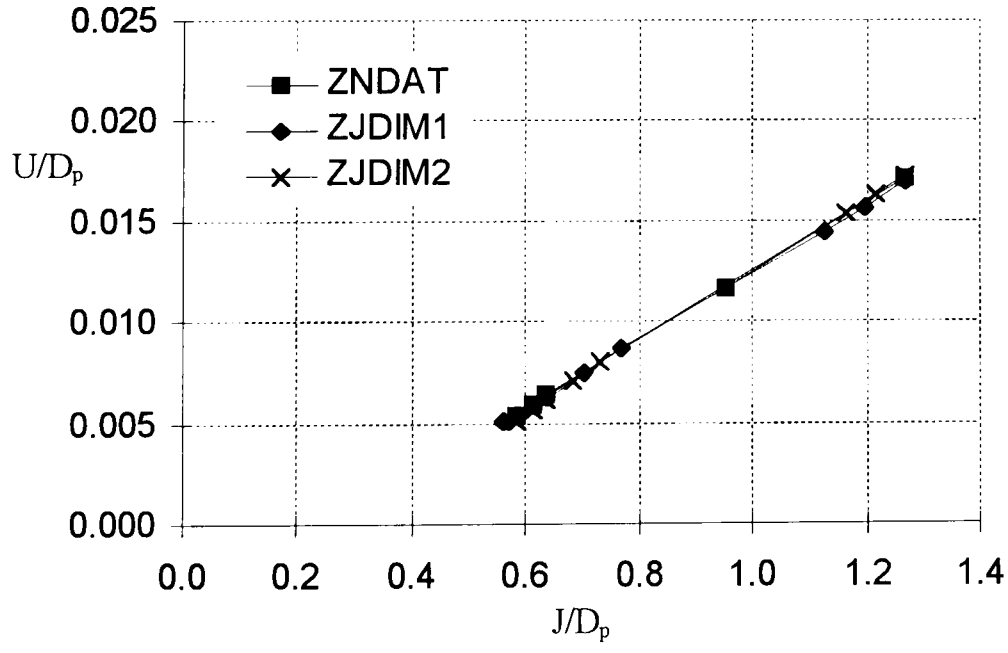

(c) Web deformation

Figure 5.61. Investigation into the effects of journal dimples under radial bending

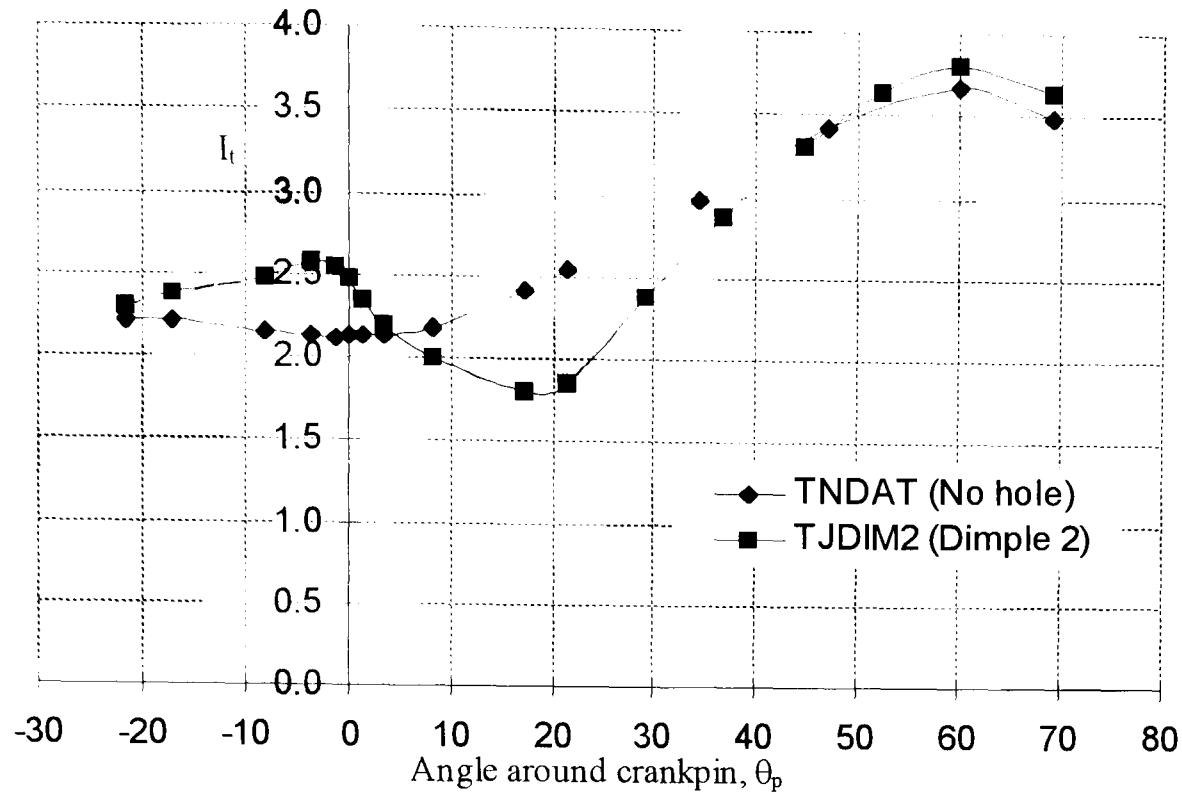

(a) Distribution around crankpin (3D analyses)

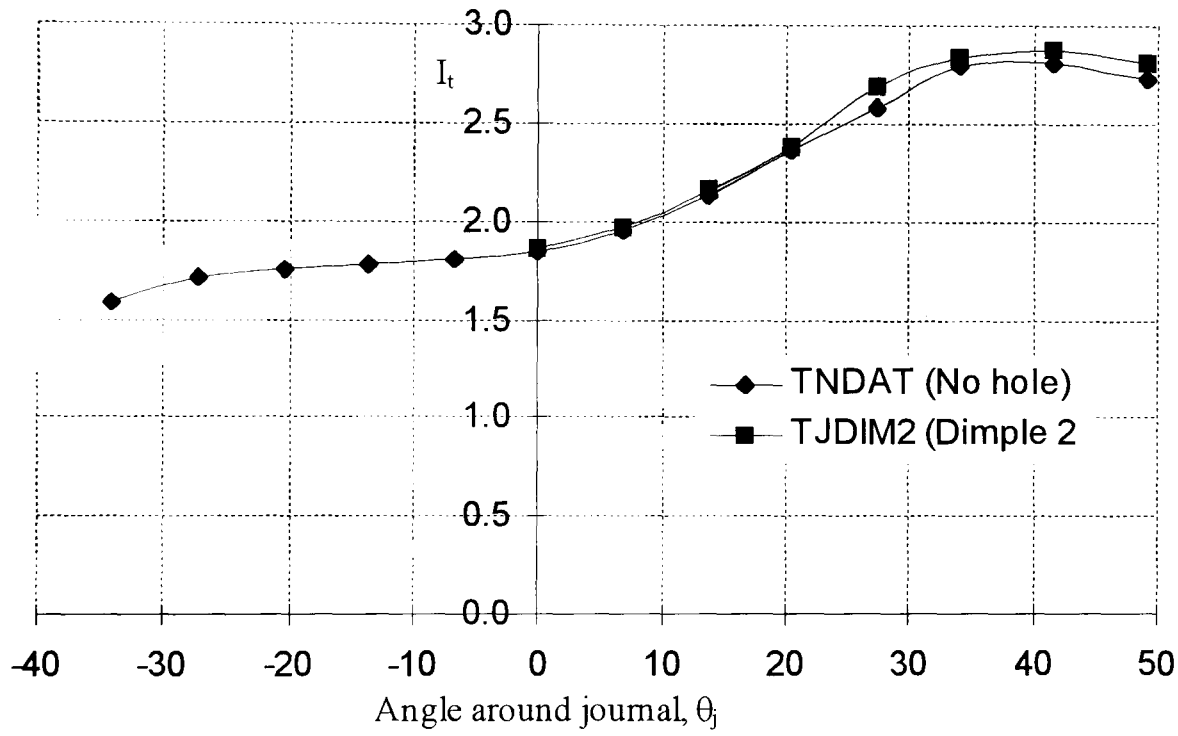

(b) Distribution around journal (3D analyses)

Figure 5.62. Investigation into the effects of journal dimples under pure torsion

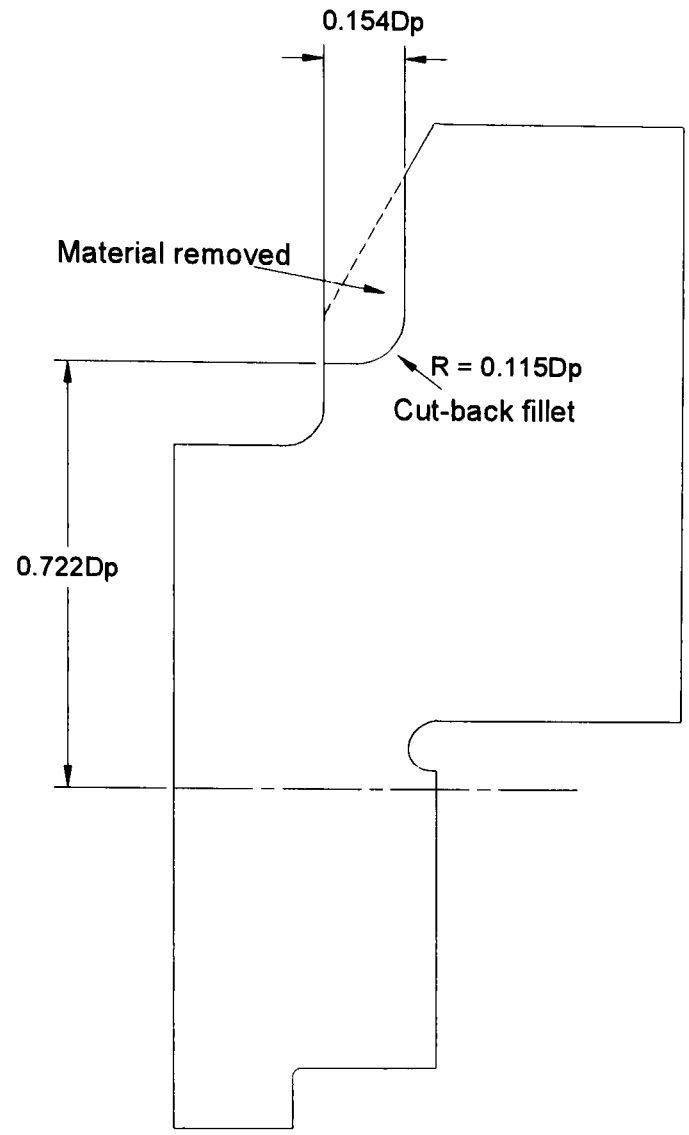

Figure 5.63. Dimensions of cut-back on journal side of web

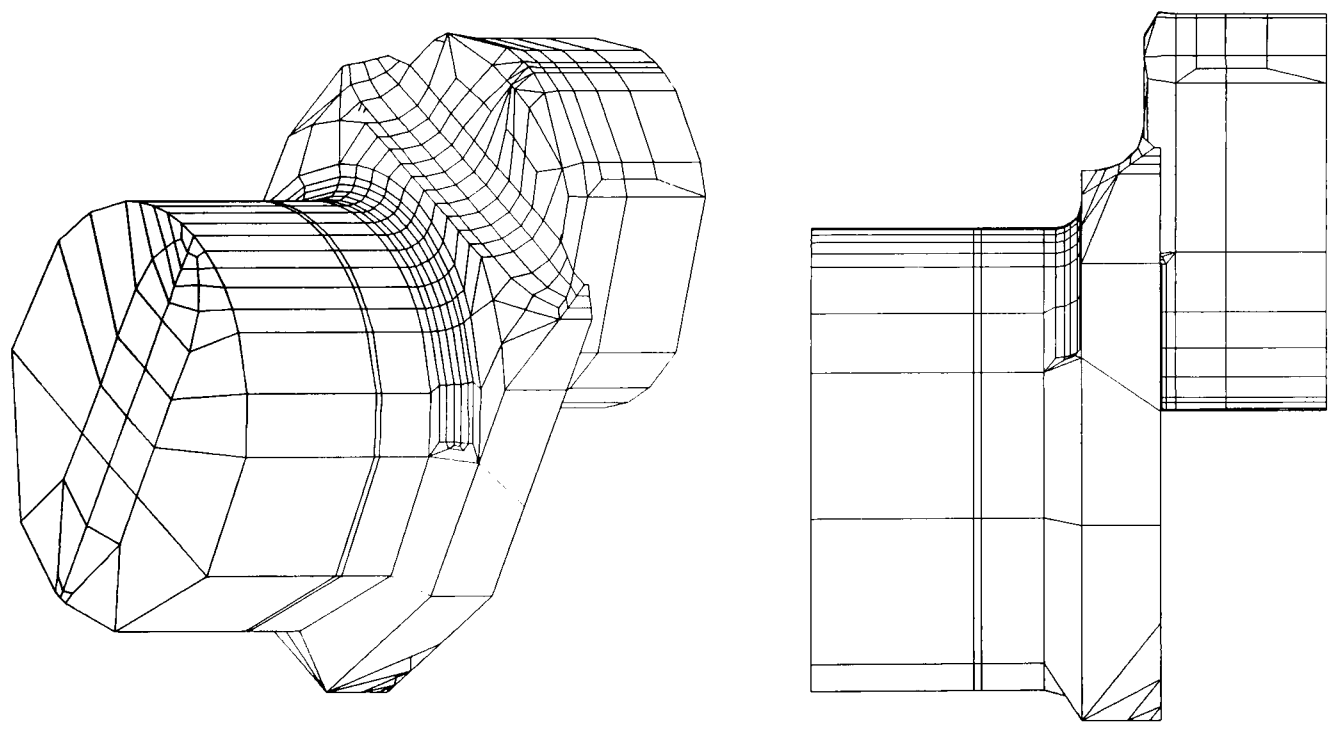

Figure 5.64. A typical BE mesh of a crankthrow with a cut-back web

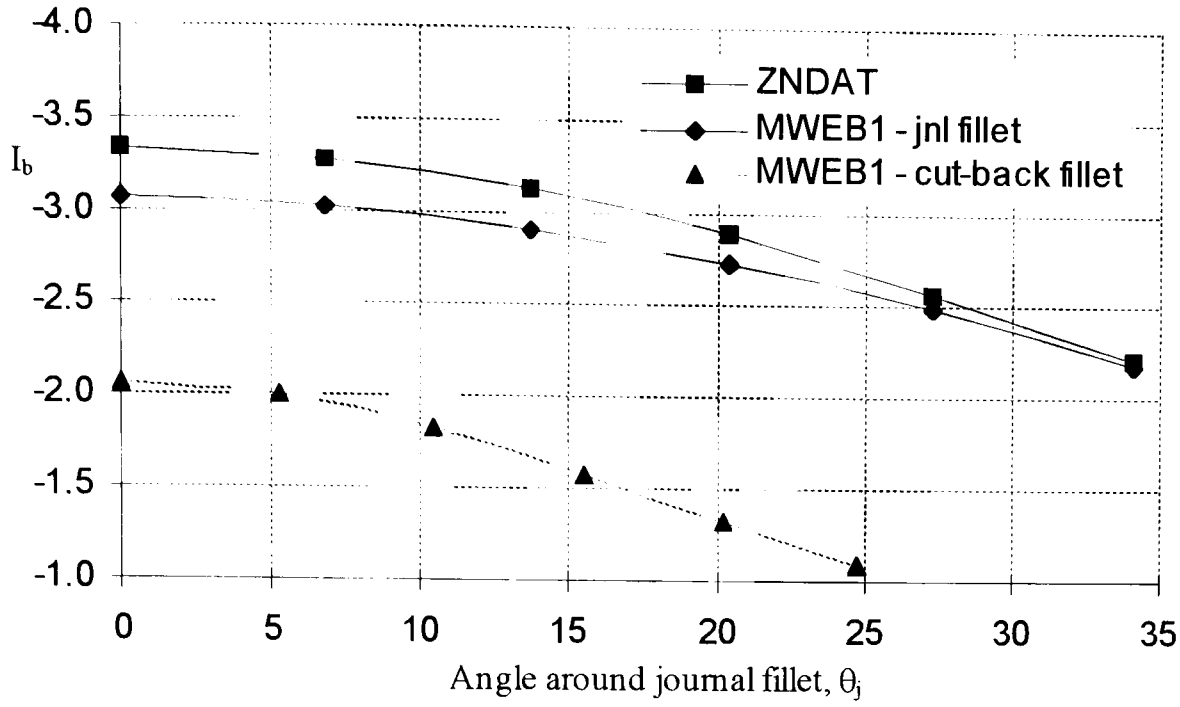

(a) Distribution around journal (3D analyses)

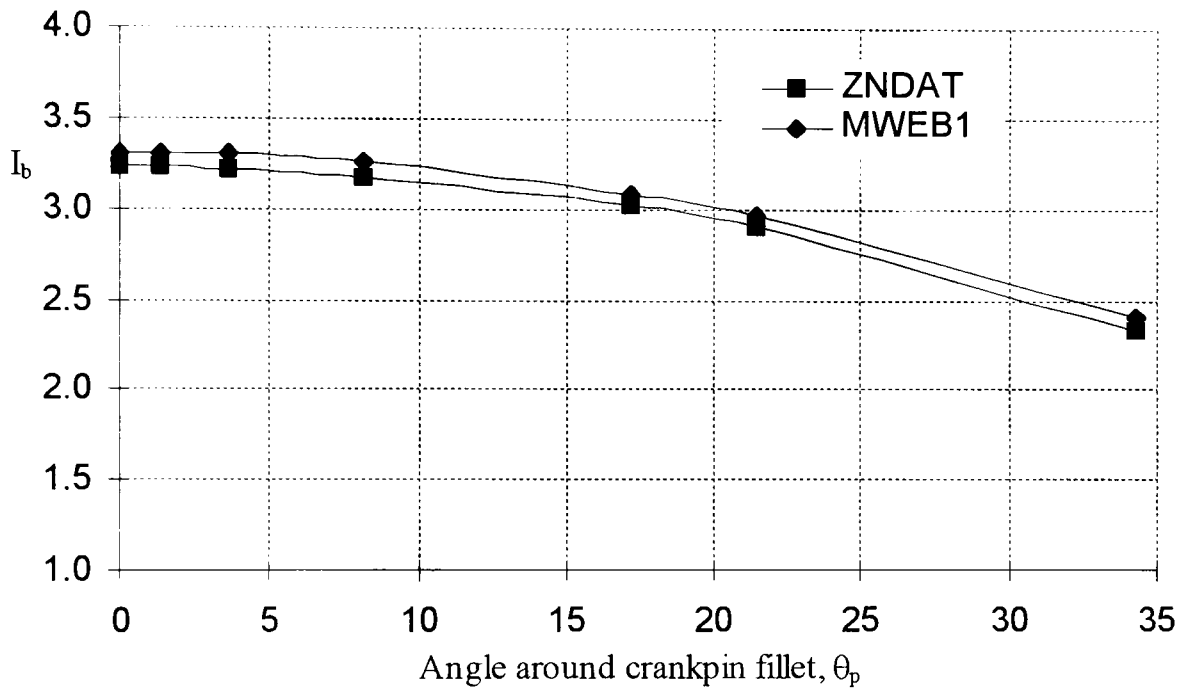

(b) Distribution around crankpin (3D analyses)

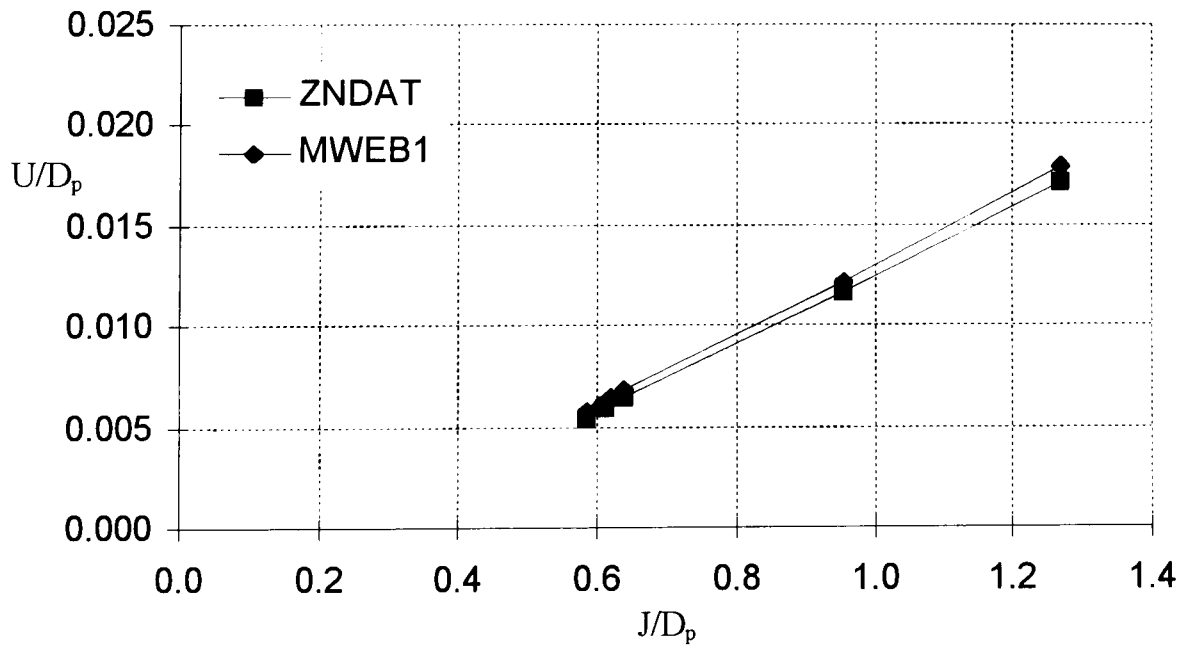

(c) Web deformation

Figure 5.65. Investigation into the effects of a cut-back web under radial bending

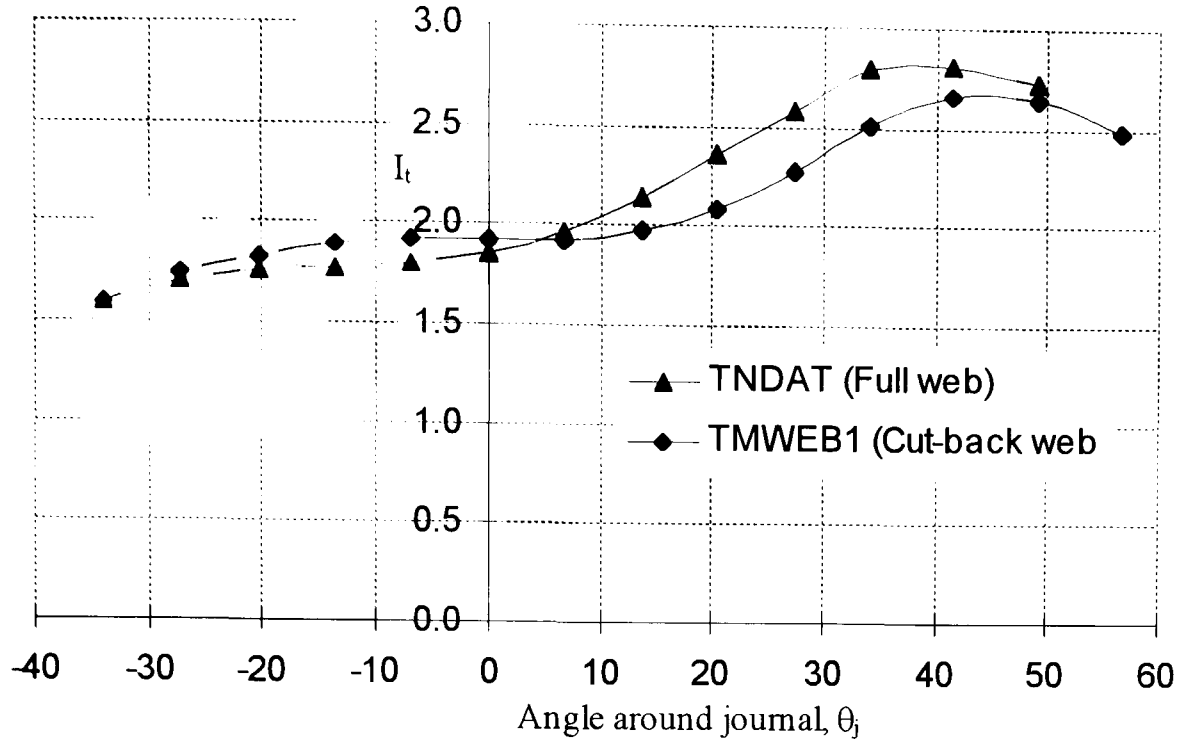

(a) Distribution around journal (3D analyses)

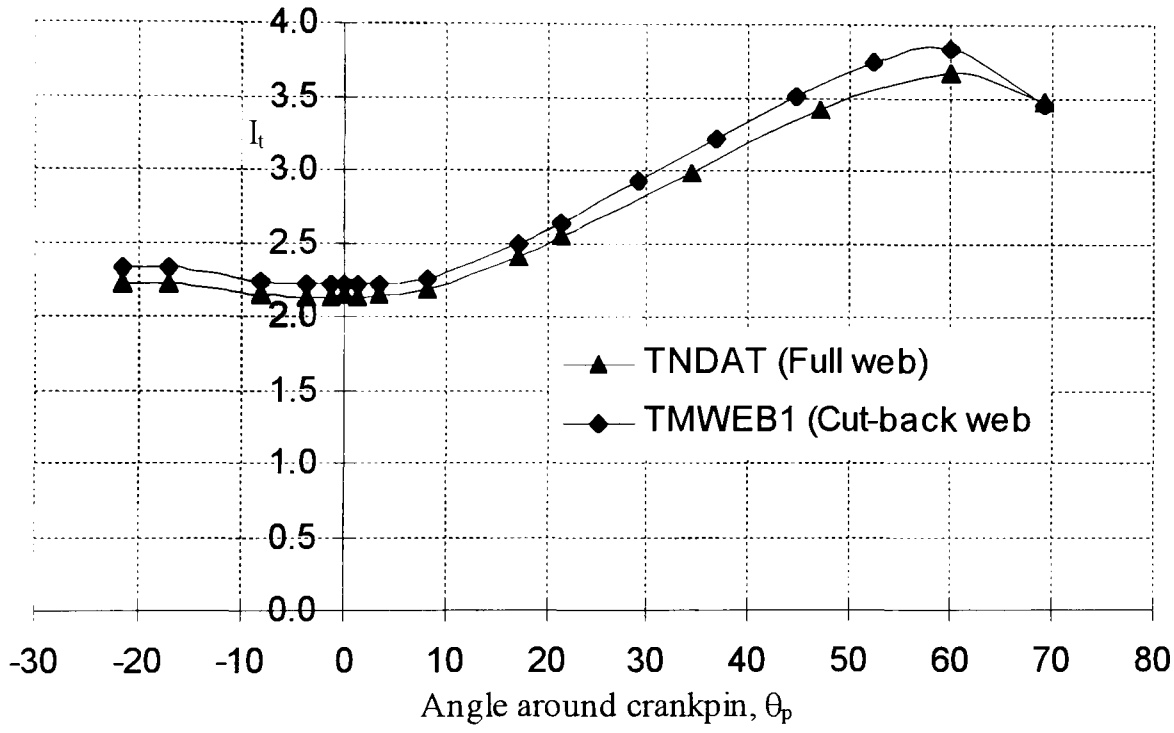

(b) Distribution around crankpin (3D analyses)

Figure 5.66. Investigation into the effects of a cut-back web under pure torsion

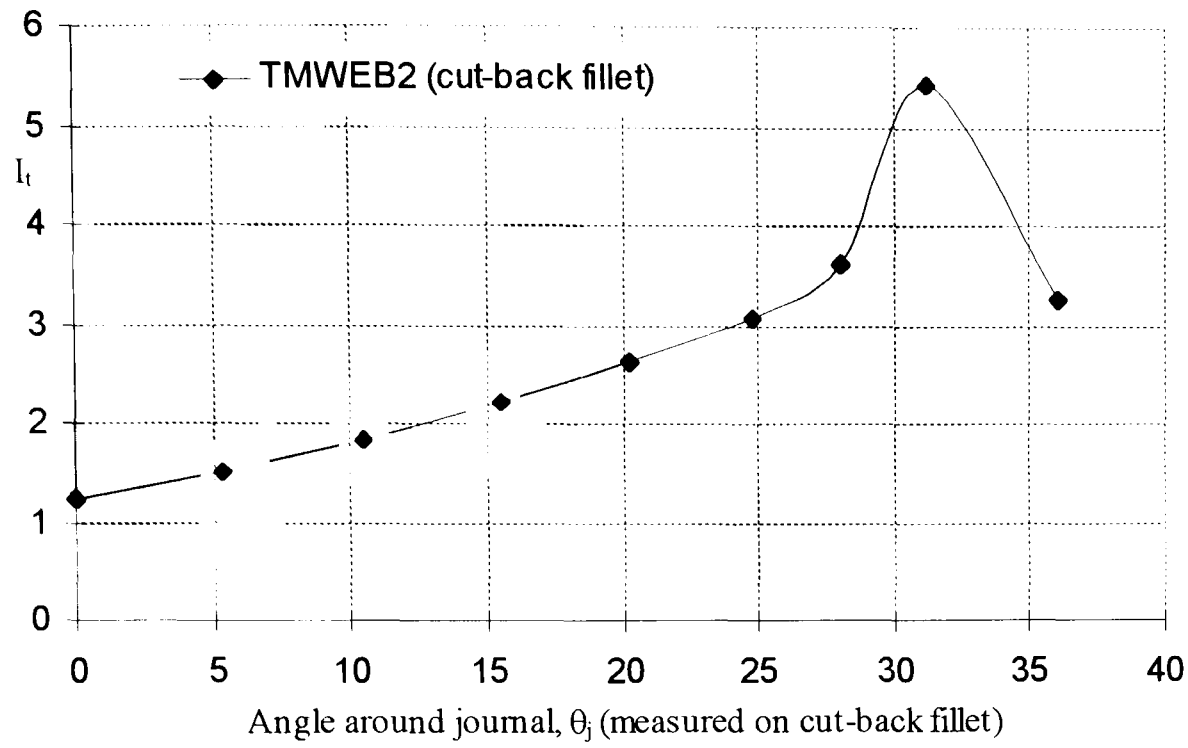

Figure 5.67. Maximum principal stress indices along the cut-back fillet under pure torsion

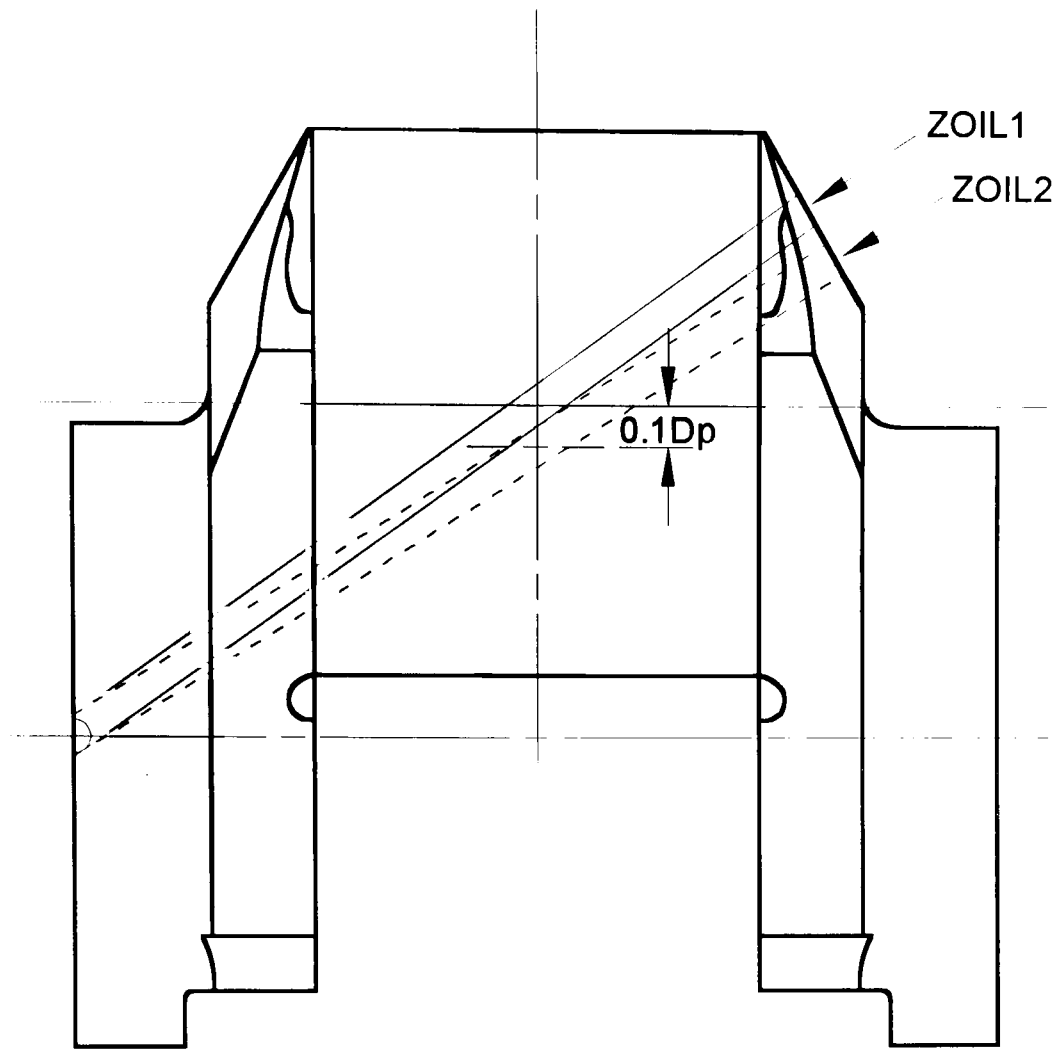

Figure 5.68. Location of oil holes modelled with the BE method

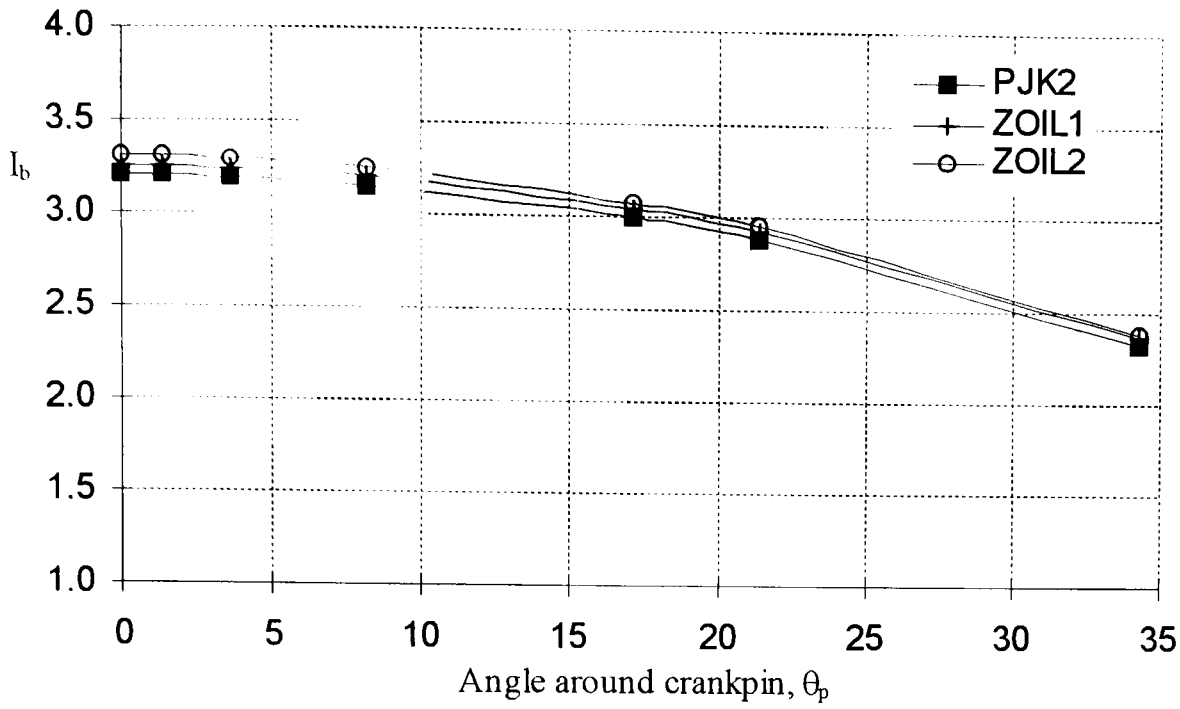

(a) Distribution around crankpin (3D analyses)

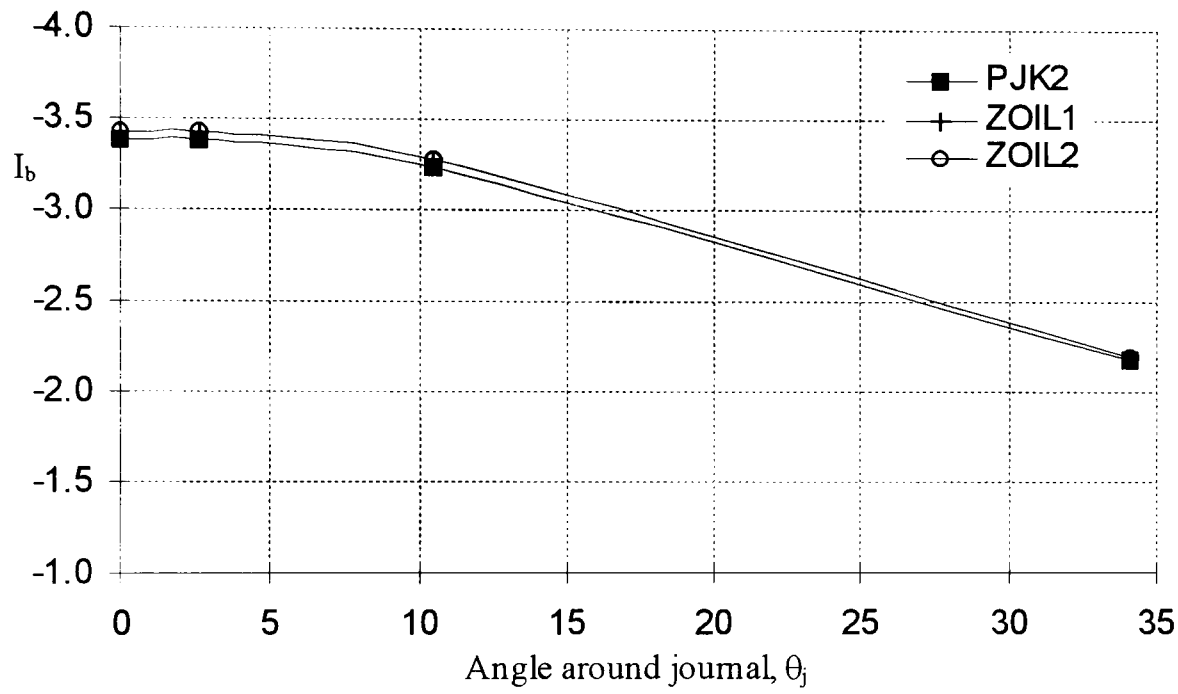

(b) Distribution around journal (3D analyses)

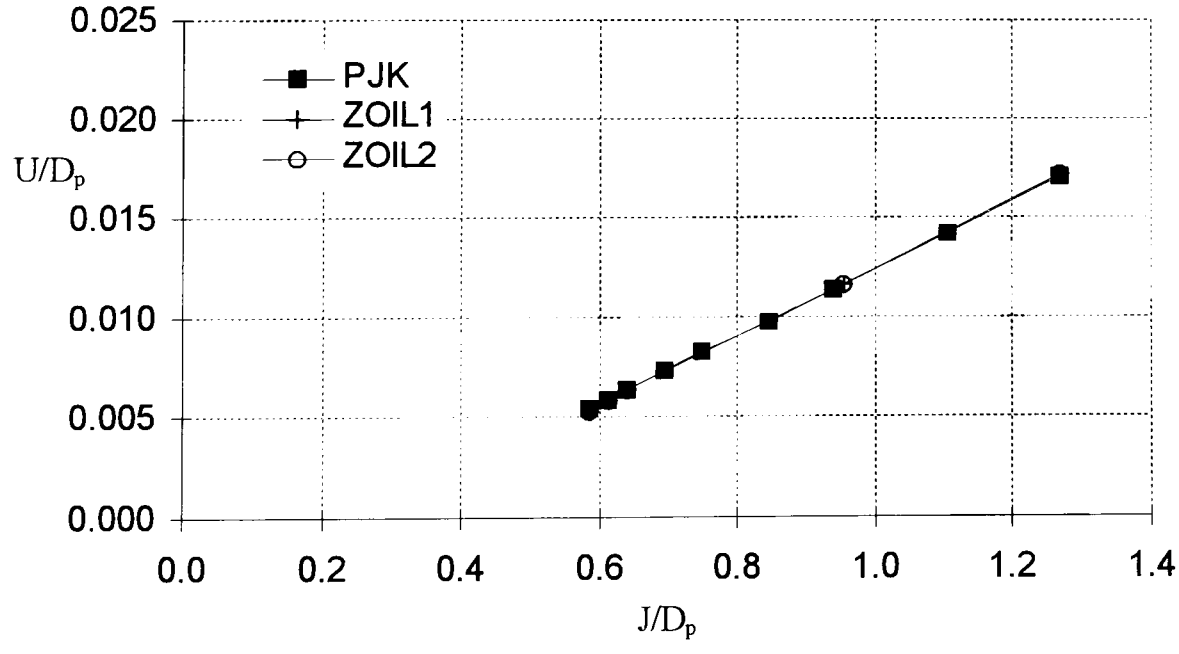

(c) Web deformation

Figure 5.69. Investigation into the effects of oil holes under radial bending

CHAPTER 6

COMBINED GEOMETRIC CHANGES

6.1 Introduction

Chapter 5 details the separate investigations into the many defining parameters of the crankshaft, but the designer will rarely change only one parameter at a time. It is necessary to see how the peak stresses are affected when several parameter changes are made simultaneously.

This chapter presents the investigations into combined geometric changes, with a view to reducing the peak fillet stresses as far as possible. It also attempts to unite the overlap and web thickness by considering them as variations of two parameters, H and ϕ. Finally, the K_b values obtained from all the investigations into individual parameters are collectively plotted against R/H and H/R, in an attempt to establish any trends that may exist.

6.2 Combining overlap and web thickness changes

There are two parameters that effectively unite the overlap and web thickness analyses. These are H, the minimum distance between fillets on the plane $\theta = 0°$, and ϕ, the angle of this minimum section to the vertical. Figure 6.1 shows the SCFs from the radial bending overlap and web thickness analyses plotted against angle ϕ. However, this graph does not readily present information about the important H term. Each point on the graph has a particular value of H, which suggests that it would be more informative to present lines of constant H against ϕ. Therefore, several more analyses were

performed to obtain this extra data, using as much existing data as possible. Results were obtained in the regions $0.383D_p < H < 0.662D_p$, $19.8° < \phi < 35.6°$, and are plotted in Figure 6.2. This figure provides general information about the effects of H and ϕ on the SCFs at both fillets, and implies the effects of the extent of overlap and web thickness. As H is increased, the SCFs increase, regardless of the value of ϕ. It has already been shown in Sections 5.4 and 5.5 that the increasing SCFs actually represent a decrease in peak stress (since the nominal stress is based in a bar dependent on H). Figure 6.2 also shows that there is generally an approximately linear decrease in SCF as angle ϕ is increased, the rate of which varies depending on the value of H. The exception to this rule is at higher values of H ($0.597D_p$ - $0.662D_p$) at the crankpin fillet, where an increase in SCF is seen with increasing ϕ.

6.3 Combined geometric changes

The parameters which define the shape of the crankthrow were investigated in Chapter 5 and several methods of reducing the peak stresses in the crankthrow were observed. These include optimising the shape of the fillets, adding crankpin and journal dimples and increasing the web thickness or overlap. Here, some of these changes are combined in an attempt to provide a stress reduction at both fillets. In order to narrow the range of analyses, only those changes which could be relatively easily implemented on the existing crankshaft, without requiring a major engine redesign, are investigated (denoted by $^{\#}$). In addition, two more models are created with reduced overlap, since this reflects a change recently made to the crankshaft analysed. The models created are detailed in Table 6.1.

Table 6.1 Models analysed with combined geometric changes

Model	Optimised Crankpin Fillet (OCF)	Crankpin Dimple (CD)	Journal Dimple (JD)	Reduced Overlap (RO)
C1#	✓		✓	
C2#		✓	✓	
C4#	✓	✓		
C6#	✓	✓	✓	
C3	✓			✓
C5	✓	✓		✓

The models are analysed with the BE method under both radial bending and torsion (the model names being prefixed by R or T respectively).

6.3.1 Radial bending

Presented in Figure 6.3 are the results for the models with combined changes (marked #), the models with the respective individual changes, and a datum crankthrow. At the crankpin fillet, compared to the datum crankthrow, the individual advantages of the optimised crankpin fillet (OCF) and the journal dimple (JD) are clear, giving reductions in crankpin fillet SCF of 11.4% and 6.2% respectively. When the two features are combined (RC1) the two stress reducing effects are superimposed to produce an SCF reduction of 18.3%, which is approximately the sum of the individual effects.

As was observed in the bore and dimple analyses, a crankpin dimple results in a slight peak stress increase at the crankpin fillet, which is probably due to the reduction in crank stiffness. This is also observed in the combined analyses, where for the models with a crankpin dimple (CD), RC2, RC4 and RC6, the stress indices increase

compared to the equivalent models without crankpin dimples; ZJDIM2, ZPFILL and RC1 respectively.

At the journal fillet, effects similar to those at the crankpin fillet are observed. As has been previously observed, the crankpin dimple produces a good stress reduction at the journal fillet (-11.1%). The optimised crankpin fillet causes a slight reduction in crankweb stiffness due to it's increased undercut into the web, which results in a stress increase at the journal fillet (+2.4%). Again, when the two features are combined (RC4), the stress effects are superimposed (+2.4% - 11.1% ≈ -10.1%).

For the models with a journal dimple added, RC1, RC2 and RC6, the stress indices increase slightly compared to the equivalent models without journal dimples; ZPFILL, ZDIMP2 and RC4 respectively. The superposition of stress effects when various geometric features are combined can be seen more clearly in Table 6.2. The changes in the peak stress figures are relative to those occurring in the datum crankthrow.

Table 6.2 Superposition of effects on stress (bending)

		COMBINED CHANGES		**INDIVIDUAL CHANGES**			
Fillet		Model	Change in	Change in peak stress, %			
Pin	Jnl	name	peak stress, %	OCF	CD	JD	Total
✓		RC1	**-18.3**	-11.4		-6.2	**-17.6**
	✓	RC1	**+2.9**	+2.4		+0.6	**+3.0**
✓		RC2	**-3.3**		+3.3	-6.2	**-2.9**
	✓	RC2	**-10.5**		-11.1	+0.6	**-10.5**
✓		RC4	**+8.1**	-11.4	+3.3		**-8.1**
	✓	RC4	**-10.1**	+2.4	-11.1		**-8.7**
✓		RC6	**-14.7**	-11.4	+3.3	-6.2	**-14.3**
	✓	RC6	**-9.5**	+2.4	-11.1	+0.6	**-8.1**

The table shows that by summing the variations in peak stress (from the datum) for individual change models (ZPFILL, ZDIMP2 and ZJDIM2) the result is very close to the change in peak stress observed on the equivalent combined change model. This is true at both fillets, and is a particularly useful method of estimating the effect of making many geometric changes to a crankthrow if the data for each individual change is available. This thesis provides such information for a wide range of geometric parameters and features.

Two further investigations are made to study the effect of combining a change of overlap with the optimised crankpin fillet and a crankpin dimple. This investigation is carried out for two reasons. Firstly because it reflects a change recently made to the crankshaft investigated. Secondly, to verify that the superposition conclusions hold true for fundamental crankthrow parameters (eg. overlap, web thickness, crankpin/journal diameters) as well as features such as crankpin/journal dimples.

The model RC5 is created with an optimised crankpin fillet, a crankpin dimple, and has the crankpin and journal overlap reduced by 17% to $0.385D_p$. At the crankpin fillet (Figure 6.4a) the SCF is reduced by 16%, but as has already been shown, because the nominal stress is based in the H × C beam (which changes shape as the overlap changes), the peak stress actually increases (by 24%). At the journal fillet (Figure 6.4b), the SCF is reduced by 20%, but the peak stress increases by 15%. The stress effects of the optimised fillet, crankpin dimple and reduced overlap (RO) are superimposed, and this is evident from Table 6.3.

Table 6.3 Superposition of effects on stress as overlap is reduced (bending)

		COMBINED CHANGES		INDIVIDUAL CHANGES			
Fillet		Model	Change in	Change in peak stress, %			
Pin	Jnl	name	peak stress, %	OCF	CD	RO	Total
✓		RC5	**+24.1**	-11.4	+3.3	+33.6	**+25.5**
	✓	RC5	**+14.7**	+2.4	-11.1	+25.0	**+16.3**
✓		RC3	**+18.9**	-11.4		+33.6	**+22.2**
	✓	RC3	**+28.1**	+2.4		+25.0	**+27.4**

Also shown in the Table 6.3 are the results for model RC3, which show the effects of superposition of the stresses for the optimised crankpin fillet and for the reduced overlap. The results at the crankpin fillet for this model are of interest because they show that the optimum fillet shape changes as the overlap is varied. Figure 6.5 shows the stress indicies at various values of α_p around the crankpin fillet. As the overlap is decreased, the latter section of the fillet determines the peak stress level to a greater extent. This indicates that the fillet could be tightened at small values of α_p. As the overlap is reduced, the minimum H section touches the crankpin fillet at a greater value of α_p, and the peak stress position moves accordingly.

It is anticipated that this will also be true as the web thickness is changed, and it highlights the fact that the optimum fillet shape is also dependent on the shape of the crankthrow (i.e. the values of H and ϕ).

6.3.2 Pure torsion

Under the loadcase of pure torsion, it is also possible to calculate the change in peak fillet stresses in a model with several geometric changes, by summing the effects on the peak stress of the individual changes. This can be seen in Table 6.4.

Table 6.4 Superposition of effects on stress (torsion)

Fillet		COMBINED CHANGES		INDIVIDUAL CHANGES			
		Model	Change in	Change in peak stress, %			
Pin	Jnl	name	peak stress, %	OCF	CD	JD	Total
✓		TC1	**+10.7**	+6.9		+3.7	**+10.6**
	✓	TC1	**+4.4**	+3.1		+2.0	**+5.1**
✓		TC2	**+5.7**		+2.1	+3.7	**+5.8**
	✓	TC2	**+1.5**		-1.2	+2.0	**+0.8**
✓		TC4	**+9.2**	+6.9	+2.1		**+9.0**
	✓	TC4	**+2.0**	+3.1	-1.2		**+1.9**
✓		TC6	**+13.1**	+6.9	+2.1	+3.7	**+12.7**
	✓	TC6	**+4.6**	+3.1	-1.2	+2.0	**+3.9**

Figure 6.6 presents the data from the torsion analyses at the crankpin and journal fillets. At the crankpin fillet, the optimised crankpin fillet and the journal dimple both cause the peak stress to increase. When these two features are combined in model TC1, the stress distributions are superimposed. Adding a crankpin dimple in each subsequent model causes a further slight increase in the peak stress.

At the journal fillet, the stress distributions caused by the optimised crankpin fillet and the crankpin dimple are superimposed in model TC4. Other models with an added journal dimple are subject to a slight peak stress increase due to the reduction in the crankthrow stiffness.

The results for the two models with reduced overlap are displayed in Figures 6.7. As mentioned in Section 6.3.1, the overlap is reduced to $0.385D_p$. No torsion analyses have been carried out for this value of overlap, so the change from the datum peak stress for such a model is not directly available. However, it is possible to extrapolate the increase in peak stress from the data that has been obtained from torsion analyses

over a range of overlaps. This data is presented in Section 5.4, Figure 5.43. The increase in peak stress at the crankpin fillet (compared to the datum overlap of $0.462D_p$) is calulated as approximately 15%. At the journal fillet, the increase is approximately 12%. These figures are used in the summation calculations in Table 6.5, and the resulting total change in peak stress shows good agreement with the combined change stress increase. This also shows that the linear relationship between peak torsional stress and overlap which is suggested in Figure 5.43 is valid.

Table 6.5 Superposition of effects on stress as overlap is reduced (torsion)

		COMBINED CHANGES		**INDIVIDUAL CHANGES**			
Fillet		Model	Change in	Change in peak stress, %			
Pin	Jnl	name	peak stress, %	OCF	CD	RO*	Total
✓		TC3	**+23.2**	+6.9		*+15**	**+21.9**
	✓	TC3	**+16.8**	+3.1		*+12**	**+15.1**
✓		TC5	**+23.9**	+6.9	+2.1	*+15**	**+24.0**
	✓	TC5	**+11.2**	+3.1	-1.2	*+12**	**+13.9**

* Extrapolated data from Figure 5.43

6.4 The relationship between K_b, R and H.

This thesis presents the results of several analyses that have been carried out in order to investigate the effects of the crankshaft geometry on the fillet SCFs. It is found that parameters such as overlap, web thickness, and crankpin/journal diameter simply change the stress level, whereas features such as bores and dimples significantly change the stress distribution. Here, the K_b values obtained from the former list of analyses are united in order to achieve an understanding of the general relationships between K_b, R and H.

Figure 6.8 presents every K_b value from the 3D crankpin/journal diameter, overlap and web thickness analyses. The SCFs at both the crankpin and journal fillets are plotted on one graph against R/H. For ease of comparison of SCFs at the two fillets, the journal fillet K_b values are taken to be positive, but still represent compressive stresses. All K_b values are based on the H × C nominal stress, including the web compression component.

Although there is a degree of scatter of the K_b values, the general trend is that the SCFs fall as R/H increases. It is also apparent that the journal fillet SCFs are more widely spread than those at the crankpin fillet.

Neuber [21] formulated equations relating to grooved shafts in bending and torsion, and Peterson [22] calculated and plotted values using the Neuber theory. It is noteable that Figure 6.8 shows agreement with the Neuber graph relating to bending of a notched shaft (Figure 6.10). The K_b values in Figure 6.8 are generally higher, but this is simply due to the chosen nominal stress. This has already been discussed in Chapter 4, where it is found that the H × C method does lead to SCFs which are higher those based on the 'exact' slanted eye-shape. The Neuber chart also highlights the fact that the scatter in Figure 6.8 could be due to different D/d ratios (where d is equivalent to H). However, it is difficult to define Neuber's D on the crankshaft, yet it must effectively be changing to account for the scatter of results. The only way in which this is possible is if the inclination of the H × C beam is changed. The angle of the minimum H section to the vertical is defined as ϕ, and as the crankthrow geometry is changed, this angle will also change. It is then possible to see how Neuber's D might

vary as the crankshaft geometry is changed. This theory is tested by plotting the data presented in Figure 6.8, as series of approximately constant ϕ (i.e. so that Neuber's D does not change for each series of data). The crankpin and journal fillet K_b values are shown on separate graphs for clarity, and are plotted against H/R (instead of R/H). The resulting curves are presented in Figures 6.9.

The relationships between the data points having approximately equal values of ϕ are obvious (especially so at the journal fillet). As ϕ is increased, the SCFs generally decrease, and as was observed in the crankpin/journal diameter analysis, the projected intercept K_b values at H/R = 0 are unity.

It should be noted that in many cases, a change in ϕ is due to a variation in the web thickness. In these analyses, the reaction at the journal is moved axially. It has been shown in the validation of the FE method (Section 3.2.2.3) that the K_b values are sensitive to the axial position of the loads and this is a possible reason for the differing magnitudes of the various ϕ data sets.

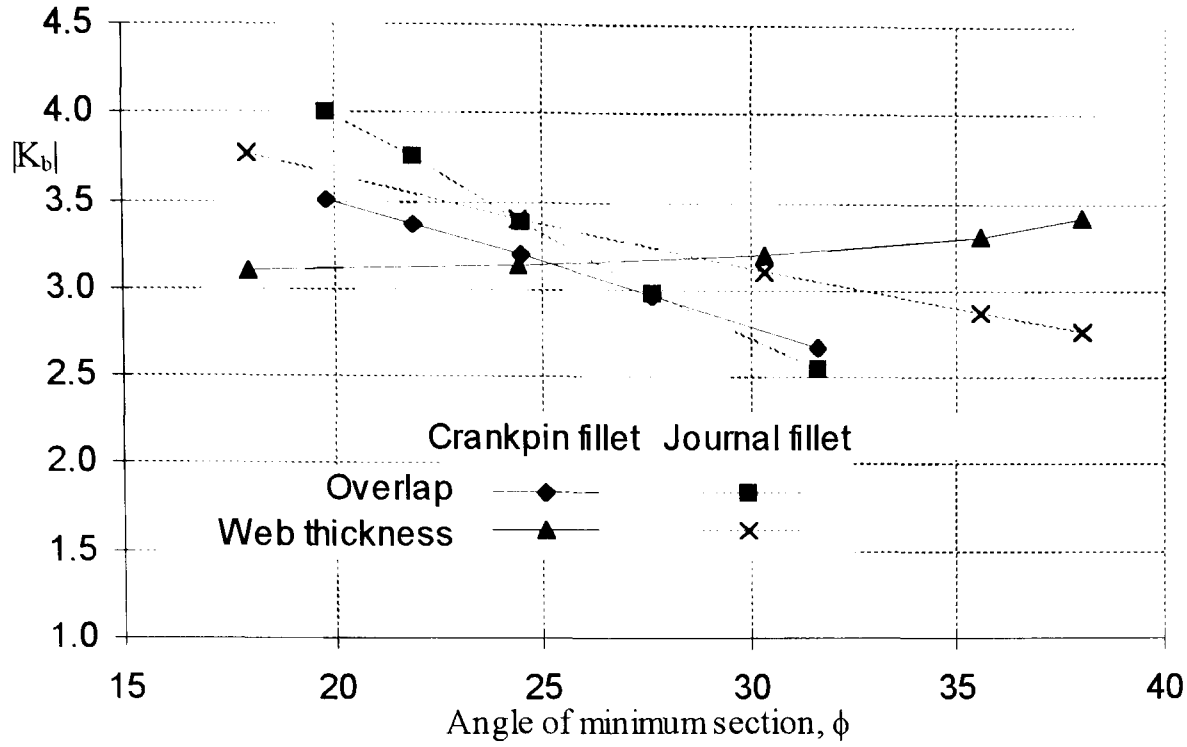

Figure 6.1. Stress concentration factors obtained from radial bending analyses of overlap and web thickness, plotted against angle ϕ

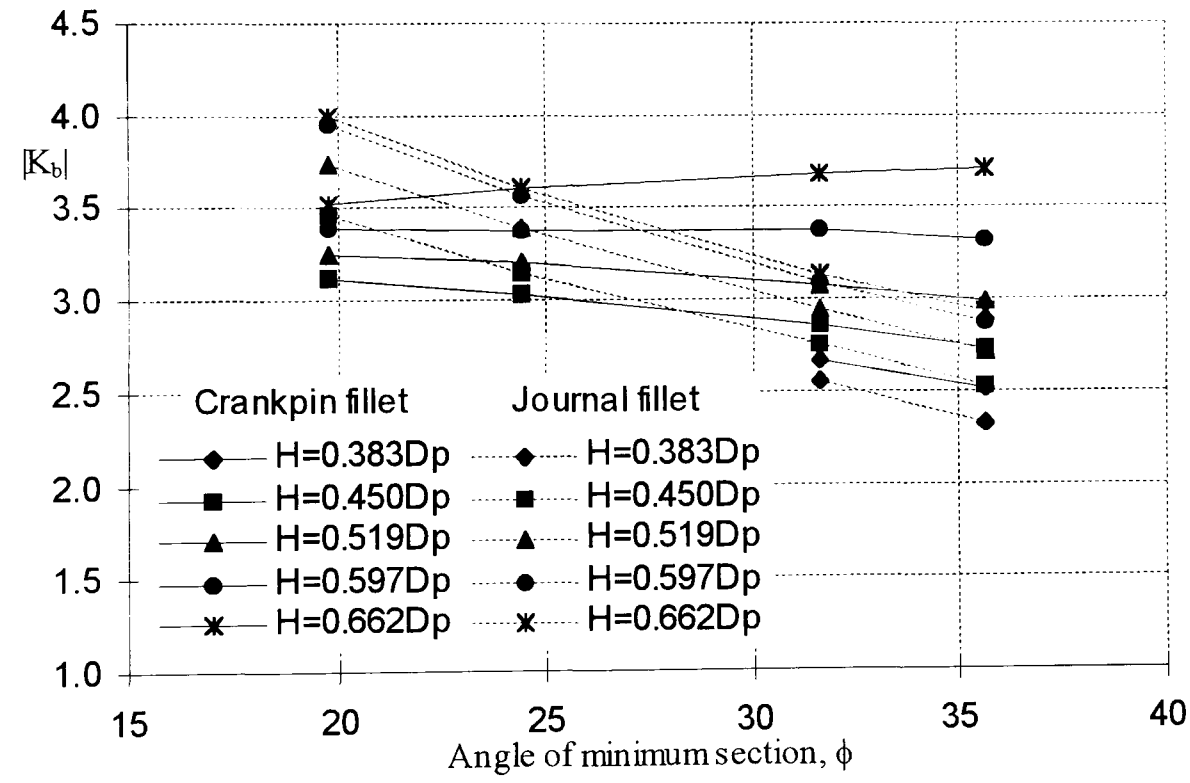

Figure 6.2. Stress concentration factors obtained from radial bending analyses of overlap and web thickness, plotted in data sets of constant H against angle ϕ

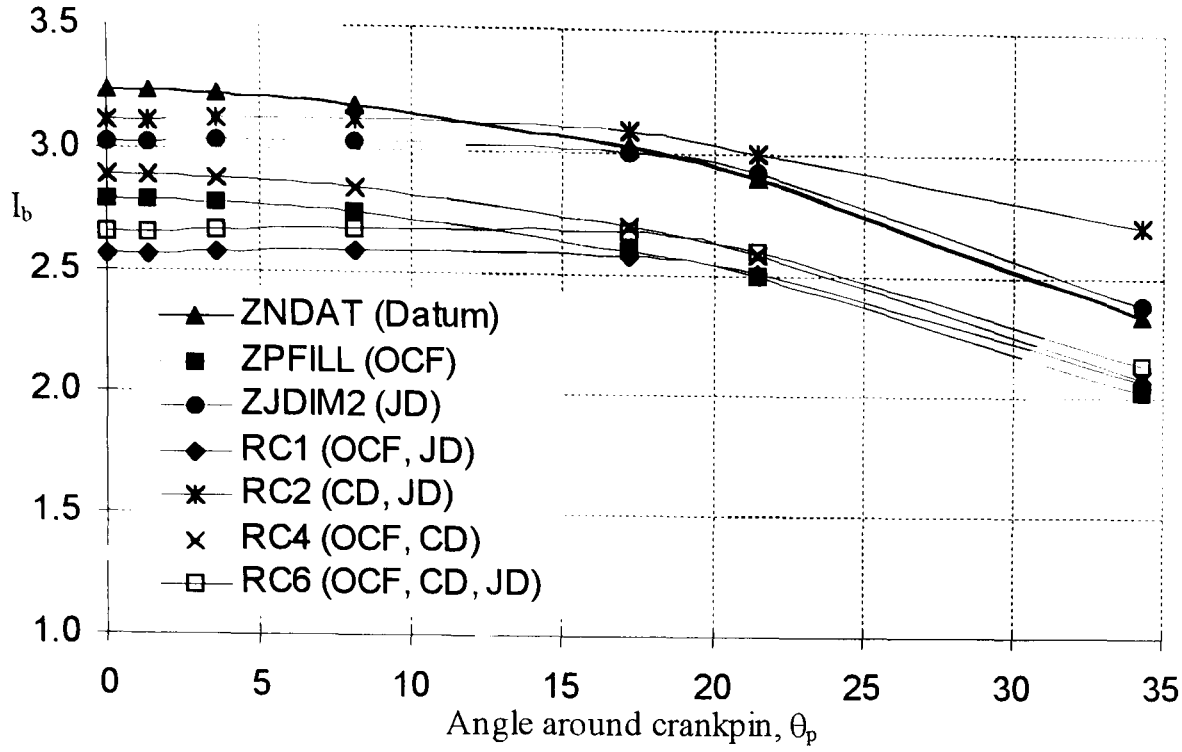

(a) Distribution around crankpin (3D analyses)

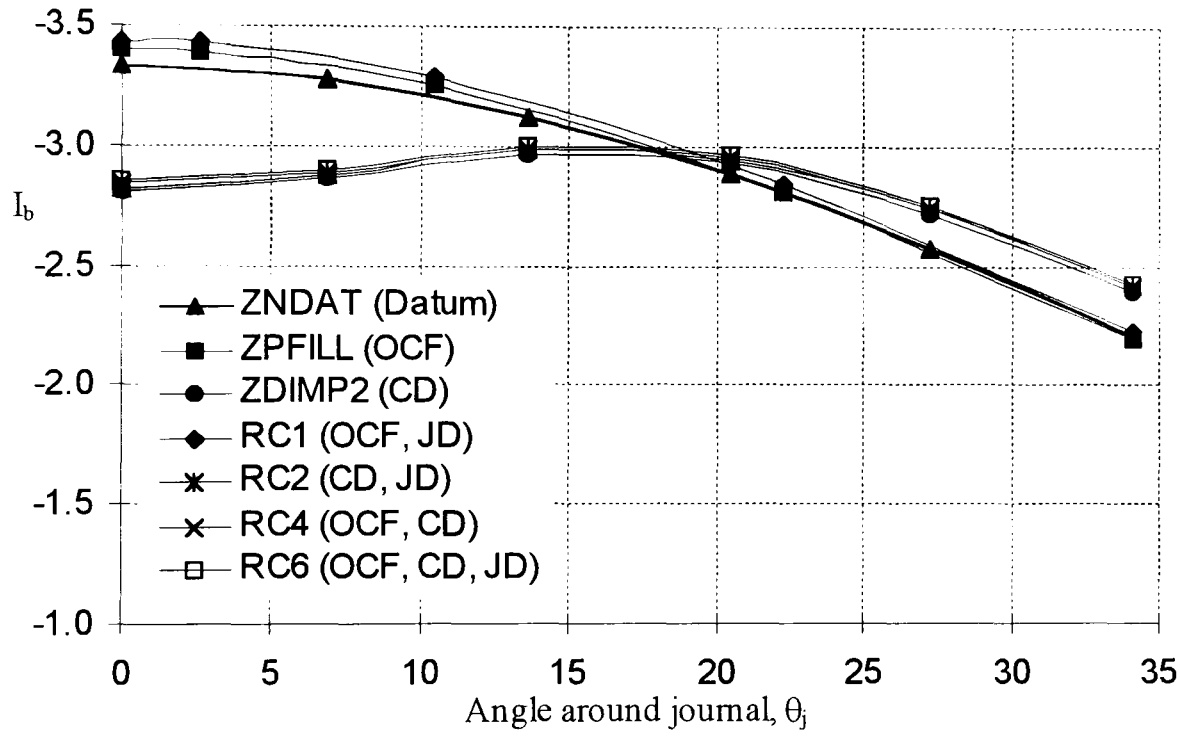

(b) Distribution around journal (3D analyses)

Figure 6.3. Investigation into the effects of combining geometric features on a crankthrow under radial bending

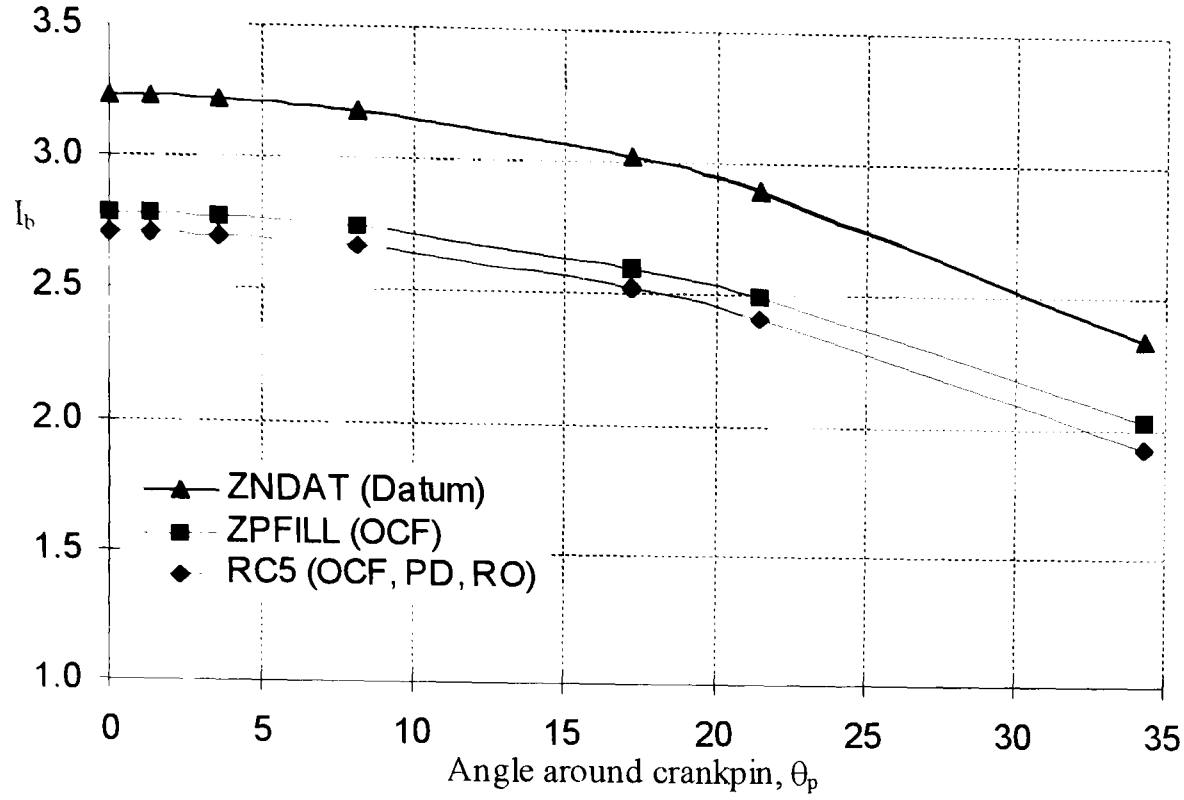

(a) Distribution around crankpin (3D analyses)

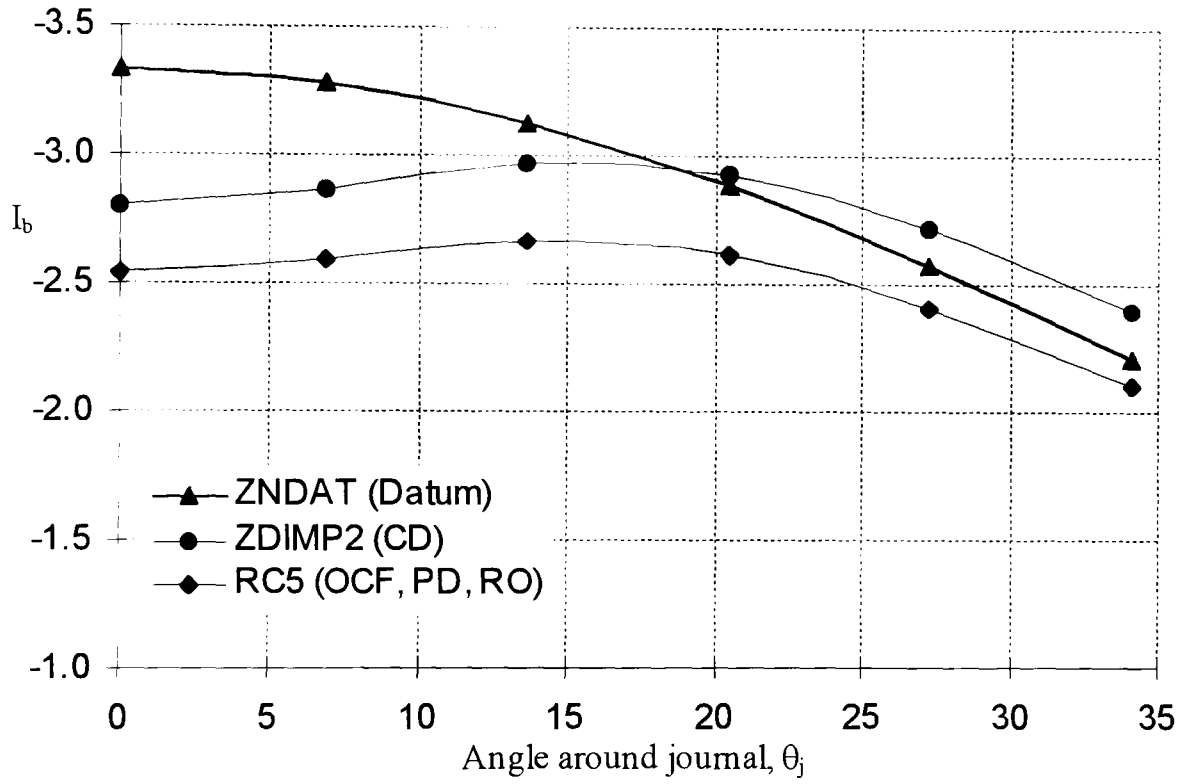

(b) Distribution around journal (3D analyses)

Figure 6.4. Investigation into the effects of combining individual variations in crankthrow geometry under radial bending

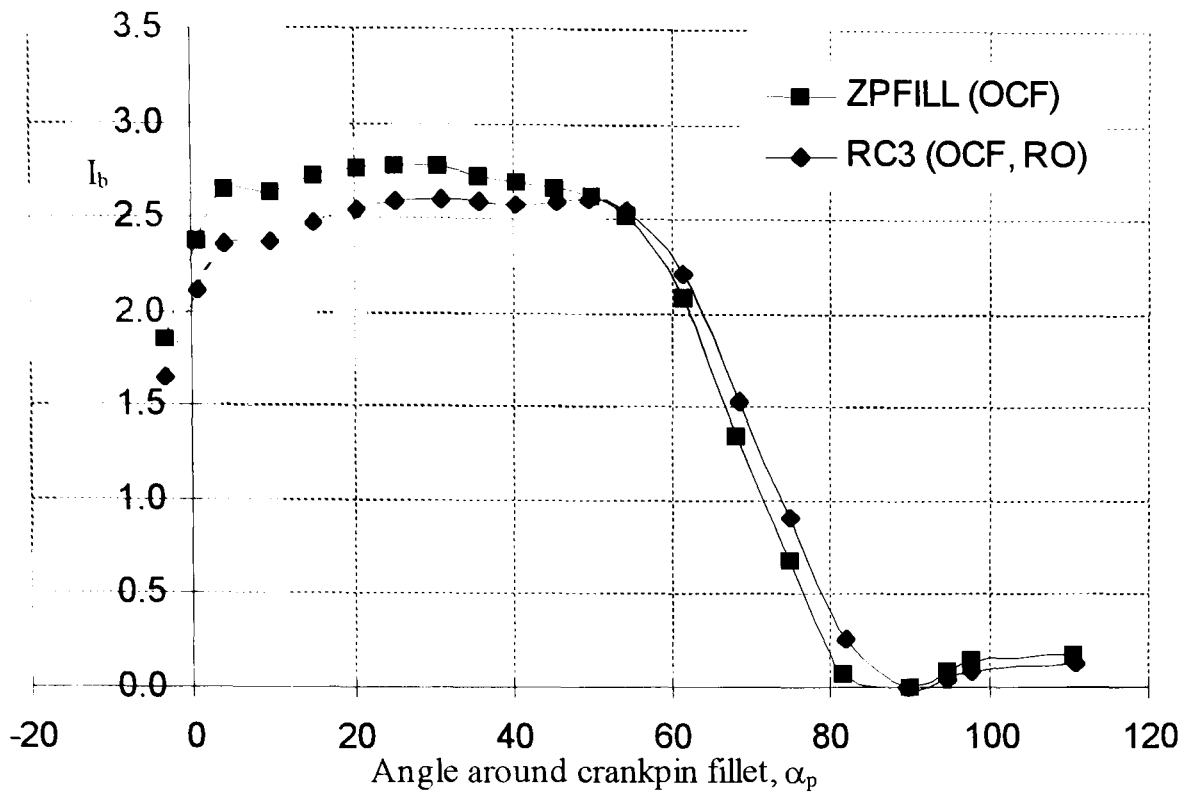

Figure 6.5. Investigation into the effects on the stress distribution under radial bending in the optimised crankpin fillet when the overlap is reduced

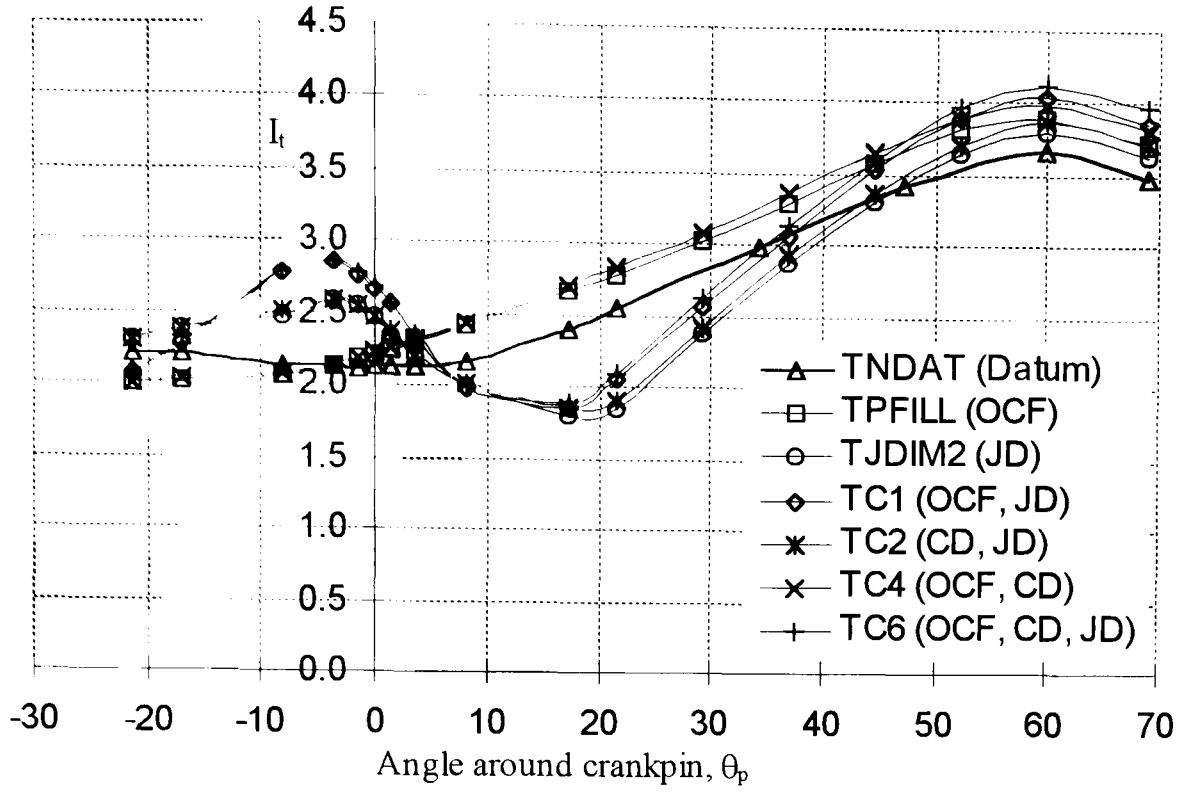

(a) Distribution around crankpin (3D analyses)

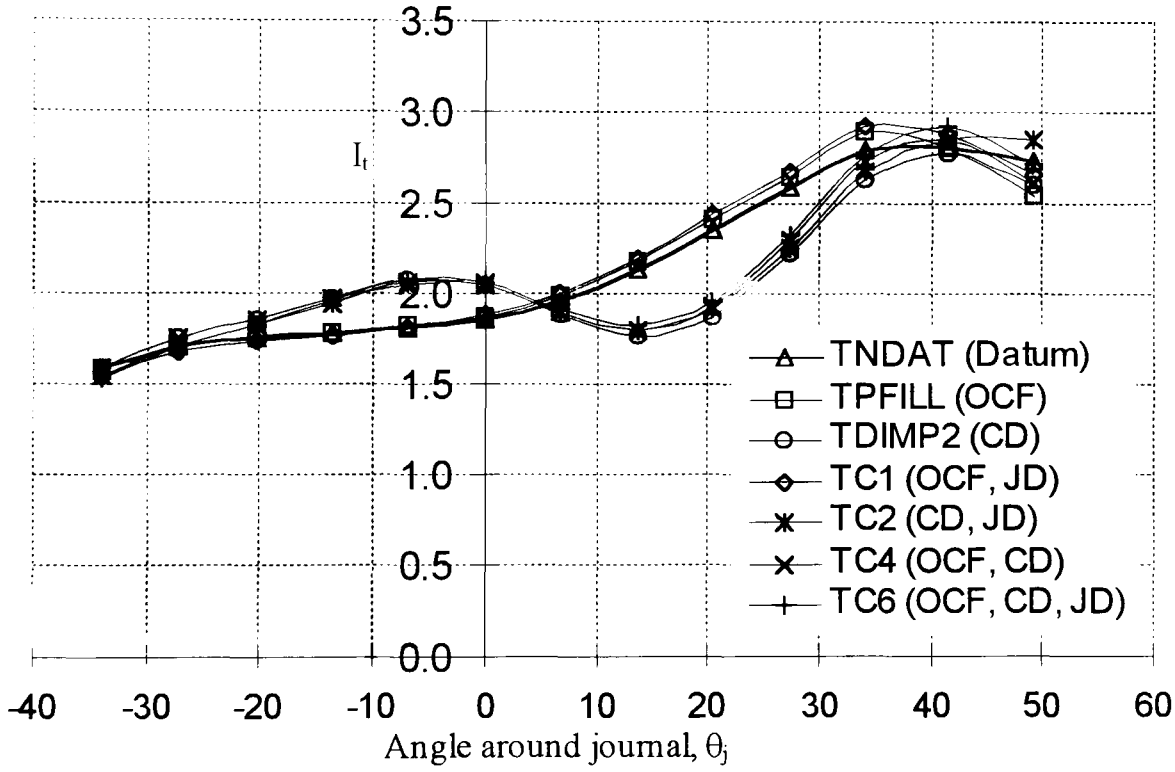

(b) Distribution around journal (3D analyses)

Figure 6.6. Investigation into the effects of combining geometric features on a crankthrow under pure torsion

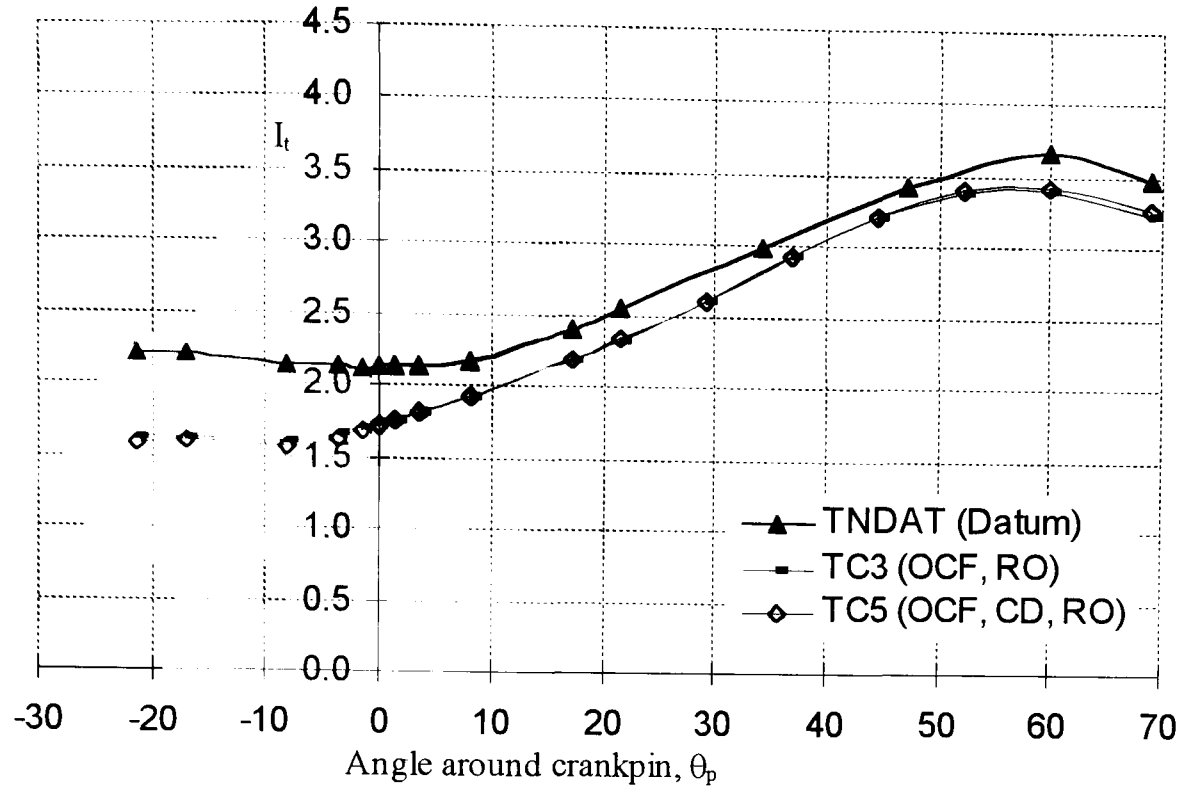

(a) Distribution around crankpin (3D analyses)

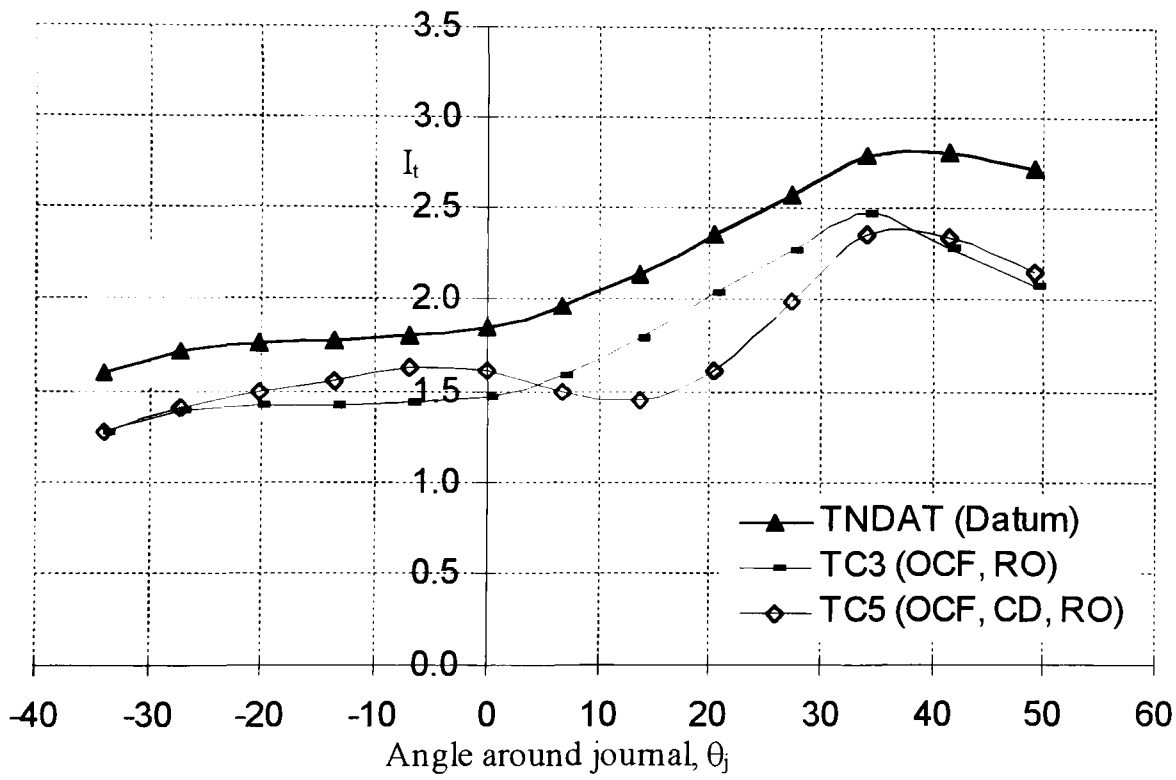

(b) Distribution around journal (3D analyses)

Figure 6.7. Investigation into the effects of combining individual variations in crankthrow geometry under pure torsion

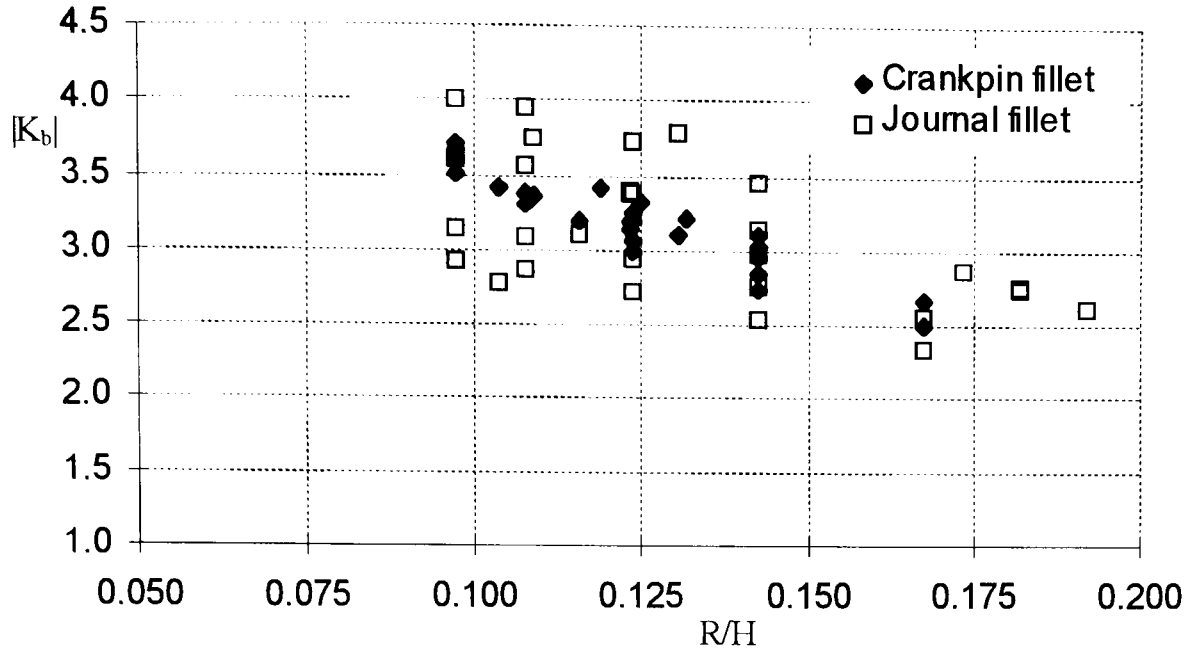

Figure 6.8. K_b plotted against R/H for comparison with Neuber curves [22]

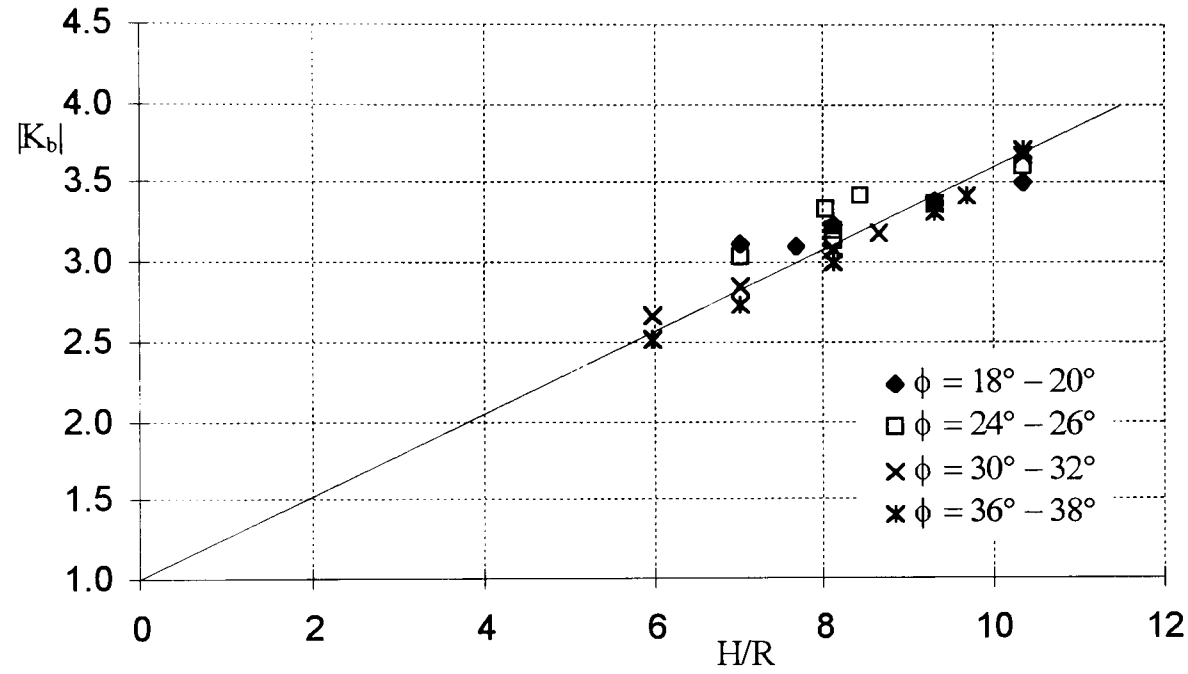

(a) 3D crankpin fillet

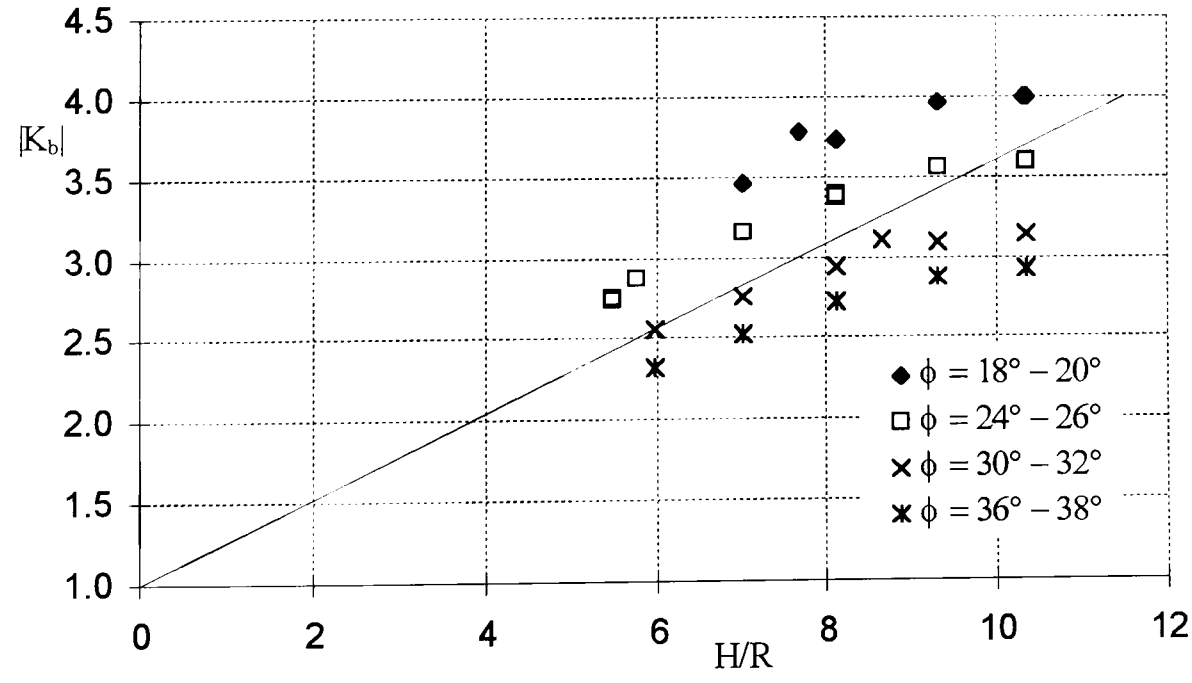

(b) 3D journal fillet

Figure 6.9. K_b plotted against H/R in data sets of constant ϕ

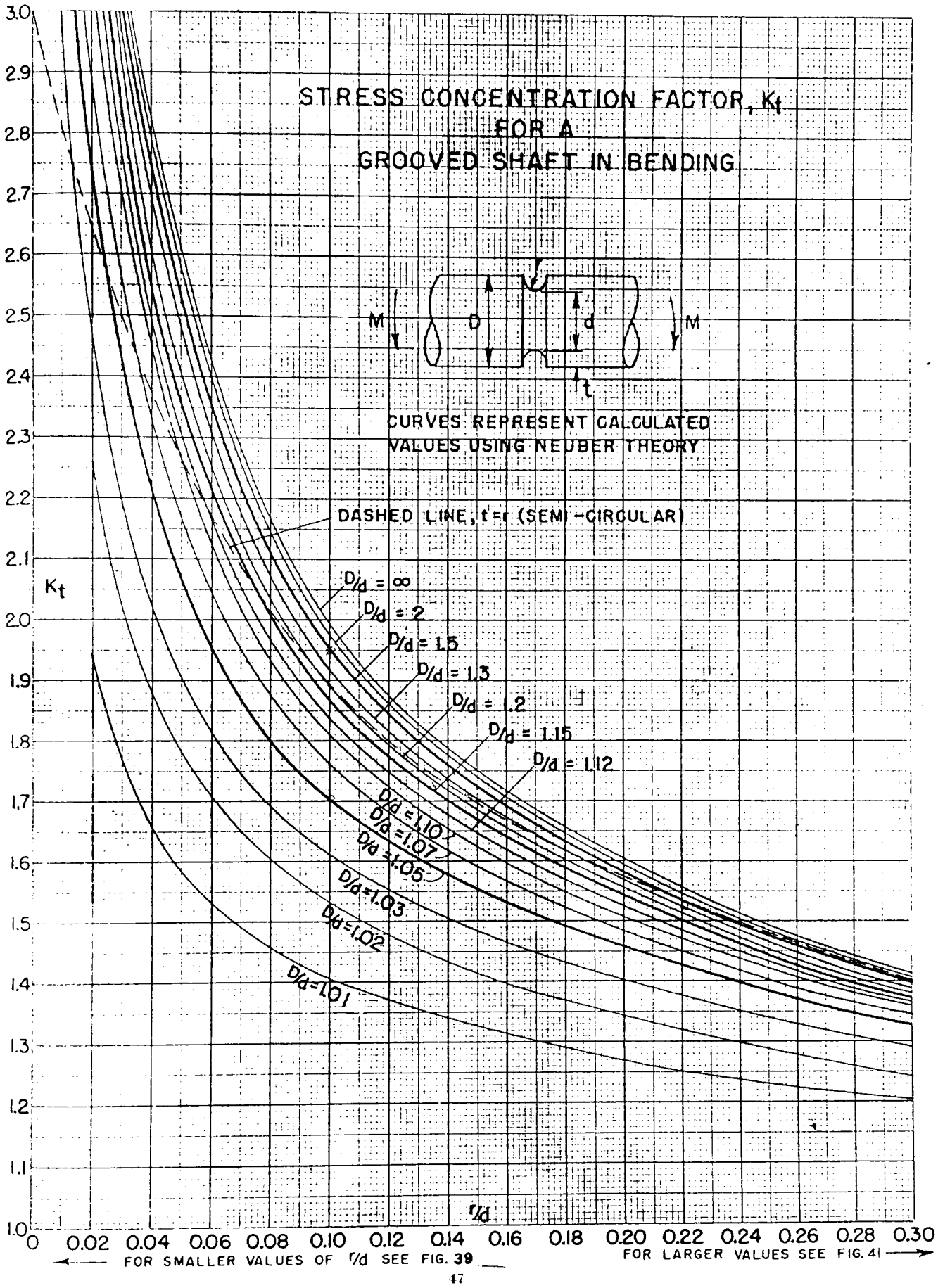

Figure 6.10. Neuber curves plotted by Peterson relating to SCFs in a grooved shaft under bending
Peterson [34]

CHAPTER 7

DISCUSSION AND CONCLUSIONS

7.1 Summary of analysis methods

Stresses in the crankshaft were investigated with the aid of the Finite Element and Boundary Element methods. With sufficient mesh refinement and care when applying loads and boundary conditions, both methods proved reliable, producing consistent, repeatable results.

The FE method, having been developed earlier and in common use for a longer period than the BE method, was found to offer benefits in the ease of use of the pre and post processors. However, the modelling process itself was substantially quicker with the BE method because of the requirement of surface only modelling. This made it possible to relatively easily add bore holes, dimples and oil holes to the crankthrow, a task which would have proved very difficult with a manually meshed FE model.

The work presented in this thesis shows that it is possible to use the FE and BE methods to accurately analyse stress distributions in crankshafts. The two methods have been validated against each other, against frozen stress photoelasticity and strain gauge data, and good agreement is obtained in all cases. The methods can detect variations in stress distributions as subtle changes are made to the crankthrow geometry. It is also true that these numerical methods offer significant advantages over the traditional experimental methods in speed of analyses, repeatability, ease of geometric modification and reduced cost of analyses.

Both the FE and BE analyses presented in this thesis made substantial demands on the computer systems in terms of workspace and processor speed, often running close to the system limits. Although this thesis only presents static stress analyses for specific loadcases, the numerical methods of analysis can be used to simulate dynamic analyses. This has been shown by Rasser, Resch and Priebsch [36], who loaded a crankthrow with the appropriate displacements at discrete angles around one operating cycle. However, it is clear that as the speed of processors and the complexity of the software increases, it will be possible to perform truly dynamic stress analyses of the cycle of a complete crankshaft.

It is intended that the results presented here, for bending and torsion, will simply provide the crankshaft designer with a sound understanding of the effects of the crankshaft geometry on the peak fillet stresses.

Several modelling aspects are investigated, including symmetry, loading and boundary conditions, and the use of 2D and 3D representations of the crankthrow. It is found that geometric symmetry can be used to reduced the problem size, even with the non-symmetrical vee-loading applied. The most appropriate methods of modelling the various loadcases are as follows;

- Radial bending - quarter crankthrow encastré (or restrained axially with appropriate full body restraints) at crankpin centre-plane, loaded at crankpin quarter point and journal centre with point loads. Journal extended to ensure regular deformation of journal.

- Pure bending - quarter crankthrow encastré at crankpin centre, loaded at free face of extended journal with a couple in the $\theta = 0°$ plane.
- Torsion - half crankthrow (one end) encastré at crankpin centre, loaded with two couples at free face of extended journal in plane of free face.

Additionally, under bending, it is noted that 2D modelling can be used to obtain a good approximation of the fillet stress distributions that exist in the 3D model. This is demonstrated in Section 5.2. This can offer significant advantages in terms of ease of modelling and reduction in analysis time, and since this loadcase sees the largest loads, optimising the crank design for bending is a good first step in the design process.

7.2 Nominal stress basis

Many different nominal stresses are used in the literature available on the subject of crankshaft stress analysis. Several alternatives are discussed in this thesis, based on their suitability for ease of calculation under bending and torsion, and also the requirement that they are based in a region that develops the fillet stresses.

The minimum H section between the crankpin and journal fillets is found to be critical in determining the peak stress levels. Therefore, the most appropriate nominal stresses are based in this neck section.

The slanted eye-shape beam is found to be the most accurate representation of the load transmission area, thus producing SCFs on the 3D model that agree well with 2D and also with classical theory. However, the nominal stress is not easy to calculate,

especially so under torsion. For this reason, a less complex beam with a similar cross-sectional area is used. This is the H × C beam, which is a rectangle defined by the minimum distance between the fillets, and the maximum width of the crankpin and journal overlap. Such a beam has several advantages over the various beams used in the literature;

1. Only one bar is needed for bending and torsion.
2. The nominal stresses are easily calculable for bending and torsion.
3. It touches the fillets near the positions of the maxima in the crankthrow due to bending and torsion.
4. It produces SCFs which are directly related to the region developing the fillet stresses.
5. The SCFs are therefore of a reasonable magnitude.
6. Good correlation is shown with Neuber's analysis of SCFs in simple notched bars.

It is important to consider the compression that occurs in the web under radial bending. Under radial bending, the web compression in the neck will cause the compressive journal fillet stress (due to bending) to increase, and the tensile crankpin fillet stresses to decrease. Thus for equal sized crankpin and journal fillets, the journal fillet stresses will be higher than those in the crankpin fillet. It is possible to take this into account when calculating SCFs at the fillets. This is achieved by adding the compressive stress to the nominal stress at the journal fillet and subtracting it from the nominal stress at the crankpin fillet. Therefore, the magnitude of the journal fillet

nominal stress is greater than that at the crankpin fillet. Under pure bending, the web compression component does not exist. This leads to different fillet stress distributions under radial and pure bending.

7.3 Geometric investigations

All of the governing dimensions of the crankshaft have been investigated, as well as more detailed features such as fillet shape and bores or dimples. Changing the governing dimensions of the crankshaft will generally have a significant effect on not only the size and shape of the crankshaft, but also many other engine components. The features can be added and optimised, yet only affect the geometry of the crankshaft.

7.3.1 The relationship between peak stress and R

The SCFs at the crankpin/web and journal/web intersections can be minimised by optimising the fillet shapes in these regions. The compound crankpin fillet is studied and optimised to produce a low, flat stress distribution over the majority of the fillet. Several important points should be noted when designing such a fillet. The following apply to the bending loadcases.

1. Increasing the size of the major radius by fixed intervals has a decreasing return on the reduction of stress levels in the fillet.
2. As the discontinuities in size between adjacent radii increase, the resulting spike in the stress distribution increases.
3. The use of a large initial blend angle with a small radius can have a detrimental effect on the peak stress level.

4. The SCF can be moved from minor radius R_{p1}, to major radius, R_{p2}, by either increasing radius R_{p1} or reducing the blend angle α_{p1}. Similarly, the SCF can be moved from the minor radius, R_{p3}, to major radius, R_{p2}, by increasing radius R_{p3}, or increasing the blend angle α_{p2}.
5. A relatively flat stress distribution and small fillet can be achieved by taking the 'step-approach' and gradually decreasing the radii as α increases.

Under radial bending, the optimised crankpin fillet produces an SCF some 11% lower than that occurring in the datum fillet. Under torsion, the peak fillet stresses occur at larger values of α, which if the fillet is optimised for bending, may lead to relatively high stresses (in this case 9% higher than the datum SCF). The designer must take this into consideration when designing the fillet and may want to design a larger radius in this region to accommodate both bending and torsion.

It is found that increasing the axial and radial depth of the undercut fillet has a small effect on the overall stiffness of the crankthrow. For the optimised fillet, the web spread increases by 2.9% under bending and 5.5% under torsion.

7.3.2 The relationship between peak stress and H

In changing the governing crankshaft dimensions, it is observed that the dimension H is critical in determining the peak fillet stress levels. H can be changed by varying the crankpin and journal diameters, the overlap of crankpin and journal, and the web thickness. In all cases, as H is reduced the peak fillet stresses increase (for constant

fillet radii). Conversely, the K_b value, when based on the H × C beam, shows a reduction as H is reduced.

It is suggested that in light of the above, it might be possible to increase the output of the engine without a major engine re-design. This could be achieved by increasing the journal diameter. This enables a greater firing pressure due to the larger bearing area. It also increases the overlap, thereby increasing H, which produces a reduction in peak stress (to offset the stress increase due to the greater loads). The greater overlap also has the effect of further stiffening the crankshaft under bending and torsion. The throw (and therefore stroke) and web thickness of the crankshaft remain constant, and the inertia forces are unchanged by a bigger journal, meaning that the balance weights do not have to be increased in size.

If the designer wants to reduce web thickness, but does not want to increase stresses, the reduction in web thickness could be accompanied by an increase of overlap. This has the advantages of combatting the increase in stress due to the thin web (by increasing dimension H), stiffens the crankshaft, and also reduces the out of balance crankpin mass, thus requiring thinner balance weights. In addition, these changes all reduce the inertia of the crankshaft, permitting a higher rate of revolution. Indeed, this has been the trend over the past few years, leading to many thin webbed, highly overlapped crankshafts. The only real constraint on this process is the required engine capacity, since the stroke is determined by the extent of overlap, and the cylinder bore is controlled by the spacing of individual crankthrows.

The value of ϕ, the angle of inclination of H, also appears to affect K_b. As ϕ is increased, a reduction in K_b is noted (except at the crankpin fillet with high values of H). However, it is felt that the variations in K_b, for a given H/R value, are at least partially due to the differing axial positions of the reactions at the journal, due to changes in the web thickness.

Briefly considering the effects of the individual changes, it is clear that for the ranges analysed:

- As the crankpin and journal diameters are increased, the peak stresses show a linear reduction under bending and little change under torsion. An increase in crankthrow stiffness is observed.
- As the overlap is increased, the peak stresses show a non-linear (decreasing) reduction under bending, and a linear reduction under torsion. An increase in crankthrow stiffness is observed.
- As the web thickness is increased, the journal fillet peak stress shows a linear reduction under bending, but there is little change in stress at the crankpin fillet. Under torsion, the peak stresses show a non-linear reduction (at a decreasing rate). An increase in crankthrow stiffness is observed.

7.3.3 Bores and dimples

Bores, which are generally used for lightening purposes, are also seen to have a significant effect on stress distributions in the fillets around the crankpin and journal. Dimples are also observed to have similar effects on the stress distributions, but have

the added benefit of being slightly more versatile in terms of parameters that can be varied.

Generally, a crankpin bore or dimple will have the greatest effect on the journal fillet stress distribution, under both bending and torsion. Similarly, a journal dimple will have the greatest effect at the crankpin fillet.

Under bending, several observations are made;

- A bore or dimple has the effect of moving the peak stress from a single peak on the plane $\theta' = 0°$ to two peaks symmetrical about the plane $\theta = 0°$ ($\pm 15° < \theta' < \pm 20°$ in the analyses performed). It is suggested that this is due to the interruption of the load-path near to the adjacent fillet. This theory is supported by the fact that as the bore/dimple diameter is increased, the peaks move to greater angles of θ.
- The peak stresses occurring in the fillet adjacent to a bore or dimple are lower than the peak stresses that would occur if the adjacent crankpin or journal was solid. The greatest reduction achieved was 11% in the journal fillet (with a crankpin dimple) and 6% in the crankpin fillet (with a journal dimple).
- Bores or dimples reduce the crankthrow stiffness, causing the stresses in the other (non-adjacent) fillet to rise slightly.

- As the diameter of the bore or dimple is increased, the stress in the adjacent fillet on the plane $\theta = 0°$ decreases, and the SCF moves to an increasing value of θ.
- The bore or dimple has a greater effect on stress reduction on the plane $\theta = 0°$ as it is moved closer to the adjacent fillet, but this can cause the peak stresses to increase.
- Increasing the depth of a dimple reduces SCFs slightly. However, there is a point where a further increase in depth has no further effect on SCFs.
- As the angle of inclination of a dimple is increased, stresses close to $\theta = 0°$ fall, but increase at greater angles of θ.

Under torsion, compared to a crankthrow with a solid crankpin and journal, crankthrows with bores and dimples are subject to significantly different stress distributions. However, there is little change in the fillet SCFs. The crankpin bore and dimple analysed cause a peak stress reduction in the journal fillet of around 2%. The journal dimple caused an increase in crankpin fillet peak stress of 4%. As was observed under radial bending, bores and dimples cause a reduction in crankthrow stiffness under torsion, resulting in slightly increased peak stresses at the non-adjacent fillet.

7.3.4 Cut-back web

The advantages of the cut-back web as a method of reducing the out of balance mass are obvious, but the BE analysis highlights an important point that must be taken into consideration when designing such a feature.

Under radial bending, the journal fillet stress distribution is flattened and the SCF is reduced by 8%, remaining on the plane $\theta_j' = 0°$. The stresses in the radius of the cut-back fillet are lower than in the journal fillet because of the larger radius. The crankpin fillet peak stress increases slightly due to the decrease in stiffness of the crankthrow.

Under torsion, the SCF at the journal fillet is reduced by 6%, but is increased at the crankpin fillet by 5%. However, it is the stress distribution in the cut-back fillet that causes most concern. The peak stress, which occurs at the thinnest point of the web is twice as high as that in the journal fillet. The web is thinnest at the point where the cut-back is close to the crankpin fillet on the opposite side of the web. It is likely that this SCF would cause the crankshaft to fracture under torsion, and highlights the fact that it is important to use a tool such as the BE method before implementing a major design change.

7.3.5 Oil holes

For the geometry analysed, oil holes through the crankthrow have little effect on fillet stress distributions, and no effect on the overall crankthrow stiffness. Under radial bending, the fillet stresses increase by 1-2% depending on how close they are to the respective fillet. The stress increase is most probably due to the increase in nominal stress in the neck region due to the reduction in the cross-sectional area of the highly stressed material here.

Stress concentrations at the breakouts of oil holes at the crankpin and journal bearing surfaces are not analysed in this thesis because of the availability of literature detailing analyses of breakouts in flat plates and cylinders. It is however suggested that breakouts specifically at crankshaft bearing surfaces could be investigated as a further piece of work.

7.4 Combined geometric changes

The effects on the fillet stress distributions of individual geometric changes to the crankthrow have been documented in this thesis. It is found that it is possible to predict the effects of combined geometric changes by superimposing the effects of the individual changes. This is true under the loadcases of bending and torsion. In nearly all cases analysed, the change in peak stress predicted by superimposing the effects of the individual geometric changes, was accurate to within 1% of the change in peak stress observed on the crankthrow with several geometric changes.

For example, under radial bending, a crankthrow with an optimised crankpin fillet, and a crankpin and journal dimple shows a peak crankpin stress which is 14.7% lower than that occurring in the datum crankthrow. The individual effects on stress due to the optimised crankpin fillet, crankpin dimple and journal dimple are -11.4%, +3.3% and -6.2% respectively. Superimposing these effects leads to a predicted decrease in stress of 14.3%.

This is a particularly useful method of estimating the effect of making many geometric changes to a crankthrow, as long as the data for each individual change is available.

This thesis provides such information for a wide range of geometric parameters and features.

7.5 Comparison of numerical results with CIMAC method

It is clearly of interest to compare the peak stresses predicted by the numerical FE and BE methods with those predicted by the CIMAC M53 method, which is based on formulae derived from bending and torsion investigations made by the German Internal Combustion Engine Research Association (FVV). The datum crankthrow geometry is used as the basis for comparison, and the calculations are detailed in Appendix 10. There is much talk in the literature of hidden safety factors in the M53 calculation of peak fillet stresses (e.g. [35]). This is supported by the finding that under radial bending, the M53 method overpredicts the peak stresses by 34% at both fillets. However, under torsion, the results obtained from the numerical methods suggest that M53 underpredicts the peak stress by 42% at the crankpin fillet and 47% at the journal fillet. This may be due to the fact that the FE and BE methods simulate a free torsion loadcase.

Otherwise, if the torsional loadcase is truly more important than CIMAC consider, it may explain why Rasser, Resch and Priebsch [36] conclude that when the combined stresses over a complete crankshaft cycle are considered with the FE method, M53 does not lead to oversized crankshafts. In other words, CIMAC's overprediction of radial bending stresses may be offset by the underprediction of torsional stresses.

7.6 General summary

The work has displayed the suitability of the FE and BE methods for analysing stresses in crankshafts and investigating the effects of geometric changes.

The nominal stress work is of value because it culminates in a nominal stress that is based on the critical section between the fillets, yet is simple to calculate and is perfectly suited to the loadcases of bending and torsion.

The geometric analyses investigate all of the governing parameters of an overlapped crankshaft over a relatively wide range, and also study the effects of other features such as fillet shapes and dimples. The results show that it is possible to reduce peak stresses using these features, without necessitating a major re-design of the crankshaft or engine. Stress reductions of around 15% were achieved by optimising the datum crankthrow geometry.

The author hopes that this thesis goes some way to furthering the understanding of the stresses that exist within overlapped crankshafts, the methods of analysis, and the way in which the crankshaft geometry can affect the peak stresses.

REFERENCES

[1] CIMAC, M53 Unified Rule, Calculation of crankshafts for I.C. engines, 1986

[2] Alstom Engines Ltd, Mirrlees Blackstone, Bramhall Moor Lane, Hazel Grove, Stockport, Cheshire, SK7 5AH, England

[3] Langballe, M., "Investigations into the stressing of crankshafts for large Diesel engines", The Institute of Marine Engineers, 1966, p.9

[4] Stahl, G., "Der Einfluβ der Form auf die Spannungen in Kurbelwellen", Konstruction, Vol.10, Heft 2, 1958, p.61

[5] Hoshino, J., and Arai, J., "A study on the stress concentration factors of crankshafts", Japan Shipbuilding and Marine Engineering, Vol. 1966, p.33

[6] Leikin, A.S., "Stress concentration in crankshaft fillets", Russian Engineering Journal, Vol XL, Issue 5, 1960, p.14

[7] Pfender, M., Amedick, E., and Sonntag., G., "Einfluβ der Formgebung auf die Spannungsverteilung in Kurbelkröpfungen", M.T.Z., Vol. 27, 1966, p.225

[8] Fessler, H., and Sood, V.K., "Stress distributions in some Diesel engine crankshafts", Trans. ASME Diesel and Gas Engine Power Division Conference, Toronto, Paper No. 71-DGP-1, 1971

[9] Lowell, C. M., "Practical applications of crankshaft-geometry theories", Trans. ASME Diesel and Gas Engine Power Division Conference, New York, Paper No. 64-WA/OGP-5, 1964

[10] Arai, J., "The bending stress concentration factor of solid crankshaft", Bulletin of JSME, Vol. 8, 1965, p.322

[11] Donath, G., Seidemann, H., "Design of marine Diesel engine crankshafts: comparison of measured and calculated stresses using the proposed CIMAC rules", Trans. of The Institute of Marine Engineers, Vol. 97, Paper No. 25, 1985

[12] Volcy, G.C., Discussion of paper by Donath, G., Seidemann, H., "Design of marine Diesel engine crankshafts: comparison of measured and calculated stresses using the proposed CIMAC rules", Trans. of The Institute of Marine Engineers, Vol. 97, Paper No. 25, 1985, p.14

[13] Guagliano, M., Terranova, A., Vergani, L., "Theoretical and experimental study of the stress concentration factor in Diesel engine crankshafts", Journal of Mechanical Design, Trans. ASME, Vol. 115, 1993, p.47

[14] McNamara, P.M., Trevelyan, J., "Crankshaft stress analysis - the combination of finite element and boundary element techniques", Proc. Institute of Mechanical Engineers, 1991, p.197

[15] Becker, A.A., "The boundary element method in engineering", McGraw-Hill, London, 1992, p.4

[16] Rizzo, F.J., "An integral equation approach to boundary value problems of classical elastostatics", Quarterly of Applied Mathematics, Vol. 25, 1967, p.83

[17] Dulieu-Smith, J.M., Quinn, S., "Thermoelastic stress analysis of oblique holes in flat plates", Proceedings of the 3rd International Conference on Modern Practice in Stress and Vibration Analysis, Dublin, 1997, Pub: A. A. Balkema, Rotterdam, Ed: M. D. Gilchrist, p.389

[18] Dunton, R.M., Propetto, L., Murray, G.E., "Development of the B2400 engine", Journal of Engineering for Gas Turbines and Power, Trans. ASME, No. 4, Oct 1987, p.388

[19] Leikin, A.S., "A calculation method for estimating stresses at lubrication holes in crankshaft pins", Soviet Engineering Research, Vol. 2, No. 12, 1982, p.38

[20] Lowell, C.M., "Stress concentration factors for large power engine crankshafts", Trans. ASME Diesel and Gas Engine Power Division Conference, Houston, Texas, Paper No. 74.DGP-13, 1974

[21] Neuber, H., "Theory of notch stresses", J. W. Edwards, Michigan, 1946

[22] Peterson, R.E., "Stress concentration design factors", John Wiley & Sons, New York, 1953

[23] FEMGEN/FEMVIEW. Femsys Ltd, 1 St Albans Road, Leicester, LE2 1GF, England

[24] ABAQUS. Hibbitt, Karlsson & Sorensen, Inc, 1080 Main Street, Pawtucket, RI 02860-4847, USA

[25] Zienkiewicz, O.C., "The Finite Element Method in Engineering Science", McGraw-Hill, London, 1971

[26] BEASY. Computational Mechanics International Ltd, Ashurst Lodge, Ashurst, Southampton, Hants, SO40 7AA, England

[27] Fessler, H., Hyde, T.H., "The photoelastic stress analyses of MB430 (V-12) crankshafts under radial and tangential bending conditions", Department of Mechanical Engineering, University of Nottingham, UK, Internal Report to Mirrlees Blackstone (Stockport) Ltd, 1986

[28] Warrior, N.A., Hyde, T.H., "Experimental determination of stresses in KV16 Major Mark 3 and MB430 V16 crankshafts under bending and torsion loadings", Department of Mechanical Engineering, University of Nottingham, UK, Internal Report to Mirrlees Blackstone (Stockport) Ltd, 1995

[29] Microsoft Visual Basic Version 4.0., Microsoft Ltd.

[30] Bickley, I., D'Olier, V., Fessler, H., Hyde, T.H., Warrior, N.A., "Stresses and deformations in overlapped Diesel engine crankshafts, Part 1: Experimental results", Proc I Mech E, Vol. 212, Part D, 1998, p.187

[31] Tafreshi, A., Thorpe, T.E., "Numerical analysis of stresses at oblique holes in plates aubjected to tension and bending", Journal of Strain Analysis for Engineering Design, Vol. 30, No. 4, 1995, p.317

[32] Shivakumar, K.N., Newman, J.C., "Stress concentration equations for straight-shank and countershank holes in plates", Journal of Applied Mechanics, Trans. ASME, Vol. 62, No. 1, 1995, p.248

[33] Mahinfalah, M., Harms, M., "Stress concentrations associated with circular holes in cylinders and bone in torsion", Experimental Mechanics, Vol. 34, No. 3, 1994, p224

[34] Peterson, R.E., "Stress concentration design factors", John Wiley & Sons, New York, 1953, p.47

[35] Discussion of paper by Donath, G., Seidemann, H., "Design of marine Diesel engine crankshafts: comparison of measured and calculated stresses using the proposed CIMAC rules", Trans. of The Institute of Marine Engineers, Vol. 97, Paper No. 25, 1985, p.14

[36] Rasser, M.W., Resch, T., Priebsch, H.H., "Enhanced crankshaft stress calculation method and fatigue life evaluation", CIMAC Congress, Copenhagen, 1998, p.1491

APPENDIX 1

Definition of crankthrow geometry

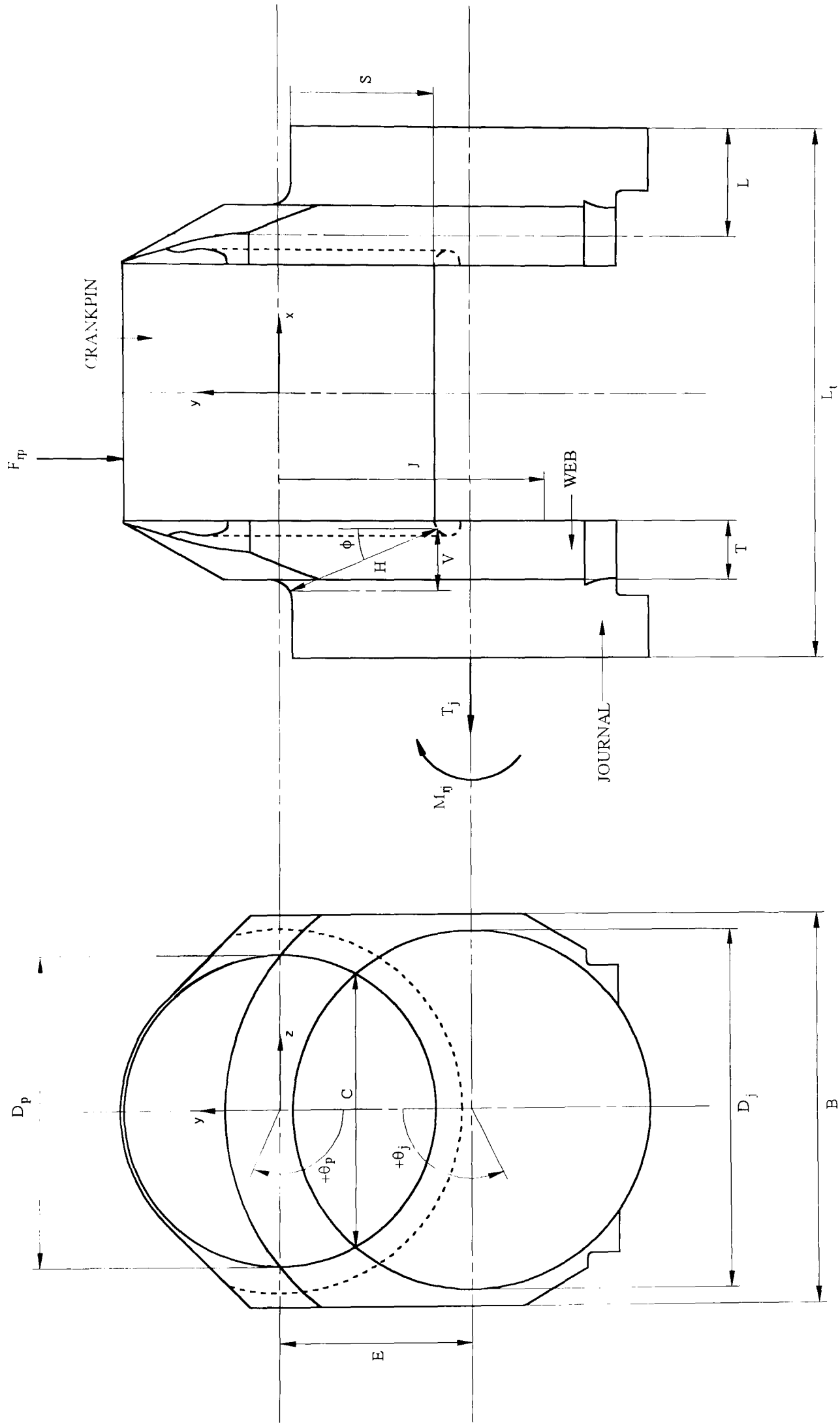

APPENDIX 2

Calculation of the reaction at the journal under radial bending

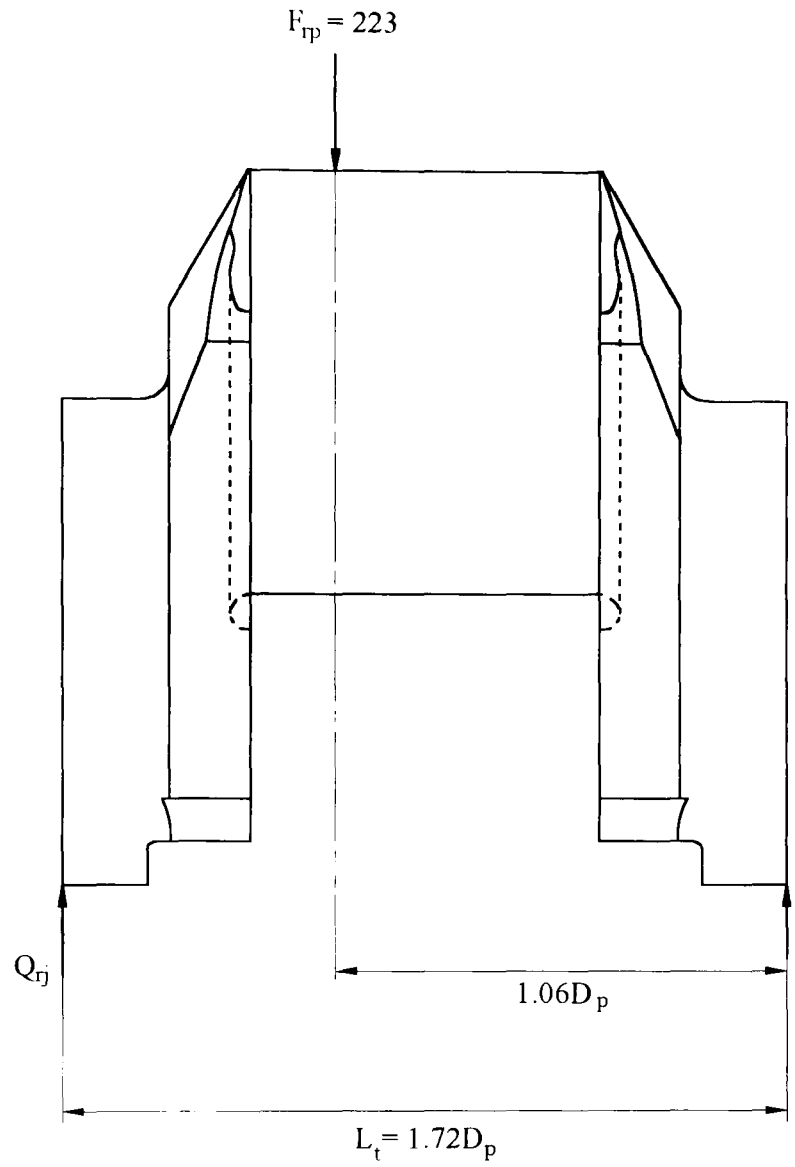

Figure A2.1

$$Q_{rj} = 223 \times \frac{1.06D_p}{1.72D_p}$$

$$\underline{\underline{Q_{rj} = 138}}$$

It is suggested that it is possible to apply loads $F_{rp} = 223$ to the crankpin, and $Q_{rj} = 138$ to a half crankthrow which is encastré at the crankpin centre, thus achieving the same bending moment distribution as in the full crankthrow.

APPENDIX 3

Calculation of central crankpin load

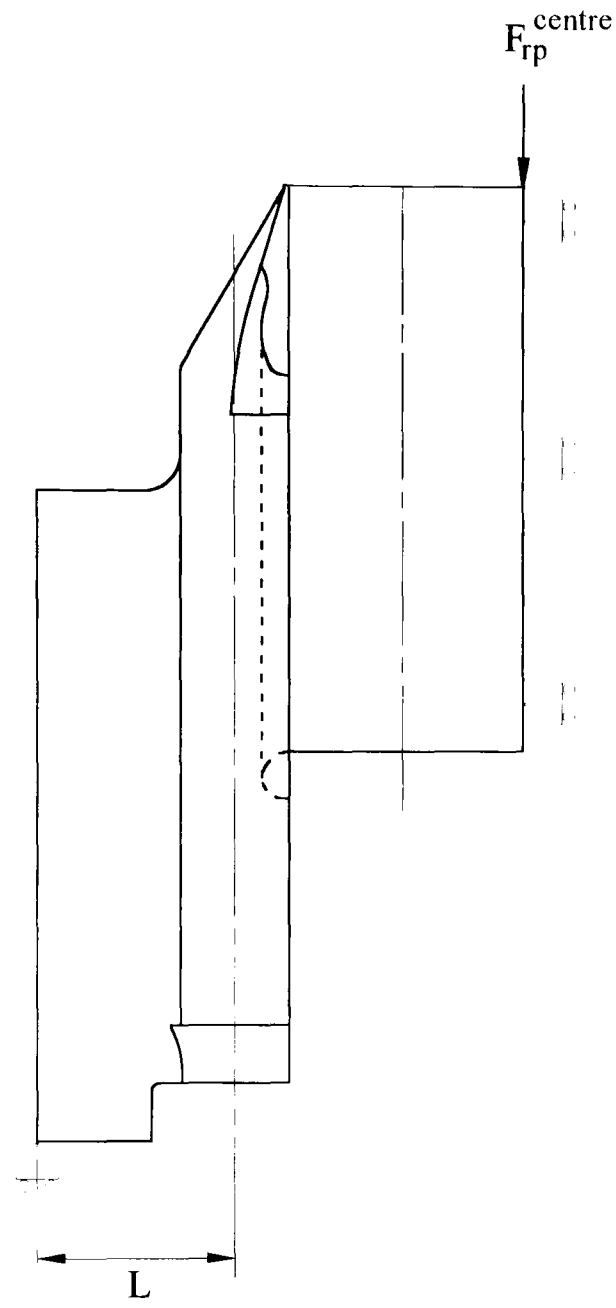

Figure A3.1

It has been shown in Appendix 2 that for a load $F_{rp} = 223$ applied at the quarter point of the crankpin, the reaction at the journal will be $Q_{rj} = 138$ for the analysed crankthrow geometry. This creates a bending moment at the web centre of 138L. Therefore, to preserve this bending moment when the arrangement in Figure A3.1 is used, F_{rp}^{centre} must also be equal to 138.

APPENDIX 4

Calculation of an eye-shape second moment of area about the neutral axis

Note: All notation relates to the figures presented in Appendix 4

Area of sector, A

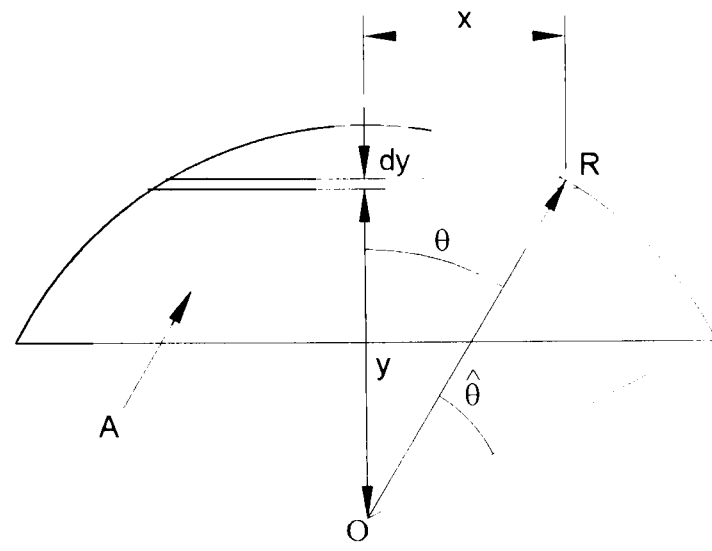

Figure A4.1

$$y = R\cos\theta$$

$$x = R\sin\theta$$

$$dy = -R\sin\theta\ d\theta$$

$$A = -\int_{\theta=0}^{\theta=\hat{\theta}} 2R\sin\theta \times \left(-R\sin\theta\right) d\theta$$

$$A = 2R^2 \int_0^{\hat{\theta}} \sin^2\theta\ d\theta$$

$$A = R^2 \int_0^{\hat{\theta}} \left(1 - \cos 2\theta\right) d\theta \qquad *$$

$$A = R^2 \left[\theta - \frac{\sin 2\theta}{2}\right]_0^{\hat{\theta}}$$

$$A = R^2 \left[\hat{\theta} - \frac{\sin 2\hat{\theta}}{2}\right]$$

Position of centroid, $\bar{y}$

$$A\bar{y} = -\int_{\theta=0}^{\theta=\hat{\theta}} 2R\sin\theta \times R\cos\theta\left(-R\sin\theta\right)\, d\theta$$

$$A\bar{y} = 2R^3\int_0^{\hat{\theta}} \sin^2\theta\cos\theta\, d\theta$$

$$A\bar{y} = \frac{2R^3}{2}\int_0^{\hat{\theta}} \left(1-\cos 2\theta\right)\cos\theta\, d\theta$$

$$A\bar{y} = R^3\int_0^{\hat{\theta}} \cos\theta - \cos\theta\cos 2\theta\, d\theta$$

$$A\bar{y} = R^3\left[\sin\theta - \frac{\left(2\cos\theta\sin 2\theta - \sin\theta\cos 2\theta\right)}{3}\right]_0^{\hat{\theta}} \quad **$$

$$A\bar{y} = R^3\left[\sin\hat{\theta} - \frac{\left(2\cos\hat{\theta}\sin 2\hat{\theta} - \sin\hat{\theta}\cos 2\hat{\theta}\right)}{3}\right]$$

$$\bar{y} = R\left[\frac{\sin\hat{\theta} - \dfrac{\left(2\cos\hat{\theta}\sin 2\hat{\theta} - \sin\hat{\theta}\cos 2\hat{\theta}\right)}{3}}{\hat{\theta} - \dfrac{\sin 2\hat{\theta}}{2}}\right]$$

Second moment of area about O, $\sum Ay^2$

$$\sum Ay^2 = -\int_{\theta=0}^{\theta=\hat{\theta}} 2R\sin\theta(-R\sin\theta)\,d\theta \times R^2\cos^2\theta$$

$$\sum Ay^2 = 2R^4\int_0^{\hat{\theta}} \sin^2\theta\cos^2\theta\,d\theta$$

$$\sum Ay^2 = 2R^4\int_0^{\hat{\theta}} \frac{\sin^2 2\theta}{4}\,d\theta \qquad ***$$

$$\sum Ay^2 = \frac{2R^4}{4}\int_0^{\hat{\theta}} \frac{(1-\cos 4\theta)}{2}\,d\theta$$

$$\sum Ay^2 = \frac{R^4}{4}\left[\theta - \frac{\sin 4\theta}{4}\right]_0^{\hat{\theta}}$$

$$\sum Ay^2 = \frac{R^4}{4}\left(\hat{\theta} - \frac{\sin 4\hat{\theta}}{4}\right)$$

* $\sin^2\theta = \dfrac{1-\cos 2\theta}{2}$

** $i = \int \cos\theta\cos 2\theta\,d\theta$

$i = \sin\theta\cos 2\theta + 2\int \sin\theta\sin 2\theta\,d\theta$

$i = \sin\theta\cos 2\theta + 2\left[-\sin 2\theta\cos\theta + \int \cos\theta\cos 2\theta\,d\theta\right]$

$i = \sin\theta\cos 2\theta - 2\sin 2\theta\cos\theta + 4i$

$i = \dfrac{2\cos\theta\sin 2\theta - \sin\theta\cos 2\theta}{3}$

*** $\sin 2\theta = 2\sin\theta\cos\theta$

Application to intersecting circles

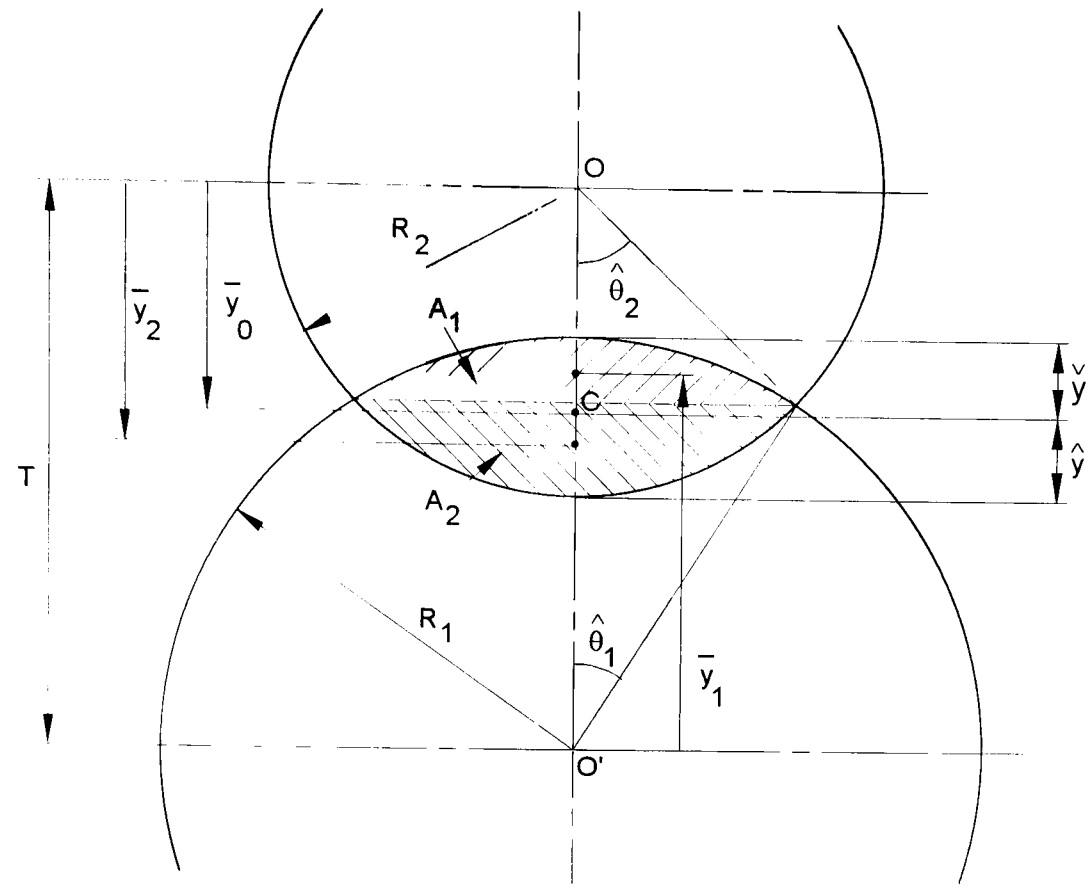

Figure A4.2

$$R_1 \cos\hat{\theta}_1 + R_2 \cos\hat{\theta}_2 = T$$

$$R_1 \sin\hat{\theta}_1 = R_2 \sin\hat{\theta}_2$$

$$\cos\hat{\theta}_2 = \frac{T - R_1 \cos\hat{\theta}_1}{R_2}$$

$$\cos^2\hat{\theta}_2 = \frac{T^2 - 2TR_1 \cos\hat{\theta}_1 + R_1^2 \cos^2\hat{\theta}_1}{R_2^2}$$

$$\sin^2\hat{\theta}_2 = \frac{R_1^2 \sin^2\hat{\theta}_1}{R_2^2}$$

$$\sin^2\hat{\theta}_2 + \cos^2\hat{\theta}_2 = \frac{T^2 - 2TR_1 \cos\hat{\theta}_1 + R_1^2 \cos^2\hat{\theta}_1 + R_1^2 \sin^2\hat{\theta}_1}{R_2^2}$$

$$R_2^2 = T^2 - 2TR_1 \cos\hat{\theta}_1 + R_1^2$$

$$\hat{\theta}_1 = \cos^{-1}\left(\frac{T^2 + {R_1}^2 - {R_2}^2}{2TR_1}\right)$$

$$\hat{\theta}_2 = \sin^{-1}\left(\frac{R_1 \sin\hat{\theta}_1}{R_2}\right)$$

$$A_1 = {R_1}^2\left[\hat{\theta}_1 - \frac{\sin 2\hat{\theta}_1}{2}\right]$$

$$A_2 = {R_2}^2\left[\hat{\theta}_2 - \frac{\sin 2\hat{\theta}_2}{2}\right]$$

$$\overline{y_1} = R_1\left[\frac{\sin\hat{\theta}_1 - \frac{\left(2\cos\hat{\theta}_1 \sin 2\hat{\theta}_1 - \sin\hat{\theta}_1 \cos 2\hat{\theta}_1\right)}{3}}{\hat{\theta}_1 - \frac{\sin 2\hat{\theta}_1}{2}}\right]$$

$$\overline{y_2} = R_2\left[\frac{\sin\hat{\theta}_2 - \frac{\left(2\cos\hat{\theta}_2 \sin 2\hat{\theta}_2 - \sin\hat{\theta}_2 \cos 2\hat{\theta}_2\right)}{3}}{\hat{\theta}_2 - \frac{\sin 2\hat{\theta}_2}{2}}\right]$$

Position of overall centroid from O, $\bar{y}_o$

$$A_1\left(T-\bar{y}_o\right)+A_2\bar{y}_o=\left(A_1+A_2\right)\bar{y}_o$$

$$\bar{y}_o=\frac{A_1\left(T-\bar{y}_o\right)+A_2\bar{y}_o}{\left(A_1+A_2\right)}$$

Second moments of area about O, $\bar{I}_{1_o}$ and $\bar{I}_{2_o}$

$$\bar{I}_{1_o}=\frac{R_1^{\,4}}{4}\left(\hat{\theta}_1-\frac{\sin 4\hat{\theta}}{4}\right)-A_1\bar{y}_1^{\,2}+A_1\left(T-\bar{y}_1\right)^2$$

$$\bar{I}_{2_o}=\frac{R_2^{\,4}}{4}\left(\hat{\theta}_2-\frac{\sin 4\hat{\theta}_2}{4}\right)$$

Second moment of area about C, $\bar{I}_c$

$$\bar{I}_c=\bar{I}_{1_o}+\bar{I}_{2_o}-\left(A_1+A_2\right)\bar{y}_o^{\,2}$$

Maximum and minimum bending stresses

$$\hat{y} = R_2 - \bar{y}_o$$

$$\check{y} = R_1 - \left(T - \bar{y}_o\right)$$

$$\check{y} = \bar{y}_o + R_1 - T$$

$$\hat{\sigma} = \frac{M\hat{y}}{I_c}$$

$$\check{\sigma} = \frac{M\check{y}}{I_c}$$

APPENDIX 5

Calculation of a slanted eye-shape second moment of area about the neutral axis

Note: All notation relates to the figures presented in Appendix 5

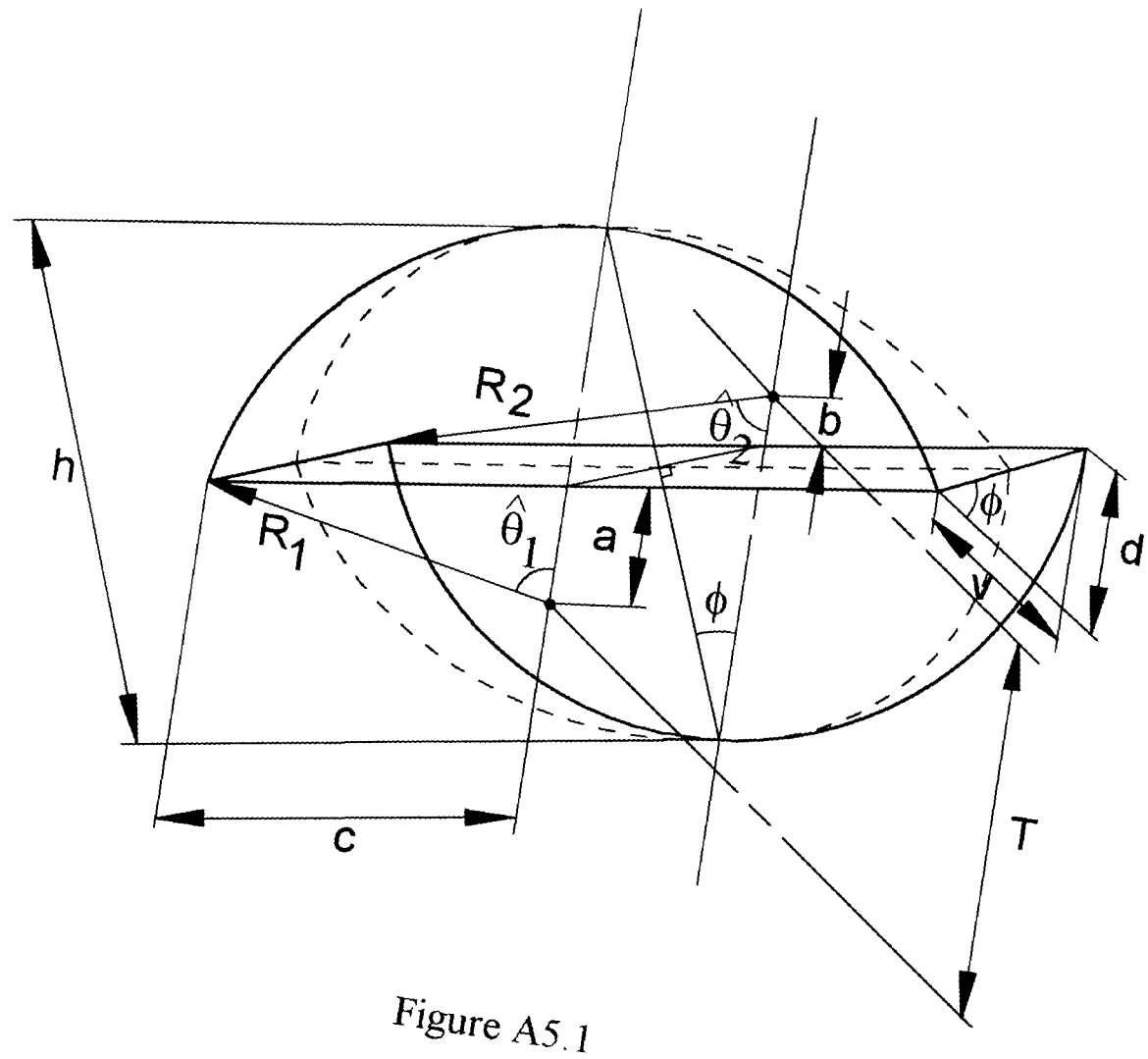

Figure A5.1

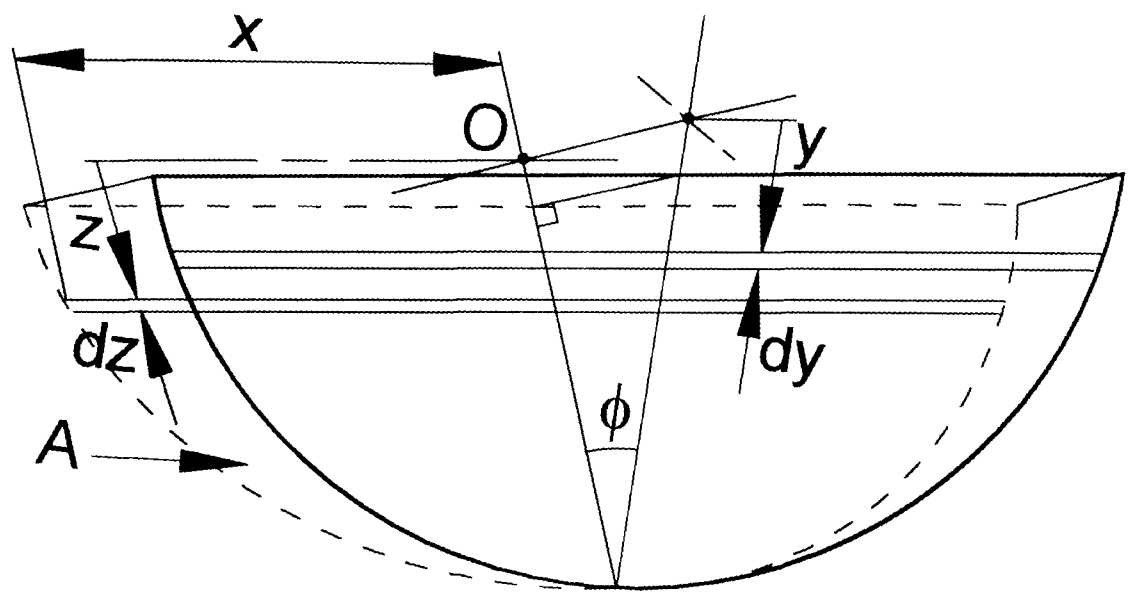

Figure A5.2

Area of sector, A

$$z = y\cos\phi$$
$$y = R\cos\theta$$
$$x = R\sin\theta$$
$$z = R\cos\theta\cos\phi$$
$$dz = -R\sin\theta\cos\phi\, d\theta$$

$$A = -2\int_{\theta=0}^{\theta=\hat{\theta}} x\, dz$$

$$A = 2\int_{\theta=0}^{\theta=\hat{\theta}} R\sin\theta \times R\sin\theta\cos\phi\, d\theta$$

$$A = 2R^2\cos\phi\int_0^{\hat{\theta}} \sin^2\theta\, d\theta$$

$$A = R^2\cos\phi\int_0^{\hat{\theta}} (1-\cos 2\theta)\, d\theta$$

$$A = R^2\cos\phi\left[\theta - \frac{\sin 2\theta}{2}\right]_0^{\hat{\theta}}$$

$$A = R^2\cos\phi\left[\hat{\theta} - \frac{\sin 2\hat{\theta}}{2}\right]$$

Position of centroid, $\bar{z}$

$$A\bar{z} = -2\int_{\theta=0}^{\theta=\hat{\theta}} xz\,dz$$

$$A\bar{z} = 2\int_{\theta=0}^{\theta=\hat{\theta}} R\sin\theta \times R\cos\theta\cos\phi \times R\sin\theta\cos\phi\,d\theta$$

$$A\bar{z} = 2R^3\cos^2\phi\int_0^{\hat{\theta}} \sin^2\theta\cos\theta\,d\theta$$

$$A\bar{z} = R^3\cos^2\phi\int_0^{\hat{\theta}} (1-\cos 2\theta)\cos\theta\,d\theta$$

$$A\bar{z} = R^3\cos^2\phi\int_0^{\hat{\theta}} \cos\theta - \cos\theta\cos 2\theta\,d\theta$$

$$A\bar{z} = R^3\cos^2\phi\left[\sin\theta - \frac{(2\cos\theta\sin 2\theta - \sin\theta\cos 2\theta)}{3}\right]_0^{\hat{\theta}}$$

$$A\bar{y} = R^3\cos^2\phi\left[\sin\hat{\theta} - \frac{\left(2\cos\hat{\theta}\sin 2\hat{\theta} - \sin\hat{\theta}\cos 2\hat{\theta}\right)}{3}\right]$$

$$\bar{z} = R\cos\phi\left[\frac{\sin\hat{\theta} - \frac{\left(2\cos\hat{\theta}\sin 2\hat{\theta} - \sin\hat{\theta}\cos 2\hat{\theta}\right)}{3}}{\hat{\theta} - \frac{\sin 2\hat{\theta}}{2}}\right]$$

Second moment of area about O, $\sum Az^2$

$$\sum Az^2 = -2\int_{\theta=0}^{\theta=\hat{\theta}} xz^2\, dz$$

$$\sum Az^2 = 2\int_{\theta=0}^{\theta=\hat{\theta}} R\sin\theta R^2\cos^2\theta\cos^2\phi(-R\sin\theta\cos\phi)\, d\theta$$

$$\sum Az^2 = 2R^4\cos^3\phi\int_0^{\hat{\theta}}\sin^2\theta\cos^2\theta\, d\theta$$

$$\sum Az^2 = 2R^4\cos^3\phi\int_0^{\hat{\theta}}\frac{\sin^2 2\theta}{4}\, d\theta$$

$$\sum Az^2 = \frac{2R^4\cos^3\phi}{4}\int_0^{\hat{\theta}}\frac{(1-\cos 4\theta)}{2}\, d\theta$$

$$\sum Az^2 = \frac{R^4\cos^3\phi}{4}\left[\theta - \frac{\sin 4\theta}{4}\right]_0^{\hat{\theta}}$$

$$\sum Az^2 = \frac{R^4\cos^3\phi}{4}\left(\hat{\theta} - \frac{\sin 4\hat{\theta}}{4}\right)$$

Application to intersecting ellipses

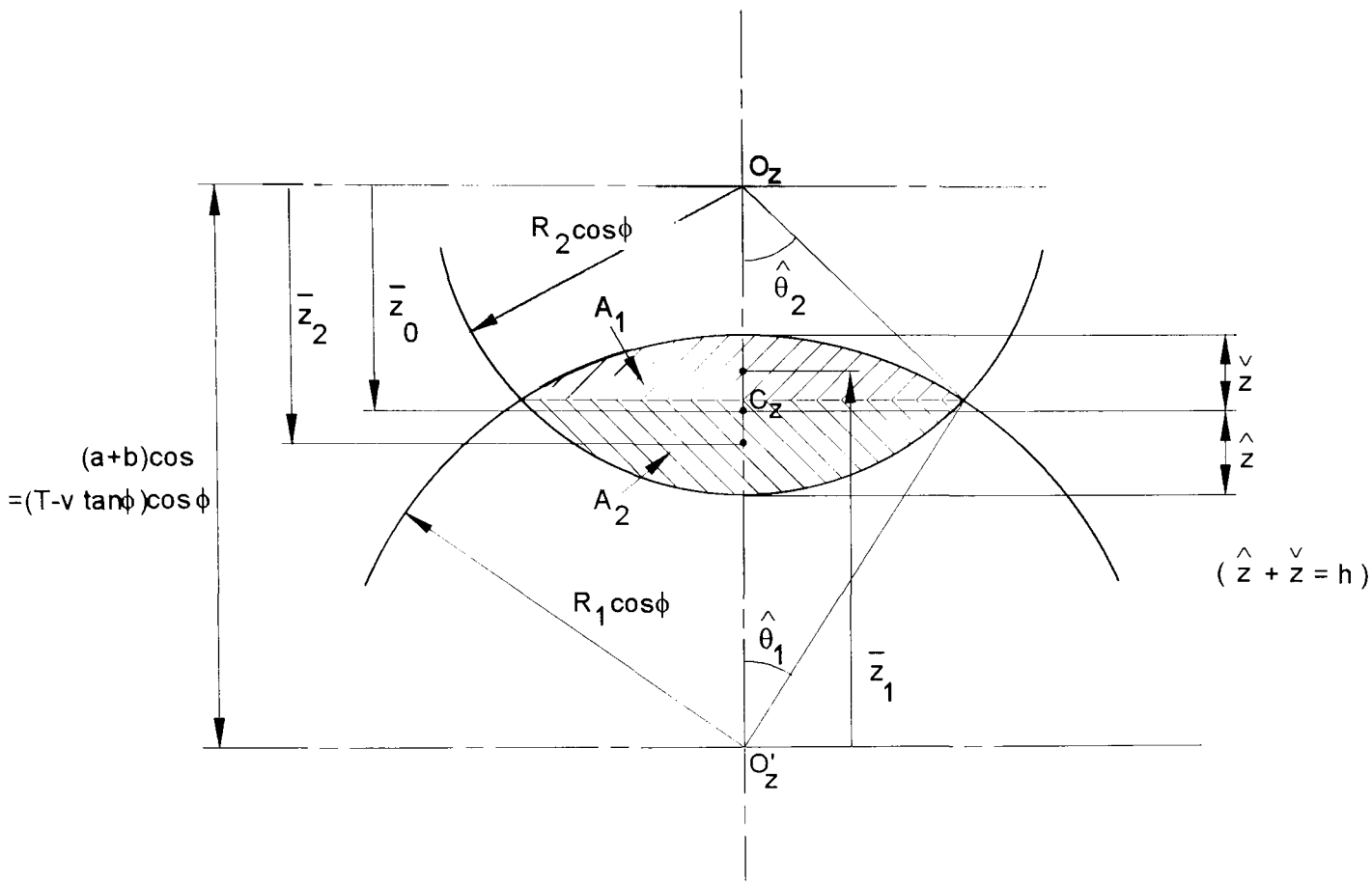

Figure A5.3

$$a = R_1 \cos\phi$$

$$R_1 \sin\hat{\theta}_1 = R_2 \sin\hat{\theta}_2$$

$$b^2 + c^2 = R_2{}^2$$

$$a^2 + c^2 = R_1{}^2$$

$$a^2 + R_2{}^2 - b^2 = R_1{}^2$$

$$a^2 - b^2 = R_1{}^2 - R_2{}^2$$

$$a + v\tan\phi + b = T$$

$$b^2 = (T - a - v\tan\phi)(T - a - v\tan\phi)$$

$$b^2 = T^2 + a^2 + v^2\tan^2\phi - 2Ta - 2Tv\tan\phi + 2av\tan\phi$$

$$a^2 - b^2 = a(2T - 2v\tan\phi) - T^2 - v^2\tan^2\phi + 2Tv\tan\phi$$

$$R_1^2 - R_2^2 = R_1\cos\theta_1(2T - 2v\tan\phi) - T^2 - v^2\tan^2\phi + 2Tv\tan\phi$$

$$\theta_1 = \cos^{-1}\left(\frac{T^2 + R_1^2 - R_2^2 + v^2\tan^2\theta - 2Tv\tan\phi}{2R_1(T - v\tan\phi)}\right)$$

$$\theta_2 = \sin^{-1}\left(\frac{R_1\sin\theta_1}{R_2}\right)$$

$$A_1 = R_1^2\cos\phi\left[\hat{\theta}_1 - \frac{\sin 2\hat{\theta}_1}{2}\right]$$

$$A_2 = R_2^2\cos\phi\left[\hat{\theta}_2 - \frac{\sin 2\hat{\theta}_2}{2}\right]$$

$$\bar{z}_1 = R_1\cos\phi\left[\frac{\sin\hat{\theta}_1 - \frac{\left(2\cos\hat{\theta}_1\sin 2\hat{\theta}_1 - \sin\hat{\theta}_1\cos 2\hat{\theta}_1\right)}{3}}{\hat{\theta}_1 - \frac{\sin 2\hat{\theta}_1}{2}}\right]$$

$$\bar{z}_2 = R_2\cos\phi\left[\frac{\sin\hat{\theta}_2 - \frac{\left(2\cos\hat{\theta}_2\sin 2\hat{\theta}_2 - \sin\hat{\theta}_2\cos 2\hat{\theta}_2\right)}{3}}{\hat{\theta}_2 - \frac{\sin 2\hat{\theta}_2}{2}}\right]$$

Position of overall centroid from O_z, $\bar{z}_o$

$$A_1\left(\left(T - v\tan\phi\right)\cos\phi - \bar{z}_1\right) + A_2\bar{z}_2 = \left(A_1 + A_2\right)\bar{z}_0$$

$$\bar{z}_0 = \frac{A_1\left(\left(T - v\tan\phi\right)\cos\phi - \bar{z}_1\right) + A_2\bar{z}_2}{\left(A_1 + A_2\right)}$$

Second moments of area about O_z, $\bar{I}_{1_{o_z}}$ and $\bar{I}_{2_{o_z}}$

$$I_{1_{o_z}} = \frac{R_1{}^4\cos^3\phi}{4}\left(\hat{\theta}_1 - \frac{\sin 4\hat{\theta}_1}{4}\right) - A_1\bar{z}_1{}^2 + A_1\left(\left(T - v\tan\phi\right)\cos\phi - \bar{z}_1\right)^2$$

$$I_{2_{o_z}} = \frac{R_2{}^4\cos^3\phi}{4}\left(\hat{\theta}_2 - \frac{\sin 4\hat{\theta}_2}{4}\right)$$

Second moment of area about C_z, $\bar{I}_{c_z}$

$$\bar{I}_{c_z} = \bar{I}_{1_{o_z}} + \bar{I}_{2_{o_z}} - \left(A_1 + A_2\right)\bar{z}_o{}^2$$

Maximum and minimum bending stresses

$$\hat{z} = R_2 \cos\phi - \bar{z}_o$$

$$\check{z} = R_1 \cos\phi - \left(\left(T - v\tan\phi\right)\cos\phi - \bar{z}_o\right)$$

$$\check{z} = \bar{z}_o + R_1 \cos\phi - \left(T - v\tan\phi\right)\cos\phi$$

$$\hat{\sigma} = \frac{M\hat{z}}{I_{c_z}}$$

$$\check{\sigma} = \frac{M\check{z}}{I_{c_z}}$$

APPENDIX 6

Slanted eye-shape overlap angles

(a)

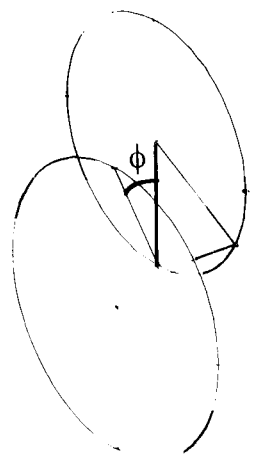

Consider 2 overlapping circles, seperated by some distance representing the web. Note the slanted minimum section at angle ϕ from the vertical.

(b)

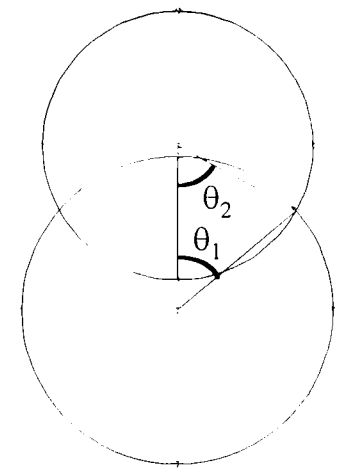

Look on one end to see the overlap angles θ_1 and θ_2.

(c)

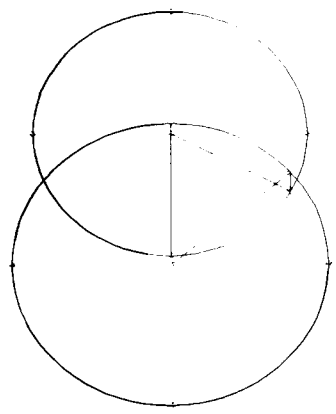

Rotate down through an angle of ϕ so that the minimum section is vertical. The overlap angles have now changed.

(d)

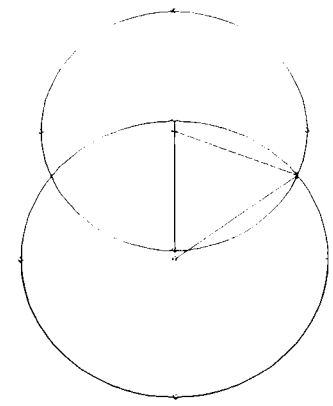

Mark on the new overlap angles, and consider that the drawing is still at angle ϕ. The new eyeshape has a larger area.

(e)

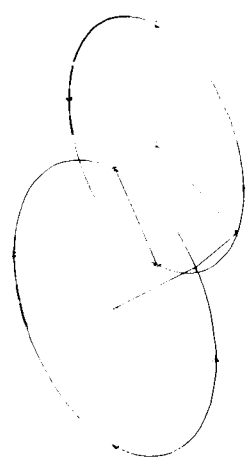

Rotate back to the original view and it is clear that the new eyeshape is now slanted.

(f)

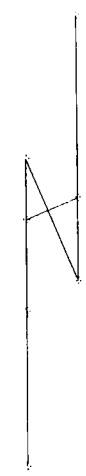

Looking sideways on, the angle of slant is perpendicular to the minimum section between the two circles.

Figure A6.1

APPENDIX 7

Calculation of the compressive stress in the web under radial bending

Normal force on minimum section, N

$$N = Q_{rj} \sin\phi$$

Compressive stress, σ_c

$$\sigma_c = \frac{N}{HC}$$

To include the compressive stress in the calculated nominal stress, subtract it from the tensile nominal stress at the crankpin fillet, and add it to the compressive nominal stress at the journal fillet.

$$\sigma^{+c}_{nom\,p} = \sigma_{nom\,p} - \sigma_c$$

$$\sigma^{+c}_{nom\,j} = \sigma_{nom\,j} + \sigma_c$$

APPENDIX 8

Procedure for calculating the reaction at the journal for various web thicknesses

For the purposes of the web thickness analyses, the applied crankpin load is kept constant. As the web thickness is varied, the axial distance between the applied crankpin load and journal reaction varies accordingly. For example, if the web thickness is increased from $0.27D_p$ to $0.35D_p$, the axial distance between the two loads increases by $0.08D_p$ from $0.65D_p$ to $0.73D_p$.

If the web thickness changes by P, then the crankthrow span, L_t, changes by 2P. The reaction at the journal, Q_{rj1}, is calculated as follows;

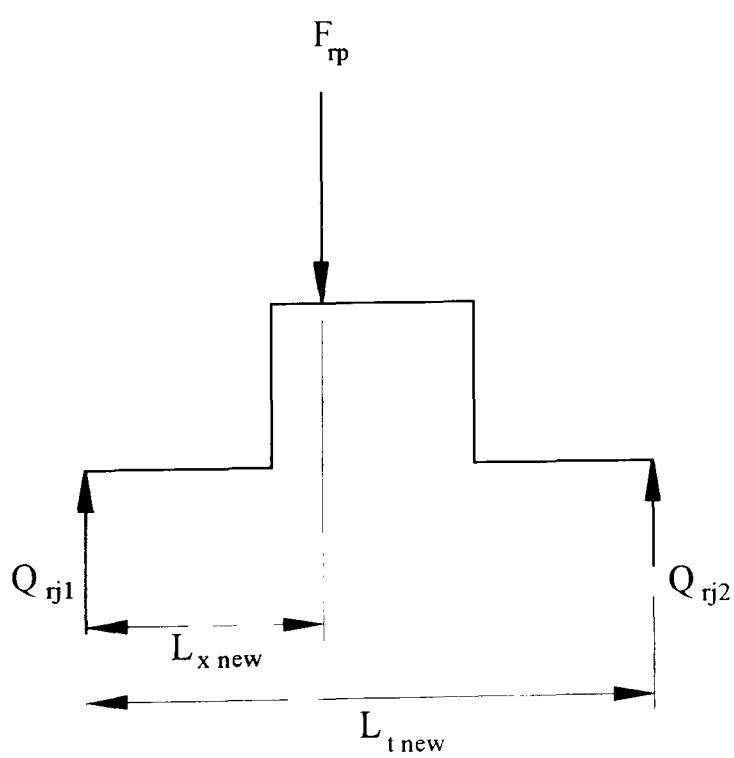

Figure A8.1

$$Q_{rj1} = \frac{F_{rp} \times (L_{tnew} - L_{xnew})}{L_{tnew}}$$

where

$$L_{tnew} = L_t + 2P$$
$$L_{xnew} = L_x + P$$

Using this method, the journal reactions calculated for the web thicknesses investigated are as detailed in Table A8.1.

Table A8.1 Reactions applied at journal for various web thicknesses

T/D_p	P/D_p	Q_{rj1} *
0.12	-0.077	140.6
0.19	0.000	138.0
0.27	0.077	135.8
0.35	0.154	134.0
0.38	0.192	133.2

*F_{rp} = 223N

APPENDIX 9

Comparison of numerical results with CIMAC method

The formulae used in the CIMAC M53 method of calculating crankshaft acceptability are detailed fully in Chapter 2. The method involves the calculation of nominal stress values, σ_{bnom} and τ_{nom} and (for radial bending and torsion), a shear stress value, σ_{qnom}, and stress concentration factors K_{bp}, K_{bj}, K_{tp} and K_{tj}. The nominal stress values are multiplied by the stress concentration factors to obtain values for the maximum bending and torsional fillet stresses, σ_{bp}, σ_{bj}, τ_p and τ_j.

The maximum fillet stresses are calculated using the M53 method, for the datum crankthrow geometry used in the numerical analyses. The radial bending load is applied to the FE model at the crankpin centre to assist comparison of the numerical and M53 results. The following data is obtained.

Nominal stresses:

$\sigma_{bnom} = 0.371$

$\sigma_{qnom} = 0.034$

$\tau_{nom\ p} = 0.037$

$\tau_{nom\ j} = 0.024$

Stress concentration factors:

$K_{bp} = 0.731$

$K_{bj} = 0.743$

K_q = 2.244

K_{tp} = 2.651

K_{tj} = 2.755

Maximum stress:

$\sigma_{bp} = K_{bp}.\sigma_{bnom}$

$= \underline{0.271}$ Maximum crankpin fillet bending stress

$\sigma_{bj} = K_{bj}.\sigma_{bnom} + K_q.\sigma_{qnom}$

$= \underline{0.352}$ Maximum journal fillet bending stress

$\tau_p = K_{tp}.\tau_{nom\,p}$

$= \underline{0.098}$ Maximum crankpin fillet torsional stress

$\tau_j = K_{tj}.\tau_{nom\,j}$

$= \underline{0.066}$ Maximum journal fillet torsional stress

The equivalent values calculated with the FE method are presented in Table A9.1

Table A9.1 Maximum fillet stresses calculated by M53 and FE methods

	M53 method	**FE method**	**Difference** (M53-FE)/FE
σ_{bp}	0.271	0.203	+34%
σ_{bj}	0.352	0.263	+34%
τ_p	0.098	0.169*	-42%
τ_j	0.066	0.126*	-47%

*Free torsion